

Chemistry of Atmospheric Excitation Processes

G.E. Caledonia
D.B. Oakes
B.L. Upschulte
R.H. Krech
H.C. Murphy
J.F. Cronin

L.G. Piper
W.T. Rawlins
W.J. Marinelli
B.D. Green
M.E. Fraser
K.W. Holtzclaw

Physical Sciences, Inc.
20 New England Business Center
Andover, MA 01810

January 2002

Final Report

APPROVED FOR PUBLIC RELEASE; DISTRIBUTION IS UNLIMITED.



AIR FORCE RESEARCH LABORATORY
Space Vehicles Directorate
29 Randolph Rd
AIR FORCE MATERIEL COMMAND
Hanscom AFB, MA 01731-3010

20020520 219

This technical report has been reviewed and is approved for publication.



DEAN F. KIMBALL
Contract Manager



JOHN H. SCHUMMERS, Chief
Advanced Optical Technologies Branch

This report has been reviewed by the ESC Public Affairs Office (PA) and is releasable to the National Technical Information Service (NTIS).

Qualified requestors may obtain additional copies from the Defense Technical Information Center (DTIC). All others should apply to the National Technical Information Service (NTIS).

If your address has changed, if you wish to be removed from the mailing list, or if the addressee is no longer employed by your organization, please notify PL/IM, 29 Randolph Road, Hanscom AFB MA 01731-3010. This will assist us in maintaining a current mailing list.

Do not return copies of this report unless contractual obligations or notices on a specific document require that it be returned.

REPORT DOCUMENTATION PAGE			Form Approved OMB No. 0704-0188	
Public reporting burden for this collection of information is estimated to average 1 hour per response, including the time for reviewing instructions, searching existing data sources, gathering and maintaining the data needed, and completing and reviewing the collection of information. Send comments regarding this burden estimate or any other aspect of this collection of information, including suggestions for reducing this burden, to Washington Headquarters Services, Directorate for Information Operations and Reports, 1215 Jefferson Davis Highway, Suite 1204, Arlington, VA 22202-4302, and to the Office of Management and Budget, Paperwork Reduction Project (0704-0188), Washington, DC 20503.				
1. AGENCY USE ONLY (Leave blank)		2. REPORT DATE January 2002		3. REPORT TYPE AND DATES COVERED Final - 9/93 - 8/00
4. TITLE AND SUBTITLE Chemistry of Atmospheric Excitation Processes			5. FUNDING NUMBERS F19628-93-C-0131 PE 61102F PR 2303 TA GD WU AB	
6. AUTHOR(S) G.E. Caledonia, D. B. Oakes, B.L. Upschulte, R.H. Krech, H.C. Murphy, J.F. Cronin, L.G. Piper, W.T. Rawlins, W.J. Marinelli, B.D. Green, M.E. Fraser, and K.W. Holtzclaw				
7. PERFORMING ORGANIZATION NAME(S) AND ADDRESS(ES) Physical Sciences Inc. 20 New England Business Center Andover, MA 01810			8. PERFORMING ORGANIZATION REPORT NUMBER PSI-1192/TR-1706	
9. SPONSORING/MONITORING AGENCY NAME(S) AND ADDRESS(ES) Air Force Research Laboratory/VSBM 29 Randolph Rd. Hanscom Air Force Base, MA 01731-3010 Contract Manager: Dean Kimball			10. SPONSORING/MONITORING AGENCY REPORT NUMBER AFRL-VS-TR-2001-1543	
11. SUPPLEMENTARY NOTES				
12a. DISTRIBUTION/AVAILABILITY STATEMENT Distributed unlimited; approved for Public Release.			12b. DISTRIBUTION CODE	
13. ABSTRACT (Maximum 200 words) We present here the findings of several investigations into the sources and magnitudes for excitation and collisional processes giving rise to atmospheric signatures from vibrationally and rotational excited molecular states including: vibrational energy transfer from nitrogen to CO ₂ , (Continued)				
14. SUBJECT TERMS chemical reactors, fast atoms, NO, vibrational excitation, collisional relaxation, chemiluminescence, COCHISE			15. NUMBER OF PAGES 178	
			16. PRICE CODE	
17. SECURITY CLASSIFICATION OF REPORT Unclassified	18. SECURITY CLASSIFICATION OF THIS PAGE Unclassified	19. SECURITY CLASSIFICATION OF ABSTRACT Unclassified	20. LIMITATION OF ABSTRACT SAR	

NSN 7540-01-280-5500

Standard Form 298 (Rev. 2-89) (EG)
Prescribed by ANSI Std. Z39-18
Designed using Perform Pro, WHS/DIOR, Oct. 94

UNCLASSIFIED
SECURITY CLASSIFICATION OF THIS PAGE

CLASSIFIED BY:

DECLASSIFY ON:

13. ABSTRACT (Continued)

production processes for high levels of NO(v,J), the NO dipole moment (including centrifugal distortion) and infrared transition strengths, relaxation mechanisms for relaxation of high rotational states of vibrationally excited OH, the role of translational energy in increasing the reaction cross-section and product molecule excitation for nitrogen atoms to produce NO and for atomic oxygen collisions with hydrocarbon molecules. We also present data acquired using a hyperspectral imager to extract excited molecular emissions from structured scenes, and report on refurbishment activities on the COCHISE cryogenic facility.

SECURITY CLASSIFICATION OF THIS PAGE
UNCLASSIFIED

CONTENTS

<u>Section</u>	<u>Page</u>
1. REVIEW OF N ₂ /CO ₂ VIBRATIONAL EXCHANGE KINETICS	1
1.1 Introduction	1
1.2 Review	1
1.3 CO ₂ Excited State Transfer Rate Studies	5
1.4 Experimentally Derived Rate Constants	7
1.5 Bibliography of Papers Reviewed	11
2. INVESTIGATIONS OF NO (v,J) FORMATION	13
2.1 Experimental	13
2.2 Results	15
3. THE DIPOLE MOMENT AND INFRARED TRANSITION STRENGTHS OF NITRIC OXIDE	21
4. THE EFFECTS OF CENTRIFUGAL DISTORTION ON THE INFRARED RADIATIVE TRANSITION PROBABILITIES OF NO(X ² Π).....	22
5. ROTATIONAL RELAXATION OF HIGH-N STATES OF OH (X ² Π, v=1-3) by O ₂	23
6. THE REACTION OF FAST N-ATOMS WITH O ₂	24
6.1 Introduction	24
6.2 Beam Composition	24
6.3 Directed Velocity	26
6.4 Crossed Beam Experiments	29
6.5 Beam Composition	32
7. EVALUATION OF FAST ATOM CONTRIBUTIONS IN COCHISE EXPERIMENTS	37
7.1 Introduction	37
7.2 Discharge Tube Configuration	37
7.3 Kinetic Modeling Analysis	38
7.4 Contributions from N ⁺	41
7.5 COCHISE Observations	42
7.6 Conclusions	43
8. FAST ATOM INTERCITONS WITH HYDROCARBONS	44
9. ONE KILOMETER PER SECOND ATOMIC OXYGEN SOURCE	47

CONTENTS (Continued)

<u>Section</u>	<u>Page</u>
10. ADAPTIVE INFRARED IMAGING SPECTRORADIOMETER.....	48
10.1 Overview	48
10.2 Hyperspectral Imaging Band Selection and Analysis.....	48
10.3 Data Collection and Analysis	50
11. COCHISE REFURBISHMENT.....	54
12. REFERENCES.....	56

LIST OF APPENDICES

1 - Energy Transfer of Carbon Dioxide by Electron Irradiated Nitrogen	59
2 - The Dipole Moment and Infrared Transition Strengths of Nitric Oxide.....	81
3 - The Effects of Centrifugal Distortion on the Infrared Radiative Transition Probabilities of NO($X^2\Pi$)	115
4 - Rotational Relaxation of High-N States of OH ($X^2\Pi$, $v=1-3$) by O ₂	129
5 - Products of the Reaction of 8 km/s N(⁴ S) and O ₂	139
6 - Infrared Emission Produced in the Reaction of Fast Oxygen Atoms and Armine Molecules	147
7 - <i>AIRIS</i> Hyperspectral Imaging of Aircraft and Backgrounds	159

FIGURES

<u>Figure</u>	<u>Page</u>
1	Simplified vibrational energy level diagram showing the three normal modes of CO ₂ with their associated mode temperatures T ₁ , T ₂ , and T ₃ 2
2	CO ₂ -N ₂ collisional deactivation probability..... 4
3	Experimentally derived rate constant k ₁₀ (M) as a function of temperature T for the deactivation of the bending mode of CO ₂ by various collision partners M 7
4	Experimentally derived rate constants k(A,B) as a function of temperature T for the transfer of 1 quantum of energy from species A to species B 8
5	Experimentally derived rate constant k(M) as a function of temperature T for the transfer of 1 quantum of energy from the asymmetric stretch mode of CO ₂ to 3 quanta in one of the two bending modes of CO ₂ by various collision partners M..... 9
6	Schematic of discharge-flow reactor used in these studies 14
7	Schematic of LIF pumping and detection system 15
8	Comparison of LIF spectrum from pumping between 554 and 57 nm with a simulated spectrum for pumping the NO(B, v'=2 - X, v''=18) band..... 16
9	Comparison of LIF spectrum from pumping between 557.3 and 560.3 nm with a simulated spectrum for pumping the NO(B, v'=6 - X, v''=21) band..... 16
10	Comparison of LIF spectrum from pumping between 560.2 and 562.8 nm with a simulated spectrum for pumping the NO(B, v'=6 - X, v''=21) band..... 17
11	Comparison of LIF spectrum from pumping between 563 and 566 nm with a simulated spectrum for pumping the NO(B, v'=6 - X, v''=21) band..... 17
12	Comparison of LIF spectrum from pumping between 565.8 and 568.8 nm with a simulated spectrum for pumping the NO(B, v'=3 - X, v''=19) band..... 18
13	Comparison of LIF spectrum from pumping between 568.8 and 571.7 nm with a simulated spectrum for pumping the NO(B, v'=3 - X, v''=19) band..... 18
14	Variation in the logarithm of the integrated intensity of the NO(B, v'=6 - X, v''=21) band head around 558 nm with the normalized number density of N(² P) in the discharge afterglow 20

FIGURES (Continued)

<u>Figure</u>	<u>Page</u>
15	Species number densities in fast-nitrogen beam, directed velocity 8 km/s 25
16	Composite spectrum of fast-N beam, 25 scan average - CW operation of OMA samples plasma and beam emissions..... 27
17	Composite spectrum of fast-N beam, 25 scan average - gated operation of OMA samples near-field beam emission only 28
18	NIR radiometer traces of nitrogen beam 29
19	Schematic of the FAST system configured for measurements of reaction cross sections by detection of IR emission..... 30
20	Temporal profiles of the 8 km/s nitrogen beam measured with the mass spectrometer for the $m/e = 14$ and $m/e = 28$ species 33
21	Schematic of the CVF-based detection system used to measure higher resolution spectra of the NO fundamental..... 35
22	Relative response curve of the CVF system as a function of wavelength..... 36
23	Response corrected spectrum of the NO fundamental for the $N(8 \text{ km/s}) + O_2$ reaction measured with the CVF system 36
24	Schematic of COCHISE discharge tube showing position of microwave cavity and Al foil extensions 38
25	Evolution of N_{hot} and precursors in discharge afterglow: no charge transfer 40
26	Evolution of N_{hot} and precursors in discharge afterglow: $N_2^+ + N$ charge transfer included 41
27	Experimental layout for medium resolution spectral measurements with the CVF 44
28	$O(8 \text{ km/s}) + \text{UDMH}$ - preliminary data..... 45
29	Emission observed on Delta 181 during methylamine release..... 45

FIGURES (Continued)

<u>Figure</u>	<u>Page</u>
30	Summary results of target discrimination studies showing percent improvement as a function of band and averaged results..... 49
31	Visible image of scene used for sub-pixel target identification using two-band correlation approach..... 51
32	IR image of scene in Figure 31 recorded at 4.56 μm using early prototype AIRIS system 51
33	Spectra of the torch, treed background, and road recorded for the AIRIS imager..... 52
34	Correlation plot of IR imagery showing data, fit to date, and $\pm 5\sigma$ bounds on fit 53
35	High contrast image from correlation analysis of IR imagery identifying the location of a sub-pixel flame in the scene 53

TABLES

<u>Table</u>	<u>Page</u>
1 Measured Rate Constants for Fermi Resonance V-V Exchange	3
2 Band Origins of the CO ₂ ($\Delta v_3=1$) Vibrational States Transitions (mn101) \rightarrow (mn111)	6
3 Cross sections for Formation of Vibrationally Excited NO via the N + O ₂ Reaction in Addition to Some of the Relevant Parameters.....	31
4 Results of the InSb Detector Calibration.....	32
5 Summary of the FAST Nitrogen Beam Composition Measurements Determination	34
6 Summary of the Cross Section Measurements for the N + O ₂ Reaction Adjusted for Beam Composition.....	34
7 Summary of Optimized Band Sets and Comparison to Proposed System Wavelength Ranges	50

1. REVIEW OF N₂/CO₂ VIBRATIONAL EXCHANGE KINETICS

1.1 Introduction

This section presents the results of a review of measurements involving vibrational exchange between N₂ and the CO₂(v₃) band and the subsequent intra-mode relaxation among CO₂ vibrational states. This system underwent considerable study during the 1960's and 1970's since these kinetics are fundamental to the operation of the CO₂ 10.6 μm laser. Subsection 1.4 presents a brief but not complete review of relevant kinetic information on this system as performed at Physical Sciences Inc. (PSI) in 1976.

In the present effort, we have reviewed measurements performed since 1980. Many of these studies involved lower mode exchange in CO₂-CO₂ collisions only. Since these are not relevant to atmospheric applications, they have not been included. We have recently accessed some Russian literature which is included in the CO₂ inter-intra-mode kinetics review in Subsection 1.2. A brief review of CO₂(v₂) deactivation by oxygen atoms is given in Subsection 1.3.

1.2 Review

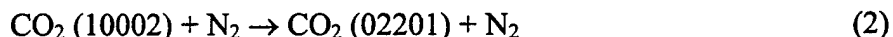
An energy chart depicting the lowest energy states of the CO₂ v₁, v₂, and v₃ bands and several combination states is given in Figure 1, as excerpted from Dang et al. (1983). A word on notation is in order. There is a Fermi resonance between the symmetric stretch mode (10001) and the upper state of 2v₂ (10002).

Perhaps the major breakthrough of the 1980's was the resolution of the rate constant for the mixing reaction between these two Fermi resonance states, i.e.,

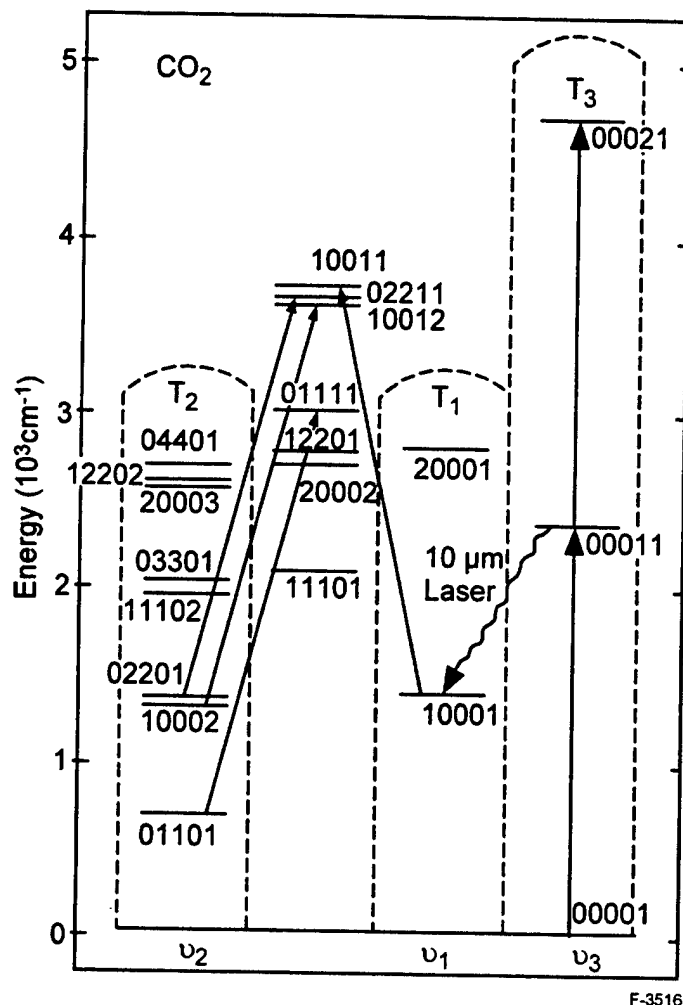


The history of measurements for this rate constant is summarized in Table 1 as taken from Orr and Smith (1987). For many years it was thought that this reaction occurred very efficiently; indeed, theoretical treatments were developed in order to rationalize the high efficiency. It is now clear that the reaction is not efficient, even though near resonant. The room temperature reaction rate constant for M = N₂ is now estimated to be about 6000 Torr⁻¹ s⁻¹, or to have a probability ≈ 10⁻³. Thus there is the real possibility that these states will not be vibrationally coupled at higher altitudes.

Furthermore, according to Dang et al., the reaction rate constant for the mixing between the 2v₂ modes, i.e.,



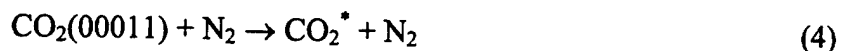
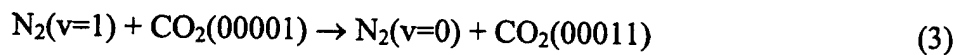
is 1.6 x 10⁴ s⁻¹ Torr⁻¹, also inefficient. We have not yet located a corroborative measurement for this rate.



F-3516

Figure 1. Simplified vibrational energy level diagram showing the three normal modes of CO₂ with their associated mode temperatures T₁, T₂, and T₃. The solid lines indicate typical vibrational bands in the 4.3 μm region. From Dang et al. (Ref. T10).

The vibrational exchange between N₂(v=1) and CO₂(v₃), followed by subsequent deactivation of the v₃ state, i.e.,



is a well studied system (see Subsection 1.4). A recent measurement, Bauer et al. (see Subsection 1.5), of the room temperature reaction rate constants for reactions (3) and (4) was in good agreement with earlier results (all comparisons in this paper were to pre-1980 measurements suggesting that other measurements were not available between 1980-87). The low temperature dependence of the rate constant for reaction (4) was established over a limited range, however, as shown in Figure 2.

Table 1. Measured Rate Constants^a for Fermi Resonance V-V Exchange CO₂ (10001)
 $+M \xrightarrow{k_1} \text{CO}_2(10002) + M$ 102.8 cm⁻¹ (Excerpted from Ref. T 1)

Partner M	Method of Determination ^b	$k_1/\text{ms}^{-1} \text{ Torr}^{-1}$	$(P^{(1)})^c$	Ref.
CO ₂	T; SSH theory	30	0.0034	T2
CO ₂	E; IR-IR double resonance ^d	10 ³	≥0.1	T3
CO ₂	T; long-range theory	10 ³ (assumed)	≥0.1	T4
CO ₂	T; SSH theory ^e	74	0.0085	T5
CO ₂	E; IR-IR double resonance ^e	450 ± 150 (373 K)	0.046	T6
CO ₂	E; IR fluorescence (LIVF)	1100	≥0.13	T7
CO ₂	E; Raman-CARS	>>100 (assumed)	>>0.01	T8
CO ₂	E; Raman-CARS	70	≤0.008	T9
CO ₂	E; IR-IR double resonance	48 ± 8	0.0055	T10
CO ₂	E; hot atoms, IR absorption	not necessarily fast		T11
He	E; IR-IR double resonance ^e	120 ± 50 (373 K)	0.005	T6
He	T; SCF + VCC-IOS theory	8.72	0.0004	T12
He	E; IR-IR double resonance	~6	0.0003	T10
N ₂	T; SSH theory	25	0.0027	T2
N ₂	E; IR-IR double resonance ^e	450 ± 150 (373 K)	0.044	T6
N ₂	E; IR-IR double resonance	~6	0.0007	T10
f	E; CO ₂ laser gain	330 ± 110 (400 K)		T13

a. Rates are for the forward reaction at a temperature of 300 K, unless otherwise indicated
 b. E = experiment; T = theory
 c. Interconversion of V-V transfer rate constants k_1 , collisional efficiencies ($P^{(1)}$), and collision numbers $Z(= P^{(1)})^{-1}$ is made in terms of the following gas kinetic rates (in units of $\text{ms}^{-1} \text{ Torr}^{-1}$) for CO₂-M hard-sphere collisions at 300 K: 8.7×10^3 for M = CO₂; 20.1×10^3 for M = He; 9.1×10^3 for M = N₂
 d. A very rapid decrease in observed signal was attributed, probably erroneously, to the rate process of interest
 e. Calculated from the reported reverse rate k_{-1} , using detailed balance constraints
 f. Measured in a CO₂ laser gas discharge (He/CO₂/N₂ = 12:4:1) at 270 Torr and 400 K.

References (Table 1)

- T1. B.J. Orr, I.W.M. Smith, *J. Phys. Chem.* **91**, 6106 (1987).
- T2. K.F. Herzfeld, *J. Chem. Phys.* **47**, 743 (1967).
- T3. C.K. Rhodes, M.J. Kelly, A.J. Javan, *J. Chem. Phys.* **48**, 5730 (1968).
- T4. R.D. Sharma, *J. Chem. Phys.* **49**, 5195 (1968).
- T5. K.N. Seeber, *J. Chem. Phys.* **55**, 5077 (1971).
- T6. R.R. Jacobs, K.J. Pettipiece, S. Thomas, *J. Phys. Rev. A* **11**, 54 (1975).
- T7. R.K. Huddleston, E. Weitz, *Chem. Phys. Lett.* **33**, 174 (1981).
- T8. A.M. Brodnikovsky, S.M. Gladkov, N.I. Koroteev, *Opt. Commun.* **40**, 312 (1982).
- T9. S.M. Gladkov, M.G. Karimov, N.I. Koroteev, *JETP Lett.* (Engl. Transl.) **35**, 470 (1982); *Opt. Lett.* **8**, 298 (1983).
- T10. C. Dang, J. Reid, B.K. Garside, *Appl. Phys. B* **31**, 163 (1983).
- T11. J.O. Chu, C.F. Wood, G.W. Flynn, R.E. Weston, Jr., *J. Chem. Phys.* **81**, 5533 (1984).
G.W. Flynn, private communication (1985).
- T12. D.C. Clary, *Chem. Phys. Lett.* **74**, 454 (1980); D.C. Clary, *J. Chem. Phys.* **75**, 209 (1980); D.C. Clary, *Mol. Phys.* **43**, 469 (1981); D.C. Clary, *Chem. Phys.* **65**, 247 (1982).
- T13. E.E. Stark, Jr., *Appl. Phys. Lett.* **23**, 335 (1973).

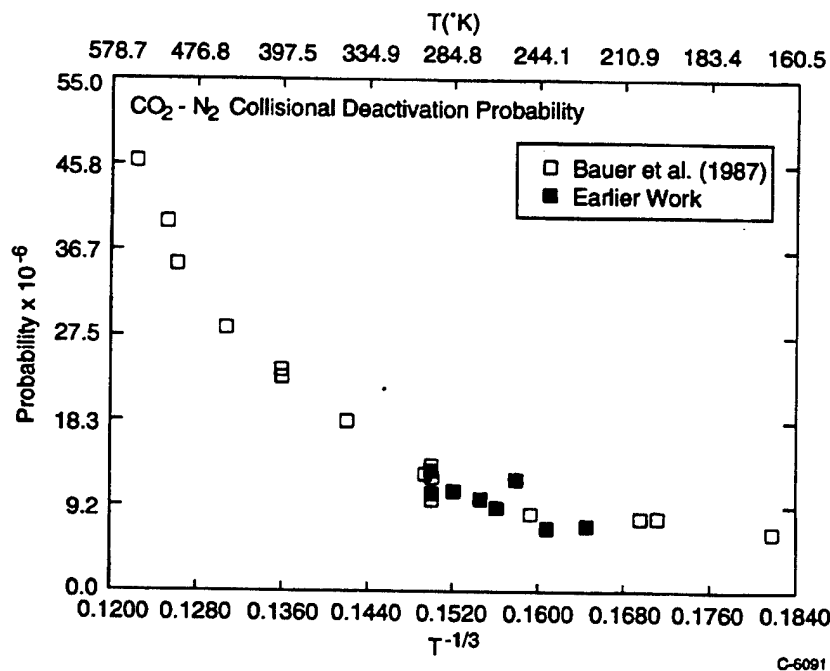


Figure 2. CO₂-N₂ collisional deactivation probability.

We note that there are no recent measurements on the products of reaction (4). It is generally assumed that quenching is to the $3\nu_2$ state. In the light of the possible uncoupling amongst ν_1 and ν_2 states, knowledge of the ultimate products of this reaction may be important for upper atmospheric modeling.

Our review found no new data on the (11001) state, other than collisions with CO_2 itself.

We found no recent studies of reactions between $\text{CO}_2(\nu_3) + \text{N}_2$ vibrational states higher than $n = 1$. Recent diode laser studies in CO_2 laser discharges, Dang et al. (T10), have monitored vibrational levels as high as $\text{CO}_2(00091)$, however. Indeed, these workers demonstrated that many hot bands in the $4.3 \mu\text{m}$ region could be monitored by tunable diode laser spectroscopy, see, for example, the transitions shown in Figure 1. In principle, this technology could be utilized to investigate hot band vibrational kinetics between N_2 and CO_2 with particular emphasis on deducing product state distributions, e.g., reaction (4) as well as reaction rate constraints.

1.3 CO_2 Excited State Transfer Rate Studies

Due to the resonance between $\text{N}_2(\nu)$ and $\text{CO}_2(\nu_3)$, collisions between vibrationally excited nitrogen and CO_2 can efficiently transfer energy into the $\text{CO}_2 \nu_3$ mode. Collisions of excited nitrogen with CO_2 molecules already in vibrationally excited states (with ν_1 , ν_2 , or ν_3 excitation) will also transfer energy producing additional internal excitation in the ν_3 state. The fraction of molecules containing internal excitation will change as a function of time and scenario. Even under conditions when there are fewer collisions with vibrationally excited molecules than ground state ones, the absorption of transitions originating from the ground state by the unperturbed atmosphere increases the contribution of the excited state transitions in the total radiant signature.

Preliminary analyses of the signatures resulting from electron irradiated nitrogen transferring excitation to CO_2 have shown that molecules are excited into the 01111, 10011, and 10012 excited states and significantly contribute to the signature. These states are populated either by a single step excitation of ground state molecules or by vibrationally excited molecules accepting a single quantum of ν_3 energy from the nitrogen.

As can be seen from Table 2, the band origins of the $\Delta\nu_3 = 1$ transitions arising from the first four vibrationally excited states all fall within 12 cm^{-1} of each other. The high density of lines has complicated analysis of the radiant signatures resulting from the transfer of $\text{N}_2(\nu)$ to excited CO_2 as observed in LABCEDE and EXCEDE III. However, under low pressure conditions, the Doppler broadened CO_2 lines from the separate vibrational states can be spectrally resolved, and the diode laser can be tuned to sequentially probe individual populations. In the 2330 cm^{-1} spectral region P branch transitions from the 01101 state and R branch transitions from the next three higher states in the table can all be accessed.

Table 2. Band Origins of the CO₂ ($\Delta v_3=1$) Vibrational States Transitions (mnl01) \rightarrow (mnl11)

00011 - 00001	2349.1 cm ⁻¹	fundamental transition (ground state)
01111 - 01101	2336.6 cm ⁻¹	first bending mode excited state transition
10012 - 10002	2327.4 cm ⁻¹	lower 1285 cm ⁻¹ energy Fermi state transition
10011 - 10001	2326.6 cm ⁻¹	upper 1388 cm ⁻¹ Fermi state transition
02211 - 02201	2324.1 cm ⁻¹	1335 cm ⁻¹ energy state transition

The populations in excited vibrational states of CO₂ have been studied using tunable diode lasers. Internal states up to $v_3, v=9$ (with about 2.5 eV of vibrational energy) have been observed inside laser discharges. The time evolution dynamics of the populations in many hot bands states were monitored in these experiments.

Diode lasers provide the high resolution and controlled tunability to monitor particular rotational transitions within excited vibrational states. The excited state line positions and strengths are well established. In the compact CO₂ band many transitions will be accessible within the diode tuning range.

To understand this effect, we suggest a series of diode laser experiments to accurately probe the populations and dynamics of the transfer from excited nitrogen. Initially, CO₂ excited states will be created at high densities in a nitrogen /CO₂ discharge operating at a few Torr pressure. The optimum frequencies to probe each vibrational state will be determined based upon the well known spectroscopy in this region and the performance characteristics of the diode. Multiple rotational lines will be probed for each transition to accurately establish a rotational distribution in each state and look for non-equilibrium effects. Detection limits for CO₂ excited vibrational states (molecules/cm²) will be established. This well-characterized diode will then be used to probe the distributions inside the LABCEDE facility. The detection limits will be used to guide LABCEDE experimental operation conditions.

In LABCEDE pure nitrogen will first be excited using pulsed electron irradiation. CO₂ molecules will then be introduced into the excited nitrogen well after the electron pulse so that only excited nitrogen remains to excite the CO₂. The states of CO₂ created by collisions with the nitrogen will be probed by the diode. Next CO₂ will be electron irradiated and nitrogen introduced later in the electron pulse. Electron irradiation will initially create substantial vibrational excitation into all internal modes as established previously in LABCEDE. Collisions of the excited CO₂ with excited nitrogen later in the pulse will excite the CO₂ further. The time-resolved populations of the CO₂ internal states will be analyzed to extract the relative excitation rates. Our review of these rates and suggested experiments were presented at the 1994 Fall American Geophysical Union Meeting. The material presented is included as Appendix 1 of this report.

1.4 Experimentally Derived Rate Constants

Figures 3 through 5, with references, represent the state of knowledge of CO_2 vibrational kinetics in 1976. They are taken from a PSI Technical Report by Taylor et al.¹ and are an update of the key review by Taylor and Bitterman.²

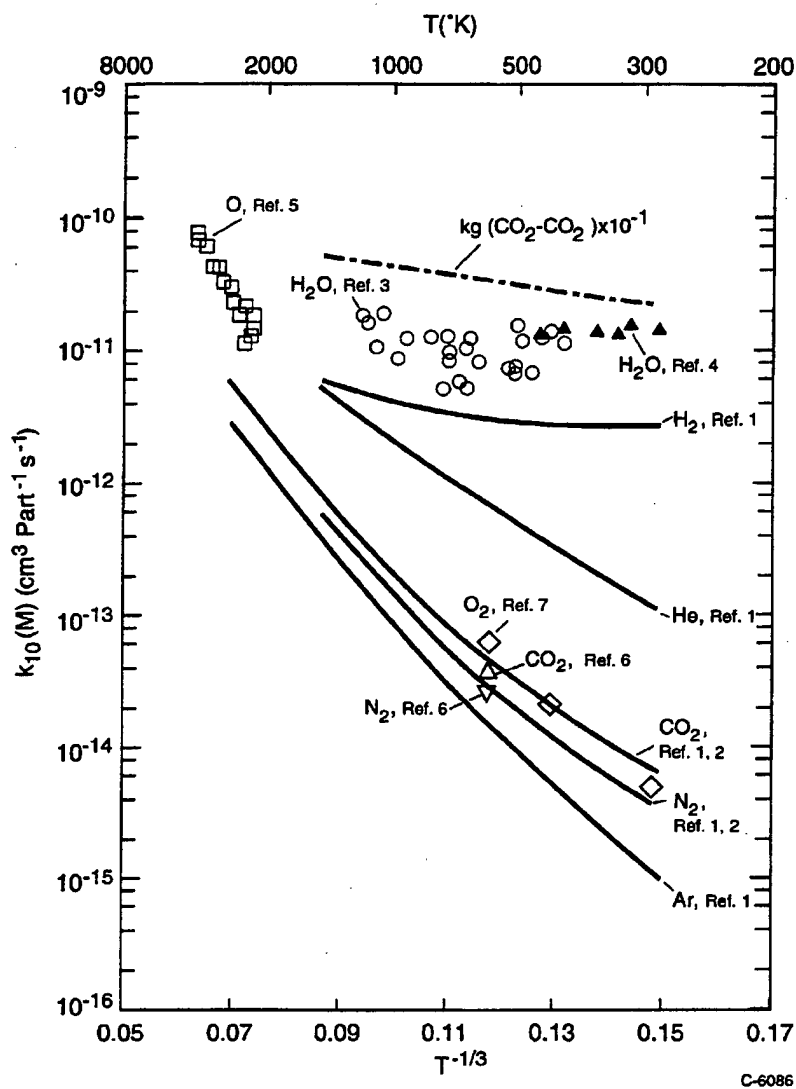


Figure 3. Experimentally derived rate constant $k_{10}(M)$ as a function of temperature T for the deactivation of the bending mode of CO_2 by various collision partners M . The dashed line represents a gas kinetic rate constant for $M = \text{CO}_2$ divided by 10.

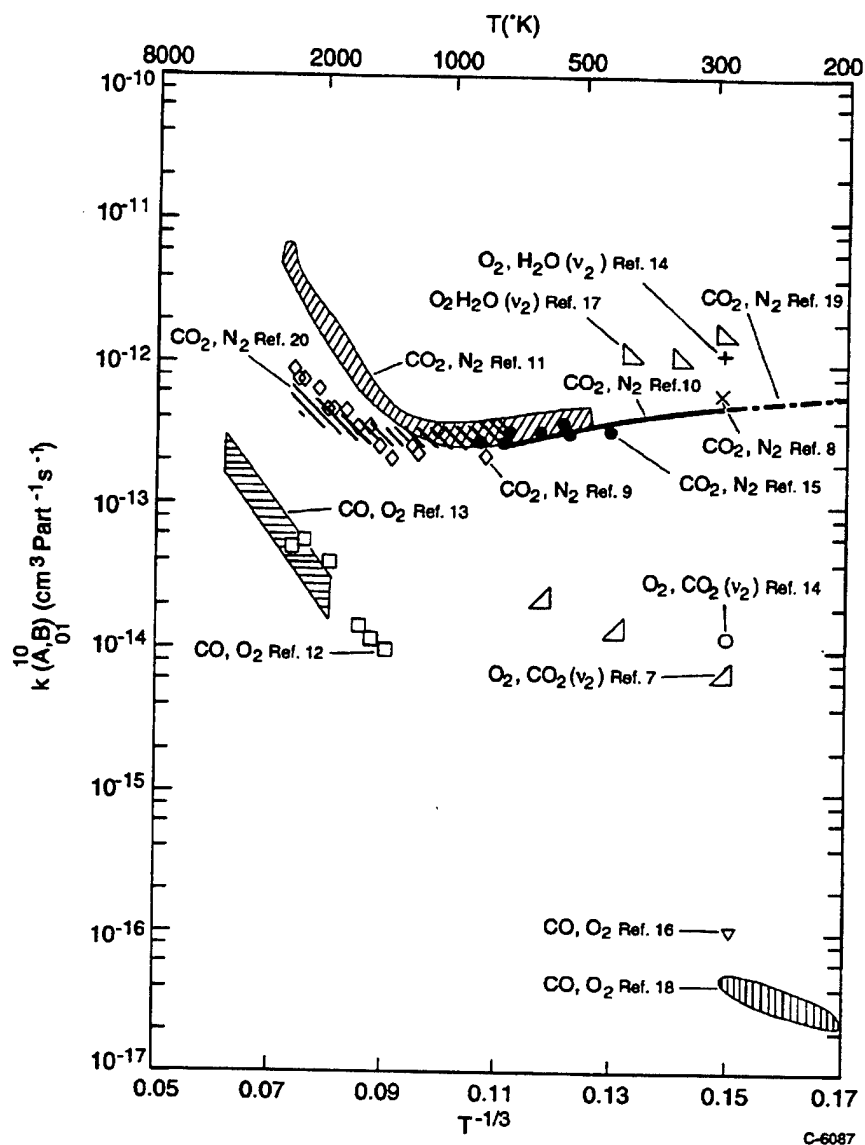


Figure 4. Experimentally derived rate constants $k(A,B)$ as a function of temperature T for the transfer of 1 quantum of energy from species A to species B. Processes are given in the exothermic direction and are labeled by couplet (A,B).

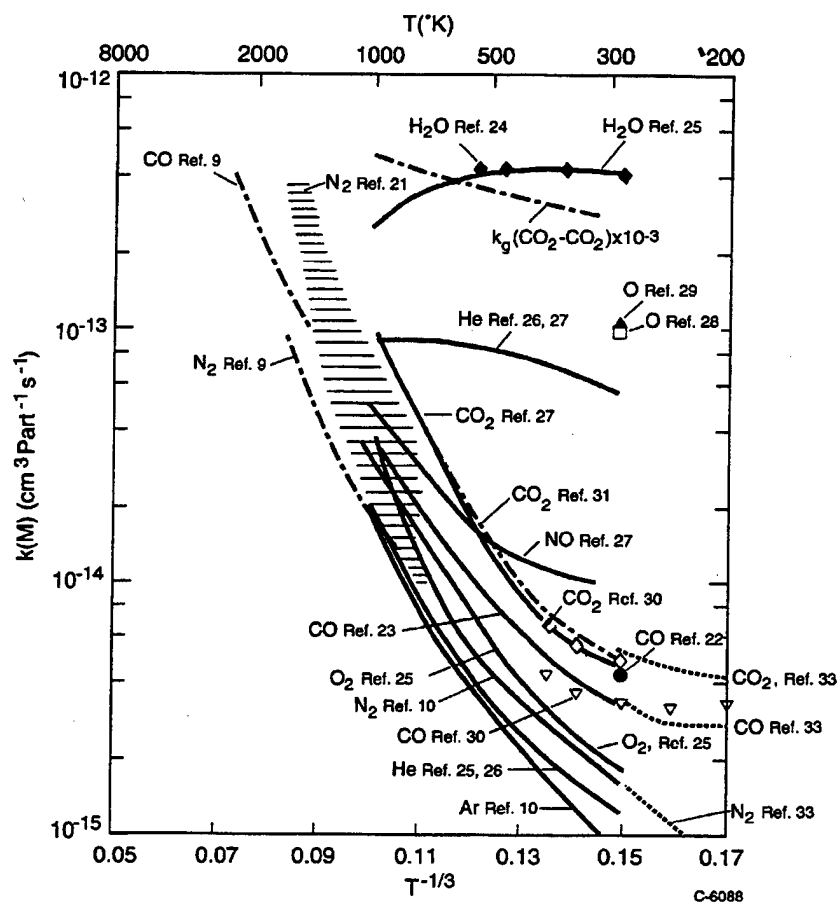


Figure 5. Experimentally derived rate constant $k(M)$ as a function of temperature T for the transfer of 1 quantum of energy from the asymmetric stretch mode of CO_2 to 3 quanta in one of the two bending modes of CO_2 by various collision partners M . The dashed line represents a gas kinetic rate constant for $M = \text{CO}_2$ divided by 1000.

References for Figures 3 through 5

1. C.J.S.M. Simpson and T.R.D. Chandler, *Proc. Roy. Soc. Lond. A* **317**, 265 (1970).
2. C.J.S.M. Simpson, T.R.D. Chandler, and A.C. Strawson, *J. Chem. Phys.* **51**, 2214 (1969).
3. M.I. Buchwald and S.H. Bauer, *J. Phys. Chem.* **76**, 3108 (1972).
4. J.W.L. Lewis and K.P. Lee, *J. Acoust. Soc. Amer.* **38**, 813 (1965).
5. R.E. Center, *J. Chem. Phys.* **59**, 3523 (1973).
6. F.D. Shields, C.C. Warf, and H.E. Bass, *J. Chem. Phys.* **58**, 3837 (1973).
7. H.E. Bass, *J. Chem. Phys.* **58**, 4783 (1973).
8. C.B. Moore, R.E. Wood, B-L Hu, and J.T. Yardley, *J. Chem. Phys.* **46**, 4222 (1967).
9. Y. Sato and S. Tsuchiya, *J. Phys. Soc. Jap.* **33**, 1120 (1972).
10. W.A. Rosser, Jr., A.D. Wood, and E.T. Gerry, *J. Chem. Phys.* **50**, 4996 (1969).
11. R.L. Taylor and S.A. Bitterman, *J. Chem. Phys.* **50**, 1720 (1969).
12. Y. Sato, S. Tsuchiya, and K. Kuratani, *J. Chem. Phys.* **50**, 1911 (1969).
13. R.E. Center, *J. Chem. Phys.* **58** 5230 (1973).
14. R.G. Monk, *J. Acoust. Soc. Amer.* **46**, 580 (1969). (Note: Error in original publication.)
15. K. Balthuis, *J. Chem. Phys.* **58**, 5786 (1973).
16. W.H. Green and J.K. Hancock, *J. Chem. Phys.* **59**, 4326 (1973).
17. H.E. Bass and F.D. Shields, *J. Acoust. Soc. Am.* **56**, 856 (1974).
18. D.J. Miller and R.C. Millikan, *Chem. Phys. Lett.* **27**, 10 (1974).
19. G. Inoue and S. Tsuchiya, *J. Phys. Soc. Japan* **38**, 870 (1975).
20. G. Kamimoto and H. Matsui, *Trans. Japan Soc. Aero. Space Sci.* **13**, 57 (1970).
21. R.L. Taylor and S. Bitterman, 7th Shock Tube Symposium, pg. 577.
22. M.D. Kovacs, *J. Chem. Phys.* **58**, 4704 (1973).
23. W.A. Rosser, Jr., R.D. Sharma, and E.T. Gerry, *J. Chem. Phys.* **54**, 1196 (1971).
24. D.F. Heller and C.B. Moore, *J. Chem. Phys.* **52**, 1005 (1970).
25. W.A. Rosser, Jr. and E.T. Gerry, *J. Chem. Phys.* **51**, 2286 (1969).
26. J.C. Stephenson, R.E. Wood, and C.B. Moore, *J. Chem. Phys.* **54**, 3097 (1971).
27. W.A. Rosser, Jr. and E.T. Gerry, *J. Chem. Phys.* **51**, 4131 (1971).
28. J.H.W. Cramp and J.D. Lambert, *Chem. Phys. Lett.* **22**, 146 (1973).
29. M.I. Buchwald and G.L. Wolga, *J. Chem. Phys.* **63**, 4730 (1975).
30. D.F. Starr and J.K. Hancock, *J. Chem. Phys.* **63**, 4730 (1975).
31. L. Doyennetti, M. Margotten-Maclou, H. Greguen, A. Carion, and L. Henry, *J. Chem. Phys.* **60**, 697 (1974).
32. G. Inoue and S. Tsuchiya, *J. Phys. Soc. Japan* **39**, 479 (1975).

1.5 Bibliography of Papers Reviewed

- Bailey, D., Rossetti, C., and Guelachvili, G., " $^{12}\text{C}^{16}\text{O}_2$: Vibrational Population Distributions in $\text{CO}_2\text{-N}_2$, $\text{CO}_2\text{-He}$ and $\text{CO}_2\text{-N}_2\text{-He}$ dc Discharges from High-Excitation Emission Fourier Spectra", *Chem. Phys.* **100**, 101 (1985).
- Bauer, S.H., Caballero, J.F., Curtis, R., and Wiesenfeld, J.R., "Vibrational Relaxation Rates of $\text{CO}_2(001)$ with Various Collision Partners for $T < 300\text{ K}$ ", *J. Chem. Phys.* **91**, 1778 (1987).
- Cenian, A., "Study of Non-equilibrium Vibrational Relaxation of CO_2 Molecules During Adiabatic Expansion in a Supersonic Nozzle. The Treanor Type Distribution - Existence and Generation", *Chem. Phys.* **132**, 41 (1989).
- Chu, J.O., Wood, C.F., Weston, Jr., R.E., and Flynn, G.W., "Counting Vibrational Quanta With a Diode Laser Probe: Bending and Stretching Excitation in CO_2 Caused by Collisions with Hot Atoms From Excimer Laser Photolysis", *J. Chem. Phys.* **81**, 5533 (1984).
- Dang, C., Reid, J., and Garside, B.K., "Detailed Vibrational Population Distributions in a CO_2 Laser Discharge as Measured with a Tunable Diode Laser", *Appl. Phys. B* **27**, 145 (1982).
- Dang, C., Reid, J., and Garside, B.K., "Dynamics of the CO_2 Lower Laser Levels as Measured with a Tunable Diode Laser", *Appl. Phys. B* **31**, 163 (1983).
- Field, D., "Energy Transfer in Gases", *Sci. Prog., Oxf.* **67**, 309 (1981).
- Haixing, Y., "Vibrational Relaxation Processes in $\text{CO}_2\text{-N}_2\text{-H}_2\text{O}$ Laser Systems", *Jiquang* **8/11**, 11 (1981) and FTD-10(RS) T-0258-88.
- Kreutz, T.G., O'Neill, J.A., and Flynn, G.W., "Diode Laser Absorption Probe of Vibration-Vibration Energy Transfer in CO_2 ", *J. Chem. Phys.* **91**, 5540 (1987).
- Offenhauser, F., "Kinetic Model For The Vibrational Energy Exchange in Flowing Molecular Gas Mixtures", NASA TM-88500, (March 1987).
- Orr, B.J., and Smith, I.W.M., "Collision-Induced Vibrational Energy Transfer in Small Polyatomic Molecules", *J. Phys. Chem.* **91**, 6106 (1987).
- O'Neill, J.A., Wang, C.X., Cai, J.Y., Weston, Jr., R.E., and Flynn, G.W., "Rotationally Resolved Hot Atom Collisional Excitation of CO_2 $00^{\circ}1$ and $00^{\circ}2$ Stretching Vibrations By Time-Resolved Diode Laser Spectroscopy", *J. Chem. Phys.* **88**, 6240 (1988).
- Rahbee, A., "Vibrationally Inelastic Collision of CO_2 with N_2 and Ar", *J. Phys. Chem.* **88**, 4488 (1984).
- Reddy, K.P.J., "Population Inversions Behind Normal Shock Waves in $\text{CO}_2\text{-N}_2\text{-He}$ Mixtures Seeded with Solid Particles", *J. Appl. Phys.* **67**, 3565 (1990).

Rich, J.W., "Relaxation of Molecules Exchanging Vibrational Energy", in *Applied Atomic Collision Physics*, Vol. 3, 99, Academic Press, Inc. (1982).

Ryali, S.B., Fenn, J.B., Kolb, C.E., and Silver, J.A., "Collisional Excitation of CO₂ by N₂, O₂, and Ar", *J. Chem. Phys.* **76**, 5878 (1982).

Sedlacek, A.J., Flynn, G.W., and Weston, Jr., R.E., "Br^{*} + CO₂ revisited: An Interrogation of E-V Energy Transfer with Time-resolved Diode Laser Spectroscopy", *J. Chem. Phys.* **93**, 2812 (1990).

Solodukhin, A.S., Starovoitov, V.S., Trushin, S.A., and Churakov, V.V., "Measurement of the Deactivation Rate of Asymmetric Vibrations in ¹²CO₂-¹³CO₂ Mixtures", *Chem. Phys. Lett.* **158**, 70 (1989).

Venkateshan, S.P., Ryali, S.B., and Fenn, J.B., "High-Resolution Emission Spectroscopy of CO₂ Collisionally Excited By N₂. Rotational Distribution", *Chem. Phys. Lett.* **92**, 606 (1982).

Uzer, T., with Miller, W.H., "Theories of Intramolecular Vibrational Energy Transfer", *Phys. Rep. in Phys. Lett.* **199**, 73, (1991).

2. INVESTIGATIONS OF NO (v, J) FORMATION

We investigated the excitation of highly vibrationally excited, ground-electronic-state nitric oxide in the reactions between metastable nitrogen and molecular oxygen. These studies were performed in a discharge-flow reactor in which the metastable nitrogen was made in a microwave discharge in N_2 dilute in argon or helium. Molecular oxygen mixed with the metastable nitrogen downstream from the discharge and any resultant NO produced was detected a few milliseconds later via laser-induced fluorescence. We have detected NO(X, v) in both low ($v''=0-9$) and high ($v''=18-21$) vibrational levels.

This section presents preliminary results of our investigation on excitation of the higher vibrational-level group. We have positively identified the presence of vibrational levels 19 and 21 in the flow, and also have strong evidence for the presence of vibrational level 18. In addition we made measurements of the various metastable species in the afterglow in order that we might, eventually, be able to correlate observed NO(X, v) number densities with metastable number densities. This correlation should provide evidence for the kinetic mechanism responsible for the high- v excitation.

2.1 Experimental

The apparatus used for these studies is illustrated schematically in Figure 6. It is the 5.1 cm diameter discharge-flow reactor we have described in some detail previously.³⁻¹⁰ Basically, metastable nitrogen is formed in a microwave discharge in a mixture of N_2 dilute in either argon or helium at the reactor's upstream end. Molecular oxygen enters the flow reactor through a loop injector downstream from the discharge. The gases then flow into a detection cell where the metastable number densities can be determined spectroscopically and where the NO(X, v) number densities can be determined by laser induced fluorescence. The distance between the discharge and the loop injector and between the injector and the detection region is infinitely variable over the fixed distance between the flow reactor's upstream end and the detection region.

Metastable $N(^2D, ^2P)$ number densities are determined by the technique of vacuum ultraviolet resonance absorption.^{6,11-13} The resonance lines are generated in a microwave discharge lamp on one side of the flow reactor, and are detected with the aid of a 0.2 m monochromator/solar-blind photomultiplier combination. A picoammeter determines the magnitude of the photomultiplier's output.

Other metastable species are monitored by passive fluorescence techniques. Metastable $N_2(A^3\Sigma_u^+)$ and $N_2(a'^1\Sigma_u^-)$ are followed by measurements on the Vegard-Kaplan bands,¹⁴ $N_2(A^3\Sigma_u^+ - X^1\Sigma_g^+)$, between 250 and 300 nm and the Ogawa-Tanaka-Wilkinson-Mulliken bands,¹⁰ $N_2(a'^1\Sigma_u^- - X^1\Sigma_g^+)$, between 130 and 180 nm, respectively. Vibrationally excited ground-electronic-state nitrogen number densities can be estimated by measuring fluorescence intensities of the N_2 first-positive bands, $N_2(B^3\Pi_g - A^3\Sigma_u^+)$ and ratioing the measurements to the $N_2(A)$ number density determination.⁸

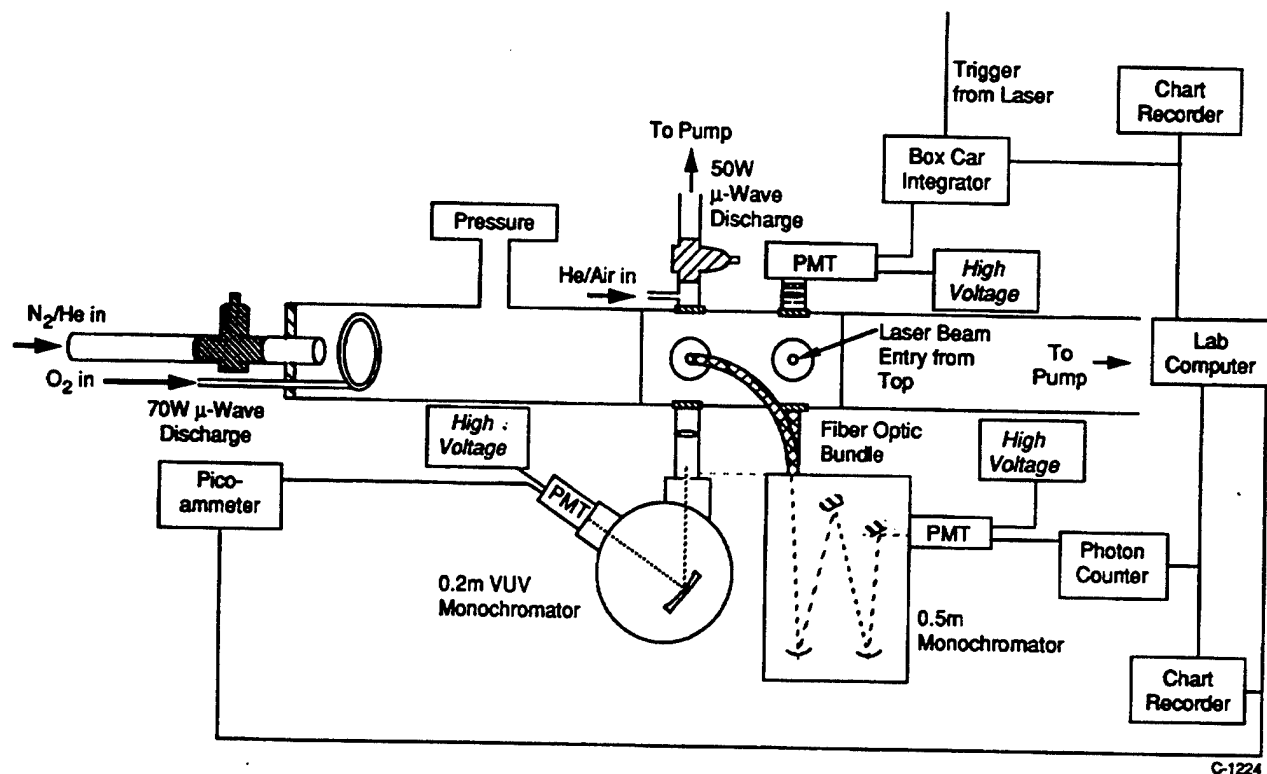
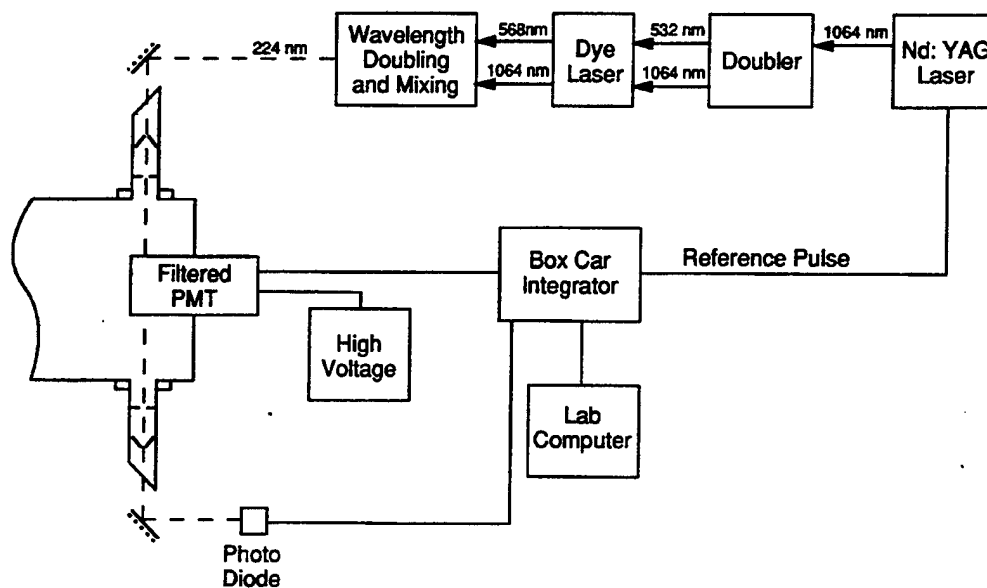


Figure 6. Schematic of discharge-flow reactor used in these studies.

The uv/visible measurements use a 0.5 m monochromator/thermoelectrically-cooled photomultiplier combination, while the vuv measurements employ the aforementioned 0.2 m monochromator. A picoammeter determines the output of both photomultipliers. Because the window accessible to the uv/visible monochromator is blocked by the vuv resonance lamp, we used a fiber-optic bundle to transmit light from a window, whose optic axis is normal to the optical axis of the vuv detection system, to the 0.5 m monochromator's entrance slit.

Figure 7 illustrates the configuration of the laser and detection system used in the NO(X, v) measurements. The laser system is a frequency doubled Nd:YAG laser pumped, tuneable dye laser. The laser dye used was rhodamine 6-G which gave access to a wavelength range between 555 and 572 nm in the dye's fundamental output. The output from the dye laser could be frequency doubled to give access to the wavelength range between 278 and 285 nm, and mixing the doubled laser beam with the Nd:YAG laser's fundamental beam provided operation between 221 and 226 nm. For the studies described in this report, the dye was operated in the fundamental mode.

A photometer consisting of an interference filter/photomultiplier combination⁵ detected the NO fluorescence pumped by the laser. For these experiments the interference filter had a transmission maximum at about 220 nm with a half band width of about 25 nm. The photomultiplier in the photometer had a solar-blind photocathode that responded negligibly to wavelengths longer than 300 nm. The experiments thus involved pumping various bands of the NO beta system,¹⁵ NO(B²Π - X²Π), in the visible, and observing fluorescence from the pumped upper states in the ultraviolet, thereby essentially eliminating scattered laser light from the



C-1225

Figure 7. Schematic of LIF pumping and detection system.

detector. The major difficulty with this scheme is that dc background fluorescence in the flow tube was also at a maximum over the wavelength region detected. The large dc background added considerable noise to the LIF signals. In addition, to avoid damaging the photomultiplier, its gain had to be reduced. The effect of this was to reduce observed LIF signal levels, which, in turn, further degrades the signal-to-noise ratio of the data. We did succeed in partially alleviating the dc background problems by severely restricting the field of view of the photomultiplier.

In addition to the photometer used to monitor LIF fluorescence, we also had a photodiode set up to monitor the intensity of the laser beam. This allowed us to correct the LIF signals for any changes in laser intensity. The signals from the photomultiplier and the monitor photodiode were both processed by box-car integrators with the processed signals stored on a lab computer for later analysis.

2.2 Results

The results of a survey of the LIF spectra excited over the laser wavelength region between 554 and 572 nm are shown in Figures 8 through 13. The top spectrum in each figure is the observed LIF spectrum while the bottom spectrum is a spectral simulation of the band we think we are pumping. In Figures 9 through 11 the simulation refers to pumping the $\text{NO}(\text{B}, v'=6-X, v''=21)$ band. The match between the observed and simulated spectrum is quite good, and we think there can be no doubt as to the proper identification.

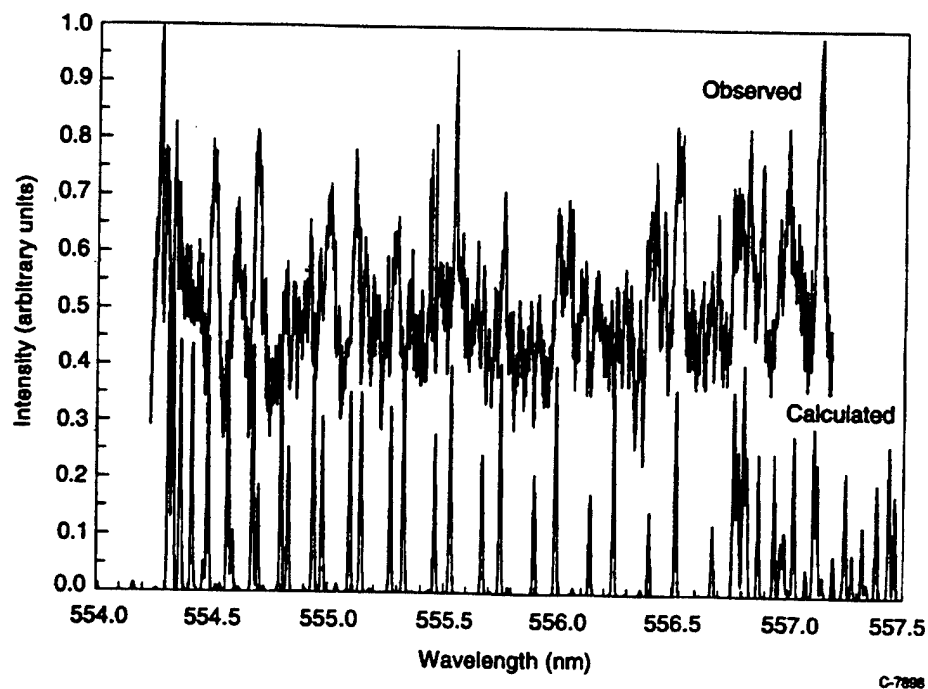


Figure 8. Comparison of LIF spectrum from pumping between 554 and 557 nm with a simulated spectrum for pumping the NO(B, $v'=2$ - X, $v''=18$) band.

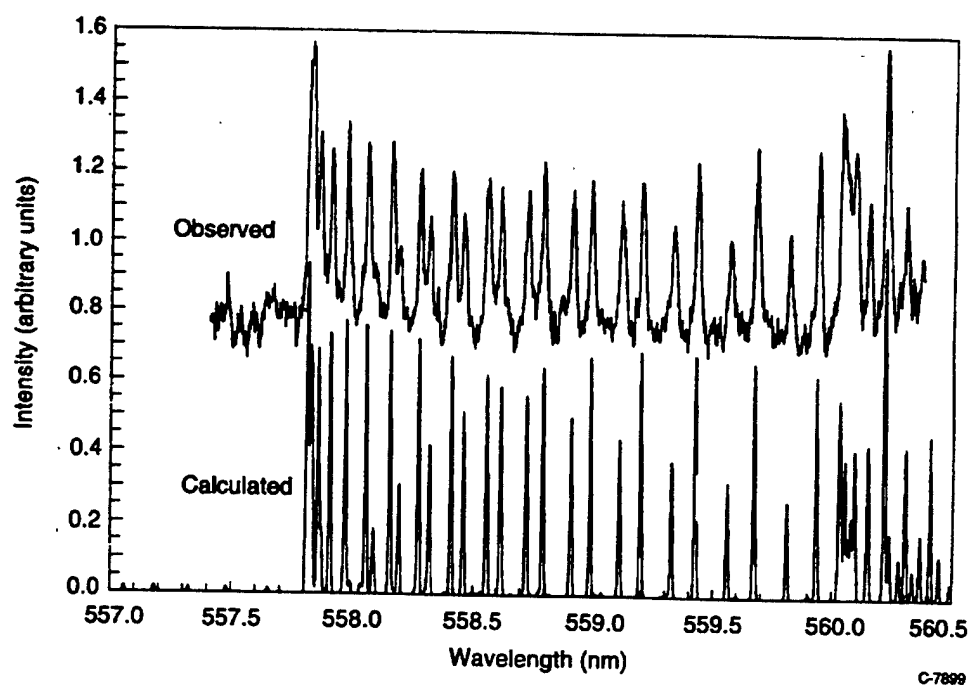


Figure 9. Comparison of LIF spectrum from pumping between 557.3 and 560.3 nm with a simulated spectrum for pumping the NO(B, $v'=6$ - X, $v''=21$) band.

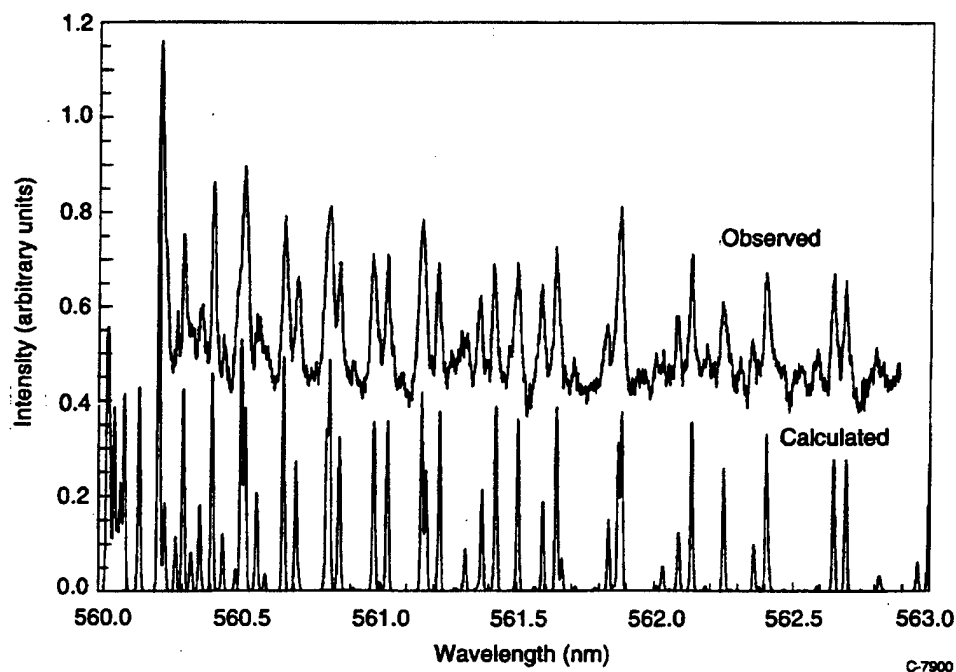


Figure 10. Comparison of LIF spectrum from pumping between 560.2 and 562.8 nm with a simulated spectrum for pumping the NO(B, $v'=6 - X, v''=21$) band.

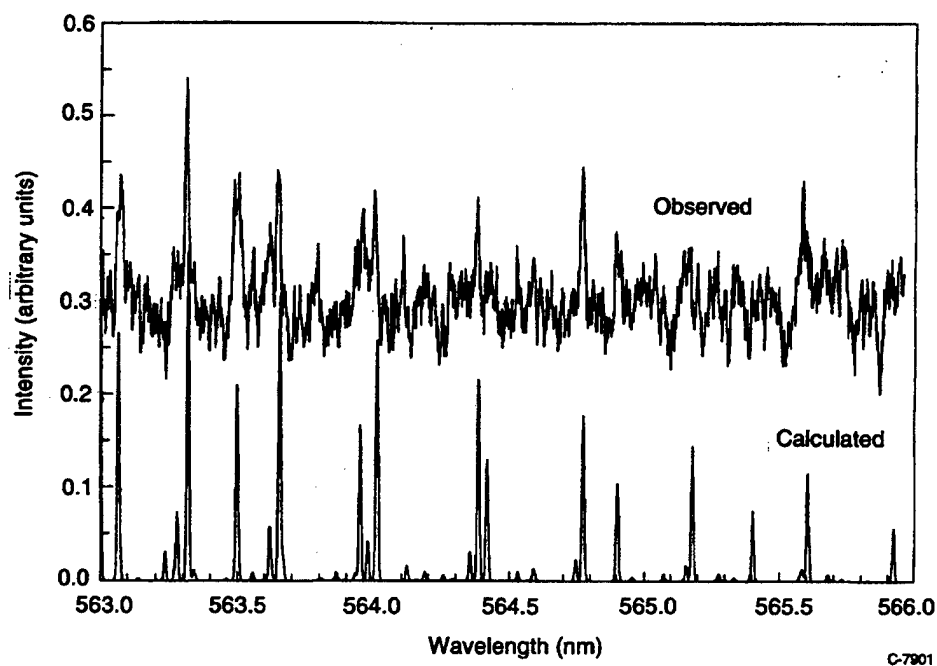


Figure 11. Comparison of LIF spectrum from pumping between 563 and 566 nm with a simulated spectrum for pumping the NO(B, $v'=6 - X, v''=21$) band.

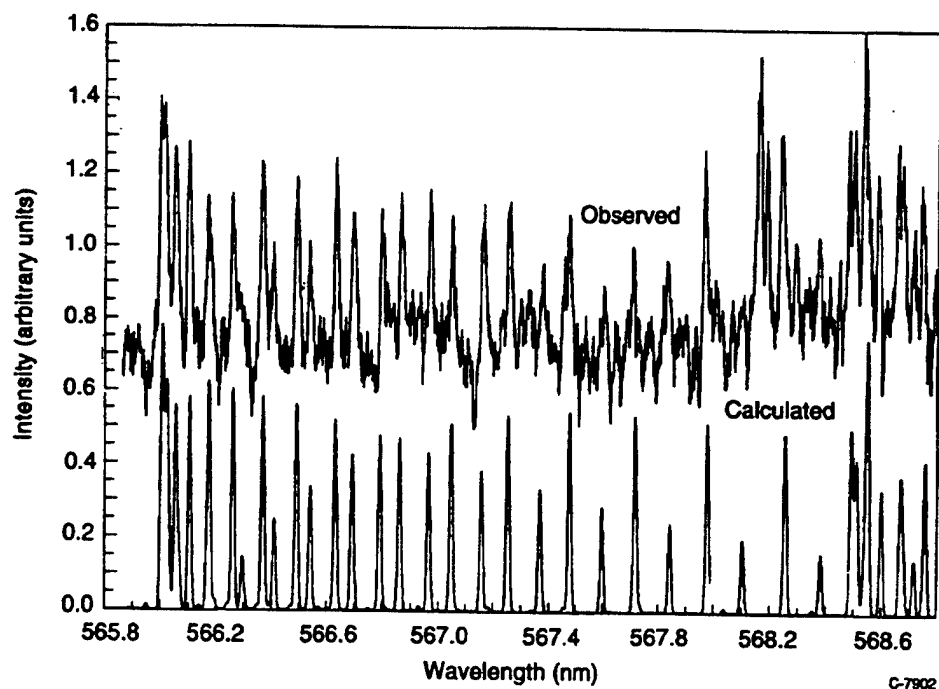


Figure 12. Comparison of LIF spectrum from pumping between 565.8 and 568.8 nm with a simulated spectrum for pumping the NO(B, $v'=3$ - X, $v''=19$) band.

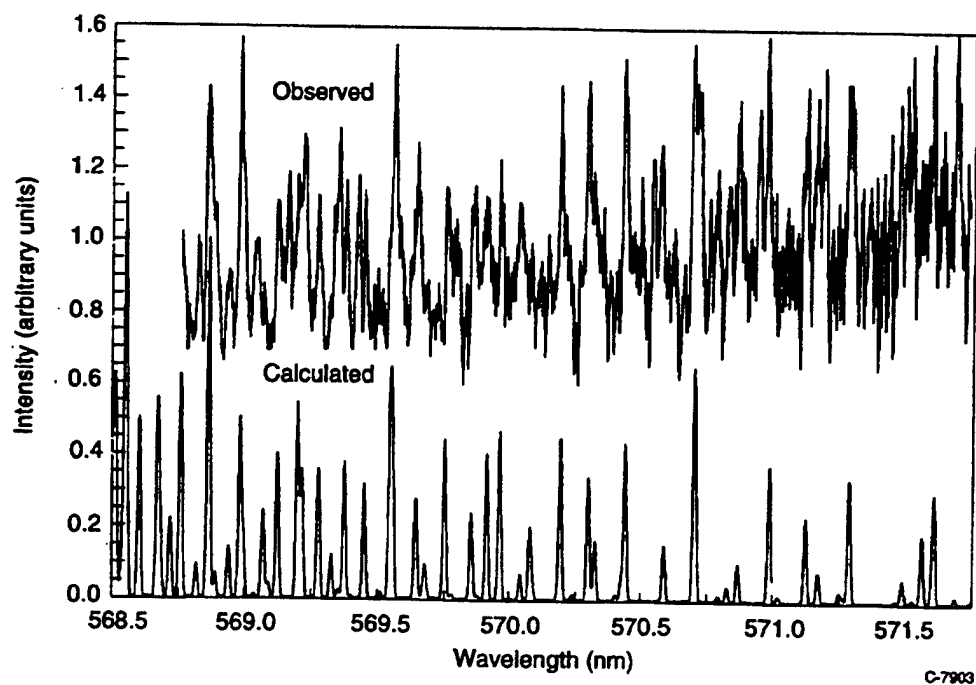


Figure 13. Comparison of LIF spectrum from pumping between 568.8 and 571.7 nm with a simulated spectrum for pumping the NO(B, $v'=3$ - X, $v''=19$) band.

The comparison between the observed spectra in Figures 12 and 13 and the accompanying simulated spectra for pumping in the $\text{NO}(\text{B}, v'=3 \rightarrow \text{X}, v''=19)$ is also quite good. In this case, however, several major discrepancies do occur. The most notable of these is the appearance of two strong LIF lines at about 568.15 nm that do not appear in the simulation. Several other additional lines not in the simulated spectra also show up throughout the two scans included in Figures 12 and 13. We think these are related to a separate band but we have not identified what it is.

Finally, we compare the observed spectrum in Figure 8 with a simulation of LIF pumping the $\text{NO}(\text{B}, v'=2 \rightarrow \text{X}, v''=18)$ band. The match in the band-head region around 556.75 nm is sufficiently good that we think the identification is correct. Quite a number of discrepancies exist, however, so the identification isn't certain. One reason for the discrepancies might be caused by non-linearity in the laser wavelength drive.

As mentioned above, we began a series of measurements to characterize the number densities of the various metastable nitrogen species exiting the discharge under several sets of conditions so that we might try to correlate these number densities with $\text{NO}(\text{X}, v)$ number densities measured by LIF. For this series of measurements, we chose to maintain a constant set of flow conditions, and vary metastable number densities by varying the discharge power or position of the discharge along the length of the discharge tube. We have not been able to analyze these data in any detail. We can, however, present some preliminary observations.

Figure 14 shows how the intensity of $\text{NO}(\text{B}, v'=6 \rightarrow \text{X}, v''=21)$, which will be proportional to the number density of $\text{NO}(\text{X}, v''=21)$, varies as a function of a parameter that is proportional to the number density of $\text{N}(^2\text{P})$. Also shown in the figure, for comparison purposes are two lines, one representing a unit slope, i.e. a direct one-to-one correlation between the number densities of the two species, and the other representing a half-unit slope which would imply a the $\text{NO}(\text{X}, v''=21)$ number density varies as the square of the $\text{N}(^2\text{P})$ number density. The data more nearly correlate with the half-unit slope. This should not be taken as evidence of an excitation mechanism involving $\text{N}(^2\text{P})$, however. The number densities of the other metastables in the flow need to be evaluated. Because of the way in which the experiments were done, it is likely that there will be some proportionality between the magnitude of the $\text{N}(^2\text{P})$ number density and that of the other metastables.

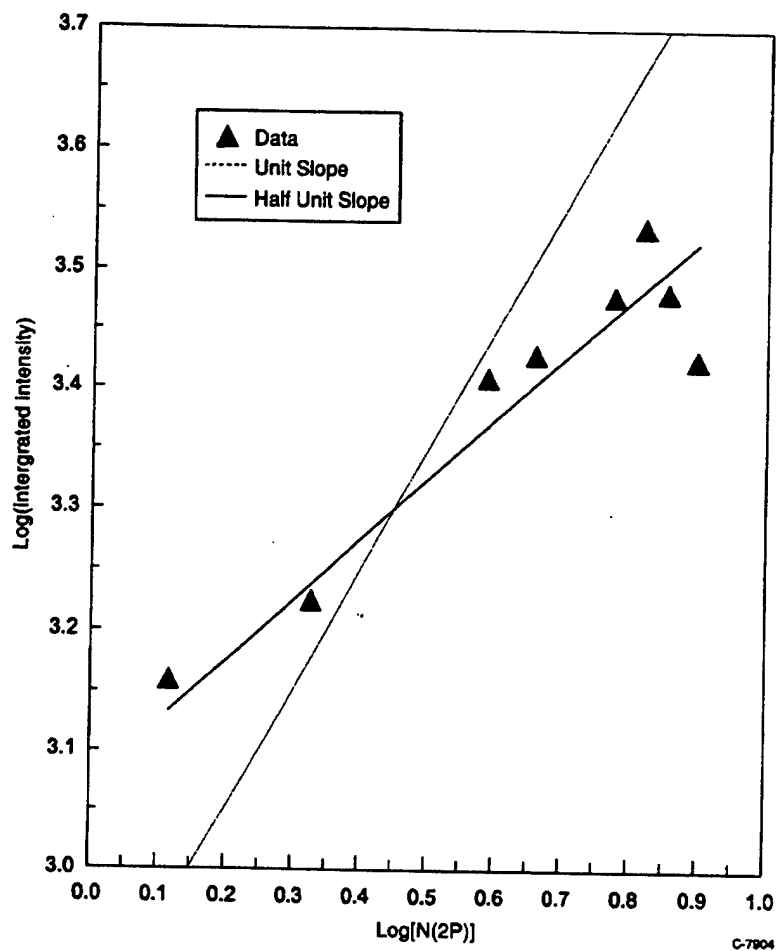


Figure 14. Variation in the logarithm of the integrated intensity of the NO(B, $v'=6 - X, v''=21$) band head around 558 nm with the normalized number density of $N(2P)$ in the discharge afterglow.

3. THE DIPOLE MOMENT AND INFRARED TRANSITION STRENGTHS OF NITRIC OXIDE

The electric dipole moment function for $\text{NO}(X^2\Pi)$ was determined by non-linear least squares analysis of experimental data, including previously reported $(\Delta v=2)/(\Delta v=1)$ transition branching ratios for $v' \leq 13$. Polynomial fits to the dipole moment function were determined over the range of inter-nuclear separation 0.97 to 1.50 Å. The fitted dipole moment functions agree well with previous *ab initio* predictions, but differ somewhat at the larger inter-nuclear separations. The observed dipole moment functions were used to compute rotationless Einstein coefficients for $\Delta v = 1$ through 4 vibrational transitions with $v' \leq 20$. The absolute $\Delta v=1$ and $\Delta v=2$ Einstein coefficients were well determined by this analysis, especially for $v' \leq 12$. The results provide a firm basis for determinations of vibration-rotation emission intensities of $\text{NO}(X^2\Pi)$ in high-temperature or non-equilibrium chemi-excitation systems.

These results were summarized in a journal article for the *Journal of Chemical Physics* that is included in this report as Appendix 2.

4. THE EFFECTS OF CENTRIFUGAL DISTORTION ON THE INFRARED RADIATIVE TRANSITION PROBABILITIES OF NO($X^2\Pi$)

State-to-state and thermally averaged Einstein A-coefficients were computed for the fundamental and first three overtone sequences of the NO ($X^2\Pi$ - $X^2\Pi$) system with the aim of examining the effects of centrifugal distortion on the high-J transitions that occur as a result of upper atmospheric chemistry. The Einstein coefficients were calculated using an experimentally derived dipole moment function (described in Appendix 2), and the *ab initio* dipole moment functions of Langhoff et al.,¹⁶ and de Vivie and Peyerimhoff¹⁷ for J' ranging up to 139.5. The state-specific Einstein coefficients show that, regardless of dipole moment function employed, centrifugal distortion has a relatively small effect on the $\Delta v = 1$ sequence which is manifest primarily as a reduction in the high-J R-branch intensities. However, the effect on the overtone rotational intensities is larger and results in enhanced R-branch intensities and reduced P-branch intensities relative to those calculated neglecting centrifugal distortion. For example, in the first overtone system for J' \approx 80.5, $v' = 2$ to 14, the ratio of R- to P-branch Einstein coefficients is larger by about 1.7 than the R/P ratio predicted in the absence of centrifugal distortion.

These results were summarized in a journal article published in the *Journal of Quantitative Spectroscopy and Radiative Transfer* and included in this report as Appendix 3.

5. ROTATIONAL RELAXATION OF HIGH-N STATES OF OH ($X^2\Pi$, $v=1-3$) by O_2

We have studied the relaxation of OH($X^2\Pi$, v , N) produced by the reaction $O(^1D) + H_2 \rightarrow OH^* + H$. Infrared emission measurements of the fundamental vibration-rotation band of OH were acquired at a temperature of 100 K in a large cryogenic chamber. Trace amounts of ozone were added to mixtures of H_2 , O_2 , and Ar at low (≤ 38 mT) pressures. The ozone was photolyzed to produce $O(^1D)$. Rapid reaction with H_2 produced OH^* . Spectrally and temporally resolved emissions from levels up to the exothermic limit were observed with sufficient spectral resolution to permit kinetic analysis of individual level populations. The production rate was observed to scale as the rotational quantum number except at the highest levels populated. At early times we observed inverted rotational state distributions that subsequently relaxed to form thermal distributions in each vibrational level. Under these conditions, rotational relaxation was rapid in comparison with vibrational relaxation. Rotational relaxation within a given vibrational state could be represented by single quantum collisional exchange at near-gas-kinetic rates. The rotational level dependence of the deduced relaxation was determined.

These results were summarized in a journal article published in the *Journal of Geophysical Research*, and included in this report as Appendix 4.

6. THE REACTION OF FAST N-ATOMS WITH O₂

6.1 Introduction

This section describes work in progress on a task to investigate the reaction of high-velocity atomic nitrogen with molecular oxygen. The reaction



may be responsible for the excitation of rovibrationally excited NO(v,J) in auroras and in the quiescent dayglow. This reaction has been implicated in the analysis of infrared excitation spectra of NO from the EXCEDE 3 and CIRRIS 1A flight experiments, and its reaction dynamics have been modeled by classical trajectory calculations. The objective of the current task is to use the PSI fast-atom molecular beam apparatus to determine reaction cross sections for excited NO formation as functions of interaction velocity, and to observe product excitation distributions. The excited NO product molecules are monitored by low-resolution, high-sensitivity infrared emission from the interaction of a high-velocity N/N₂ beam with thermal O₂.

The experiments are conducted in the PSI FAST-2 crossed molecular beam chamber. The fast N-atoms are generated by pulsed laser-induced breakdown of N₂ in the throat of a synchronized, pulsed molecular beam valve/nozzle combination. The pulsed beam, which contains fast N-atoms, N₂, and the ions N⁺ and N₂⁺, propagates out of the nozzle and into the reaction chamber. O₂ is admitted to the reaction chamber either as an orthogonal molecular beam or as a slowly flowing gas filling the chamber at low pressure (1 to 8 x 10⁻⁵ Torr). The directed velocity of the N-atoms in the pulsed beam is determined by a bank of fast-response, near-infrared (NIR) radiometers as discussed further below. The infrared radiation from the reaction volume is viewed with a wide field by fast-response, bandpass-filtered infrared radiometers and/or a circular-variable filter (CVF) spectrometer. The filter bandpasses are selected to probe various portions of the NO fundamental (~5 μm) and first overtone (2.5 to 3.5 μm) vibrational bands in order to determine both total excited NO production and the extent of vibrational and rotational excitation.

6.2 Beam Composition

The pulsed nitrogen beam was directly observed by a time-of-flight mass spectrometer, which was used to determine the N/N₂ and ion/neutral ratios reaching the interaction zone. The performance of the mass spectrometer was validated by observing fragmentation ratios and responsivities for CH₄, N₂, O₂, and NO. These measurements resulted in calibrations of the mass spectrometer for known pressures of static and flowing gases, which were consistent with manufacturer's specifications. Preliminary measurements of the pulsed nitrogen beam were then performed, monitoring the signal voltage versus time at m/e = 14 and 28 with the ionizer on and off. These measurements and the accompanying data processing and analysis established our ability to determine the relative fluxes of N, N₂, N⁺, and N₂⁺ as functions of time in the pulsed beam.

The results of mass spectrometer measurements for an 8 km/s N-atom beam are shown in Figure 15. The curves in Figure 15 were determined by correcting the raw voltage-vs-time profiles for the mass spectrometer response as determined from the calibrations described above. With the ionizer off, the $m/e = 14$ and 28 signals sample the beam species N^+ and N_2^+ , respectively. These ions are detected with almost unit efficiency, giving a much higher signal voltage for a given sample number density than can be obtained for initially neutral species with the ionizer on. It is clear from the ratio of the two signals that, for the time where the neutral N signal is largest, the ionic component of the beam consists of $\approx 95\% N^+$.

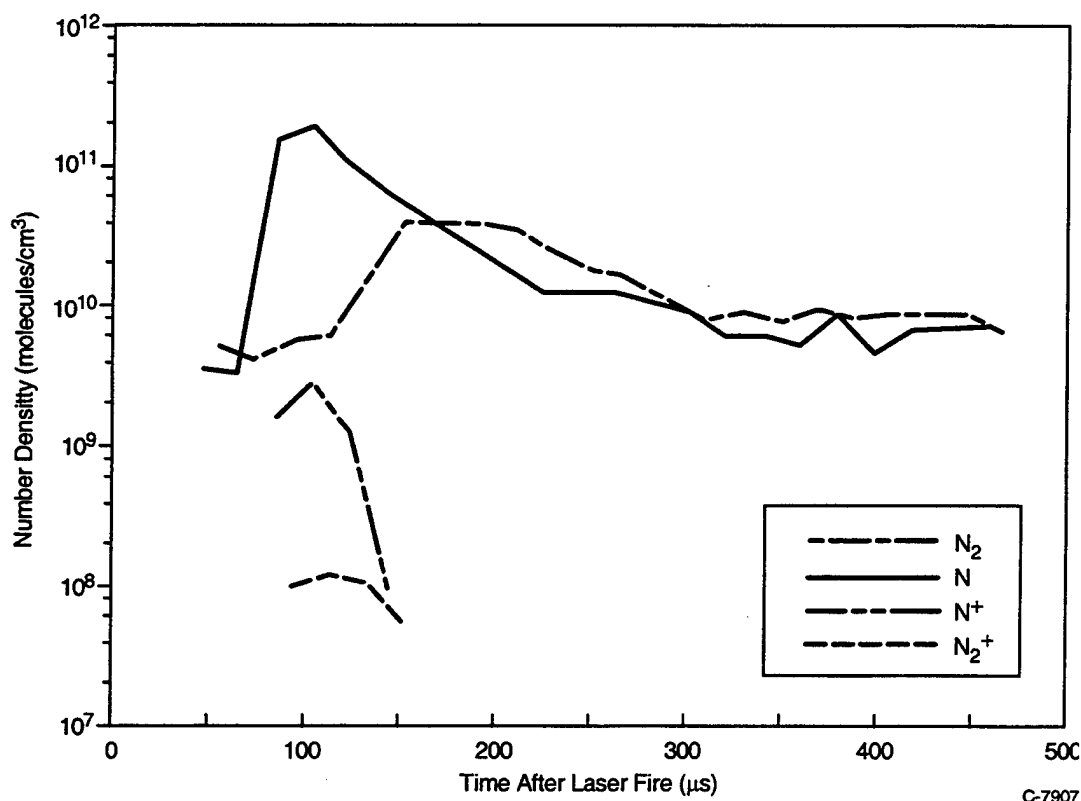


Figure 15. Species number densities in fast-nitrogen beam, directed velocity 8 km/s.

When the ionizer is on, the $m/e = 14$ signal samples both N^+ from the beam and N^+ that has been formed in the ionizer from N (and N_2) in the beam. (The contribution from N_2 is a small correction which has been removed from the data plotted in Figure 15.) Similarly, the $m/e = 28$ signal samples both N_2^+ and N_2 . Although the detection efficiency for N^+ is much higher than that for N, the observed voltage at $m/e = 14$ is actually reduced when the ionizer is turned on. This is because the incoming N^+ ions are repelled and/or charge neutralized by the ionizer. To generate the N and N_2 curves plotted in Figure 15, we have assumed that all of the signal observed with the ionizer on is due to the neutral species, giving an upper bound to the neutral species number densities. However, the mass spectrometer measurements alone cannot rule out the possibility that much of the signal with the ionizer on is still due to incoming ions from the beam.

Separate measurements with a Langmuir probe have been used to determine the ion/neutral ratio of the beam. From comparison of measured ion currents to the known mass flow processed by each pulse, the total ion mole fraction in the beam is about 0.01 or less. Comparison of this result with the N^+/N ratios shown in Figure 15 supports our assumption for the mass spectrometer that the incoming ions from the beam make little or no contribution to the signals observed with the ionizer on.

Thus we conclude from these data that for the time scales of interest ($\leq 200 \mu\text{s}$ after the laser pulse), the beam consists primarily of fast N-atoms. The N_2 mole fraction increases substantially at longer times as the initial pulse of fast N decays away and the slower, undissociated gas slug arrives. We note that the fast N-atoms in the beam could be in the ground $N(^4S)$ state and/or in one or both of the low-lying metastable states, $N(^2D)$ and $N(^2P)$.

6.3 Directed Velocity

The fast-atom directed velocities are determined by a pair of radiometers viewing NIR radiation (roughly 700 to 900 nm) from N-atoms in the beam. These radiometers consist of bandpass-filtered photomultipliers (PMTs) which view orthogonally to the beam axis at two different axial locations. As the radiating atoms travel along the axis, their arrival times are determined by each radiometer in succession, and the time interval between radiometer signals gives the velocity. This method relies on the principle that the observed radiation consists of Rydberg transitions from a small number of excited neutral N atoms formed by electron-ion recombination in the breakdown region, and thus is representative of the fast neutral N. However, in nitrogen plasmas there are many other potential radiators in this spectral region, most notably the $N_2^+(A \rightarrow X)$ Meinel bands, $N_2(B \rightarrow A)$ First Positive bands, and possible Rydberg emission from N^+ . To validate the radiometric beam velocity determination, we measured detailed, high-resolution spectra in the NIR region for comparison to two different choices of radiometer filters.

The NIR spectrum from 720 to 920 nm of a 9 km/s N/N_2 beam was obtained in the FAST-2 source chamber using an optical multichannel analyzer diode array spectrometer (OMA) with a field of view corresponding to that of the PMT radiometers. Radiometer signals were recorded with two different bandpass filters: (1) 780 ± 10 nm interference filters, and (2) RG 715 colored glass filters with a cut-on at 715 nm.

The OMA was positioned at the center of the optical port located on the door of the FAST-2 source chamber. The field of view was arranged to observe the center of the source chamber between the radiometers' fields of view. Both the OMA and the radiometer fields of view were orthogonal to the flow, and as focusing optics were not used with the OMA, the field of view was approximately 3 cm on beam centerline. An RG 715 colored glass filter was used to prevent radiation below 715 nm from being observed by the OMA. The 1200 groove/mm grating was blazed at 500 nm, giving a spectral dispersion of approximately 2.5 nm/mm. Each spectrum spanned approximately 43 nm. Five spectra were recorded to scan the NIR from 720 to 920 nm. The slits were set at 100 μm to give a spectral resolution of 0.25 nm. The OMA scan time was fixed at 10 seconds to record a five-shot cumulative spectrum with the atom beam pulsing at 0.5 Hz.

The five combined spectra shown in Figure 16 were recorded with the OMA running CW to observe all possible radiation in the NIR region of interest. This composite spectrum provides additional information on the plasma flash generated by the breakdown, and indicates all possible interferences within the radiometer bandpasses. It should be noted that the indicated wavelength is approximate, and the intensity is not corrected for relative or absolute responsivity.

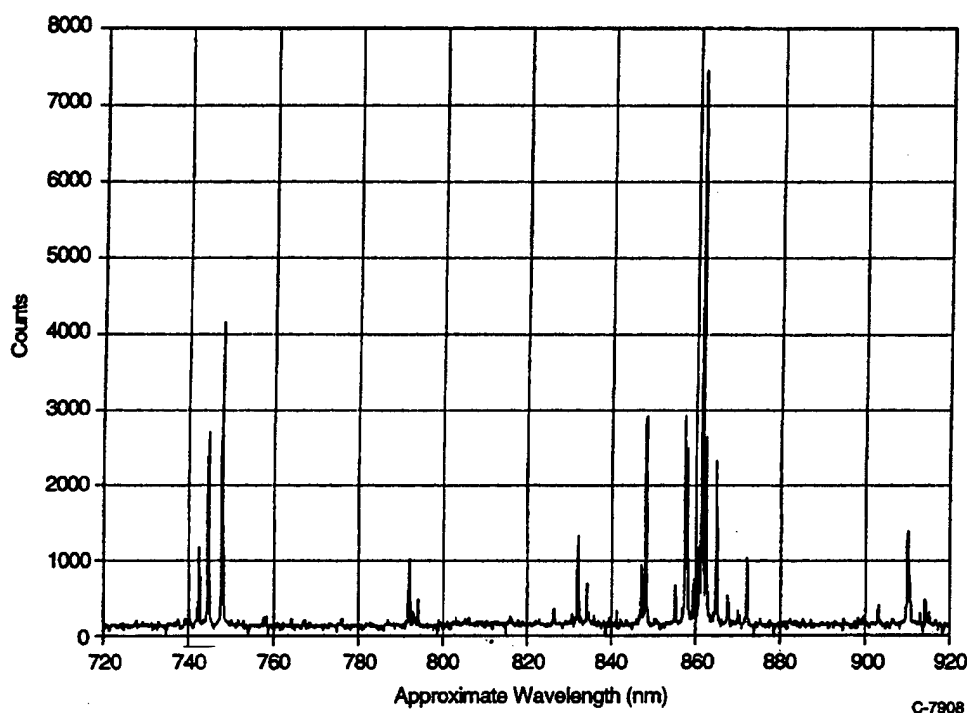


Figure 16. Composite spectrum of fast-N beam, 25 scan average. CW operation of OMA samples plasma and beam emissions.

The five combined spectra shown in Figure 17 were obtained by gating the OMA for the 25 μ s time period when the radiometer signals are used to determine the beam velocity. This spectrum shows the wavelengths at which the radiation occurs in both radiometer bandpasses during the velocity determination. Again the indicated wavelength is approximate, and the intensity is not calibrated. Note that the 760 to 800 nm portion of the spectrum is slightly more intense than that of the original spectrum as it was recorded at a later time as explained above. The gated spectra are about four times less intense than the CW spectra; this is because far more radiation is emitted during the breakdown than in the free-stream flow, and some fraction of this radiation reaches the radiometers as scattered light.

A preliminary examination of the NIR spectral content indicates that atomic nitrogen is the dominant emitter. The strongest features, located in the 740 to 750 and 850 to 870 nm regions correspond to N(I) Rydberg transitions, and the weaker features around 790, 830, and

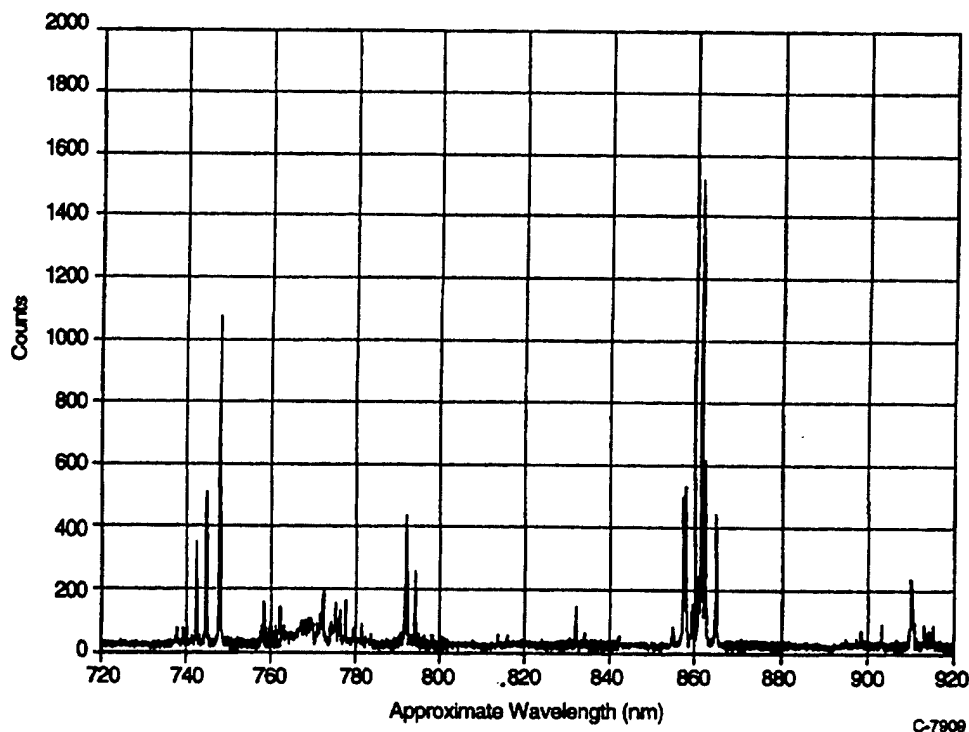


Figure 17. Composite spectrum of fast-N beam, 25 scan average. Gated operation of OMA samples near-field beam emission only.

910 nm also appear to be due to N-atoms. No significant N_2 or N_2^+ features are observed. These observations are consistent with the beam composition results described above. Very little radiation is observed in the region of the 780 nm narrow bandpass filter where the N_2^+ Meinel bands are located, however the source of the radiation in this bandpass is not readily apparent. We will continue to analyze these spectra for more conclusive identification of the radiating species as atomic nitrogen.

Figure 18 shows two sets of radiometer signals recorded after the above spectra were obtained, and the location of the OMA gate pulse. In each trace, the initial peak observed at early time is due to scattered light from the laser-initiated plasma, and the second pulse at later time is due to passage of the pulsed beam through the field of view of the radiometer. The narrow band radiometer traces were obtained with 750 volts applied to each PMT, and the wide band radiometer traces required only 450 volts applied to each PMT to provide an equivalent signal. This represents a 100-fold increase in photon flux with the RG 715 filter set over 780 nm narrow-band filter set. A beam velocity of 8.9 km/s was obtained from the narrow band traces, as compared to a beam velocity of 9.4 km/s for the wide band traces. This is reasonably good agreement, indicating that the radiometric method is a valid means for determining the N-atom directed velocities.

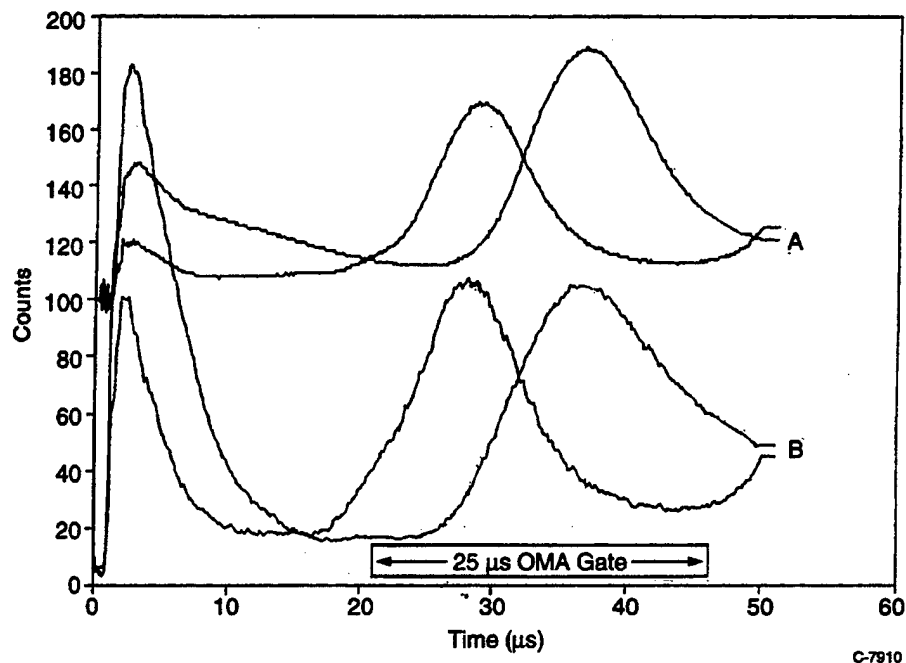


Figure 18. NIR radiometer traces of nitrogen beam. (a) RG715 (wide-band) filter, directed velocity = 9.4 km/s; (b) 780 ± 10 nm (narrow-band) filter, directed velocity = 8.9 km/s. The OMA gate used for the spectrum in Figure 17 is also shown.

We have validated the experimental methods for determining beam composition and number density and for determining the directed velocity of the fast N-atoms. At times near 100 μ s after the laser pulse, the beam is predominantly fast N, with a small amount of N_2 , $\approx 1\%$ N^+ , and negligible N_2^+ . NIR radiometer measurements provide an accurate measure of the directed N-atom velocity, especially with wide-bandpass filters.

6.4 Crossed Beam Experiments

Calibration measurements and cross-section measurements for the reaction of fast nitrogen atoms (8 and 10 km/s) with molecular oxygen were performed. A product of the reaction of fast N with O_2 is vibrationally excited nitric oxide which emits radiation in both its fundamental and overtone bands near 5.2 μ m and 2.6 μ m respectively. One of PSI's FAST systems, described previously and shown in Figure 19, was used in its cross beam configuration to measure fundamental and overtone emission of vibrationally excited NO formed by this reaction.

Molecular oxygen was injected into the FAST source as a supersonic molecular beam, at 90 deg with respect to and 85 cm down stream from the nitrogen valve through a pulsed molecular beam valve (General Valve). The backing pressure in the oxygen valve was approximately 1300 Torr which produced an intra-pulse density in the vacuum chamber in a range such that only a single collision between nitrogen atoms and oxygen molecules was expected. Operation in this single collision regime was verified experimentally by demonstrating a linear relationship between IR emission and O_2 backing pressure up to 1300 Torr.

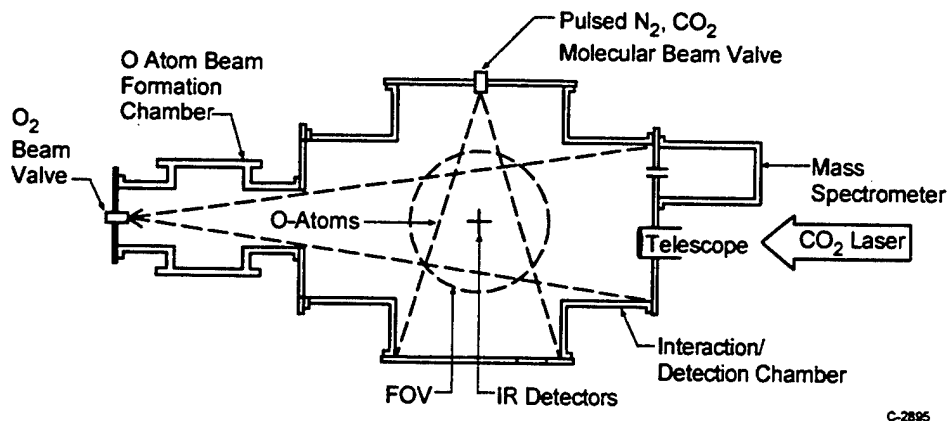


Figure 19. Schematic of the FAST system configured for measurements of reaction cross sections by detection of IR emission.

The experiments were run with a master clock operating at 2 Hz and two digital delay generators. The master clock triggered the oxygen valve which opened for 1000 μ s. After a 1000 μ s delay, the nitrogen valve was pulsed and, after an additional 500 μ s delay, the CO₂ laser was triggered. The delay between the nitrogen valve firing and the CO₂ laser trigger is chosen to produce the desired N atom beam velocity (8 or 10 km/s). The delay between the pulsing of oxygen and nitrogen valves was chosen so that the fast N atom beam pulse reached the center of the interaction region concurrent with the arrival of the peak of the 1000 μ s duration oxygen pulse.

Infrared emission was detected with an InSb detector (Cincinnati Electronics, 0.8 mm diam, 60 deg FOV, at 77 K). Bandpass filters were used for detection of NO fundamental (5.07 to 5.5 μ m) and overtone (2.56 to 2.99 μ m) emission. The measured signals were used in the calculation of cross sections, σ , for the reaction of fast N with O₂ by Eq. (6):

$$\sigma(\text{cm}^2) = \frac{\text{sig}}{\text{gain}} \frac{\lambda_m}{hcR_\lambda A_v T \text{CE} \text{Col}_N \text{O}_{2\text{vol}}} \quad (6)$$

where:

sig	=	measured signal in volts
gain	=	amplifier gains for the InSb detector
λ_m	=	center wavelength of the detection bandpass
h	=	Planck's constant
c	=	speed of light
R_λ	=	response of the InSb detector at λ_n , Amps/Watt
A_v	=	Einstein Coefficient for the fundamental or overtone transition
T	=	transmission through detection optics
CE	=	collection efficiency of the detector
Col_N	=	column density of N atoms, /cm ²
$\text{O}_{2, \text{vol}}$	=	number of O ₂ in the interaction volume

The cross-sections for the fundamental and overtone region are summarized in Table 3 along with values for several of the elements of Eq (6) used in the calculation. The percentage of the nitrogen beam that is atomic is based upon a previous mass spectrometer analysis of the fast nitrogen beam.

Table 3. Cross Sections for Formation of Vibrationally Excited NO via the $N + O_2$ Reaction in Addition to Some of the Relevant Parameters

50% Bandpass (μm)	N Atom Velocity (km/s)	R_λ (A/W)	A_ν (s^{-1})	$O_{2, \text{vol}}$	Col_N ($/\text{cm}^2$)	Atomic % of N Beam	(cm^2)
5.07 to 5.50	8	3.16	13.3	1.69×10^{18}	5.71×10^{14}	78	4.13×10^{-18}
5.07 to 5.50	10	3.16	13.3	1.69×10^{18}	3.93×10^{14}	91	1.03×10^{-17}
2.56 to 2.99	8	2.46	0.9	1.69×10^{18}	5.71×10^{14}	78	1.41×10^{-17}
2.56 to 2.99	10	2.46	0.9	1.69×10^{18}	3.93×10^{14}	91	2.95×10^{-17}

The cross sections recorded in Table 3 are considerably less than expected based upon a theoretical prediction by J. Duff.^{18,19} For example, Duff's model can be used to predict a cross-section for formation of vibrationally excited NO (by the reaction of 8 km/s N with O_2) emitting in the fundamental band equal to 3.6×10^{-16} , a factor of 87 times greater than reported in Table 3.¹⁹ For this reason a series of calibration measurements was undertaken to verify the performance of critical instruments used in the cross-section determination.

Mass flow meters are used to measure the flow of nitrogen and oxygen into the vacuum chamber. The measured mass flows are used in the determination of the column density of N atoms (Col_N) and the number of oxygen molecules in the interaction volume ($O_{2, \text{vol}}$). The calibrations of both the mass flow meters were checked and found to be within 0.5% of expectations.

The responsivity (A/W) of the InSb detector recorded in Table 3 was determined by the detector manufacturer's responsivity curve (detector response versus wavelength) supplied when the detector was purchased in 1992 and PSI's measurement of the transmission of the bandpass filters. Since it is possible for the detector responsivity to degrade with time, and some inherent inaccuracies are involved in overlaying the filter transmission curves over the detector responsivity curve, the detector was recalibrated. The calibration procedure involved measuring the detector output in front of a NIST traceable blackbody standard at 1000°C. The detector response was measured with the bandpass filters installed and the actual amplifiers used for the cross-section measurements. Therefore the entire detector "system" was calibrated, which should compensate for variations in filter transmission and amplifier offsets. The irradiance onto the blackbody (W) was calculated from Planck's law and the measured filter transmission curves and compared to the detector output (A) to determine the responsivity in both bandpasses. The results of the measurements are summarized in Table 4.

As is evident from Table 4, the new detector calibration affects the cross-sections only minimally.

Table 4. Results of the InSb Detector Calibration

50% Bandpass (μm)	Manufacturer's Calibration (A/W)	March 1997 Calibration (A/W)	Revised σ (cm^2) 8 km/s N
5.07 to 5.50	3.16	2.94	4.44×10^{-18}
2.56 to 2.99	2.16	2.24	1.36×10^{-17}

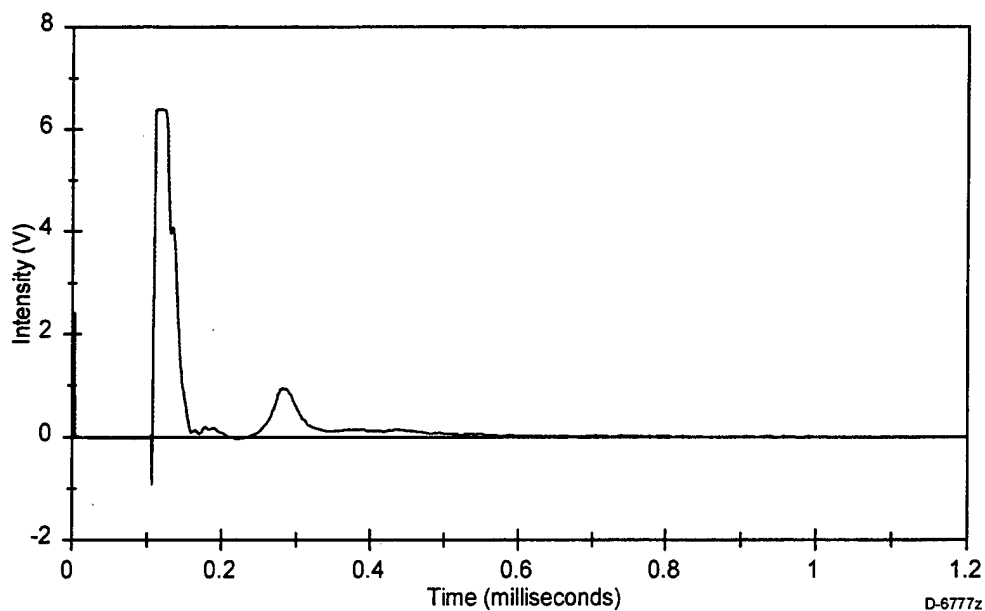
Another area of uncertainty in the calculation of the cross-section is the Einstein coefficient. Although both the work by Duff and our own bandpass spectra suggest significant vibrational excitation of the nitric oxide product (note that the cross-section for the overtone recorded in Table 3 is larger than the fundamental), the Einstein coefficients for the 1 - 0 and 2 - 0 transitions have been assumed for the fundamental and overtone respectively. Since the Einstein coefficients increase in magnitude with vibrational level, a population-weighted value for A_v will be greater than the values of A_v assumed in Table 3. Thus the cross-sections calculated in this way are an upper bound. Compensating for this discrepancy will not improve the comparison to Duff's predictions.

6.5 Beam Composition

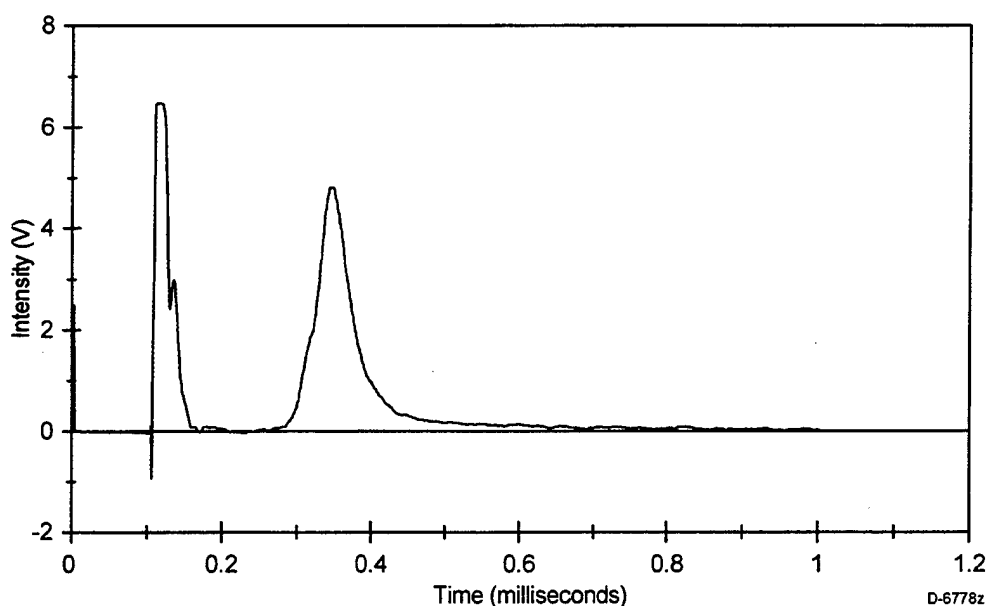
Because the atom/molecule fraction varies with beam velocity and affects the cross section determination, we undertook the determination of the composition of the beam and its impact on the measured cross sections. In addition, a higher resolution spectrum of the NO fundamental band was measured for the $\text{N} + \text{O}_2$ reaction using a Circular Variable Filter (CVF) system.

PSI's FAST system used for these measurements is shown schematically in Figure 19. The system includes a differentially pumped mass spectrometer which was used for the beam composition measurements. The mass spectrometer was operated with a 1-mA emission current and an 80-V ionizing potential. To determine the composition of the beam the mass spectrometer signals at mass to charge values of 14 and 28 (N atoms and molecules respectively) were measured and compared. To determine the beam composition from the measured signals, the signals were normalized by the relative cross section for ionization by 80 eV electrons in the ionizer²⁰ and the transmission function of the mass spectrometer. The transmission function describes the sensitivity of the mass spectrometer as a function of mass-to-charge ratio. Previous measurements of the transmission function for this mass spectrometer found that its sensitivity decreased by a factor of 0.73 from $m/e = 14$ to $m/e = 28$. In addition, molecular nitrogen will contribute to the mass 14 signal due to dissociation in the ionizer. Therefore in order to make a measurement of beam composition, the cracking pattern for N_2 must also be taken into account. It was found that the mass 14 signal that resulted from dissociation of N_2 in the ionizer was 10.2% of the mass 28 signal.

Temporal profiles of the mass 14 and 28 signals measured with the fast nitrogen beam operating at a velocity of 8 km/s are shown in Figure 20a and b respectively. The digital oscilloscope used to collect these temporal profiles was set so that the CO_2 laser of the FAST



(a)



(b)

Figure 20. Temporal profiles of the 8 km/s nitrogen beam measured with the mass spectrometer for the (a) $m/e = 14$ and (b) $m/e = 28$ species.

source fired 100 μs into the traces. The off scale feature originating 100 μs into the profiles with a duration of approximately 50 μs is due to scattered light from the plasma initiation reaching the channeltron detector of the mass spectrometer and causing electron emission. The time-of-arrival of the fast atomic and molecular species in the beam can be predicted based upon the expected time of flight to the ionizer (located 126 cm from the nozzle throat) for 8 km/s species,

which is 157 μs and the measured time of flight of mass 14 and 28 ions from the ionizer to the detector, 30 and 40 μs respectively. With the laser firing 100 μs into the profiles, the expected time of arrival of mass 14 and 28 species at the detector is 187 and 197 μs respectively. As observed in Figure 20, the time-of-arrival of the N atoms is as expected from this prediction. However, the fast nitrogen molecules are traveling at approximately 6.3 km/s. Note that with the laser turned off, the "cold" flow of nitrogen beam is expected to arrive at the mass spectrometer at 1.9 milliseconds (off scale). The relative signal levels of the atomic and molecular features in Figure 20 indicate that the 8 km/s beam contains a significant fraction of molecules.

It should be noted that velocities are measured in the FAST source by the time-of-flight of radiating species between two filtered radiometers. Much of the detected radiation is due to ionic emission and thus the quoted velocity may not represent the N atoms velocity. Although the nitrogen atoms in the 8 km/s nitrogen beam were observed to travel at the same velocity as measured by the radiometers, this was not the case for the 10 km/s beam. With a radiometer determined velocity of 10 km/s, the nitrogen atom and molecule velocity measured by time-of-arrival at the mass spectrometer was 8.7 and 7.4 km/s respectively.

The beam composition was determined by subtracting temporal profiles measured with the ionizer turned off from the profiles measured with the ionizer on. The resulting signal levels were then corrected for the cracking pattern of molecular nitrogen and normalized by the relative ionization cross section and the transmission function. The beam composition was then determined from the relative intensities of the corrected atomic and molecular features. The results of this analysis are summarized in Table 5.

Table 5. Summary of The FAST Nitrogen Beam Composition Measurements

Velocity (km/s)	Atomic % of the Beam	Previous Estimate of Atomic %
8	20.7	78
10	23.9	91

The procedure used to measure the cross section for the $\text{N} + \text{O}_2$ reaction described above was repeated for the new nitrogen beam composition. The resulting cross sections are summarized in Table 6.

Table 6. Summary of the Cross Section Measurements for the $\text{N} + \text{O}_2$ Reaction
Adjusted for Beam Composition

50% Band Pass (μm)	Velocity (km/s)	Atomic % of Beam	(cm^2)	Previously Reported (cm^2)
5.07 to 5.50	8	20.7	3.59×10^{-17}	4.13×10^{-18}
5.07 to 5.50	10	23.9	5.34×10^{-17}	1.03×10^{-17}
2.56 to 2.99	8	20.7	8.78×10^{-17}	1.41×10^{-17}
2.56 to 2.99	10	23.9	1.67×10^{-16}	2.95×10^{-17}

The increase in the cross section reported due to the new beam composition measurement is significant. At 8 km/s the cross section reported in Table 6 for the fundamental is still a factor of 10.0 smaller than that predicted by Duff's model.

A higher resolution (1.8%) spectrum of NO fundamental emission produced in the N (8 km/s) + O₂ reaction was measured with a CVF in the experimental configuration shown schematically in Figure 21. The emission intensity at each wavelength setting of the CVF was measured from the peak of the temporal profile measured with the InSb detector. The resulting intensity was then normalized by the relative response curve measured for the detection system to determine the spectral intensity at a particular wavelength. The relative response curve for this system is shown in Figure 22. The response curve was determined by measuring the detector response as a function of wavelength with a blackbody (1000°C) positioned in the detector's field-of-view. The detector response was compared to the irradiation expected from the blackbody at the detection wavelength to determine the response curve.

The measurement of the temporal profile at each wavelength setting included a background subtraction determined by measuring the temporal profile with the O₂ valve turned off. This background subtraction allowed for correction due to emission that might arise from the N atom beam itself or from interaction of the beam with contaminants on the vacuum chamber wall. Each temporal profile averaged approximately 500 pulses of the FAST source operating at 2 Hz. It therefore took approximately 10 min to record data from each CVF rotation position. To correct for long term drift of the system, a second InSb detector, filtered to detect emission from 4.0 to 5.5 μm, was operated during each measurement with the CVF. The CVF spectrum was normalized at each point by the signal measured with this second detector to correct for system drift. The response corrected spectrum of the NO fundamental emission from the N(8 km/s) + O₂ reaction is shown in Figure 23.

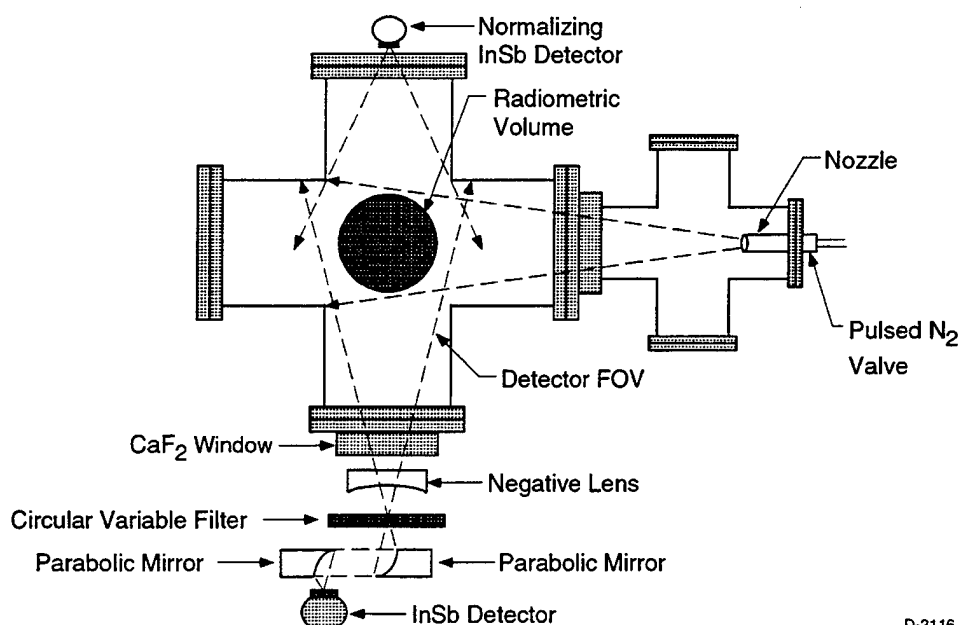


Figure 21. Schematic of the CVF-based detection system used to measure higher resolution spectra of the NO fundamental.

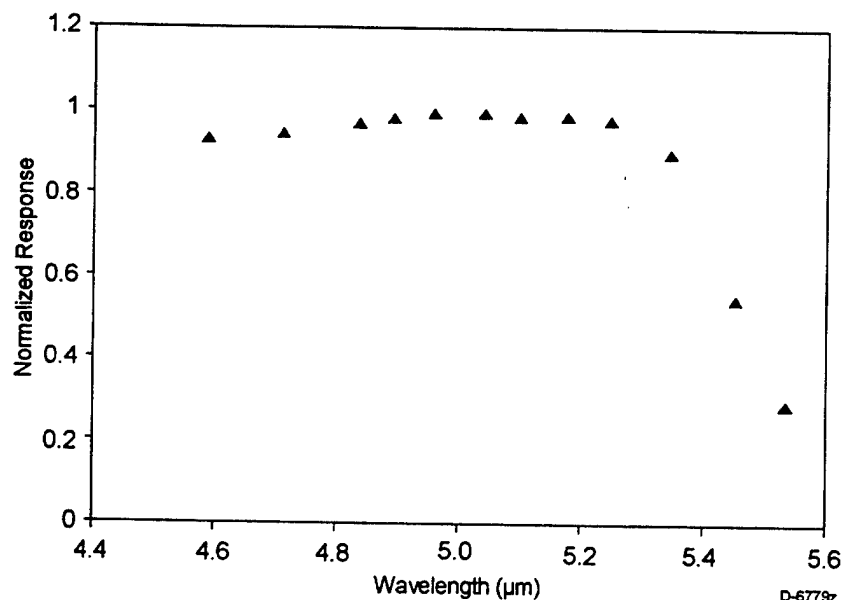


Figure 22. Relative response curve of the CVF system as a function of wavelength.

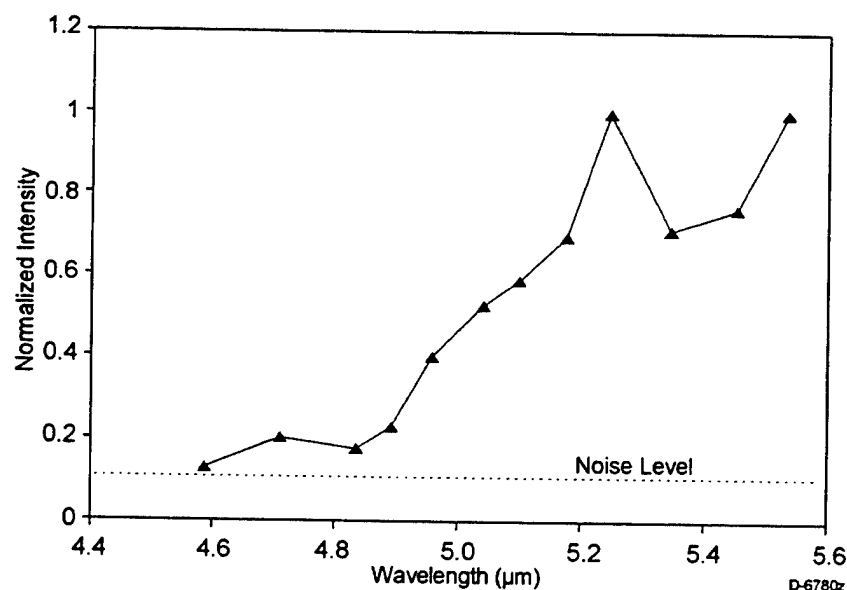


Figure 23. Response corrected spectrum of the NO fundamental for the N(8 km/s) + O₂ reaction measured with the CVF system.

Based on this approach, we completed additional measurements of fundamental and overtone emission for the N + O₂ reaction as a function of N atom velocity and, more precisely, determined the spectral shape of the fundamental for comparison to the predictions of Duff's model. The final measurements were summarized in a journal article published in the *Journal of Geophysical Research*, and included in this report as Appendix 5.

7. EVALUATION OF FAST ATOM CONTRIBUTIONS IN COCHISE EXPERIMENTS

7.1 Introduction

This section discusses an analysis of the potential fast-atom contribution in COCHISE NO(v,J) excitation experiments. This effort was undertaken in the light of recently emerging high-altitude and laboratory observations and theoretical predictions indicating that the reaction of translationally "hot" N-atoms with O₂ results in the rapid formation of rovibrationally excited NO(v,J). Previous COCHISE infrared chemiluminescence experiments have been interpreted in terms of NO(v,J) formation by reaction of the translationally thermal metastables, N(²D) and N(²P), with O₂.²¹ More recent COCHISE experiments have observed NO(v,J) excitation ascribed to energy transfer from nitrogen metastables.²² In both cases the nitrogen metastables were generated in a microwave discharge of rapidly flowing N₂/Ar mixtures at \approx 1 Torr and \approx 80 K. This report addresses the issue of whether translationally "hot" N-atoms generated in these discharges could have contributed to the observed NO(v,J) excitation phenomena.

We have assessed the production of hot N-atoms in the COCHISE microwave N₂/Ar discharges, using detailed kinetic modeling to evaluate the quenching in the afterglow region between the end of the discharge and the expansion into the reaction cell. A worst-case prediction agrees with earlier estimates and indirect experimental observations that hot atoms are present in the reaction cell at number densities too low to contribute to observable IR fluorescence. In addition, the role of N⁺ in the chemiluminescence is addressed.

7.2 Discharge Tube Configuration

The present discharge tubes, installed in 1985, are four 1/2 in. (o.d.) sapphire tubes with external microwave tunable cavities. Each tube is 9 in. long, with 5 in. of active discharge region. The configuration of a tube and microwave discharge cavity is illustrated in Figure 24. The cavity is a McCarroll-Evenson design with the McCarroll extended sidearms cut short to give a 2 in. long discharge region. The discharge region is extended by wrapping with aluminum foil 1-1/2 in. past the upstream and downstream ends of the McCarroll sidearms. The discharges cannot be viewed during cryogenic operations inside the COCHISE chamber; however, experience with these discharges at room temperature has shown that the active discharge does not extend past the end of the foil wrapping, and is indeed somewhat less visually intense under the foil than it is under the cavity.

Beyond the downstream end of the active discharge region, there is another 3/4 in. of flow length to the outlet of the tube. At this point the flow expands into the reaction cell, and there are no further collisions until the gas reaches the stagnation region where it mixes with the counterflow (reagent) gas. Typical linear flow velocities in the discharge tubes are \approx 3300 cm/s at 1 Torr and 80 K, so the residence time in the 3/4 in. afterglow section is \approx 600 μ s.

Earlier discharge tubes, installed in 1981, were 10 in. long and had a 2-1/4 in. afterglow section (\approx 1.8 ms residence time). Those tubes actually protruded about 1 in. into the cell, while

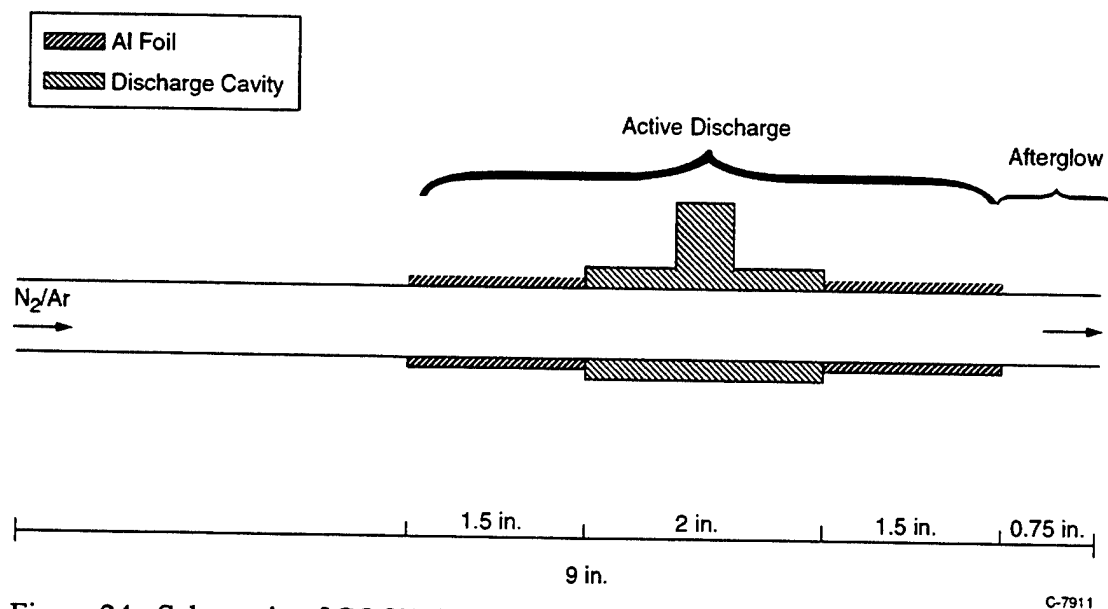


Figure 24. Schematic of COCHISE discharge tube showing position of microwave cavity and Al foil extensions.

the present tubes are flush with the inner wall of the cell. We have obtained very similar $NO(v,J)$ excitation data with both configurations.

7.3 Kinetic Modeling Analysis

The approach to the kinetic modeling calculations was as follows:

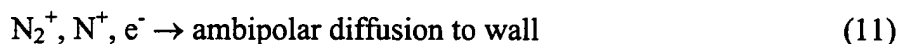
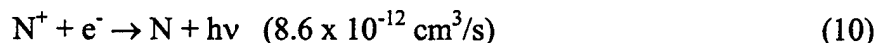
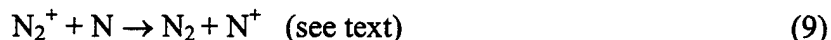
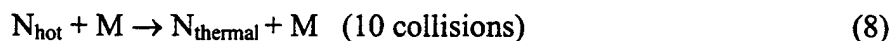
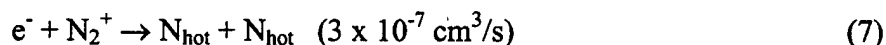
- (1) Use steady-state approximations to estimate the electron, ion, and hot-atom number densities within the active discharge.
- (2) Use these number densities as initial conditions for a time-resolved kinetic modeling calculation of the hot-atom production and quenching in the afterglow region. This determines the electron, ion and hot-atom number densities at the tube outlet.
- (3) Apply the tube-to-cell expansion factor of $\approx 1/300$ to determine the number densities of electrons, ions, and hot atoms delivered to the mixing region.
- (4) Use steady-state approximations for the cell axial stagnation zone to estimate the continued production of hot atoms by electron-ion recombination in the mixing region, and the maximum possible $NO(v,J)$ production by hot atoms reacting with counterflow NO or O_2 .

Hot N-atoms are produced in the discharge, the afterglow, and the reactant mixing volume by dissociative recombination of cold electrons with N_2^+ . Additional N_{hot} production may occur in the active discharge by electron-impact dissociation of N_2 ; we have neglected that process for this analysis. The formation of N_{hot} by electron impact dissociation typically requires

excitation to a high-lying dissociative state with energy substantially greater than the dissociation energy (9.7 eV). Formation of highly translationally excited atoms is a relatively minor dissociation pathway for discharges in 1 torr of N₂/Ar, which have electron "temperatures" of only 2 to 5 eV. In general, the electron impact process for these electron energy distributions mainly produces N-atoms via excitation and predissociation of medium-energy electronic states, giving atoms with relatively low translational energies which are quickly thermalized by collisions at 1 Torr. On the other hand, dissociative recombination of N₂⁺ can potentially produce atoms with much greater translational energies which are more likely to survive short residence times at 1 Torr.

The dissociative recombination process is about 5.8 eV exoergic for 2N(⁴S) production, but only about 1 eV exoergic for 2N(²D). The latter was observed to be the primary reaction pathway by Queffelec et al,²³ so we expect that the hot atoms generated in the COCHISE apparatus are primarily N(²D) with relatively low translational energies. From analysis of the NO(v,J) excitation distributions in the COCHISE energy transfer (discharged N₂/Ar + NO/Ar) experiments,²² we estimate via conservation of angular momentum that an N-atom velocity of ≈ 4 km/s (1.2 eV) would be required to produce the observed excitation by T→R transfer. Since the 1 eV of excess energy in the dissociative recombination process to form 2N(²D) must be shared between the two separating atoms, there is clearly not enough energy imparted to account for the NO(v,J) excitation by T→R transfer alone, even neglecting collisional moderation of the atoms. Of course, chemically reactive energy transfer, in which the electronic and translational excitation of the atoms both contribute to product excitation, could still explain the observations. Similarly, the observed energetics of NO(v,J) produced by discharged-N₂/Ar + O₂ (estimated to be 4 to 5 eV²¹) could perhaps be accounted for by reaction of sub-eV N(²D) with O₂ (3.8 to 4.8 eV).

For the sake of establishing a conservative bound, we proceed with the kinetic analysis of the fate of hot N-atoms without distinction for whether the atoms are formed as N(⁴S) with high translational energy or N(²D) with low translational energy. The discharge modeling included collisional gas phase and wall thermalization of N_{hot}, and ambipolar diffusive loss of the electrons and ions to the wall. The ambipolar diffusion is much faster in the active discharge than in the afterglow where the electrons are thermal. Rate coefficients were drawn from values given by Kaufman.²⁴ The following reactions were considered for the active discharge and afterglow regions:



Note that we assumed 10 collisions were required to thermalize N_{hot}. The steady-state electron number density was taken to be $\approx 10^{11} \text{ cm}^{-3}$ for the active discharge, based on Kaufman's paper.²⁴

The calculations give a steady-state $[N_{\text{hot}}] \approx 10^9 \text{ cm}^{-3}$ in the active discharge. To first order, it seems that N_2^+ is the dominant positive ion, however note our comments about N^+ later in this report (Subsection 7.4).

The kinetic model predictions for the afterglow region, assuming the charge transfer reaction (9) is negligible and that N_2^+ is the dominant positive ion, are shown in Figure 25. Time zero signifies the end of the active discharge, and $600 \mu\text{s}$ is the end of the discharge tube. Despite continued production by dissociative recombination after cessation of the discharge, $[N_{\text{hot}}]$ decays in the afterglow region by a factor of 200 due to the effects of collisional moderation and loss of the precursors. $[e^-]$ and $[N_2^+]$ each decay by a factor of 20 due to reaction with each other and loss at the wall.

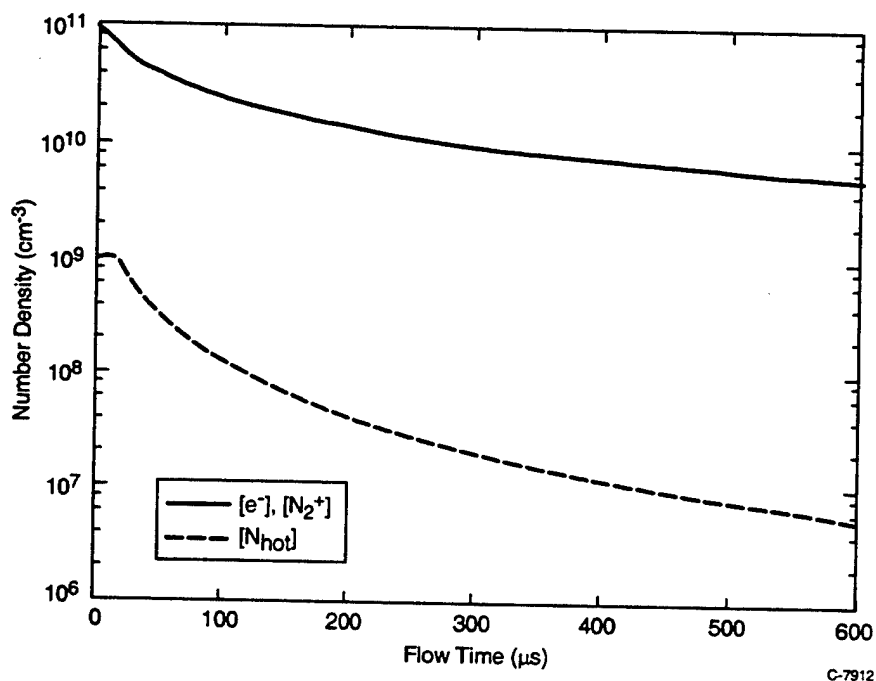


Figure 25. Evolution of N_{hot} and precursors in discharge afterglow: no charge transfer.

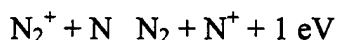
Dividing the computed number densities at the outlet by 300, we see that the number densities delivered to the mixing region are $[e^-] = [N_2^+] = 2 \times 10^7$, $[N_{\text{hot}}] = 2 \times 10^4 \text{ cm}^{-3}$. During the $300 \mu\text{s}$ residence time in the mixing region, continued dissociative recombination makes at most another $5 \times 10^4 N_{\text{hot}}/\text{cm}^{-3}$, giving a total $[N_{\text{hot}}] = 7 \times 10^4 \text{ cm}^{-3}$. This is in fact a substantial overestimate, since the additional reaction of e^- with N_2^+ is far from steady state on the time scale of the residence time in the mixing region. This number density should be compared to the expected $N(^2D, ^2P)$ number densities of $>10^9 \text{ cm}^{-3}$. If this amount of N_{hot} reacts on every collision (gas kinetic rate coefficient) with counterflow gas ($[O_2] = 2 \times 10^{14} \text{ cm}^{-3}$) to produce excited NO, the resulting steady-state $NO(v, J)$ number density would be $\approx 1 \times 10^6 \text{ cm}^{-3}$. By comparison, we typically observe $NO(v, J)$ number densities of $>10^8 \text{ cm}^{-3}$, with a radiometric detection limit for NO of $\approx 10^7 \text{ cm}^{-3}$.

It is unlikely that this two-order-of-magnitude shortfall in the hot-atom chemistry can be overcome by errors in the estimated N_{hot} production and loss rates, or by unexpectedly proficient

production of N_{hot} by electron impact dissociation. However, if the active discharge can be extended to the end of the tube, eliminating the afterglow region, the N_{hot} number densities reaching the interaction volume should be large enough to generate observable $\text{NO}(v,J)$ emission.

7.4 Contributions from N^+

Now consider the charge transfer between N_2^+ and $N(^4S)$:



Since the ionization potentials of N_2 and N are 15.5 and 14.5 eV respectively, this process is exoergic and should be important in microwave discharges, where N -atom concentrations are large (probably $2 \times 10^{14} \text{ cm}^{-3}$ for the COCHISE discharges). To our knowledge, the only rate coefficient for this reaction published in the literature is an upper bound of $1 \times 10^{-11} \text{ cm}^3/\text{s}$ reported by Ferguson et al in 1968. If the reaction actually occurs with this rate coefficient, then 2/3 of the ions leaving the active discharge will be N^+ . The subsequent afterglow kinetics are profoundly altered, as shown in Figure 26. Since $[e^-] > [N_2^+]$, the N_2^+ is rapidly consumed and N_{hot} is miniscule both in the afterglow and in the mixing region. Furthermore, since there are no fast loss processes for N^+ or e^- , substantial number densities of these species are predicted to reach the mixing region ($\approx 2 \times 10^8 \text{ cm}^{-3}$ of each species).

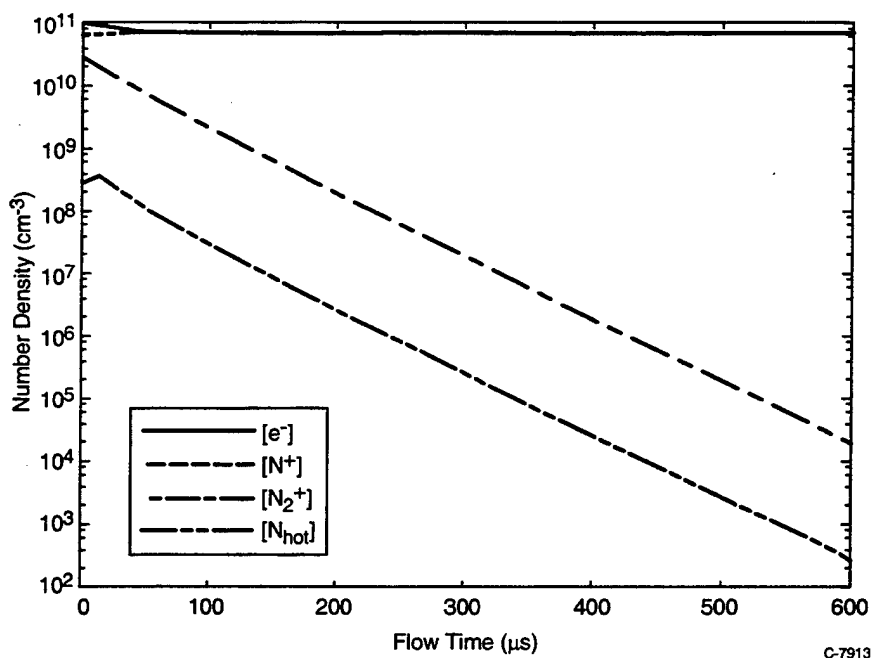


Figure 26. Evolution of N_{hot} and precursors in discharge afterglow: $N_2^+ + N$ charge transfer included.

The electrons are fully thermalized at this point, and so should not cause any gas excitation. However, in the O_2 counterflow experiments, the N^+ should react with O_2 to form vibrationally excited $\text{NO}^+(v)$ as is well known from the work of Leone and coworkers.²⁵ The reported rate coefficient at room temperature for this product channel is $2.6 \times 10^{-10} \text{ cm}^3/\text{s}$. Thus

in 300 μs we would expect $[\text{NO}^+(\text{v})] = 3.6 \times 10^9 \text{ cm}^{-3}$. This would give intense emission at 4.3 to 5 μm , probably as bright as or brighter than the $\text{NO}(\text{v},\text{J})$ spectrum that we observe from $\text{N}^+ + \text{O}_2$. While there have been no dedicated COCHISE measurements for discharged $\text{N}_2/\text{Ar} + \text{O}_2$ concentrated on the region between 4.3 and 5 μm , we have not observed any noticeable emission from $\text{NO}^+(\text{v})$ in incidental scans through portions of this region. A systematic set of COCHISE measurements in this spectral region would serve to quantify this statement better.

In any event, the absence of an obvious $\text{NO}^+(\text{v})$ spectrum in COCHISE suggests that the upper bound rate coefficient for charge transfer from N_2^+ to N^+ should be about $1 \times 10^{-13} \text{ cm}^3/\text{s}$. This raises an interesting question, since exoergic charge transfer reactions typically have much larger rate coefficients than this. Is the N_2^+ -to- N^+ charge transfer reaction truly this inefficient, and if so, why? If the reaction indeed occurs with a larger rate coefficient as expected, why do we apparently not observe significant $\text{NO}^+(\text{v})$ chemiluminescence in COCHISE from the interaction of discharged N_2/Ar with O_2 ?

7.5 COCHISE Observations

As observational points on the possibility of hot-atom effects in COCHISE, we have never observed any excitation resulting from the interaction of discharged Ar with CO and NO counterflows. Thus no hot-Ar processes have been observed in COCHISE. More importantly, we have searched for the $\text{O}_{\text{hot}} + \text{CO}$ excitation process in the interaction of discharged O_2/Ar with CO. The only emission was a relatively weak, rotationally thermal fluorescence from $\text{CO}(\text{v}=1)$, perhaps excited by energy transfer from vibrationally or electronically excited O_2 (or possibly $\text{O}_3(\text{v})$). There was clearly no evidence of rotational excitation, or of vibrational excitation of the higher levels. From previous fast-atom measurements at PSI, we know that the $\text{O}_{\text{hot}} + \text{CO}$ cross section for $\text{CO}(\text{v})$ excitation is large and that the IR spectral distribution is extensive. If hot atoms were present in the interaction volume we should have observed their $\text{T} \rightarrow \text{R}, \text{V}$ transfer effects on the CO emission spectrum. This is a small data set which still needs to be analyzed quantitatively.

As a final point, we consider COCHISE observations of $\text{NO}(\text{v},\text{J})$ emanating from the discharge tubes. This is a weak fluorescence spectrum that appears as an impurity from the N_2/Ar discharges, and must be subtracted from the chemiluminescence spectra observed in the interaction region. The discharge-produced $\text{NO}(\text{v},\text{J})$ apparently forms from reactions involving ppm-level impurities of O_2 in the N_2 and/or Ar gas. Although this intensity is very weak, the typical spectrum qualitatively shows low- v rotational bandhead excitation characteristic of $\text{NO}(\text{v},\text{J})$, with relatively little apparent thermal $\text{NO}(\text{v})$ component. While the reactions of metastable $\text{N}(\text{}^2\text{D})$ and $\text{N}(\text{}^2\text{P})$ with O_2 impurity can be expected to generate excited NO in the discharged gas, the reaction of N_{hot} with O_2 in the active discharge could be equally significant owing to the likelihood of a much larger rate coefficient. The signal levels from the discharge-produced $\text{NO}(\text{v},\text{J})$ could undoubtedly be increased substantially by adding controlled levels of O_2 to the discharge gas mixture. Thus COCHISE experiments to observe $\text{NO}(\text{v},\text{J})$ spectral distributions produced in the discharges for dilute $\text{N}_2/\text{O}_2/\text{Ar}$ mixtures may provide a means to investigate the hot-atom hypothesis.

7.6 Conclusions

In conclusion, translationally excited N-atoms will not impact SWIR and MWIR emissions detectable in COCHISE, unless we find a way to extend the active discharge to the tube exit. The specific points leading to this conclusion are as follows:

- The hot atoms produced by dissociative recombination of N_2^+ with electrons are most likely $N(^2D)$ with sub-eV initial translational energies.
- Some level of translationally hot $N(^4S)$ may be produced by energetic electron impact dissociation of N_2 in the active discharge, however the probabilities depend upon detailed state-to-state N_2 excitation mechanisms and are difficult to estimate. Predissociative mechanisms probably limit the excess atom translational energies to the sub-eV range.
- Collisional moderation of hot atoms and removal of their precursors in the afterglow region greatly depletes the level of hot atoms produced in the discharge.
- The hot atoms reaching the low-pressure mixing region from the discharge and produced in situ by $e^- + N_2^+$ are at number densities that are much too low to account for the observed $NO(v,J)$ emission intensities. Indeed, we predict that these number densities are even too low to produce $NO(v,J)$ levels above the apparatus detection limit.
- The N-atom translational energy required to account for the observed $NO(v,J)$ energy distributions excited by energy transfer is considerably larger than that likely to be available from discharge-produced N_{hot} (for $T \rightarrow R, V$ transfer alone).
- COCHISE observations of the interaction of discharged O_2/Ar with CO showed no observable $CO(v,J)$ excitation, indicating negligible levels of hot O-atoms in the reaction zone.

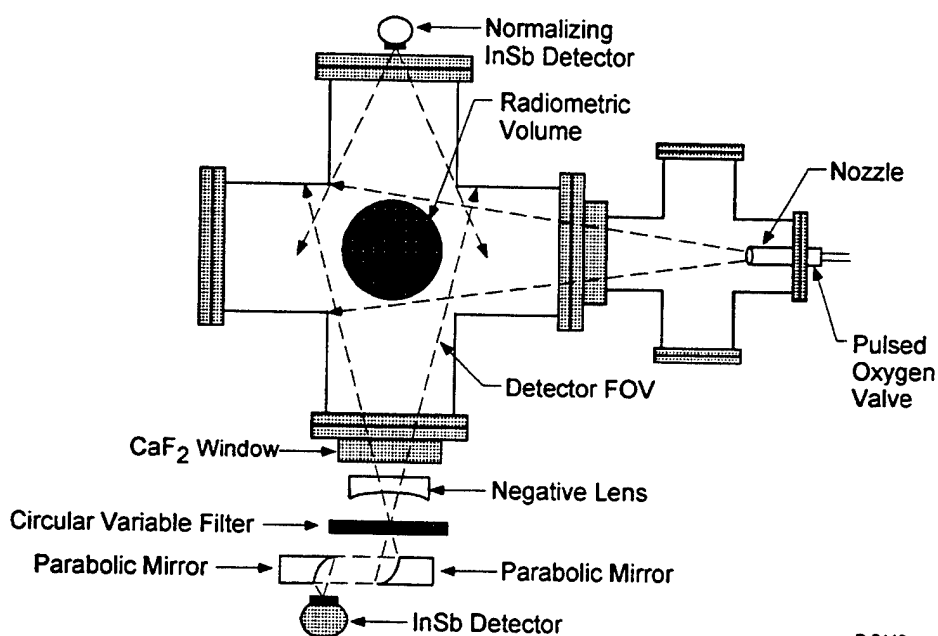
In addition, it is conceivable that N^+ could be produced by the discharges, which should greatly reduce N_{hot} formation and should also give rise to detectable $NO^+(v)$ emission in the reaction with O_2 . However, the apparent absence of such emission in COCHISE experiments suggests that N^+ formation does not occur, and that N_2^+ is indeed the dominant positive ion in the discharge and afterglow.

The foregoing analysis leads to suggestions for possible future experimental measurements in COCHISE. These are as follows:

- Observe $NO(v,J)$ spectral distributions arising in the reaction chamber field of view from discharged dilute $N_2/O_2/Ar$ mixtures using trace amounts of O_2 . This tests the possibility of contributions from the $N_{hot} + O_2$ reaction in the active discharge.
- Devise a method to extend the active discharge region to the end of the discharge tube. This will eliminate the afterglow region and ensure the delivery of significant hot-atom number densities to the low-pressure interaction volume.
- Conduct a comprehensive search for $NO^+(v)$ emission from the interaction of discharged N_2/Ar with O_2 . This will probe for the presence of N^+ in the discharge effluent.

8. FAST ATOM INTERACTIONS WITH HYDROCARBONS

We employed our fast oxygen atom source²⁶ to study the infrared excitation of unsymmetrical dimethyl hydrazine (UDMH) when impacted by 8 km/s oxygen atoms. Our system is a crossed beam experiment shown schematically in Figure 27. The fast oxygen beam enters through an 8 in. diam stainless steel cross and then interacts with a crossed beam of thermal UDMH molecules at the center of a 16 in. cross. Both beams are expanding and thus the interaction area is quite large. The beams are designed to ensure that the densities in the interaction region allow single collision chemistry.



D-2116

Figure 27. Experimental layout for medium resolution spectral measurements with the CVF. UDMH valve is out of plane of figure.

The field of view of the optical system is designed to encompass all of the interaction region. The primary measurement instrument is a circular variable filter (CVF) as shown in Figure 27. A secondary function of the optical design was to minimize the angle of incidence of light entering the CVF so as to preserve the $\approx 2\%$ spectral resolution.

A preliminary IR emission spectrum observed upon the impact of 8 km/s oxygen atoms on UDMH is shown in Figure 28. The primary emission feature seen centered at above $3.3\ \mu\text{m}$ is presumably from the CH stretch mode. Subsidiary peaks are also seen at ~ 4.25 and $4.6\ \mu\text{m}$. The first of these features is suspect in that $4.25\ \mu\text{m}$ corresponds to the last spectral point attainable with a given filter segment and corresponds to a region where the background signal noise is increasing. We believe that this peak is an experimental artifact. The second feature corresponds to measurements performed with a different filter segment. The background is lower here and this peak may truly be an emission feature, perhaps resulting from CO emission. An expanded database will have to be developed in order to address these uncertainties.

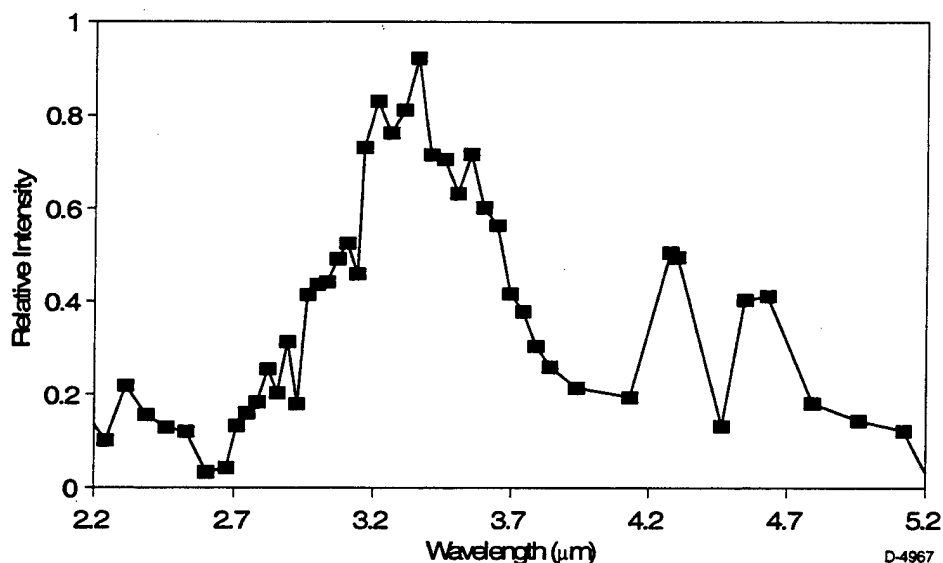


Figure 28. O (8 km/s) + UDMH - preliminary data.

We know of no spaceflight observations of UDMH IR emissions under low earth orbit conditions, i.e., where the dominant collision partner is fast oxygen atoms. There was an observation of methyl amine emissions produced by 8 km/s oxygen atoms on a Delta 181 Flight.²⁷ The observed emission spectrum of this simpler molecule as excerpted from Reference 27 is shown in Figure 29. Note the good comparison between this data and our results for UDMH in the CH stretch region. There are no apparent MWIR emissions in the methyl amine data, however.

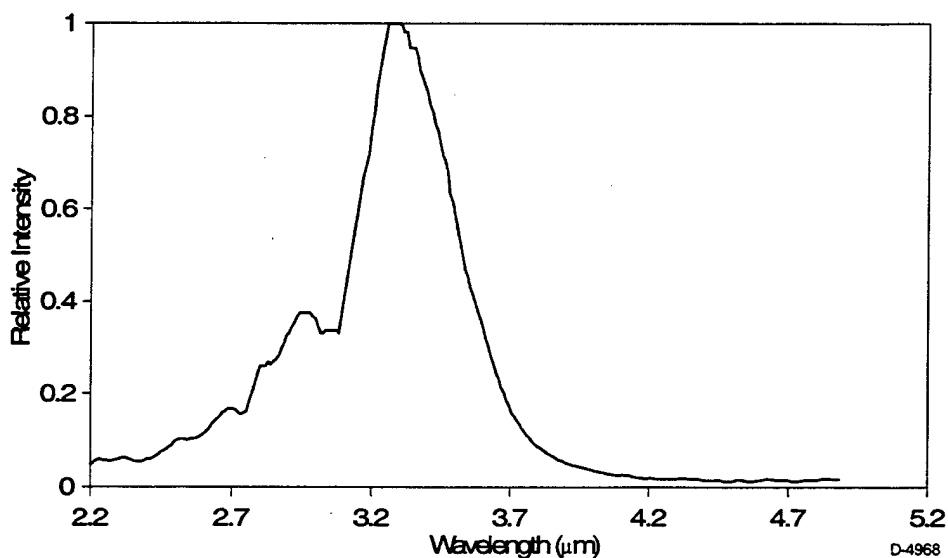


Figure 29. Emission observed on Delta 181 during methylamine release.

We performed a more comprehensive set of experiments on UDMH, developed an absolute calibration for the system, and then continued the investigations over a class of fuel/oxidizer species. These results were summarized in a journal article submitted for approval for publication in the Journal of spacecraft and Rockets. This manuscript is included in this report as Appendix 6.

9. ONE KILOMETER PER SECOND ATOMIC OXYGEN SOURCE

We have begun evaluating our atmospheric microwave system as a potential source for ~ 1 km/s oxygen atoms. This AO source has a nominal 150 W - 7.5 GHz magnetron. The 7.5 GHz magnetron has a limited power band of about 130 to 170 W. It was chosen because it operates at lower power and hence with a lower gas load for the vacuum chamber. We are hoping to be able to operate at 200 W/liter. Based on earlier experiences with a kilowatt source, if we can operate at 200 W/liter, then at 130 W power the gas flowrate could be as low as 0.65 SLPM. If we can only operate at nominal operating conditions of 150 W/liter then the gas flowrate would be 1.00 SLPM at the nominal 150 W power rating. The extreme operating condition could be 75 W/liter at 170 W for a gas flow rate of 2.27 SLPM.

Our objective is to use the AO source under free molecular flow conditions in FAST-2. FAST-2 currently has a 4000 LPS cryopump attached to the 150 liter main chamber, and therefore we need to restrict cw gas flowrates to < 30 SCCM to maintain chamber pressures $< 10^{-4}$ Torr. This vacuum level cannot be obtained by simply bolting the source directly to the chamber because the 650 SCCM minimum gas flowrate would result in a chamber pressure $> 2 \times 10^{-3}$ Torr or equivalently a mean free path of about 2.5 cm.

To permit the maintenance of pressures $< 10^{-4}$ Torr, or mean free path > 50 cm, we must differentially pump an intermediate beam skimming chamber. For this we have constructed a $2.5 \times 5 \times 30$ cm chamber to be pumped with an ~ 80 lps roots blower stack. This should reduce the pressure in the intermediate chamber to approximately $100 \mu\text{m}$, and with a Beam Dynamics skimmer installed opposite to the source exit nozzle, we should be able to skim off $> 97\%$ of the nozzle flow. The reduced load to the main chamber cryopump will permit vacuum in the low 10^{-5} Torr range.

10. ADAPTIVE INFRARED IMAGING SPECTRORADIOMETER

10.1 Overview

In this section, we describe our development of algorithms and applications which employ the Advantive InfraRed Imaging Spectroradiometer (*AIRIS*) hyperspectral imager. PSI and PL personnel working jointly acquired data using AIRIS and then developed analysis approaches to utilize the data sets. We reviewed the acquisition and preliminary analysis of data acquired from the penthouse of Building 1105 at HAFB overlooking a field, surrounded by a perimeter road, with a coniferous treeline beyond the road. We first reviewed some basic conclusions about the utility of hyperspectral imagery from the literature before discussing the data acquisition and analysis.

10.2 Hyperspectral Imaging Band Selection and Analysis

In tactical multispectral imaging the goal is to exploit unique thermal signatures (vehicle exhaust) or differences in emissivity as a function of wavelength for the target relative to the background scene. Several measurement programs and data analysis efforts have been conducted to define and exploit these signatures,²⁸⁻³¹ most notably under the Joint Multispectral Sensor Program conducted by the Environmental Research Institute of Michigan (ERIM). The metric of detection for this problem is the signal-to-clutter ratio (SCR). The SCR quantifies the separation, in N-dimensional space, of a target mean from a background mean relative to the variability in the background distribution. Schwartz and coworkers²⁸ have shown that good detection performance (low PF_a) is achieved for an SCR value greater than 8. They examined the behavior of the wavelength-optimized SCR, as a function of the number of bands sampled, in a series of measurements spanning the MWIR to LWIR spectral regions for ground targets in vegetated and desert backgrounds. Similar measurements were conducted by Eismann and coworkers²⁹ for military targets in a winter environment. In both studies various camouflage types were employed. Optimum wavelengths were also identified in these studies. Finally, Billingsley and coworkers³⁰ used a Chicken Little measurement program data set to quantify SCRs as a function of number of bands for a data set which included 15 VIS/SWIR bands and 6 MWIR/LWIR bands. They performed this quantification within the context of a Spectral Matched Filter (SMF) algorithm which used linear combinations of target and background spectral vectors to describe the scene. The reader is referred to the specific references for the mathematical details of the approaches.

Several distinct conclusions can be derived from analysis of the various papers. Both Eismann et al.²⁹ and Billingsley et al.³⁰ show that single band night detection is best done in the MWIR (4.15 or 4.96 μm in the specific studies). Furthermore, Billingsley et al.³⁰ and Preston and coworkers³¹ have successfully demonstrated variants of the SMF approach for multispectral target detection. An analysis of the reported data, shown in Figure 30, reveals that the improvement in SCR with number of bands is most dramatic for the use of two bands (65%), marginal for the inclusion of a third band (20%), and almost negligible in going from 3 to 4 bands (10%). Finally, Schwartz et al.²⁹ showed that the percentage of observances with an $SCR > 8$ improves from 17% to 79% in going from single to dual band detection, increases to

94% for the addition of a third band, and rises to 97% for the addition of a fourth band. These data are also shown in Figure 30. Thus, algorithms which use only two or three bands are most efficient in the discrimination of specific targets.

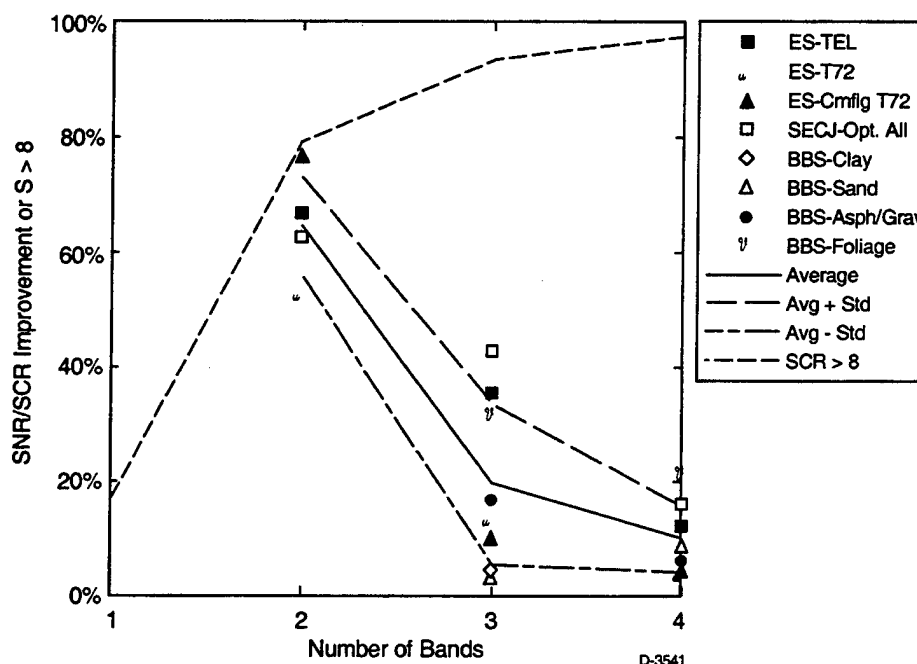


Figure 30. Summary results of target discrimination studies (Refs. 29-31) showing percent SCR improvement (symbols) as a function of band and averaged results. The percent of observations with SCR > 8 as a function of band is also shown.

The work of Billingsley et al.³⁰ also provides insight into the wavelength bands within his data set having the greatest utility for a broad range of targets and illumination types (day vs night - solar/observer geometry). These results are summarized in Table 7.

The results presented by the groups at ERIM^{28,29} suggest that a limited number of bands (2 to 3) are sufficient to provide high quality object identification and classification. The results of Billingsley et al.³⁰ show that linear combinations of target and background vectors can be combined to classify objects in a scene. Both approaches are valid, with the 2 or 3 band problem often solved by simple correlation approaches while the multiband problem is best addressed by the vector approach.

Table 7. Summary of Optimized Band Sets (Ref. 31) and Comparison to Proposed System wavelength Ranges. Superscripted bands in the table are equally effective and may be used alternately.

Spectral Region	Optimized Spectral Bands (μm)	
Scenario	Daytime - All Backgrounds	Night - All Backgrounds
VIS/NIR/SWIR	0.620	
	0.715	
	0.865	
	1.255	
	1.585	
	2.140	
MWIR	4.960 ²⁸	4.960
LWIR	11.450 ²⁸	8.945 ²⁹
		11.450 ²⁹

10.3 Data Collection and Analysis

10.3.1 Data Collection

To explore different analysis approaches we acquired data at Hanscom AFB for a number of different scenes. Initial experiments concentrated on backgrounds and employed an older version of the *AIRIS* imager which used a slower, CE-IRC160 focal plane array. A two-temperature absolute radiometric calibration approach was employed. The calibration was acquired using a portable, two temperature blackbody consisting of 2 in. square blackened aluminum plates heated using thermoelectric devices powered by 2 D-cell batteries. A pair of type-K thermocouples are used to determine the temperatures of the plates. These experiments were conducted viewing scenes from the fourth floor penthouse area of Bldg 1105B at the Geophysics Directorate of Phillips Laboratory. In one series of experiments a human holding a propane torch was located at a tree line approximately 300 ft distant from the imaging system. The torch flame subtends only approximately one pixel, simulating a cruise missile at long range. This experiment allows us to explore sub-pixel target ID using multispectral imagery. A visible image of the scene (without the torch) is shown in Figure 31. An IR image of the same scene (with torch) recorded at 4.56 μm is shown in Figure 32.

The residual ring in the IR image is due to imperfect gain and offset correction, which is highlighted in the transformation of the imagery to a printed form. The presence of the residual ring structure in the data was the primary reason why we expended significant effort in cooling the FPA lens assembly. Because of the impact of lens thermal emission on the observed background, small drifts in the lens temperature can have a significant impact on the apparent offset coefficient in the radiance calibration. The ring structure in the image is a result of these drifts.



E-7093

Figure 31. Visible image of scene used for sub-pixel target identification using two-band correlation approach.



E-7094

Figure 32. IR image of above scene recorded at 4.56 μm using early prototype AIRIS system. The scene contains a human positioned next to a propane torch.

10.3.2 Data Analysis

The basic spectra of different objects within the scene has been determined from the imagery. These spectra are similar to the target and background vectors described by Billingsley et al.³⁰ These spectra are shown in Figure 33 for the torch, the tree background, and the roadway. The spectra of the trees and roadway are typical of blackbodies modified by atmospheric transport. The road is hotter than the trees because it has been sunlit for several hours and because the treed region is in shade. The spectrum of the torch is characteristic of the hot CO₂ emission expected from a clean flame (no broadband soot emission). However, the intensity is indicative of a much lower temperature than normally associated with the torch. The reduced intensity is most likely a result of the sub-pixel flame dimension. Note in the spectra that, at longer wavelengths, the intensity of the flame location approaches that of the treed background.

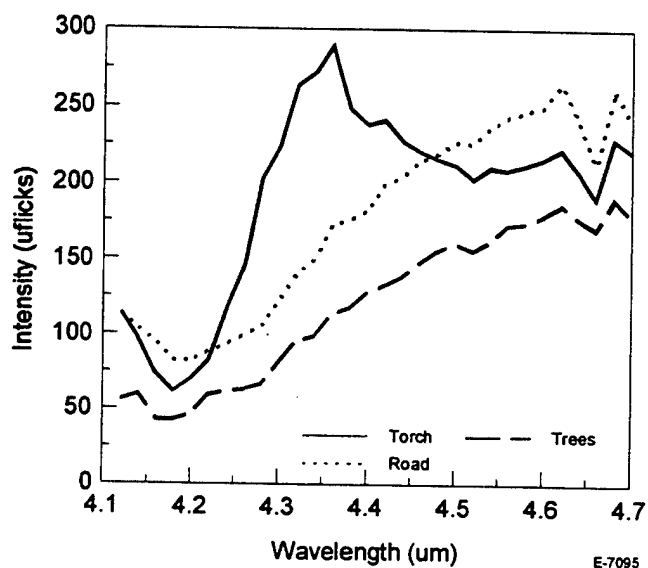


Figure 33. Spectra of the torch, treed background, and road recorded for the AIRIS imager.

The primary issue in automated target detection is the selection of proper bands and the processing of the spectral information in the imagery to isolate the target in the clutter. To exploit the target/background differences we chose the wavelengths 4.36 μm and 4.56 μm to highlight the differences between the target and background. To identify the region in the image set containing the torch we used a common correlation approach.²⁸ The approach is illustrated in Figure 34 where the intensity of a pixel at 4.36 μm is plotted as a function of the intensity of the pixel at 4.56 μm . This approach will highlight regions with an emissivity which is a strong function of wavelength regardless of small differences in temperature.

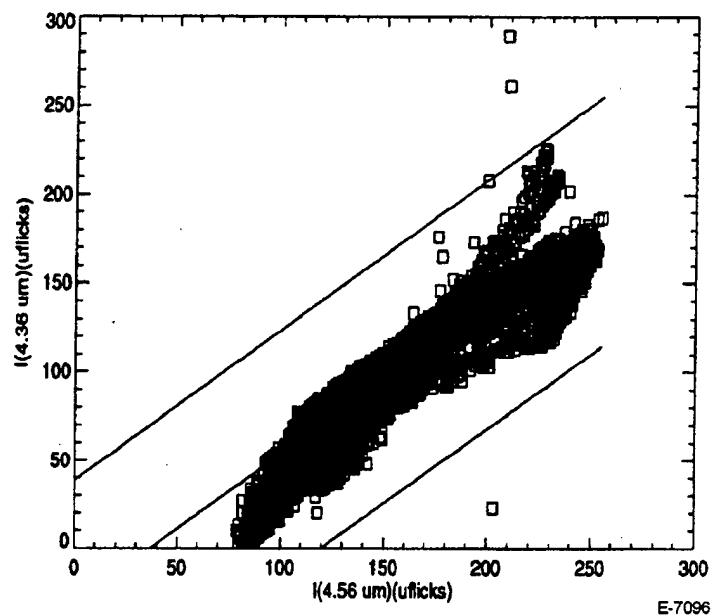


Figure 34. Correlation plot of IR imagery showing data (\square), fit to data, and $\pm 5\sigma$ bounds on fit.

The correlation plot shows that most data points lie roughly on a line. The intensity ratio is characteristic of the background. The line through the data is a linear least-squares fit to the intensity variations. The parallel lines on either side of the fit represent $\pm 5\sigma$ bounds in the uncertainty of the fit. Only a few points lie outside this region. When these points are plotted against a black field in Figure 35, the known single pixel location of the flame is highlighted. In the processing language used for this algorithm, only five lines of code are required to execute the identification scheme. A fuller description of the concept, instrument, and demonstration of its performance is given in Appendix 7.



E-7097

Figure 35. High contrast image from correlation analysis of IR imagery identifying the location of a sub-pixel flame in the scene.

11. COCHISE REFURBISHMENT

The primary activity during this period was the refurbishment of the COCHISE Facility at Phillips Laboratory/Geophysics Directorate. An outline summary of the activities provided by PSI is provided below.

1. Design of gas flow manifold

Manifold is in two parts, the first being the gas handling feature including the valves and flowmeters and the second being the control panel with the switches and the LED (indicating function lamps).

- Did the design work for the manifold panel
- Produced panel layout for the machine shop to fabricate
- Made artwork for panel markings
- Assisted with the assembly and installation
- Performed vacuum leak testing for integrity and functionality.

2. Control panel with switch and indicating lamps

- Designed for fabrication
- Did artwork for panel markings
- Ordered and installed parts
- Did the control wiring at panel and tested with simulated loads
- Instructed on the interconnected wiring between panel and valves

3. Gas-handling distribution lines into the reaction cell

- Designed feed lines with the appropriate interconnection flanges and orientation for gas distribution

4. Design and fabrication of vacuum pumping station for the sole purpose of evacuation of the gas-handling system

- After fabrication, designed a testing section for vacuum leak testing of the installation

5. Refrigeration system for chamber to achieve operation test temperature. Included are the refrigerator and three massive compressor units.

- After installing the main control box and mounting of the switch contractors to service the compressors, created control wiring from the refrigerator to the compressors.

6. Added flow and temperature interlocks for the diffusion pump water system.

7. Interconnecting chamber section valves
 - Chamber valves used for isolation of the reaction cell side from the monochromator detection section which were troublesome and inaccessible for service.
 - Designed for fabrication a mounting bracket system to be installed at the front of chamber, allowing easy access for service.
8. Assisted on design of the vacuum feedthrough control systems for the monochromator.
9. Performed combined effort in installing a raised floor, both around the refrigerator in the pump room and at the rear of the test chamber in the main lab.

12. REFERENCES

1. Taylor, R.L., Lewis, P.F., and Caledonia, G.E., PSI Technical Report #51, 1976.
2. Taylor, R.L. and Bitterman, S., *Rev. Mod. Phys.* **41**, 21, 1969.
3. Piper, L.G., Caledonia, G.E., and Kennealy, J.P., "Rate Constants for Deactivation of $N_2(A) v'=0,1$ by O_2 ," *J. Chem. Phys.* **74**, 2888 (1981).
4. Piper, L.G., Cowles, L.M., Rawlins, W.T., "State-to-State Excitation of $NO(A^2\Sigma^+, v'=0,1,2)$ by $N_2(A^3\Sigma_u^+, v'=0,1,2)$," *J. Chem. Phys.* **85**, 3369 (1986).
5. Piper, L.G. and Rawlins, W.T., "O-Atom Yields from Microwave Discharges in N_2O/Ar Mixtures," *J. Phys. Chem.* **90**, 320 (1986).
6. Piper, L.G., Donohue, M.E., and Rawlins, W.T., "Rate Coefficients for $N(^2D)$ Reactions," *J. Phys. Chem.* **91**, 3883 (1987).
7. Piper, L.G., "State-to-State $N_2(A^3\Sigma_u^+)$ Energy-Pooling Reactions. I. The Formation of $N_2(C^3_u)$ and the Herman Infrared System," *J. Chem. Phys.* **88**, 231 (1988).
8. Piper, L.G., "The Excitation of $N_2(B^3\Pi_g, v'=1-12)$ in the Reaction between $N_2(A^3\Sigma_u^+)$ and $N_2(X, v \geq 5)$," *J. Chem. Phys.* **91**, 864 (1989).
9. Piper, L.G., "The Excitation of $N(^2P)$ by $N_2(A^3\Sigma_u^+)$," *J. Chem. Phys.* **90**, 7087 (1989).
10. Piper, L.G., "Quenching Rate Coefficients for $N_2(a^1\Sigma_u^-)$," *J. Chem. Phys.* **87**, 1625 (1987).
11. Clyne M.A.A. and Piper, L.G., "Kinetic Spectroscopy in the Far Vacuum Ultraviolet, Part 3. Oscillator Strengths for the 3s, 4s, and 5s $^3S - 2p^4\ ^3P_2$ Transitions in Atomic Oxygen," *JCS Faraday 2* **72**, 2178 (1976).
12. Rawlins, W.T. and Piper, L.G., "Effect of Excitation Mechanism on Line-width Parameters of Conventional VUV Discharge Line Sources," *Proc. Soc. Photo.-Opt. Instrum. Eng.* **279**, 58 (1981).
13. Mitchell, M. and Zemansky, M.W., *Resonance Radiation and Excited Atoms*, New York: Academic Press (1934).
14. Piper, L.G., "Re-evaluation of the Transition-Moment Function and Einstein Coefficients for the $N_2(A^3\Sigma_u^+ - X^1\Sigma_g^+)$ Transition," *J. Chem. Phys.* **99**, 3174 (1993).
15. Piper, L.G., Tucker, T.R., and Cummings, W.P., "Electronic Transition Moment Variation and Einstein Coefficients for the $NO(B^2\Pi - X^2\Pi)$ System," *J. Chem. Phys.* **94**, 7667 (1991).

16. Langhoff, S.R., Bauschlicher, C.W., and Partridge, H., *Chem. Phys. Lett.*, **223**, 416, 1994.
17. de Vivie, R. and Peyerimhoff, S.D., "Theoretical Spectroscopy of the NO Radical: I. Potential Curves and Lifetimes of Excited States," *J. Chem. Phys.*, **89**, 3027, 1988.
18. Duff, J., Spectral Sciences Inc., private communication. Results presented in Caledonia, G.E., Krech, R.H., Oakes, D.B., Lipson, S.J., and Blumberg, W.A.M., "Products of the Reaction of 8 km/s N(4S) and O₂," *J. Geophys. Res.* **105**(A6), 12833 (2000).
19. Oakes, D.B., Krech, R.H., and Caledonia, G.E., "IR Excitation by Hyperthermal Atom Collisions", presented at the 1994 AFOSR Molecular Dynamics and Inorganic Materials Chemistry Contractors' Conference, October 23 - 26, 1994.
20. Kieffer, L.J. and Dunn, Gordon H., "Electron Impact Cross-Section Data for Atoms, Atomic Ions and Diatomic Molecules: I. Experimental Data," *Rev. Mod. Phys.* **38** (1), 1 (1966).
21. Rawlins, W.T., Fraser, M.E., and Miller, S.M., "Rovibrational Excitation of Nitric Oxide in the Reaction of O₂ with Metastable Atomic Nitrogen," *J. Phys. Chem.* **93**, 1097 (1989).
22. Rawlins, W.T., Fraser, M.E., Miller, S.M., and Blumberg, W.A.M., "Sources of Rovibrationally Excited Nitric Oxide in the Aurorally Excited Upper Atmosphere," *Proc. AGU 1990 Fall Meeting*, *Eos* **71**, 1491 (1990).
23. Queffelec, J.L., Rowe, B.R., Morlais, M., Gomet, J.C., and Vallee, F., "The Dissociative Recombination of N₂⁺ (v=0,1) as a Source of Metastable Atoms in Planetary Atmospheres," *Planet. Space Sci.* **33**, 263 (1985).
24. Kaufman, F., "The Production of Atoms and Radicals in Simple Glow Discharges," *Adv. Chem. Ser.* **80**, 29 (1969).
25. Langford, A.O., V.M. Bierbaum, and S.R. Leone, "Branching Ratios for Electronically Excited Oxygen Atoms Formed in the Reactions of N⁺ with O₂ at 300 K," *J. Chem. Phys.* **84**, 2158 (1986); M.A. Smith, V.M. Bierbaum, and S.R. Leone, "Infrared Chemiluminescence from Vibrationally Excited NO⁺ Product Branching in the N⁺ + O₂ Ion-Molecule Reaction," *Chem. Phys. Lett.* **94**, 398 (1983).
26. Caledonia, G.E., R.H. Krech and D.B. Oakes, "Laboratory Simulation of Low Earth Orbit," *J. Inst. Environ. Sci.* **39**, 2, 23 (1996).
27. Green, B.D., Holtzclaw, K.W., Joshi, P.B., and Burke, H.K., "Analysis of Radiances from Orbital Gas Releases," *J. of Geophys. Res., Space Physics* **97**(A8), 12, 161 (1992).
28. Schwartz, C.R., Eismann, M.T., Cederquist, J.N., and Johnson, R.O., "Thermal Multispectral Detection of Military Vehicles in Vegetated and Desert Backgrounds," *Proc. IRIS Targets, Backgrounds, and Discrimination*, 1996, Vol. II.

29. Eismann, M.T., Schwartz, C.R., and Shaffer, W.A., "Target Detection in a Winter Environment: Infrared Hyperspectral Measurements and Analysis," *Proc. IRIS Targets, Backgrounds, and Discrimination*, 1996, Vol. II.
30. Billingsley, F.P., Benz, K.D., Sommes, A., Waters, C.R., and Wilson, W.H., "Optimal Spectral Bands for CC&D Target Detection Via Spectral Matched Filter Analysis," *Proc. IRIS Targets, Backgrounds, and Discrimination*, 1996, Vol. II.
31. Preston, R., Norton, M., and Crow, R.W., Real-Time Target Discrimination Using the Mid-Wave Infrared Spectral Imager (MIRSI)," *Proc. IRIS Targets, Backgrounds, and Discrimination*, 1996, Vol. II.

APPENDIX 1

Energy Transfer Excitation of Carbon Dioxide by Electron Irradiated Nitrogen

1994 Fall Meeting of the AGU

(reproduced in its entirety



PHYSICAL SCIENCES INC.

VG94-230

ENERGY TRANSFER EXCITATION OF CARBON DIOXIDE BY ELECTRON IRRADIATED NITROGEN

**Poster SA32A-5
1994 Fall Meeting of the AGU**

**K.W. Holtzclaw, B.L. Upschulte, and B.D. Green
Physical Sciences Inc.
20 New England Business Center
Andover, MA 01810**

**S.J. Lipson and W.A.M. Blumberg
Phillips Laboratory/Geophysics Directorate
Hanscom AFB, MA 01731**

Physical Sciences Inc.

20 New England Business Center

Andover, MA 01810

ENERGY TRANSFER AND THE THERMOSPHERIC ENERGY BUDGET

Long-lived metastable species can store significant energy and thus are an important factor in the energy budget of the thermosphere. Metastable species are made in the dayglow and in auroral events during thermalization of the electron disturbed upper atmosphere. These species can be deactivated via slow radiative decay or via energy transferring collisions with other species. We are currently studying one such transfer in the LABCED facility at the Phillips Laboratory. In this on-going work we are using a pulsed electron beam to create a volume of metastable N_2 and then, after suitable delays, CO_2 is introduced via a pulsed solenoid valve. We have recorded the infrared spectra resulting from metastable energy transfer and we have examined the metastable nitrogen decay using the CO_2 as a probe of metastable concentration. These experiments offer insight into the energy transfer process and a means of probing the loss mechanisms for metastable nitrogen.

EXPERIMENTAL PROCEDURE

T-22516

- 4 keV, 20 mA, pulsed electron beam excites molecular nitrogen

- 0.5 to 1.0 s beam durations
- 10 to 15 mt nitrogen pressures at 300 K

- Inject CO₂ with a pulsed solenoid valve (General Valve Series 9)

- 20 ms pulse duration
- inject during irradiation and delayed by ≤ 700 ms
Long delays allow quenching of all nitrogen excited states except N₂ (A⁺Σ) and N₂ (X⁺Σ, v)

EXPERIMENTAL PROCEDURE (Cont.)

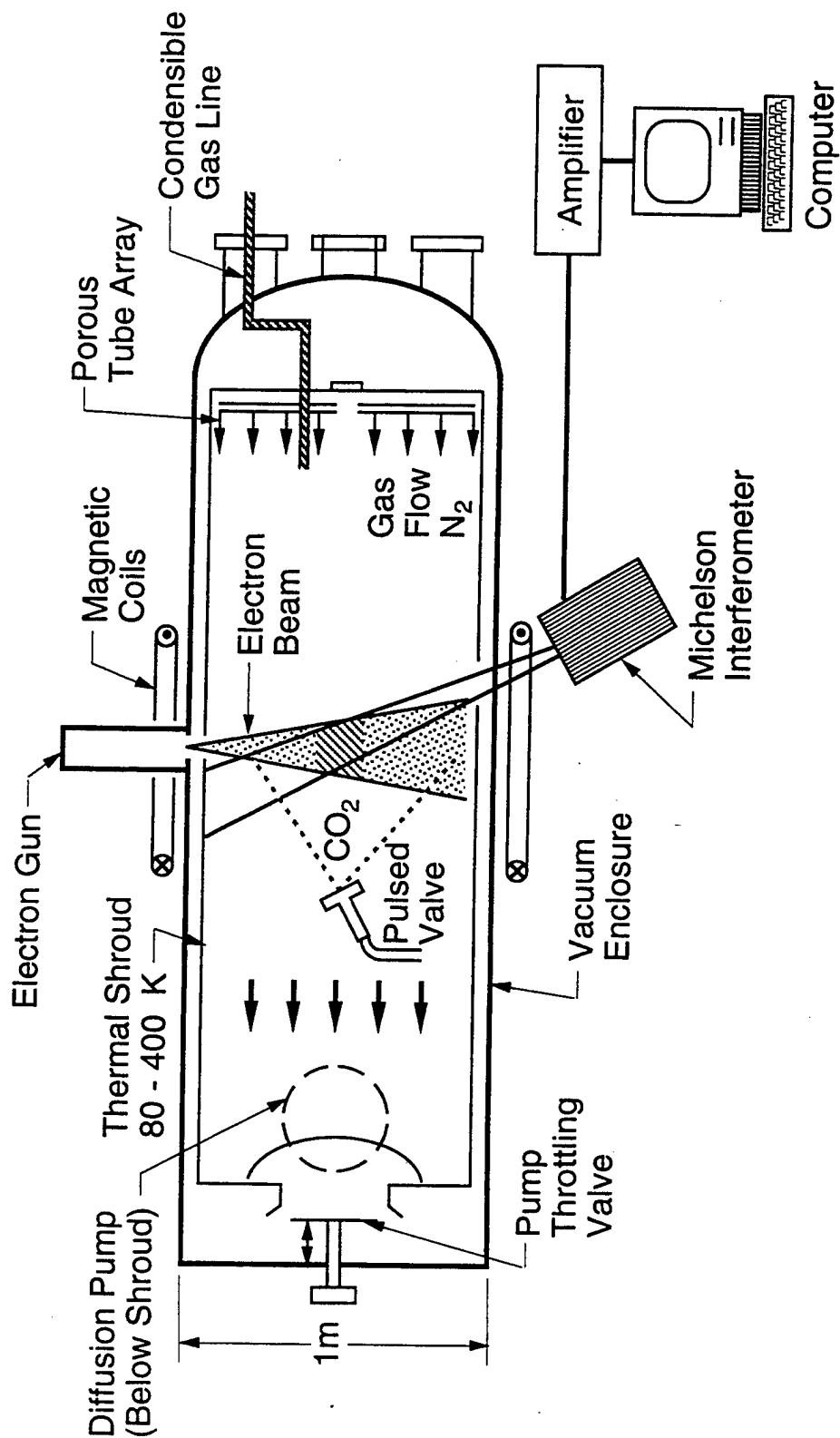
T-22516a

Slow scan Michelson interferometer records IR fluorescence

- fluorescence temporally resolved, spectra recorded before, during, and after CO₂ injection using computer based data-acquisition system (Concurrent Corp.)
- Interferometer detector and optics used as radiometer to record broadband, temporally resolved fluorescence

LABCEDE FACILITY

T-22517

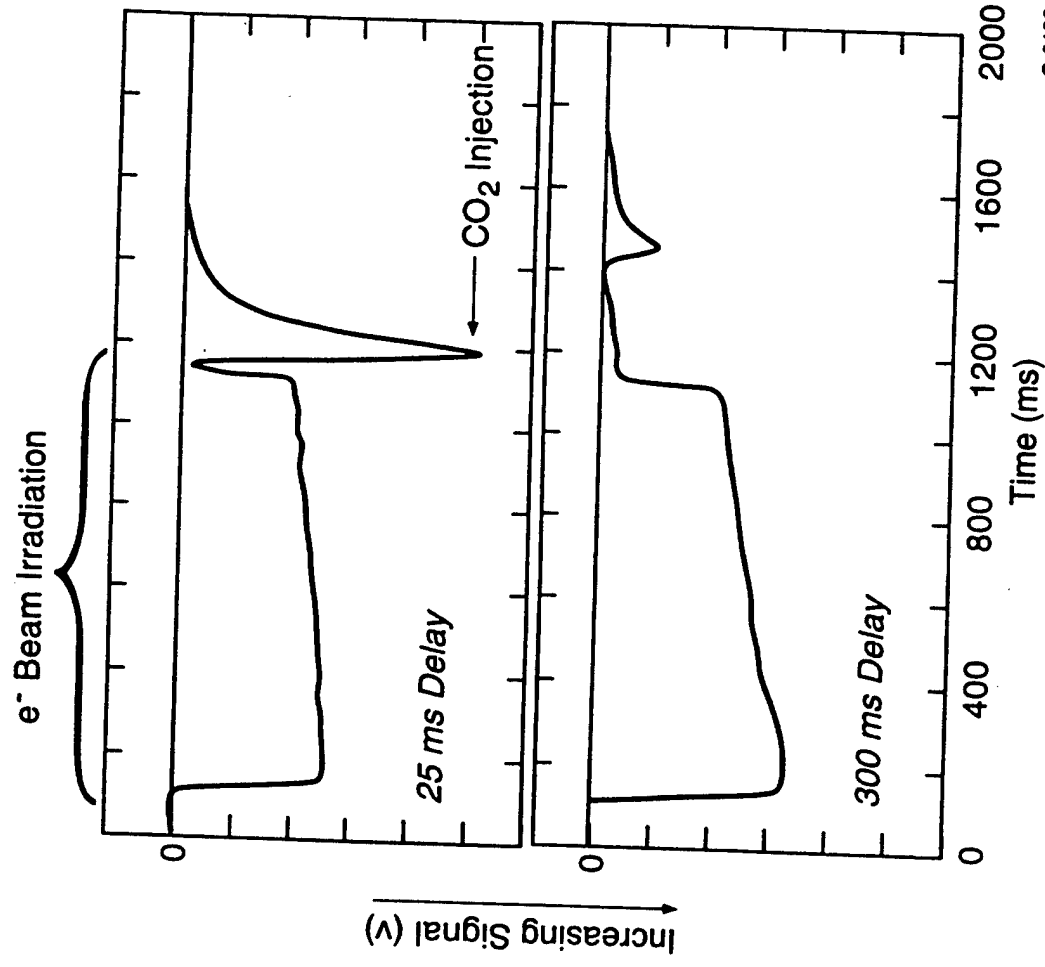


B-6263b

EXPERIMENTAL DATA: TEMPORALLY RESOLVED INFRARED FLUORESCENCE

- Easily discriminate
 - $e + \text{CO}_2 \rightarrow \text{CO}_2^* h\nu$ from
 - $e + \text{N}_2 \rightarrow \text{N}_2 + \text{CO} \rightarrow \text{CO}_2^* h\nu$
- signal during e^- irradiation arises largely from e^- impact on residual CO_2 remaining from earlier events

- Injection of CO_2 after similar irradiation of argon yielded no fluorescence
 - transfer appears to be nitrogen specific



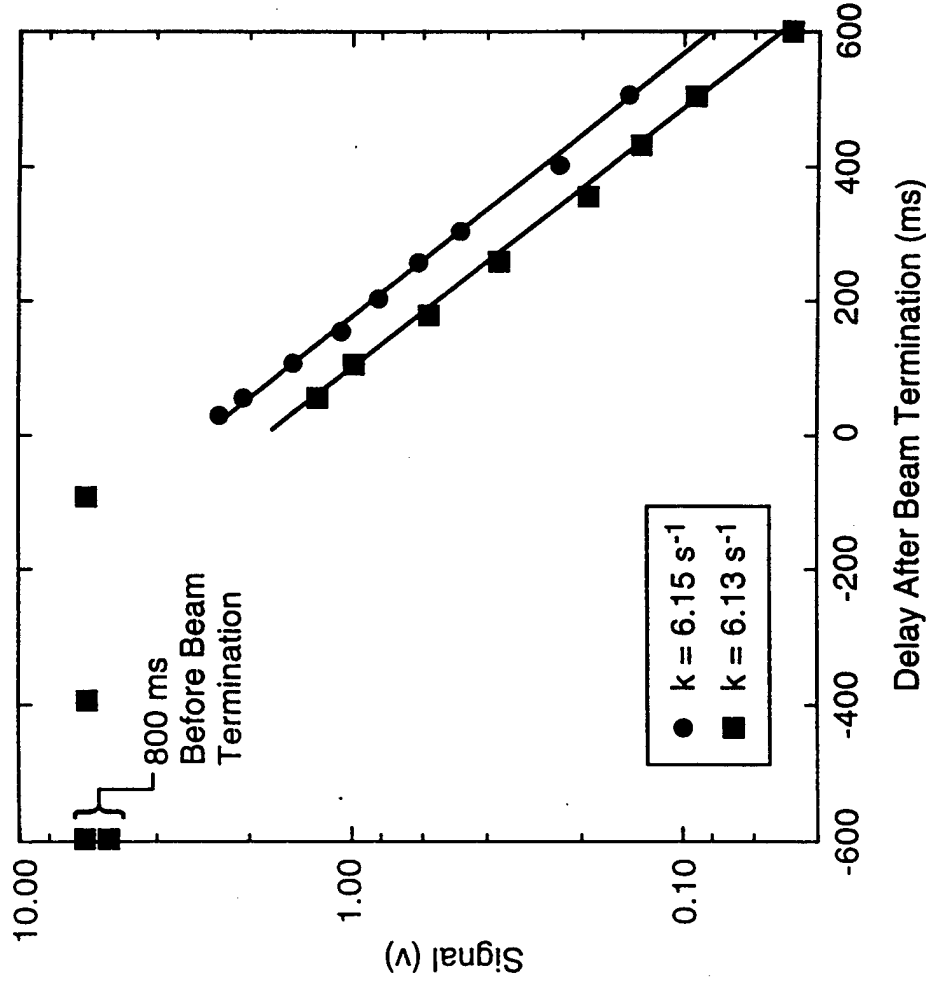
T-22518

C-8182

CO₂ FLUORESCENCE USED AS TRACER OF METASTABLE NITROGEN

69 T-22519 C-8183

- Single exponential decay of metastable nitrogen observed via CO₂ fluorescence
 - P_{N_2} 9 mT, 300 K
- First order metastable decay rates of 6 s⁻¹ indicated
 - rate represents upper bound on loss rate for metastable nitrogen
 - apparent first order decay suggests minor losses due to wall collisions



LOSS RATE IS TOTAL DEACTIVATION RATE FOR NITROGEN METASTABLE

T-22520

- Exponential decay suggests that loss rate is the sum of all loss rates first order in N_2^*
 - losses involving diffusion, e.g., wall deactivation, probably minor (diffusional loss has $1/t$ dependence)
- Contributing reactions include:
 - $N_2^* + N_2(X) \rightarrow 2 N_2(X)$ self-quenching
 - $N_2^* + CO_2 \rightarrow N_2 + CO_2 (CO_2^*)$
 - in this experiment, CO_2 arises from steady state $[CO_2]$ produced by pulsed injection
- CO_2 fluorescence is a probe of "instantaneous" N_2^* concentration
 - N_2^* loss rate due to collisions with CO_2 can be measured in experiments in which steady state $[CO_2]$ is varied

TRANSFER PARTNER IDENTITY

T-22521

- Have observed CO_2 fluorescence as late as 700 ms after e^- irradiation terminated
 - only the lowest triplet excited state of nitrogen ($\text{N}_2\text{A}^3\Sigma_u^+$) and vibrationally excited ground electronic state nitrogen $\text{N}_2(\text{X}\Sigma_g^+, v)$ have sufficiently long lifetimes to account for this excitation
- $\text{N}_2(\text{X}, v)$ is likely responsible for the transfer
 - close resonance in $\text{N}_2(\text{X})$ and $\text{CO}_2(v_3)$ vibrational frequencies enhances cross section for energy transfer, $\text{N}_2(\text{X}, v=1)$, $v = 2330 \text{ cm}^{-1}$, $\text{CO}_2 v_3 (v=1) = 2349 \text{ cm}^{-1}$

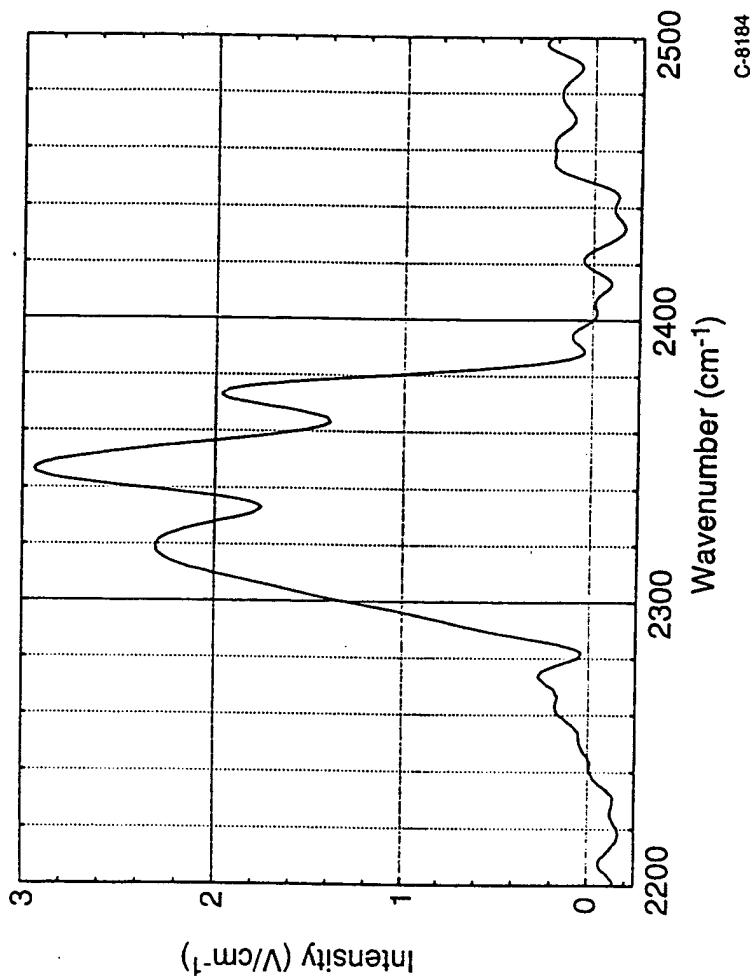
TRANSFER PARTNER IDENTITY (Cont.)

T-22521a

- Addition of an efficient triplet state quenching species, e.g., O_2 , will allow differentiation of the excitation mechanism
 - O_2 only inefficiently relaxes $N_2(X,v)$
 - experiment in progress

CO₂ EMISSION ARISING FROM NITROGEN METASTABLE ENERGY TRANSFER

T-22522



- 70 μ s after pulsed valve opened, 120 μ s after e⁻ irradiation terminated
- Similar spectra recorded throughout and following CO₂ injection indicate similar vibrational distributions at all times

CO₂ FLUORESCENCE SPECTRA

T-22523

- Sufficient CO₂ added to make the line of sight optically thick to 001 emission and, to a lesser extent, 011 emission

72

- modeling of radiative transport processes required to accurately simulate spectra
- the issue is complicated by an uneven distribution of CO₂ emitters and absorbers along interferometer line of sight, radiative transport strongly influenced by these distributions

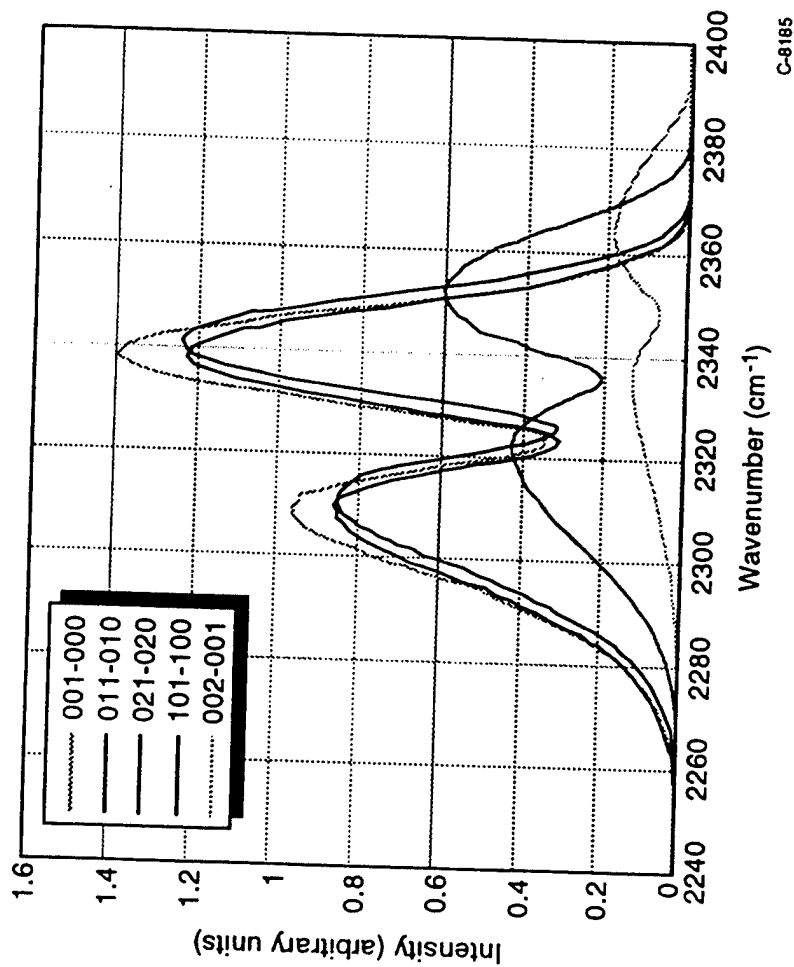
CO₂ FLUORESCENCE SPECTRA (Cont.)

T-22523a

- Code developed to model CO₂ infrared emission involving ν_3 in an approximately fashion using the spectral constants of Rothman (Appl. Opt., 25, 1795 (1986))
 - approximate the effects of self-absorption by summing the calculated emission spectra from 10 regions along path
 - calculate line-by-line absorption for CO₂ between each segment and the interferometer prior to summing to create the composite spectrum
 - several spatial distributions of CO₂ have been used in calculating spectra. The 001 spectrum is found to be strongly dependent both on the spatial distribution and the assumed CO₂ number density

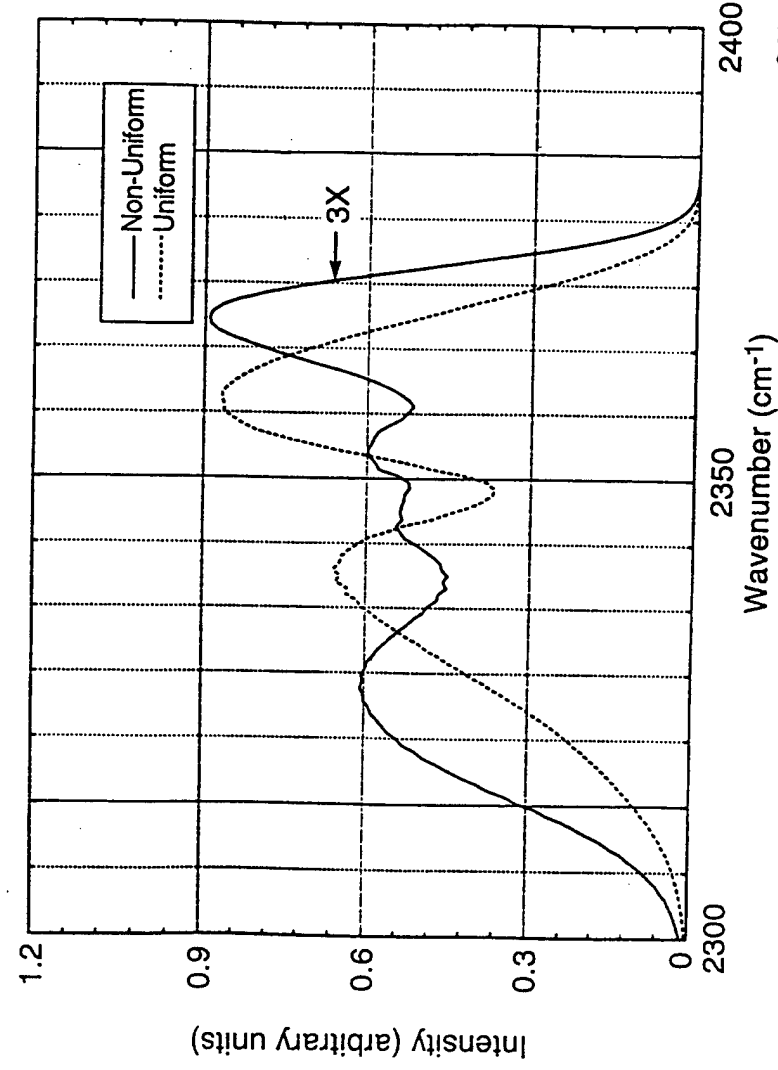
CALCULATED CO₂ SPECTRA FOR THE 001, 011, 021, 101, AND 002 LEVELS

T-22524



- Emitters and absorbers both uniformly distributed in viewing volume

COMPARISON OF CALCULATED SPECTRA FOR 001-000 TRANSITION



- The spectrum (—) was calculated with non-uniform and differing distributions of emitters and absorbers
 - have not yet arrived at satisfactory emitter/absorber spatial distributions

CO₂ VIBRATIONAL STATE CONTENT

T-22526

- The prominent feature at 2345 cm^{-1} indicates the presence of emitting levels other than 001
- Examination of calculated spectra from many vibrational states indicates that emission from 002, 021, and 101 could contribute to this feature
 - because these states lie at energies of 1300 to 2300 cm^{-1} , then are not thermally populated and there is little self-absorption
 - the populations of these excited levels can only be a small fraction of that for 001 ($\approx 20\%$). The 2345 cm^{-1} feature is still prominent due to the lack of self-absorption
- Unique vibrational distribution has not been determined from spectral fit due to optical thickness effects

SUMMARY

T-22527

- Collisional energy transfer between metastable molecular nitrogen and CO_2 has been observed in the laboratory via direct observation of infrared fluorescence from Δv_3 transitions of CO_2
 - first order decay rate of 6 s^{-1} was observed
 - sum of all decays first order in N_2^*
- Collisional excitation of CO_2 into levels containing quanta in addition to a single quantum of v_3 (001) is suggested in spectra recorded interferometrically
- Determination of the vibrational state distribution is difficult due to the excitation volume being optically thick to 001-000 radiation

FUTURE WORK

T-22528

- Perform experiment in presence of O_2 , verify $N_2(X,v)$ as transferring species
- Modify experimental procedures and conditions to allow the use of less CO_2 : reduce the optical thickness problem
 - analyze resulting spectra, determine CO_2 vibrational state distributions
- Alternative experiment: reduce contribution of optically thick 001 spectrum using gas cell of CO_2 placed in interferometer line of sight
- Explore feasibility of using CO_2 as a tracer to allow measurement of metastable nitrogen deactivation rates due to other species - CO , NO , N_2O , O_2 , O_3

FUTURE WORK (Cont).

T-22528a

- Tracer experiments:

- introduce varying steady state concentrations of species of interest (X). Difference in first order relaxation rates measured in these experiments and experiment performed without X gives loss rate due to X

- N_2O is an optional tracer species ($\nu_3 = 2249 \text{ cm}^{-1}$)

- allows measurement of deactivation due to CO_2 , eliminates complications due to varying degrees of self-absorption in the CO_2 001 band

- The LABCEDE facility allows these experiments to be performed at pressures and temperatures similar to those occurring in the electron disturbed upper atmosphere

ACKNOWLEDGEMENTS

This work is sponsored by the Air Force
Office of Scientific Research and the
Defense Nuclear Agency

APPENDIX 2

The Dipole Moment and Infrared Transition Strengths of Nitric Oxide

submitted for publication in Journal of Chemical Physics

(reproduced in its entirety)

THE DIPOLE MOMENT AND INFRARED TRANSITION STRENGTHS OF NITRIC OXIDE

W.T. Rawlins, J.C. Person, and M.E. Fraser
Physical Sciences Inc.
20 New England Business Center
Andover, MA 01810

S.M. Miller and W.A.M. Blumberg
Air Force Research Laboratory
Hanscom Air Force Base, MA 01731

ABSTRACT

The electric dipole moment function for $\text{NO}(X^2\Pi)$ is determined by non-linear least squares analysis of experimental data, including previously reported $(\Delta v=2)/(\Delta v=1)$ transition branching ratios for $v' \leq 13$. Polynomial fits to the dipole moment function are determined over the range of internuclear separation 0.97 to 1.50 Å. The fitted dipole moment functions agree well with previous *ab initio* predictions, but differ somewhat at the larger internuclear separations. The observed dipole moment functions are used to compute rotationless Einstein coefficients for $\Delta v = 1$ through 4 vibrational transitions with $v' \leq 20$. The absolute $\Delta v=1$ and $\Delta v=2$ Einstein coefficients are well determined by this analysis, especially for $v' \leq 12$. The results provide a firm basis for determinations of vibration-rotation emission intensities of $\text{NO}(X^2\Pi)$ in high-temperature or non-equilibrium chemi-excitation systems.

1. INTRODUCTION

The vibration-rotation transitions of $\text{NO}(X^2\Pi)$ are important to investigations of nitric oxide formation and excitation in combustion systems, discharge plasmas, and the Earth's atmosphere. The large variety of thermal and non-equilibrium conditions encountered in these applications necessitates description of the infrared radiative properties of NO over a wide range of vibrational and rotational energy content. While the transition strengths for the $(v',v'') = (1,0)$ and $(2,0)$ bands have been repeatedly measured in absorption near room temperature, information on the transition strengths for higher vibrational and rotational states is limited. Computation of the spontaneous emission Einstein coefficients of the higher-lying transitions requires accurate knowledge of the electric dipole moment function of the molecule over a large range of internuclear separation. In a previous paper, we reported experimental measurements of the branching ratios for the fundamental and first overtone vibration-rotation bands of $\text{NO}(X^2\Pi)$, for rotational temperatures near 60 K and vibrational levels up to $v'=13$.¹ In the present paper, we describe the analysis of the branching ratio data to determine an experimental dipole moment function and rotationless Einstein coefficients for NO. A separate paper describes the use of this dipole moment function to perform detailed computations of rovibrational transition moments and Einstein coefficients for the fundamental and first overtone systems.²

Previous evaluations of the dipole moment function of $\text{NO}(X^2\Pi)$ include an experimental determination by Chandraiah and Cho,³ based on careful absorption measurements of the $(1,0)$ and $(2,0)$ band strengths at room temperature, an empirical determination by Drabbels and Wodtke⁴ based on stimulated emission pumping of high vibrational levels, and comprehensive *ab initio* theoretical computations by Billingsley,⁵ Langhoff et al.,^{6,7} and de Vivie and Peyerimhoff.⁸ The *ab initio* dipole moment functions of Refs. 5, 7, and 8 are compared in

Figure 1. The theoretical functions exhibit marked differences in curvature at large internuclear distances characteristic of high vibrational and rotational states. The branching ratio data of Ref. 1 offer an opportunity to probe the behavior of the dipole moment function at large internuclear distances, where one might expect to observe the onset of downward curvature as the molecule approaches dissociation.

The interest in the high-energy transition strengths of nitric oxide stems from laboratory⁹ and upper atmospheric¹⁰⁻¹³ observations of infrared fluorescence from highly rovibrationally excited NO(v,J) formed by chemiluminescent reactions involving electronically and/or translationally excited precursors. As described in Ref. 1, previous descriptions of the vibrational and rotational scaling of the Einstein coefficients for NO(v,J) transitions have relied heavily on scaling relationships developed from the theoretical dipole moment function of Billingsley.^{5,14} The vibrational intensity scalings derived in this way are approximate only and are not firmly grounded, especially for higher vibrational levels in the fundamental band ($v \geq 6$) and for the overtone transitions. Previous estimates for the $\Delta v=1$ ⁹ and $\Delta v=2$ ¹ Einstein coefficients were made by combining recent experimental results with the relative scaling of the $\Delta v=1$ A-factors predicted by Billingsley.¹⁴ These estimated values are compared with the Billingsley theoretical predictions in Figure 2, illustrating substantial uncertainties in the absolute values of the Einstein coefficients.

Billingsley¹⁴ showed that the rotational intensity scalings for low to moderate J ($J \leq 33.5$) were only weakly affected by centrifugal distortion and spin uncoupling effects, such that the thermally averaged band Einstein coefficients for the fundamental and first overtone transitions were essentially independent of temperature up to at least 600 K. Recent shock tube measurements¹⁵ indicate that the Einstein coefficients for the (1,0) and (2,1) transitions are nearly

independent of temperature up to 2500 K, further supporting the insensitivity of the individual line strengths to rotational effects. However, the atmospheric processes show chemi-excitation of $J \approx 100$ for each of several vibrational levels, with effective rotational "temperatures" between 5000 and 10,000 K.⁹⁻¹³ The scaling of rotational and vibrational intensities to this extreme is subject to the effects of centrifugal distortion, spin uncoupling (transition to Hund's case (b)), and curvature in the dipole moment function at large internuclear distance.²

The branching ratio data of Ref. 1 were obtained for very low rotational temperatures, 60 K, such that centrifugal distortion, spin uncoupling, and lambda doubling effects are clearly negligible. Thus, through a straightforward least squares fitting analysis, it is possible to derive an empirical functional form for the dipole moment as a function of internuclear distance over the range sampled by the radial wavefunctions of the observed vibrational levels. The analytical procedure employed transition moment integrals computed in the conventional manner from wavefunctions evaluated by the Rees-Klein-Rydberg (RKR) method, and determined the dipole moment function giving the best least squares fit between computed and observed overtone/fundamental Einstein coefficient ratios. The resulting dipole moment function can be used to address the scaling of Einstein coefficients with v and J , and can be compared directly with *ab initio* theoretical predictions.

2. COMPUTATIONAL PROCEDURE

The Einstein coefficients for a given vibrational/rotational transition, $A(v'J'\Omega' \rightarrow v''J''\Omega'')$, are related to the dipole moment function through the square of the transition moment integral:

$$A(v'J'\Omega' \rightarrow v''J''\Omega'') = \frac{64\pi^4 v^3}{3h} \left| \int \Psi(v'J'\Omega') \mu(r) \Psi(v''J''\Omega'') dr \right|^2 \quad (1)$$

where v is the transition frequency, Ψ is the radial wavefunction for the appropriate upper or lower state, and $\mu(r)$ is the dipole moment as a function of internuclear distance r . The wavefunctions are evaluated by solution of the radial Schrödinger equation,

$$\left[-\frac{d^2}{dr^2} + E_{\text{rot}} + V(r) \right] \Psi = E \Psi \quad (2)$$

where $V(r)$ is the stretching potential, $E_{\text{rot}} = B_v J(J+1)$ is the kinetic energy of rotation, and E is the eigenvalue for the state of interest. More detailed computations of E_{rot} , incorporating the contributions of the spin sublevels appropriate for an open-shell diatomic in the Hund's case (a) limit, established that the closed-shell formula for E_{rot} given above is accurate for the range of states considered here. The potential energy functions were computed from spectroscopic constants by the RKR method as given by Tellinghuisen,¹⁶ using the Hulburt-Hirschfelder functional form¹⁷ to describe the bottom of each potential curve. The wavefunctions were evaluated by numerical inversion of Eq. (2) using the Numerov-Cooley method¹⁸ as programmed by Eccles and Malik.¹⁹ The calculations employed the spectroscopic constants of Goldman and Schmidt²⁰ with the slight modification in D_v introduced by Rawlins et al.;⁹ these values produce excellent agreement with more recent high resolution results²¹ for the range of rotational levels observed in Ref. 1.

Upper and lower state wavefunctions were calculated for an effective rotational quantum number $\langle J \rangle = 3.5$, which is the most populated rotational level at the experimental rotational temperature of 60 K. The wavefunctions were then combined with a $\mu(r)$ function in Eq. (1) to

compute rotationless transition moments and Einstein coefficients. These rotationless Einstein coefficients, $A_{v,v'}$, are approximately equivalent to the corresponding thermally averaged Einstein coefficients for low rotational temperatures; Billingsley¹⁴ has shown this approximation to be accurate for NO at rotational temperatures below 600 K.

For computational purposes, the dipole moment function $\mu(r)$ was expressed as a polynomial in r . For forward-marching calculations of Einstein coefficients from the *ab initio* dipole moment functions, the reported theoretical results were fit to high-order polynomial functions. For fitting of the experimental branching ratios of Ref. 1, $\mu(r)$ was expressed as either a cubic or quadratic function of r with unknown coefficients, e.g.,

$$\mu(r) = a_0 + a_1(r-r_e) + a_2(r-r_e)^2 + a_3(r-r_e)^3 \quad (3)$$

and the coefficients for each functional form were determined by a least squares fit between the computed and observed Einstein coefficient ratios.

The fitting procedure used the Powell-Brent multidimensional minimization routine²² to find the set of $\mu(r)$ coefficients which minimized the weighted standard deviation (at the 90% confidence level) between the computed and measured quantities, given an initial guess of the coefficients of $\mu(r)$. To constrain the fitting results for the constant and first-order terms of the $\mu(r)$ expression, we included among the measured quantities the static dipole moment values reported by Hoy et al.²³ for $\mu(v=0,1;\Omega=1/2,3/2)$, and the value $A_{10}=13.4\pm0.4 \text{ s}^{-1}$ based on room temperature absorption measurements^{24,25} as discussed in Ref. 1. Omission of the value for A_{10} resulted in unstable fitting results, i.e., the solutions were somewhat dependent on the initial guesses (see below). Additional inclusion of an absolute value for A_{20} (from Ref. 1) did not

significantly alter the fitting results and so was not employed for the final solution. Thus the complete set of measured quantities consisted of four static dipole moment values, one absolute value for A_{10} , and twelve weighted-mean overtone/fundamental branching ratios of the form $A_{v',v'-2}/A_{v',v'-1}$ for $2 \leq v' \leq 13$, with individual statistical weights specified at the 90% confidence level. The primary fitting results were values of the coefficients a_i for the cubic and quadratic expressions for $\mu(r)$, and the corresponding values for $A_{v',v'}$ as evaluated from Eq. (1).

3. RESULTS

The experimental overtone/fundamental branching ratios reported in Ref. 1 are compared in Figure 3 to the best-fit values corresponding to quadratic and cubic parameterizations of the dipole moment function. Although the cubic function gives a smaller standard deviation, the two functional fits are essentially indistinguishable from each other. However, as we will show, the quadratic fit provides a better representation of the empirical dipole moment function due to both its physical realism at large internuclear separation and its consistency with recent overtone and high- v Einstein coefficient measurements.

The computed ratios are insensitive to variations in the constant and first-order coefficients in the polynomial expression for $\mu(r)$, and are primarily sensitive to the quadratic coefficient a_2 . The sensitivities of the computed branching ratios to the terms in the polynomial $\mu(r)$ function were established through forward-marching solutions of Eq. (1) for systematic variations in assumed values of the coefficients a_i . Variations in a_0 have no effect on either the branching ratios or the Einstein coefficients, and the solution values of a_0 are primarily determined by the static dipole data. Variations in a_1 (for a linear $\mu(r)$ function) cause significant variations in $A_{v',v'}$, however, the overtone/fundamental branching ratios remain unchanged; thus,

the solution values for a_1 are primarily determined by the measurement value chosen for A_{10} . Variations in a_2 moderately affect the $\Delta v=1$ Einstein coefficients at high v' and more significantly affect the $\Delta v=2$ Einstein coefficients at all v' , resulting in high sensitivity for the overall magnitude of the branching ratios and relatively weak sensitivity for the dependence (curvature) of the ratios on v' . Variation of a_3 , which primarily governs the curvature in $\mu(r)$ at large and small r , has a large effect on the $\Delta v=3,4$ transitions and only affects the $\Delta v=1,2$ Einstein coefficients at high v' . The principal effect of a_3 on the computed branching ratios is on the v' dependence (curvature) for the higher vibrational levels: larger values of a_3 (for a given a_2) have little effect on the branching ratios at low v' , but give significantly lower overtone/fundamental ratios at high v' . For the ranges of v' and Δv sampled by the data of Ref. 1, the value of a_3 is determined with relatively low sensitivity, and extension of the $\mu(r)$ expression to a quartic term is not justified based on the experimental data.

The sensitivities described above demonstrate the necessity of constraining the values of the static dipoles and A_{10} to achieve reliable fitting results. In particular, the value of a_0 is indeterminate without specification of the static dipole values. With no constraint on the value of A_{10} , the fitting results vary slightly with changes in the initial guesses for the coefficients a_i , resulting in a $\approx 10\%$ variation in the solution values for A_{10} and A_{20} . Specification of the value $A_{10} = 13.4 \pm 0.4 \text{ s}^{-1}$, based on the critical literature review discussed in Ref. 1 and on the high-temperature measurements of Ref. 14, channels the fitting results into a consistent solution which is independent of the initial choice of a_i values.

The final best-fit a_i values for quadratic and cubic forms of $\mu(r)$ are given in Table 1. The uncertainties in the values of a_0 , a_1 , and a_2 are 0.06%, 0.1%, and 3%, respectively; for the cubic $\mu(r)$, the solution value of a_3 shows a $\pm 20\%$ uncertainty in keeping with the reduced sensitivity as

noted above. The experimental and computed static dipole values are compared in Table 2, illustrating agreement to $\approx 10^{-3}$ D for both fitting functions. The fitting procedure was tested, using as input data the $v' \leq 13$ overtone/fundamental Einstein coefficient ratios computed from the Langhoff et al.⁷ dipole moment function, with the same proportional error bars as used for the experimental data. The fit to the trial "data" set gave recovery of the initial fundamental and first overtone $A_{v',v''}$ values to better than 9% for $v' \leq 20$.

The rotationless A-factors computed from the best-fit quadratic and cubic dipole moment functions for the transitions $\Delta v = 1$ through 4 are listed in Table 3. The computed values for A_{10} and A_{20} compare well to previously determined values as reviewed in Ref. 1, showing agreement generally within $\approx 10\%$. Dana et al.²⁶ reported measurements of line intensities for the (2,1) band by high resolution absorption spectroscopy near 300 K. Their data give a transition moment corresponding to $A_{21} = 23.4 \pm 0.8 \text{ s}^{-1}$. This is in good agreement with the values of 25.46 and 25.32 listed in Table 3, and is identical to the value computed² from the theoretical dipole moment function of Langhoff et al.⁷ Clearly, the degree to which the Einstein coefficients in Table 3 agree with previous experimental and theoretical values depends heavily on our choice of the value of A_{10} constraining the fit to the branching ratio data. The value chosen here was guided by the results of Refs. 24 and 25, however several other measurements exist which support a value about 10% smaller (≈ 12 to 12.5 s^{-1}), as reviewed in Ref. 1. In general, the uncertainties of the higher and lower determinations are not mutually exclusive, so a $\approx 10\%$ uncertainty remains in A_{10} and A_{20} . This uncertainty is inherent in all the values reported in Table 3. Additional uncertainty results from extrapolation of the empirical dipole moment functions beyond their range of measurement validity; this occurs for the higher vibrational levels and the high overtones, as discussed further below.

4. DISCUSSION

The NO($X^2\Pi$) data analysis presented here offers a unique opportunity to examine the behavior of an electric dipole moment function at large internuclear separation, where the effects of mechanical and electrical anharmonicity are expected to be more substantial. The availability of *ab initio* dipole moment functions for this molecule provides a rare opportunity for comparison of experiment and theory for a fundamental molecular property. Similar analyses have been conducted for other diatomics, notably OH($X^2\Pi$),²⁷⁻²⁹ hydrogen halides,³⁰ and CO($X^1\Sigma$).³¹ NO differs from these previous examples since, although it has a $^2\Pi$ configuration like OH, its dipole moment is relatively small like that of CO, as is its departure from mechanical and electrical harmonicity at small to intermediate internuclear separation. For example, the dipole moment function of NO is so nearly linear that much of the transition strength of the first overtone arises from mechanical rather than electrical anharmonicity. The values of $A_{v',v'-2}/A_{v',v'-1}$ computed for a linear dipole moment function are only about a factor of two smaller than the observed values (independent of slope and intercept of the function). The results of the present analysis indicate that the dipole moment function of NO is somewhat steeper and less curved at large ($r-r_e$) than is predicted by the theoretical descriptions.

The experimental and two *ab initio*^{7,8} dipole moment functions are compared in Figure 4. The branching ratio data for $v = 1$ to 12 sample internuclear distances between 0.97 and 1.50 Å. Within this range of internuclear separation, the dipole moment values represented by the cubic and quadratic empirical functions are essentially indistinguishable; however, the two functions diverge significantly when extrapolated to larger separation. Specifically, the cubic representation results in physically unrealistic upward curvature beyond the range of the fit, so

this function is inappropriate for extrapolation beyond 1.50 Å. The quadratic empirical function provides a good basis for comparison to the *ab initio* dipole moment functions.

The agreement between experiment and theory is quite good, and is especially striking for the recent theoretical results of Langhoff et al.⁷ When compared to the theoretical function of Ref. 7, the present experimental result is in excellent agreement at smaller internuclear separations, and gives slightly larger dipole moment values at larger separation. As the internuclear separation approaches the dissociation limit, the molecular dipole moment function passes through a maximum and returns to zero for the separated atoms (Fig 4b). Thus the *ab initio* functions in Figure 4 exhibit significant downward curvature beyond about 1.4 Å. In contrast to the theoretical predictions, the experimental results exhibit less downward curvature in the dipole moment function near 1.5 Å. Inspection of Figure 3 indicates that this behavior is dictated by the branching ratio data for the high vibrational levels, i.e., a function giving a good fit to the branching ratio data for $v' = 9$ to 13 must have relatively little downward curvature near 1.5 Å.

The validity of the apparent differences near 1.5 Å is difficult to establish with high confidence from the data of Ref. 1 alone. Unfortunately, the effects of the apparent deviations between experimental and theoretical $\mu(r)$ become significant for vibrational levels near the end of the range of our experimental measurements, where the uncertainties of the measurements become large. Indeed, both of the theoretical dipole moment functions of Refs. 7 and 8 give branching ratios which lie within the error bars of most of the data of Ref. 1. However, due to the statistical weighting of the branching ratio data in the fitting procedure, the highly uncertain data points at high v' (e.g., $v'=13$) do not greatly impact the fitting results. For example, least squares fits including and omitting the branching ratio data points for $v'=12$ and $v'=13$ gave a

values which differed by less than 1%. In addition, fits to the 48 individual branching ratio values and uncertainties reported in Ref. 1 gave results in complete agreement with those obtained for the weighted-mean values.

The slight discrepancy with Langhoff et al.⁷ would be resolved if the reported branching ratios for $v' \geq 9$ are erroneously low. Experimental errors in response calibrations and radiant intensity measurements were carefully evaluated, as documented in Ref. 1, and are not at issue. The primary possible sources of unknown error in the branching ratios are unknown intensity contributions from radiating species other than NO(v) which are present in the experiments. As noted in Ref. 1, the (2,0) band of the $N_2(W^3\Delta_u-B^3\Pi_g)$ near 3.3 μm is present in the measurements and overlaps with the 14-12 and higher transitions of NO, preventing determination of overtone/fundamental branching ratios for $v' \geq 14$. However, contrary to the suggestion of Langhoff et al.,⁷ this and other N_2 bands do not affect the intensity determinations for the 13-11, 12-10, and lower transitions. This was verified through comprehensive spectral simulations and fitting including the results of our separate observations³² of the N_2 electronic bands in the absence of NO emission. In any case, contributions to the apparent overtone intensities at high v' by unknown radiators would result in erroneously *large* branching ratios for NO, implying an even greater discrepancy with the theoretical dipole moment behavior at large r . A more plausible possibility is that an unknown radiator near 6.5 μm could have caused erroneously large determinations of the 13-12 and 12-11 intensities in the NO fundamental band, resulting in erroneously low apparent branching ratios. Indeed, the (1,0) band of the $N_2(W-B)$ system lies in this wavelength region. However, the characteristic spectral structure of this band is not observable in the data of Ref. 1; furthermore, our previous observations³² of the intensity of this band in our apparatus, relative to that of the (2,0) and other readily observable N_2 bands, show

that its intensity should give only about a 1% contribution to the NO 13–12 and 12–11 determinations. We conclude that the $v' \geq 9$ branching ratios reported in Ref. 1 should be taken at face value; however, due to the large dynamic range in signal-to-noise ratio demanded of these measurements, corroborating measurements by other methods would greatly increase our confidence in the results.

Measurements of transition probabilities in the second and third overtones can provide additional data to support the empirical dipole moment function determination. Very recent high resolution absorption measurements in the PSI laboratory have determined rotationally resolved and band-integrated transition strengths in the (3,0) band near 1.8 μm .³³ Preliminary results give $A_{30} = 0.033 \pm 0.001 \text{ s}^{-1}$. This value is in excellent agreement with 0.037 s^{-1} from the quadratic empirical function and 0.032 s^{-1} from the Langhoff et al.⁷ theoretical function. By comparison, the theoretical function of Ref. 8 gives 0.021 s^{-1} .

Drabbels and Wodtke⁴ have very recently reported a series of measurements of high- v fundamental and overtone Einstein coefficients for NO using stimulated emission pumping to access the high vibrational levels. These investigators reported experimental values for the (21,20), (21,19), (21,18), (21,17), and (7,6) Einstein coefficients, and used their data together with that of References 1 and 23 to determine an empirical, quartic dipole moment function. In general, the A-factor data of Drabbels and Wodtke⁴ are in excellent agreement ($< 20\%$) with the thermally-averaged Einstein coefficients determined from the quadratic empirical dipole moment function presented here. In addition, their empirical dipole moment function, which covers a larger internuclear separation range of 0.9 to 1.7 Å, is almost identical to our empirical function, as illustrated in Figure 5. The Drabbels and Wodtke function is generally slightly lower than ours in absolute magnitude, and the two differ by less than 0.04 D over the range of their function

and less than 0.01 D over the range of our function. In particular, the Drabbels and Wodtke function, which samples both higher v' and larger Δv than ours, is in excellent agreement (< 0.003 D) with our quadratic function at 1.5 to 1.6 Å, lending support to the trends we have described for magnitude and curvature at large internuclear separation.

The computed rotationless Einstein coefficients (Table 3) are compared to those determined from the Langhoff et al.⁷ *ab initio* dipole moment function, and to the previous estimates of Rawlins et al.^{1,9} in Figure 6. Thermally-averaged Einstein coefficients, taken from Ref. 2 for the empirical and Langhoff et al.⁷ dipole moment functions, are compared in Table 4 to the various experimental determinations cited above. The empirical and Langhoff et al.⁷ functions give fundamental and first overtone A-factors which are in good agreement, despite the differences at large r noted above. Figure 6 also demonstrates that previous estimates^{1,9} of the A-factors were accurate up to $v'=10$, but were too low at higher v' . The comparisons in Figure 6 and Table 4 indicate that the fundamental and first overtone Einstein coefficients are now accurately determined to within $\sim 10\%$. The A-factors for the second and third overtones appear to be accurate to about 20 to 30%.

The close agreement between the experimental data base and the *ab initio* results of Langhoff et al.⁷ indicates that the theoretical dipole moment function of Ref. 7 provides a sound basis for evaluation of a comprehensive set of Einstein coefficients for NO. Holtzclaw et al.² described methods for rigorous evaluation of the line-by-line $A(v',J')$ values, specifically accounting for the effects of centrifugal distortion and spin uncoupling. Those investigators also used the computed $A(v',J')$ values to determine thermally averaged Einstein coefficients $A(v',T)$, and presented tables comparing values computed at 300 K for different dipole moment functions. Here, we provide thermally averaged $A(v',T)$ values for the $\Delta v=1$ and $\Delta v=2$ transitions at several

rotational temperatures, as computed for Boltzmann rotational population distributions using the *ab initio* dipole moment function of Langhoff et al.⁷ The values are listed in Table 5 for the $\Delta v=1$ transitions and in Table 6 for the $\Delta v=2$ transitions. We recommend the use of these Einstein coefficients for general analysis of NO vibrational emission in atmospheric, chemiluminescent, and high-temperature scenarios.

5. CONCLUSIONS

We have used experimental measurements of vibrational transition branching ratios, together with previous measurements of the static dipole moment and the $(v=0)-(v=1)$ absorption coefficient, to determine an empirical dipole moment function for NO($X^2\Pi$) by a non-linear least squares fitting procedure. The dipole moment function was determined over the range 0.97 to 1.50 Å. The empirical function is generally consistent with *ab initio* theoretical predictions, but differs in the details of slope and curvature behavior as a function of r . The solution indicates a steeper slope, with slightly larger dipole moment values and less downward curvature near 1.5 Å ($(r-r_e)/r_e \approx 0.3$) than is predicted by theory. This observation is supported by recently reported experimental determinations of the Einstein coefficients for $v'=21$, $\Delta v=1$ to 4.⁴ These differences have only minor impact on the rotationless Einstein coefficients evaluated here, but may be more significant for vibrational and rotational states approaching the dissociation limit.

We have used the empirical dipole moment functions to evaluate rotationless vibrational Einstein coefficients for the fundamental and first three overtone systems up to $v'=20$. Inter-comparisons of these with previously predicted and measured values give an indication of the remaining uncertainties in the vibrational Einstein coefficients of NO($X^2\Pi$). For the fundamental

and first overtone systems most relevant to atmospheric, combustion, and environmental applications, these uncertainties are now quite small, roughly 10% for $v' = 1$ to 20.

The recently reported *ab initio* dipole moment function of Langhoff et al.⁷ exhibits remarkable agreement with the experimental results over the range of internuclear separation sampled by the measurements. While the present analysis suggests the possibility of a discrepancy with theory at large separation, leading to a larger maximum dipole moment than predicted, the inherent limitations of the existing data base preclude definitive conclusions on this point. Additional experimental measurements could address this issue by probing high vibrational levels sampling internuclear separations near the maximum dipole moment, e.g., 1.5 to 1.9 Å, as in the stimulated emission pumping experiments of Ref. 4. In addition, experimental measurements in the second and third overtone systems would probe higher derivatives of the dipole moment function and provide improved determinations of its shape. We conclude that the empirical dipole moment function reported here provides an accurate representation for transition probability calculations within its experimental range of validity, and we recommend the *ab initio* function of Langhoff et al.⁷ for use in extrapolations to higher-lying states.

The rotationless Einstein coefficients reported here can be multiplied by the conventional Hönl-London rotational line strength factors³⁴ to determine the J-dependent transition strengths for low to medium rotational levels in the $\Delta v=1$ band. However, for applications involving high rotational temperatures or non-equilibrium chemi-excitation of high-J states, it is necessary to more rigorously account for the combined effects of spin uncoupling, centrifugal distortion, mechanical anharmonicity, and dipole moment function on the rotational intensity scaling and thermally averaged Einstein coefficients. A detailed investigation of these effects is reported in a

separate publication,² where it is shown that centrifugal distortion can significantly affect the rotational dependence of the line strengths for the first and higher overtones.

ACKNOWLEDGEMENTS

We appreciate extensive discussions with K. W. Holtzclaw, as well as enlightening comments from B. D. Green, L. G. Piper, S. J. Lipson, and J. A. Dodd. S. R. Langhoff kindly provided printouts and preprints of the *ab initio* dipole moment functions reported in Refs. 6 and 7. This work was sponsored by the Air Force Office of Scientific Research under Task 2303EP1/PL007 and by the Defense Nuclear Agency under MIPR 94-511, Work Unit 00042.

REFERENCES

1. W.T. Rawlins, M.E. Fraser, S.M. Miller, and W.A.M. Blumberg, J. Chem. Phys. 96, 7555 (1992).
2. K.W. Holtzclaw, W.T. Rawlins, and B.D. Green, J. Quant. Spectrosc. Radiat. Transfer 55, 481 (1996).
3. G. Chandraiah and C.W. Cho, J. Mol. Spectrosc. 47, 134 (1973).
4. M. Drabbels and A. M. Wodtke, J. Chem. Phys. 106, 3024 (1997).
5. F.P. Billingsley II, J. Chem. Phys. 62, 864 (1975); J. Chem. Phys. 63, 2267 (1975).
6. S.R. Langhoff, C.W. Bauschlicher, Jr., and H. Partridge, J. Chem. Phys. 89, 4909 (1988).
7. S.R. Langhoff, C.W. Bauschlicher, Jr., and H. Partridge, Chem. Phys. Lett. 223, 416 (1994).
8. R. de Vivie and S.D. Peyerimhoff, J. Chem. Phys. 89, 3028 (1988).

9. W.T. Rawlins, M.E. Fraser, and S.M. Miller, *J. Phys. Chem.* 93, 1097 (1989).
10. R.H. Picard, J.R. Winick, R.D. Sharma, A.S. Zachor, P.J. Espy, and C.R. Harris, *Adv. Space Res.* 7, 23 (1987).
11. S.J. Lipson, P.S. Armstrong, J.R. Lowell, W.A.M. Blumberg, D.E. Paulsen, M.E. Fraser, W.T. Rawlins, B.D. Green, R.E. Murphy, and J.A. Dodd, Paper SA42C-5, Proceedings of the American Geophysical Union (abstract), *Eos* 74, 469 (1993).
12. P.S. Armstrong, S.J. Lipson, J.R. Lowell, W.A.M. Blumberg, D.R. Smith, E.R. Huppi, R.M. Nadile, and J.A. Dodd, Paper SA42C-6, Proceedings of the American Geophysical Union (abstract), *Eos* 74, 469 (1993).
13. M.E. Fraser, W.T. Rawlins, B.D. Green, D.E. Paulsen, P.S. Armstrong, S.J. Lipson, W.A.M. Blumberg, and R.E. Murphy, Paper SA42C-7, Proceedings of the American Geophysical Union (abstract), *Eos* 74, 469 (1993).
14. F.P. Billingsley II, *J. Mol. Spectrosc.* 61, 53 (1976).
15. W.T. Rawlins, R.R. Foutter, and T.E. Parker, *J. Quant. Spectrosc. Radiat. Transfer* 49, 423 (1993).
16. J. Tellinghuisen, *Comp. Phys. Commun.* 6, 221 (1974).
17. G. Herzberg, Molecular Spectra and Molecular Structure: I. Spectra of Diatomic Molecules (Van Nostrand, Toronto, 1950), p. 102; erratum in H.M. Hulburt and J.O. Hirschfelder, *J. Chem. Phys.* 35, 1901 (1961).
18. J.K. Cashion, *J. Chem. Phys.* 39, 1872 (1963); *J. Chem. Phys.* 41, 3988 (1965).
19. J. Eccles and D. Malik, *Quantum Chem. Program Exchange Bull.* 13, 407 (1981).
20. A. Goldman and S.C. Schmidt, *J. Quant. Spectrosc. Radiat. Transfer* 15, 127 (1975).
21. C. Amiot, *J. Mol. Spectrosc.* 94, 150 (1982).

22. W.H. Press, S.A. Teukolsky, W.T. Vetterling, and B.P. Flannery, Numerical Recipes in FORTRAN: The Art of Scientific Computing, Second Edition (Cambridge University Press, New York, 1992), pp. 406 ff.
23. A.R. Hoy, J.W.C. Johns, and A.R.W. McKellar, *Can. J. Phys.* 53, 2029 (1975).
24. R.F. Holland, M.C. Vasquez, W.H. Beattie, and R.S. McDowell, *J. Quant. Spectrosc. Radiat. Transfer* 29, 435 (1983).
25. J.Y. Mandin, C. Amiot, and G. Guelachvili, *Ann. Phys. (Paris)* 5, 91 (1980).
26. V. Dana, J.Y. Mandin, L. Coudert, M. Badaoui, F. LeRoy, G. Guelachvili, and L.S. Rothman, *J. Mol. Spectrosc.* 165, 525 (1994).
27. D.D. Nelson, Jr., A. Schiffman, D.J. Nesbitt, and D.J. Yaron, *J. Chem Phys.* 90, 5443 (1989).
28. D.D. Nelson, Jr., A. Schiffman, and D.J. Nesbitt, *J. Chem Phys.* 90, 5455 (1989).
29. D.D. Nelson, Jr., A. Schiffman, D.J. Nesbitt, J.J. Orlando and J.B. Burkholder, *J. Chem Phys.* 93, 7003 (1990).
30. D. Oba, B.S. Agrawalla, and D.W. Setser, *J. Quant. Spectrosc. Radiat. Transfer* 34, 283 (1985).
31. C. Chackerian, Jr., R. Farrenq, G. Guelachvili, C. Rossetti, and W. Urban, *Can. J. Phys.* 62, 1579 (1984).
32. M.E. Fraser, W.T. Rawlins, and S.M. Miller, *J. Chem. Phys.* 88, 538 (1988).
33. D.M. Sonnenfroh and M.G. Allen, *Appl. Opt.* 36, 7970 (1997); D.M. Sonnenfroh, W.T. Rawlins, and M.G. Allen, manuscript in preparation.
34. G. Herzberg, Molecular Spectra and Molecular Structure: I. Spectra of Diatomic Molecules (Van Nostrand, Toronto, 1950), p. 208.

Table 1. Coefficients of $\mu(r)$ From Least Squares Fits ^{a,b,c}

	Cubic $\mu(r)$	Quadratic $\mu(r)$
a_0	- 0.1675	- 0.1681
a_1	2.344 (± 0.002)	2.345
a_2	- 1.56 (± 0.05)	- 1.26
a_3	2.1 (± 0.4)	
^a $\mu(r) = a_0 + a_1 (r-r_e) + a_2 (r-r_e)^2 + a_3 (r-r_e)^3$ ^b Units are Debye and Angstroms. ^c Uncertainties are indicated where greater than one in the last significant digit.		

Table 2. NO($X^2\Pi$) Static Dipole Moments (Debye)

$^2\Pi_{1/2}$	Observed (Hoy et al, 1975)	This Work Cubic $\mu(r)$	This Work Quadratic $\mu(r)$
$v = 0$	- 0.1574	- 0.1586	- 0.1588
$v = 1$	- 0.1416	- 0.1410	- 0.1406

Table 3. $A_{v'v''}$ Values Computed from Derived Dipole Moment Functions

v'	Cubic $\mu(r)$				Quadratic $\mu(r)$			
	$\Delta v=1$	$\Delta v=2$	$\Delta v=3$	$\Delta v=4$	$\Delta v=1$	$\Delta v=2$	$\Delta v=3$	$\Delta v=4$
1	13.40				13.37			
2	25.46	0.91			25.32	0.81		
3	36.30	2.56	0.065		35.94	2.34	0.037	
4	45.98	4.81	0.247	0.0043	45.28	4.47	0.143	0.0018
5	54.61	7.51	0.582	0.020	53.43	7.12	0.342	0.0087
6	62.25	10.54	1.10	0.058	60.47	10.20	0.657	0.025
7	68.99	13.79	1.81	0.128	66.44	13.61	1.10	0.056
8	74.89	17.17	2.72	0.242	71.44	17.30	1.69	0.11
9	80.02	20.58	3.84	0.412	75.52	21.18	2.42	0.19
10	84.45	23.96	5.15	0.649	78.74	25.19	3.31	0.30
11	88.23	27.24	6.64	0.962	81.17	29.26	4.36	0.45
12	91.44	30.37	8.29	1.36	82.87	33.34	5.55	0.64
13	94.10	33.30	10.08	1.85	83.90	37.37	6.88	0.89
14	96.29	36.00	11.98	2.44	84.31	41.31	8.35	1.19
15	98.04	38.43	13.97	3.12	84.16	45.12	9.95	1.55
16	99.40	40.57	16.02	3.90	83.50	48.75	11.66	1.97
17	100.41	42.42	18.09	4.78	82.38	52.18	13.46	2.46
18	101.11	43.96	20.15	5.76	80.85	55.37	15.35	3.02
19	101.52	45.18	22.18	6.81	78.95	58.30	17.31	3.64
20	101.69	46.10	24.15	7.95	76.73	60.94	19.31	4.34

Table 4. Comparison of Computed and Measured Einstein Coefficients for NO(v)^a

Δv	$v' \rightarrow v''$	This Work, Quadratic $\mu(r)^b$	Langhoff et al. ⁶ $\mu(r)^b$	Experimental ^c	
				$A_{v'v''}$	Reference
1	1 - 0	13.3	12.4	13.6 ± 0.5 12.0 ± 0.6	24 3
		13.2 (800 K) 13.1 (2500 K)	12.4 (800 K) 12.2 (2500 K)	13.2 ± 1.3 (800 to 2500 K)	15
	2 - 1	25.1	23.4	23.4 ± 0.8	26
	7 - 6	65.9	60.7	55.7 ± 6.8	4
	21 - 20	69.6	65.5	70.0 ± 3.6	4
2	2 - 0	0.81	0.79	0.84 ± 0.04 0.94 ± 0.11	3 1
	21 - 19	63.2	60.3	66.7 ± 3.4	4
3	3 - 0	0.037	0.032	0.033 ± 0.001	33
	21 - 18	22.9	24.8	27.2 ± 2.4	4
4	21 - 17	6.10	8.68	5.9 ± 1.7	4

- a. Units are s⁻¹.
b. Computed Einstein coefficients are thermally averaged at 300 K, except where otherwise noted.
c. See Reference 1 for a complete review of measured NO Einstein coefficients for $\Delta v = 1, 2$.

Table 5. NO($\Delta v=1$) Thermally Averaged Einstein Coefficients (s^{-1})
Computed from the Dipole Moment Function of Langhoff et al. (1994)

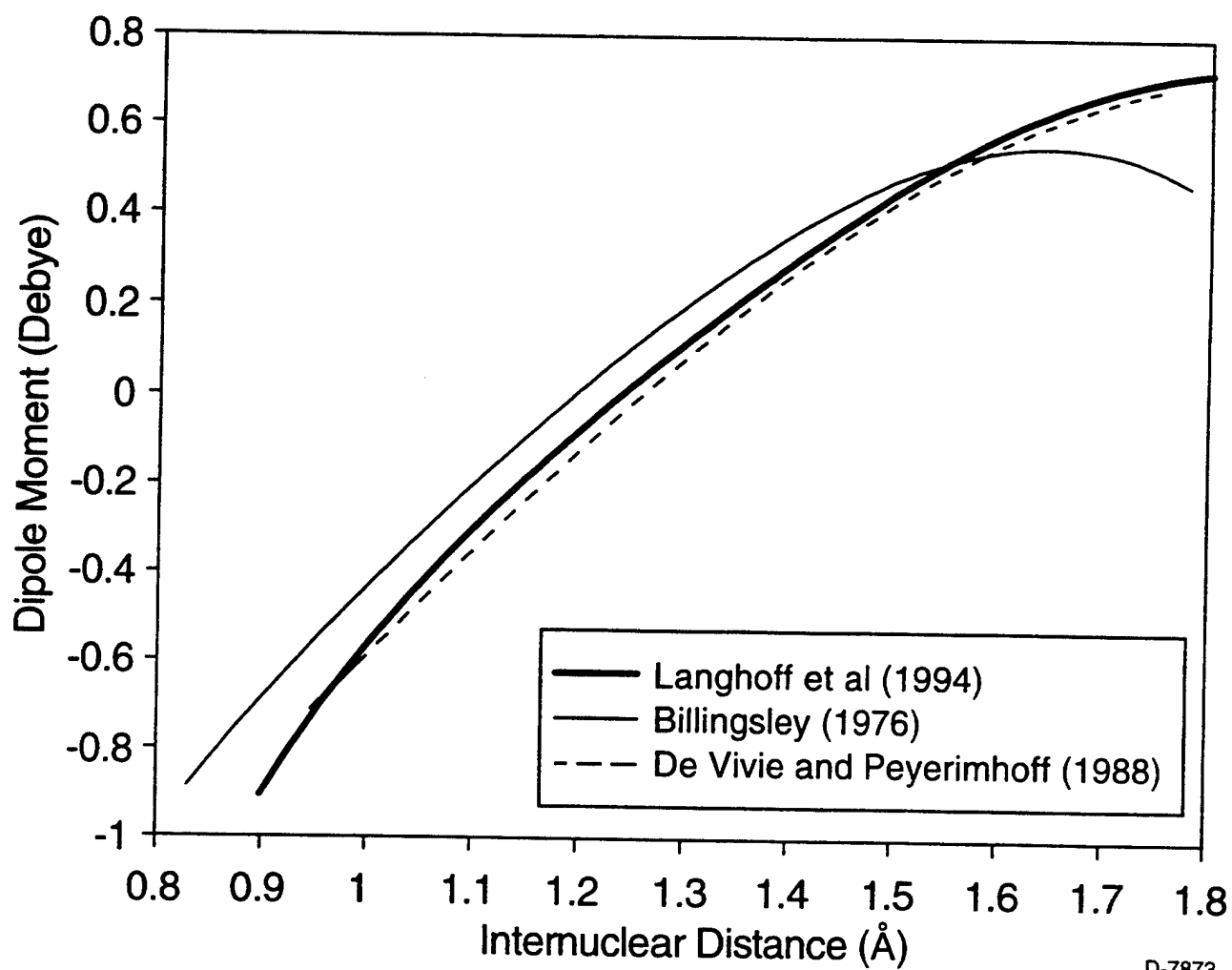
v'	Rotational Temperature (K)							
	200	300	500	1000	2000	5000	10000	20000
1	12.404	12.396	12.380	12.341	12.261	12.004	11.446	10.064
2	23.421	23.405	23.374	23.295	23.132	22.609	21.496	18.826
3	33.148	33.122	33.073	32.951	32.702	31.911	30.250	26.392
4	41.659	41.625	41.559	41.395	41.061	40.002	37.808	32.860
5	49.049	49.006	48.922	48.715	48.296	46.973	44.261	38.319
6	55.395	55.344	55.245	54.997	54.492	52.906	49.694	42.855
7	60.782	60.723	60.607	60.318	59.733	57.890	54.195	46.549
8	65.279	65.212	65.080	64.751	64.083	61.988	57.832	49.468
9	68.953	68.876	68.728	68.359	67.612	65.273	60.674	51.675
10	71.872	71.789	71.626	71.217	70.389	67.808	62.784	53.230
11	74.093	73.999	73.817	73.369	72.466	69.649	64.212	54.176
12	75.654	75.554	75.359	74.875	73.895	70.840	65.006	54.558
13	76.608	76.500	76.288	75.765	74.711	71.422	65.201	54.409
14	76.986	76.871	76.645	76.086	74.957	71.430	64.832	53.760
15	76.827	76.704	76.464	75.867	74.662	70.893	63.925	52.637
16	76.153	76.022	75.766	75.129	73.844	69.829	62.499	51.061
17	74.983	74.843	74.571	73.895	72.532	68.263	60.580	49.056
18	73.340	73.192	72.903	72.187	70.742	66.209	58.184	46.647
19	71.232	71.075	70.770	70.013	68.483	63.677	55.329	43.855
20	68.670	68.506	68.185	67.386	65.768	60.684	52.041	40.718
21	65.684	65.508	65.167	64.321	62.315	51.708	36.248	22.949
22	62.274	62.089	61.730	60.837	58.740	48.261	33.543	21.185
23	58.460	58.267	57.890	56.952	54.768	44.498	30.636	19.299
24	54.277	54.072	53.674	52.689	50.428	40.454	27.559	17.314
25	49.748	49.535	49.121	48.093	45.766	36.183	24.357	15.259
26	44.929	44.708	44.277	43.210	40.835	31.744	21.080	13.167

Table 6. NO($\Delta v=2$) Thermally Averaged Einstein Coefficients (s^{-1})
Computed from Dipole Moment Function of Langhoff et al. (1994)

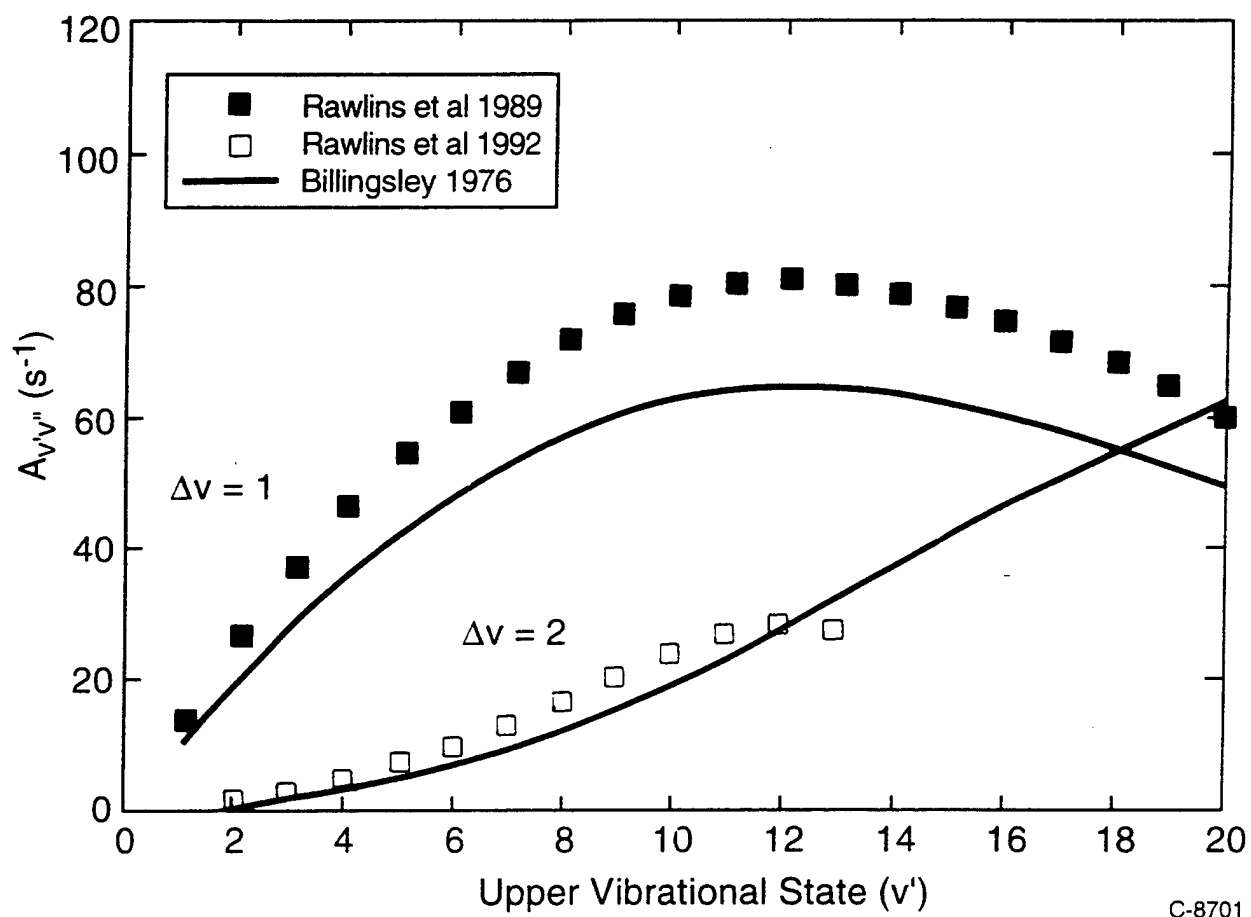
v'	Rotational Temperature (K)							
	200	300	500	1000	2000	5000	10000	20000
2	0.785	0.786	0.786	0.786	0.788	0.790	0.781	0.716
3	2.281	2.281	2.281	2.282	2.284	2.285	2.250	2.050
4	4.400	4.400	4.400	4.400	4.400	4.391	4.304	3.898
5	7.053	7.052	7.051	7.049	7.042	7.011	6.841	6.160
6	10.143	10.141	10.138	10.130	10.113	10.044	9.757	8.737
7	13.578	13.574	13.568	13.552	13.517	13.392	12.952	11.535
8	17.263	17.257	17.246	17.219	17.162	16.962	16.335	14.472
9	21.113	21.104	21.087	21.046	20.961	20.667	19.819	17.471
10	25.049	25.036	25.013	24.954	24.834	24.429	23.330	20.468
11	28.998	28.982	28.950	28.872	28.711	28.178	26.802	23.407
12	32.901	32.879	32.838	32.737	32.532	31.857	30.183	26.245
13	36.702	36.675	36.625	36.500	36.246	35.418	33.427	28.945
14	40.363	40.331	40.270	40.119	39.812	38.822	36.502	31.483
15	43.851	43.813	43.741	43.562	43.201	42.043	39.384	33.838
16	47.143	47.099	47.015	46.809	46.392	45.062	42.054	35.994
17	50.227	50.177	50.081	49.846	49.372	47.864	44.498	37.941
18	53.090	53.034	52.926	52.663	52.132	50.444	46.705	39.663
19	55.734	55.671	55.551	55.259	54.670	52.794	48.662	41.144
20	58.155	58.086	57.955	57.633	56.986	54.910	50.350	42.356
21	60.358	60.283	60.139	59.784	58.734	49.926	35.443	22.598
22	62.330	62.248	62.092	61.706	60.549	51.136	36.053	22.952
23	64.091	63.997	63.823	63.398	62.122	52.089	36.449	23.168
24	65.579	65.477	65.286	64.822	63.414	52.746	36.602	23.231
25	66.805	66.694	66.486	65.971	64.401	53.070	36.481	23.120
26	67.708	67.580	67.344	66.764	65.005	52.993	36.040	22.810

FIGURE CAPTIONS

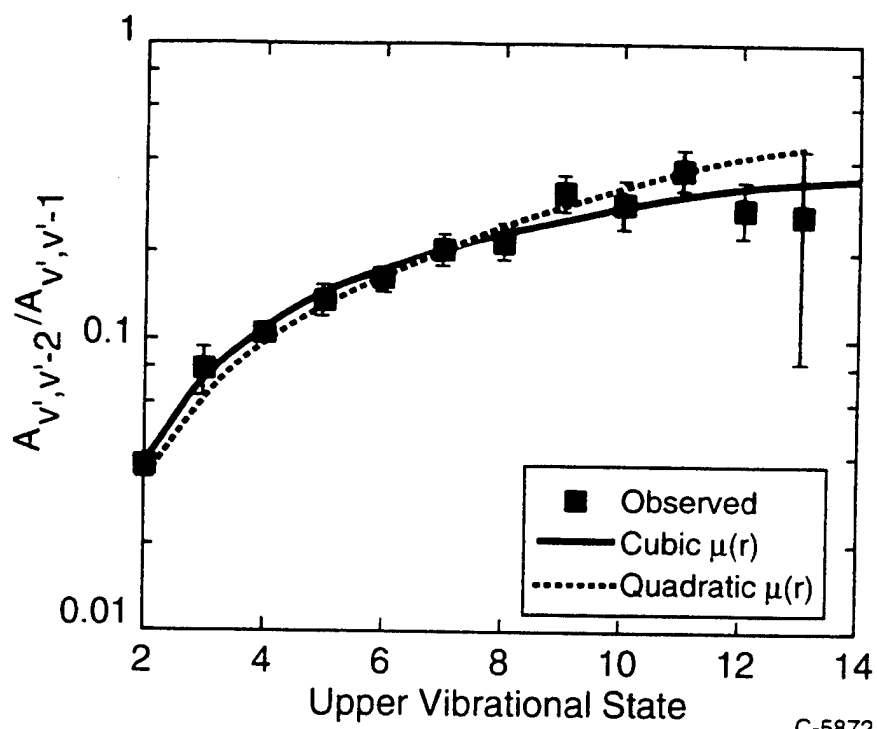
1. Comparison of previous ab initio (Refs. 5, 7, 8) dipole moment functions for NO($X^2\Pi$) ($r_e = 1.15 \text{ \AA}$).
2. Fundamental and first overtone Einstein coefficients computed by Billingsley (Ref. 14) and estimated as described in the text (Refs. 1 and 9).
3. Observed and computed best-fit overtone/fundamental Einstein coefficient ratios for cubic and quadratic representations of $\mu(r)$. Error bars represent $\pm 90\%$ confidence levels in the data points, which are the weighted-average values reported in Ref. 1.
4. Comparison of derived best-fit and theoretical dipole moment functions.
5. Comparison of empirical dipole moment functions.
6. Comparison of fundamental and first overtone $A_{v',v''}$ values determined from the best-fit quadratic $\mu(r)$ function, from the theoretical function of Ref. 7, and from the scaling relationships estimated in Refs. 1 and 9.

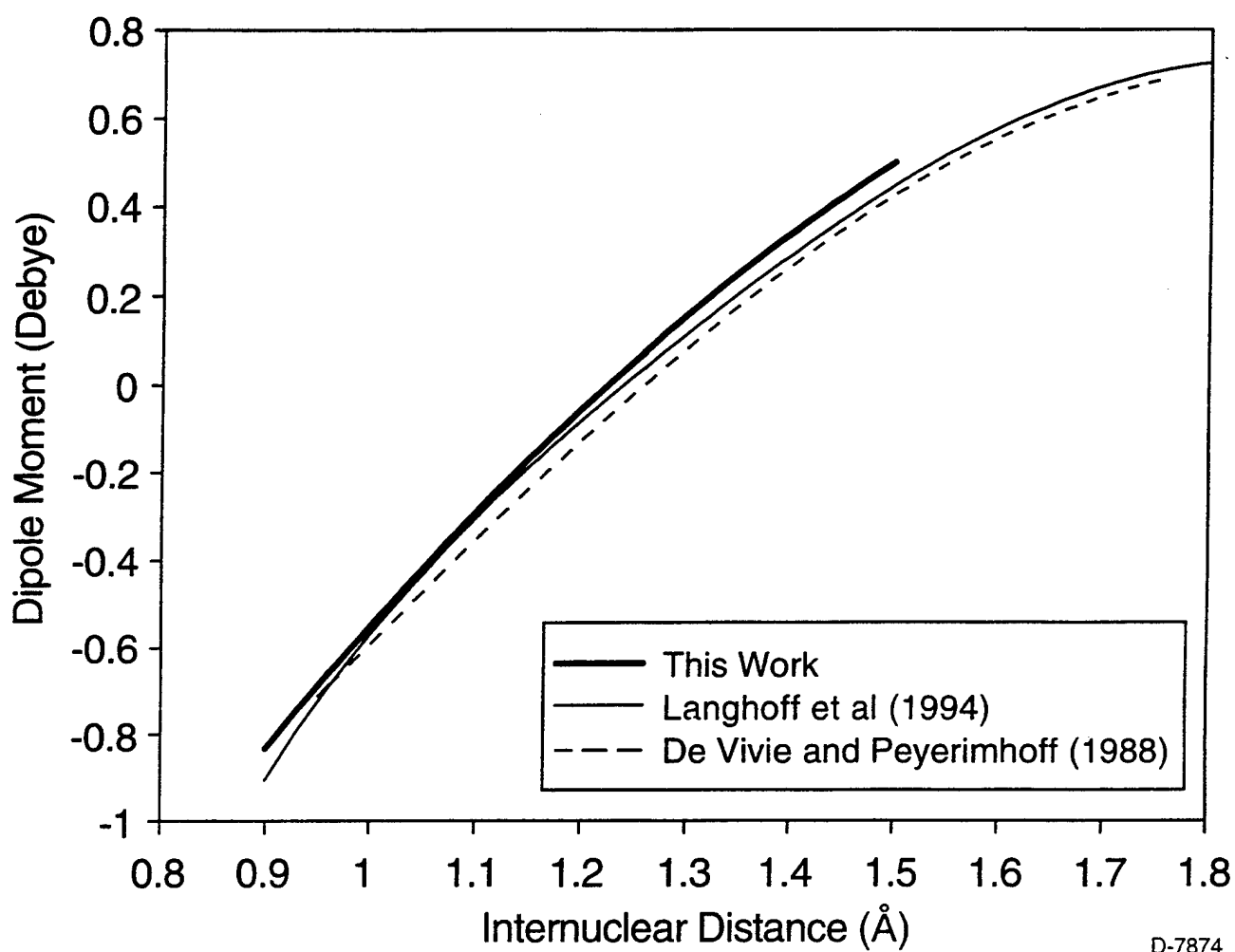


D-7873

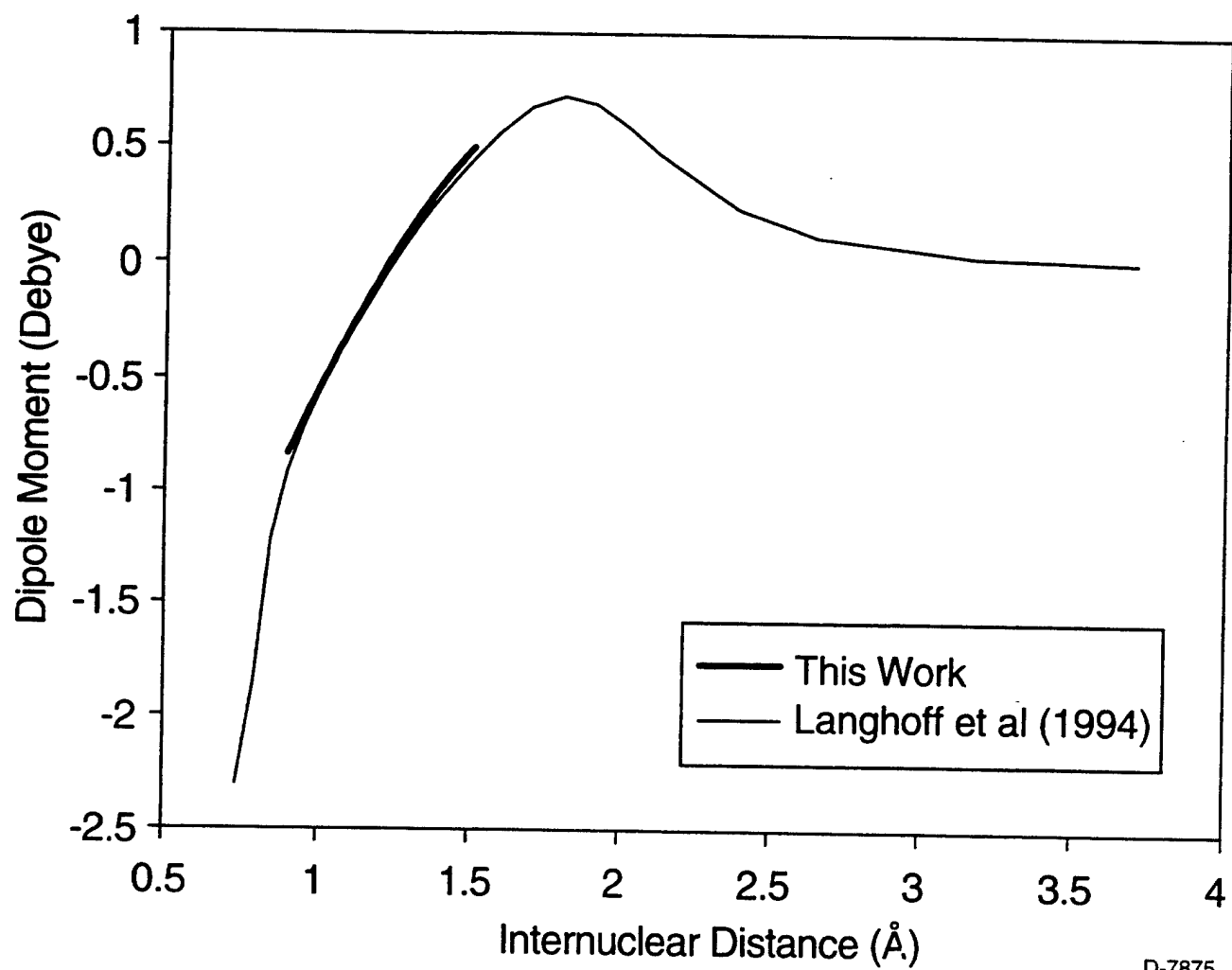


C-8701

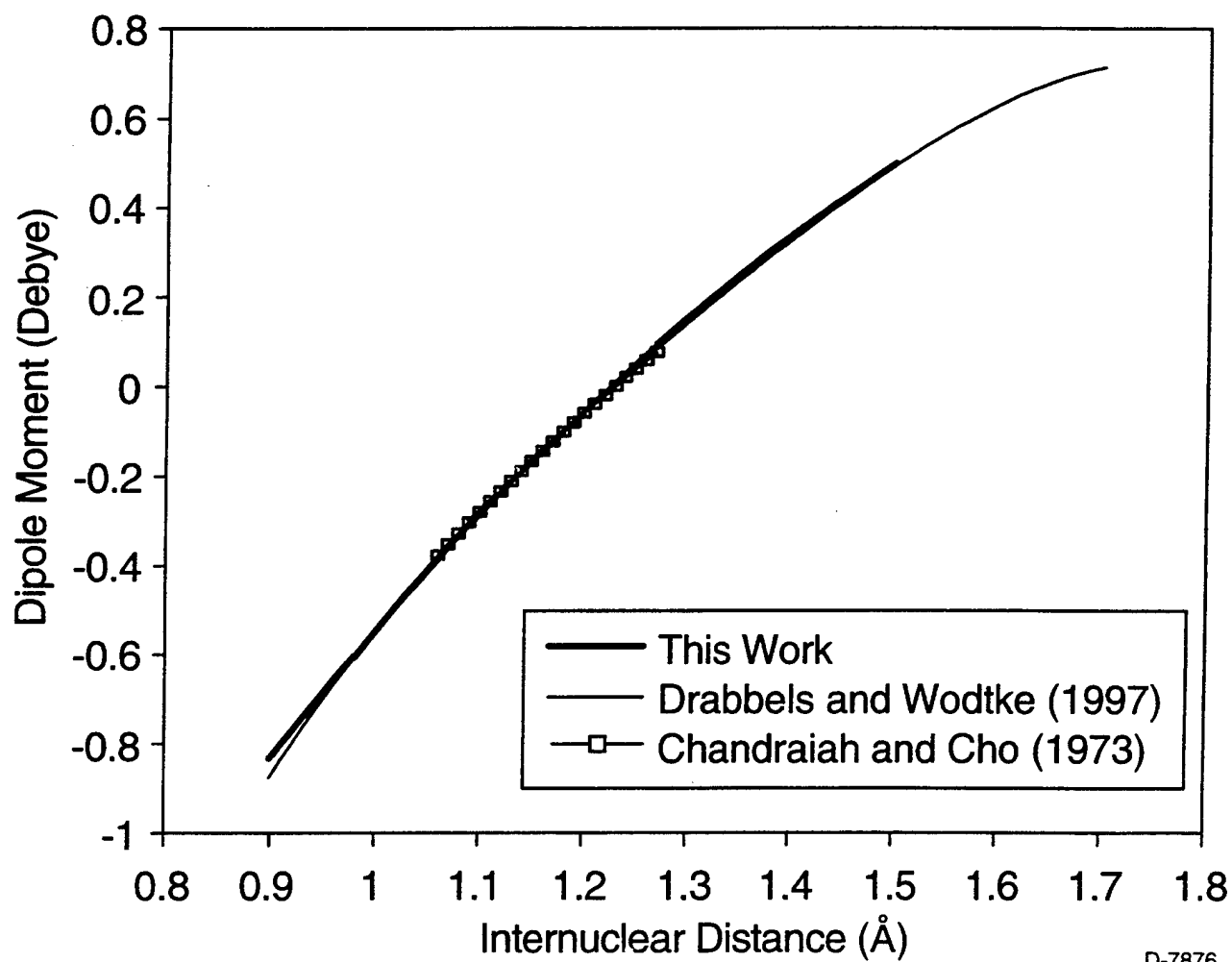




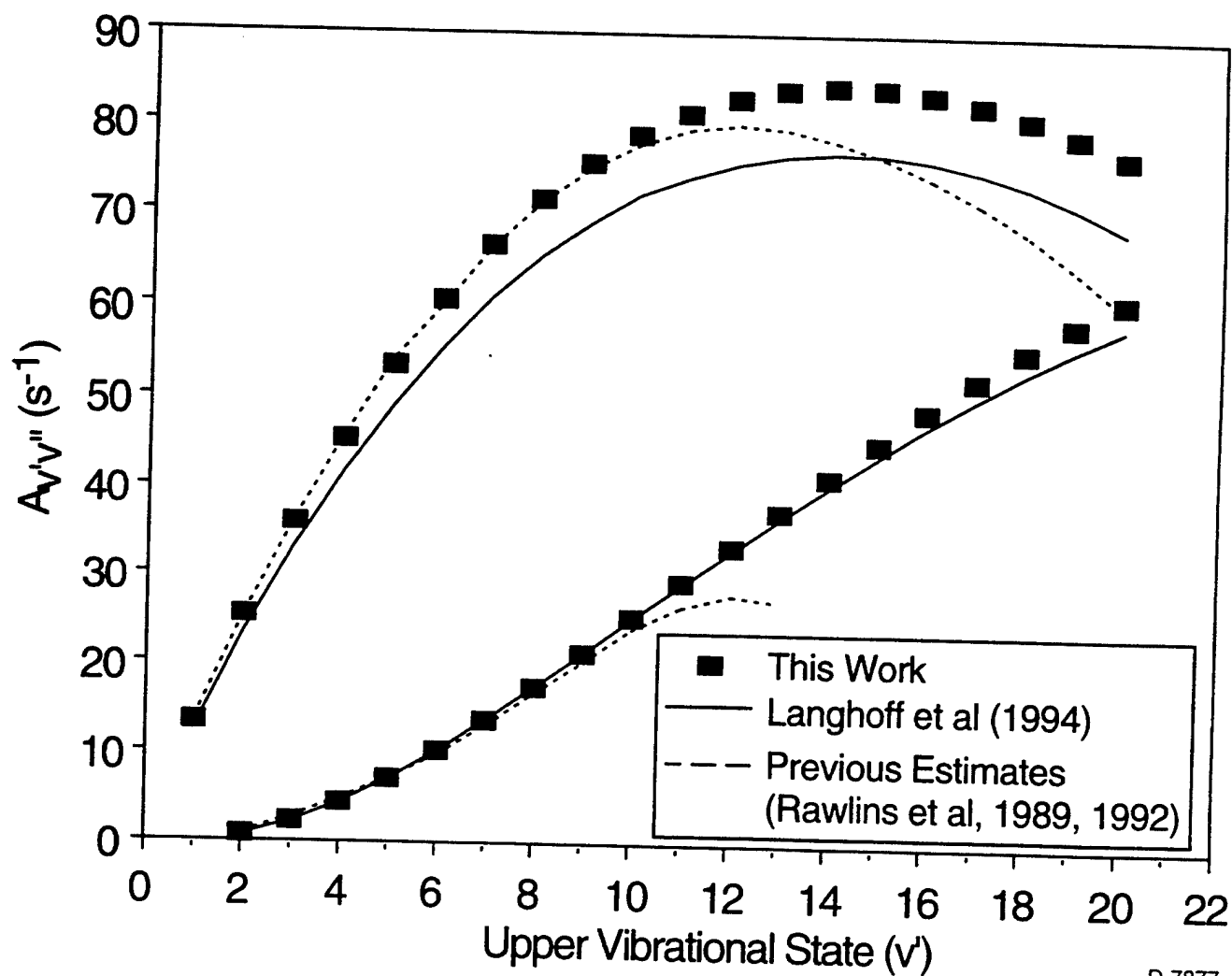
D-7874



D-7875



D-7876



D-7877

T. Rawlins
Figure 6

APPENDIX 3

The Effects of Centrifugal Distortion on the Infrared Radiative Transition Probabilities of NO($X^2\Pi$)

Journal of Quantitative Spectroscopy and Radiative Transfer

(reproduced in its entirety)



THE EFFECTS OF CENTRIFUGAL DISTORTION ON THE INFRARED RADIATIVE TRANSITION PROBABILITIES OF NO(X^2II)

K. W. HOLTZCLAW, W. T. RAWLINS† and B. D. GREEN

Physical Sciences Inc., 20 New England Business Center, Andover, MA 01810, U.S.A.

(Received 8 May 1995; received for publication 21 July 1995)

Abstract—State-to-state and thermally averaged Einstein A -coefficients have been computed for the fundamental and first three overtone sequences of the NO (X^2II – X^2II) system with the aim of examining the effects of centrifugal distortion on the high- J transitions that occur as a result of upper atmospheric chemistry. The Einstein coefficients were calculated using an experimentally derived dipole moment function of Rawlins et al (manuscript in preparation), and the *ab initio* dipole moment functions of Langhoff et al [*Chem. Phys. Lett.* **223**, 416 (1994)] and de Vivie and Peyerimhoff [*J. Chem. Phys.* **89**, 3027 (1988)], for J' ranging up to 139.5. The state-specific Einstein coefficients show that, regardless of dipole moment function employed, centrifugal distortion has a relatively small effect on the $\Delta v = 1$ sequence which is manifest primarily as a reduction in the high- J R-branch intensities. However, the effect on the overtone rotational intensities is larger and results in enhanced R-branch intensities and reduced P-branch intensities relative to those calculated neglecting centrifugal distortion. For example, in the first overtone system for $J' \approx 80.5$, $v' = 2$ –14, the ratio of R- to P-branch Einstein coefficients is larger by about 1.7 than the R/P ratio predicted in the absence of centrifugal distortion.

INTRODUCTION

Nitric oxide has important chemical and radiative roles in numerous atmospheric, combustion, environmental, and biological applications. The i.r. vibration–rotation transitions of NO(X^2II) are important for radiative balance and diagnostic applications in systems ranging from air-breathing combustion to the Earth's mesosphere and thermosphere. In many of these applications the NO is excited, either thermally or chemically, to high vibrational and rotational levels. Accurate interpretation of the resulting infrared spectral emission requires detailed knowledge of the optical transition probabilities for these high energy states. In this paper we examine the i.r. vibration–rotation transition probabilities for highly energetic vibrational and rotational states of NO(X^2II) with particular emphasis on the role played by centrifugal distortion.

Specific examples of systems where high internal excitation of NO occurs include air-breathing combustion and the upper atmosphere. In combustion systems, temperature and path-averaged concentrations^{1,2} can be deduced from spectrally resolved measurements of NO(X^2II) emission. This application requires knowledge of the effects of rotational temperature on the thermally averaged Einstein coefficients for each radiating vibrational level. In the upper atmosphere, auroral and photochemical processes lead to the chemical production of rotationally and vibrationally excited NO(X^2II). The resulting infrared fluorescence is readily observed in both the fundamental ($\Delta v = 1$, 5–7 μm) and first overtone ($\Delta v = 2$, 2.5–3.5 μm) sequences, and is characterized by non-equilibrium vibrational and rotational distributions that can be approximated by Boltzmann distributions with temperatures between 5000 and 10,000 K. These chemi-excitation processes have been investigated in the laboratory,³ and are now being examined in detail in upper atmospheric measurements.^{4–6} The quantitative analysis of high resolution spectral emission data from these

†To whom all correspondence should be addressed.

measurements relies upon knowledge of the state resolved ($v', J' - v'', J''$) Einstein coefficients for levels ranging to at least $v' \approx 15$ and $J' \approx 120$. While the $\text{NO}(v' < 15)$ Einstein coefficients for low to moderate J and temperature are now relatively well known,⁷ quantitative extrapolation to higher J has not been performed.

In a manner qualitatively similar to $\text{OH}(X^2\text{II})$, the $\text{NO}(X^2\text{II})$ radiative properties can be expected to reflect the influence of centrifugal distortion. However, the influence of centrifugal distortion is prominent in the vibration-rotation spectra of OH even at room temperature,⁸⁻¹¹ while the effects of centrifugal distortion are minor at best in corresponding NO spectra.¹² However, rotational distributions characteristic of atmospheric chemi-excitation can include up to 3 eV of rotational energy³ and the influence of centrifugal distortion may significantly affect the intensities of high- J' transitions. Earlier analyses of highly excited $\text{NO}(X^2\text{II})$ have concentrated on the $\Delta v = 1$ sequence and have assumed that the influence of centrifugal distortion is negligible.³⁻⁶ However there has been no quantitative support for this assumption. Furthermore, there is no information presently available on the influence of centrifugal distortion on the intensities of high- J overtone transitions.

In previous work, we measured the overtone/fundamental branching ratios for $\text{NO}(X^2\text{II})$, $v' = 2-13$,¹³ and used those measurements to determine empirical dipole moment functions and rotationless Einstein coefficients for NO .⁷ In this paper, we use the quadratic dipole moment function from that work, as well as two *ab initio* dipole moment functions to compute $A(v', J' - v'', J'')$ for an extensive range of vibrational and rotational states. These Einstein coefficients cover the $\Delta v = 1-4$ sequences and were used to determine band integrated, thermally averaged Einstein coefficients for use in low resolution spectral measurements. They allow a detailed examination of the influence of centrifugal distortion on the radiative properties of $\text{NO}(X^2\text{II})$. We find that, regardless of dipole moment function, the influence of centrifugal distortion is relatively minor in the $\Delta v = 1$ sequence, even for high- J transitions; however it becomes more prominent with increasing Δv in the overtone transitions.

COMPUTATIONAL METHOD

The Einstein A -coefficients for NO vibration-rotation transitions were calculated in a manner closely following that outlined in our previous paper on the $\text{OH}(X^2\text{II})$ i.r. transitions.¹¹ Numerical wavefunctions for the initial and final states were determined by solving the radial Schrödinger equation using the Numerov-Cooley method.^{14,15} Centrifugal distortion was taken into account by employing a rotating molecule potential in solving for each wavefunction, viz.:

$$V(r) = V_0(r) + E_{\text{rotation}} \quad (1)$$

where V_0 is the potential for the non-rotating molecule and E_{rotation} is the kinetic energy of the rotating molecule.¹⁶ For the non-rotating molecule, we used a numerical Rydberg-Klein-Rees (RKR) potential calculated from the spectral constants of Amiot.¹⁷ Where there is overlap between our calculated potential and that given by Amiot,^{17,18} there is excellent agreement. We assumed an expression for the rotational energy of the form:

$$E_{\text{rotation}} = B_r J(J+1). \quad (2)$$

This expression is exact for closed shell diatomics (singlet states) and is an excellent approximation for the rotational energy of an open shell diatomic in the Hund's case (a) limit at large J .

The individual vibration-rotation transition probabilities were calculated using the standard relation:

$$A(v', J', \Omega' - v'', J'', \Omega'') = \frac{64\pi^4 \nu^3}{3h} |R^2| S_{J', J''} \frac{1}{2J' + 1} \quad (3)$$

where ν is the transition frequency in cm^{-1} , R is the transition moment integral,

$$R = \langle v', J' | \mu(r) | v'', J'' \rangle, \quad (4)$$

$S_{J', J''}$ is the rotational line strength factor, and $\mu(r)$ is the electric dipole moment as a function of internuclear distance r . Since we employed Eq. (2) for the rotational energy, we did not differentiate between the two spin sublevels (F_1 and F_2) in calculating the transition moment R . While $\text{NO}(X^2\text{II})$

is well described by Hund's case (a) at lower J , at higher J it is better described by angular momentum coupling intermediate between Hund's case (a) and case (b). Consequently, we employed a subroutine¹⁹ incorporating the intermediate case line strength formulae of Hill and Van Vleck²⁰ to determine the $S_{J,J'}$. Transition frequencies were calculated using the spectroscopic constants of Amiot.¹⁷

We performed calculations using an experimentally determined dipole moment function of Rawlins et al.⁷ derived by fitting the intensity ratios of overtone and fundamental transitions observed in a cryogenic infrared chemiluminescence experiment.¹³ This dipole moment function was deduced from spectra displaying transitions from $v' = 2-13$, using RKR wavefunctions for $\langle J \rangle = 3.5$. Two empirical dipole moment functions, represented as quadratic and cubic expansions in $(r - r_e)$, were determined from non-linear least squares fits to the experimental data. We did not use the cubic dipole moment function in this work even though it produces intensity ratios that agree with the data somewhat better than the quadratic function. This is primarily due to the fact that this function, when extrapolated to internuclear distances needed to calculate high- v , high- J transitions, predicts an asymptotically increasing dipole moment which seems unphysical and does not agree with the trends observed in other dipole moment functions. The quadratic dipole moment as a function of internuclear distance is given, in units of Debye, by:⁷

$$\mu(r) = -0.1681 + 2.3453(r - r_e) - 1.2550(r - r_e)^2. \quad (5)$$

The use of different integration limits in calculating the $v' = 13$, $J' = 3.5$, $\Delta v = 1$ and $\Delta v = 2$ transition moment integrals with the quadratic dipole moment function allows a determination of the range over which the transition moment function is sampled by the corresponding wavefunctions. That range is 0.93–1.56 Å; integration with larger limits does not significantly alter the value of the corresponding Einstein-coefficient ($<0.02\%$ change). Consequently, these limits span the internuclear separations over which the dipole moment function is supported to any extent by experimental data. This range is slightly larger than that given by the turning points of the $v' = 13$ vibrational state, which are 0.96 and 1.52 Å respectively as taken from the RKR potential.

We have also calculated the corresponding coefficients using the *ab initio* dipole moment functions of Langhoff et al.²¹ and of de Vivie and Peyerimhoff.²² The purpose of these calculations is to explore the sensitivity of the resulting Einstein-coefficients to different dipole moment functions, particularly at high J where the effects of centrifugal distortion are most prominent. Furthermore, since these functions were calculated *ab initio*, they are not subject to the restrictions on internuclear distance imposed by experimental data, and thus provide convenient representations at larger internuclear separations. The function of de Vivie and Peyerimhoff²² is reported over the range of internuclear distance from 0.95 to 1.75 Å, and that of Langhoff et al.²¹ is reported over the range from 0.74 to 3.70 Å. The Langhoff function is thus reported for internuclear distances corresponding to near-complete dissociation of the molecule. We note that both *ab initio* dipole moment functions are very similar to the experimentally derived quadratic function of Rawlins et al.⁷ between 0.9 and 1.6 Å.

We fit the listed dipole moment values of Langhoff et al with an eighth order polynomial to facilitate their use in our calculations; the resulting expression is:

$$\begin{aligned} \mu(r) = & -0.18926 + 2.26914(r - r_e) - 1.24127(r - r_e)^2 \\ & - 0.76625(r - r_e)^3 - 4.22017(r - r_e)^4 + 41.74266(r - r_e)^5 \\ & - 97.65134(r - r_e)^6 + 88.57438(r - r_e)^7 - 28.08490(r - r_e)^8. \end{aligned} \quad (6)$$

This function reproduces the Langhoff function to within 0.003 Debye over the range from 0.85 to 2.11 Å. We used an eighth order polynomial since this function is reported for a range of internuclear separation which allows calculation of all Einstein coefficients without extrapolation, consequently, a high-order fit is justified for accurate reproduction of this dipole

moment function. The corresponding polynomial fit to the computed values reported by de Vivie and Peyerimhoff is:

$$\mu(r) = -0.2363 + 2.2543(r - r_e) - 0.7684(r - r_e)^2 - 0.7091(r - r_e)^3. \quad (7)$$

The three dipole moment functions used in this work are illustrated in Fig. 1.

RESULTS

We have calculated the individual $A(v', J', \Omega' - v'', J'', \Omega'')$ values for the $\Delta v = 1-4$ transitions of $\text{NO}(X^2\Pi)$. These coefficients cover $v' = 1-26$ and J' ranging from 0.5 to maxima of up to 139.5 so as to encompass all states accessible in the energetic upper atmospheric reactions $\text{N}(^2D, ^2P) + \text{O}_2 \rightarrow \text{NO}(X^2\Pi; v, J) + \text{O}$.³ Einstein coefficients are presented for the intramultiplet transitions only since the forbidden intermultiplet transitions are very weak and have little practical significance. The resulting coefficients are extremely voluminous and can only be partially presented in this paper. The complete evaluations for any of the three dipole moment functions are available from the authors upon request. Thermally averaged Einstein coefficients were calculated via the standard expression:

$$A_{v', J', \Omega'}(T) = \frac{\sum_{J'', \Omega''} A(v', J', \Omega' - v'', J'', \Omega'') (2J' + 1) \exp(-E_{v', J', \Omega'}/kT)}{\sum_{J'', \Omega''} (2J' + 1) \exp(-E_{v', J', \Omega'}/kT)}. \quad (8)$$

Tables 1-3 show the thermally averaged Einstein coefficients for each of the three dipole moment functions for a rotational temperature of 300 K, $v' = 1-26$, and $\Delta v = 1-4$.

We found that integration over the range 0.9-1.7 Å was sufficient to accurately calculate all the reported Einstein-coefficients for $v' = 1-14$. Extending the outer limit to 1.85 Å was sufficient to accurately calculate the coefficients for $v' = 15-20$, and extending the limits to 0.87 and 2.0 Å allowed precise calculation of all reported Einstein-coefficients. Significant extrapolations of the dipole moment functions of de Vivie and Peyerimhoff²² and Rawlins et al⁷ are required to calculate the high- v , high- J coefficients. These extrapolations only correspond to what is required for complete integration of the transition moment integral and they introduce some additional uncertainty into the evaluation of the Einstein-coefficients for the highest energy states.

The dependence of the thermally averaged Einstein coefficients on rotational temperature is illustrated by the values listed in Table 4, computed for the dipole moment function of Langhoff

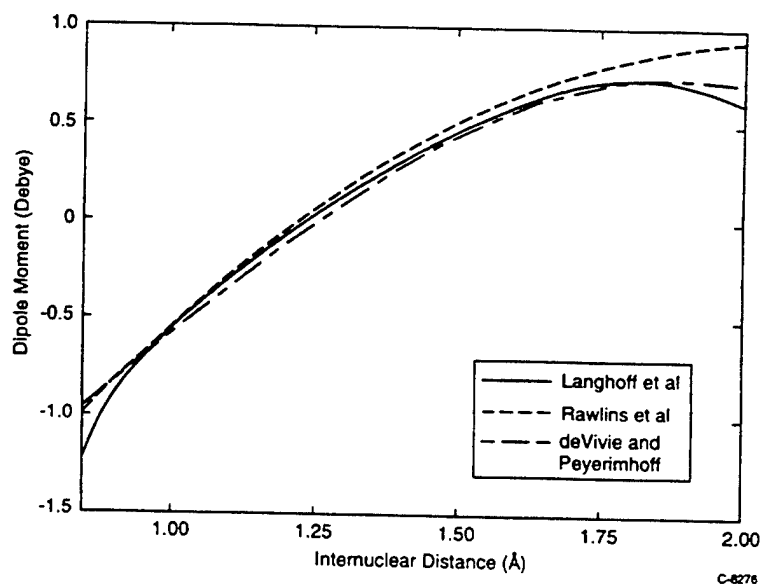


Fig. 1. The experimental and *ab initio* dipole moment functions for $\text{NO}(X^2\Pi)$ used in this work.

Table 1. Thermally averaged Einstein A -coefficients (sec^{-1}) for a rotational temperature of 300 K computed from the quadratic dipole moment function of Rawlins et al.⁷

v'	$\Delta v = 1$	$\Delta v = 2$	$\Delta v = 3$	$\Delta v = 4$
1	13.277			
2	25.142	0.811		
3	35.667	2.329	0.037	
4	44.932	4.458	0.143	0.002
5	53.006	7.104	0.344	0.009
6	59.964	10.183	0.663	0.026
7	65.873	13.610	1.116	0.058
8	70.782	17.311	1.717	0.113
9	74.790	21.215	2.476	0.197
10	77.929	25.252	3.397	0.317
11	80.254	29.363	4.484	0.482
12	81.826	33.487	5.734	0.700
13	82.696	37.570	7.145	0.976
14	82.909	41.562	8.709	1.320
15	82.512	45.414	10.417	1.738
16	81.546	49.081	12.260	2.235
17	80.053	52.520	14.223	2.819
18	78.078	55.689	16.289	3.493
19	75.650	58.550	18.443	4.262
20	72.812	61.067	20.663	5.130
21	69.597	63.184	22.926	6.098
22	66.038	64.883	25.210	7.167
23	62.178	66.114	27.483	8.336
24	58.053	66.837	29.713	9.602
25	53.699	67.017	31.863	10.961
26	49.161	66.622	33.891	12.403

Table 2. Thermally averaged Einstein A -coefficients (sec^{-1}) for a rotational temperature of 300 K computed from the dipole moment function of de Vivie and Peyerimhoff.²²

v'	$\Delta v = 1$	$\Delta v = 2$	$\Delta v = 3$	$\Delta v = 4$
1	12.312			
2	23.391	0.605		
3	33.295	1.757	0.021	
4	42.073	3.397	0.081	0.001
5	49.782	5.469	0.198	0.004
6	56.471	7.919	0.387	0.012
7	62.192	10.695	0.660	0.027
8	67.000	13.746	1.029	0.053
9	70.929	17.022	1.502	0.094
10	74.038	20.478	2.088	0.154
11	76.372	24.067	2.792	0.237
12	77.962	27.745	3.618	0.349
13	78.861	31.470	4.569	0.494
14	79.108	35.197	5.646	0.678
15	78.739	38.890	6.848	0.907
16	77.789	42.504	8.176	1.185
17	76.309	46.001	9.624	1.518
18	74.314	49.341	11.186	1.912
19	71.860	52.480	12.861	2.372
20	68.968	55.376	14.638	2.905
21	65.675	57.984	16.508	3.515
22	62.033	60.261	18.460	4.208
23	58.069	62.155	20.478	4.989
24	53.822	63.596	22.544	5.861
25	49.345	64.573	24.634	6.831
26	44.684	64.972	26.719	7.900

et al.²¹ The effect of temperature on integrated intensity is weak for all bands, as discussed further below. The band-averaged Einstein coefficient for the 1-0 transition changes little between 300 and 2000 K; this is consistent with recent shock tube determinations of a temperature invariant value of $13.2(\pm 10\%) \text{ sec}^{-1}$ for temperatures up to 2500 K.¹

Table 3. Thermally averaged Einstein A -coefficients for a rotational temperature of 300 K, computed from the dipole moment function of Langhoff et al.²¹

v'	$\Delta v = 1$	$\Delta v = 2$	$\Delta v = 3$	$\Delta v = 4$
1	12.396			
2	23.405	0.786		
3	33.122	2.281	0.032	
4	41.625	4.400	0.129	0.002
5	49.006	7.052	0.325	0.009
6	55.344	10.141	0.650	0.028
7	60.723	13.574	1.134	0.063
8	65.212	17.257	1.800	0.125
9	68.876	21.104	2.665	0.222
10	71.989	25.036	3.741	0.366
11	73.999	28.982	5.029	0.570
12	75.554	32.879	6.525	0.848
13	76.500	36.675	8.215	1.214
14	76.871	40.331	10.075	1.683
15	76.704	43.813	12.079	2.269
16	76.022	47.099	14.188	2.984
17	74.843	50.177	16.362	3.839
18	73.192	53.034	18.559	4.839
19	71.075	55.671	20.734	5.984
20	68.506	58.086	22.841	7.270
21	65.509	60.283	24.846	8.682
22	62.089	62.248	26.708	10.196
23	58.267	63.997	28.406	11.783
24	54.072	65.477	29.923	13.399
25	49.535	66.694	31.256	14.996
26	44.708	67.580	32.412	16.515

Table 4. Thermally averaged Einstein A -coefficients (sec^{-1}) for $\text{NO}(X^2\Pi)$ as a function of rotational temperature. These coefficients were computed with the dipole moment function of Langhoff et al.²¹

Transition	Rotational temperature (K)				
	300	1000	2000	5000	10,000
1-0	12.40	12.34	12.26	12.00	11.45
6-5	55.34	55.00	54.49	52.91	49.69
11-10	74.00	73.37	72.47	69.65	64.21
16-15	76.02	75.13	73.85	69.83	62.50
2-0	0.79	0.79	0.79	0.79	0.78
6-4	10.14	10.13	10.11	10.04	9.76
11-9	28.98	28.87	28.71	28.18	26.80
16-14	47.10	46.81	46.39	45.06	42.05
6-3	0.65	0.65	0.66	0.67	0.68
11-8	5.03	5.04	5.05	5.08	5.02
16-13	14.19	14.16	14.11	13.95	13.34
11-7	0.57	0.57	0.57	0.57	0.57
16-12	2.98	2.98	2.99	3.02	3.03

ANALYSIS AND DISCUSSION

The influence of spin uncoupling

The use of Eq. (2) to describe the kinetic energy of the rotating molecule relies upon two assumptions. They are the neglect of spin uncoupling due to molecular rotation in considering the effects of centrifugal distortion, and the neglect of the differences in kinetic energy between the two spin sublevels in the case (a) limit. To test the validity of these assumptions for NO, we calculated transition moment integrals using the Hund's case (b) expression for rotational kinetic energy:¹⁶

$$E_{\text{rotation}} = B_r N(N+1) - \Lambda^2, \quad (9)$$

and using the exact expression for the rotational kinetic energy in the Hund's case (a) limit:²³

$$E_{\text{rotation}} = B_r(J(J+1) - \Omega^2 + S(S+1) - \Sigma^2). \quad (10)$$

Calculations of the intramultiplet transition moment integral for each of the spin components using Eq. (10) for the rotational energy gave results essentially indistinguishable from those using the simple expression given by Eq. (2) at all J , consequently, using the approximate form for the case (a) rotational energy incurs no significant error. Calculations using the Hund's case (b) expression [Eq. (9)] for rotational energy produce Einstein-coefficients for a particular J' which differed by no more than 0.7% from the corresponding coefficients computed using Eq. (2). The largest differences occur at highest J for all v' and Δv , consistent with the case (a) approximation being less appropriate in this regime. Nonetheless, for all J reported here, the use of Eq. (2) for the rotational kinetic energy also incurs negligible error.

The insensitivity of NO to the assumed angular momentum coupling scheme stems in part from the small inertial constant of NO. Only small differences in rotational angular momentum distinguish the Hund's cases for a given J . The influence of these small differences is reflected in the corresponding differences in rotational kinetic energy which are proportional to B_r . Consequently, the same differences in angular momentum have a much larger effect on the potential energy and wavefunctions of a molecule such as OH⁸ than on those of NO, whose rotational constants are an order of magnitude smaller.

The influence of L-uncoupling

In this work we have assumed that the effects of the uncoupling of electron orbital angular momentum due to molecular rotation or L-uncoupling are negligible. The issue is of concern since small components of higher lying $^2\Sigma$ and $^2\Delta$ states are introduced into the $X^2\Pi$ wavefunction via this phenomenon. These components can then contribute to the transition moment integral with the transition moments characteristic of the electronic transitions between these higher lying states and $X^2\Pi$. Since there are many potential perturbing states, it is difficult to quantify these effects. Nonetheless, they appear to be unimportant for the data presented here. This is indicated in a comparison of the Λ -doubling spectroscopic constants and splittings in NO($X^2\Pi$) with those for OH($X^2\Pi$), for which the influence of L-uncoupling on the corresponding radiative rates has been estimated.²⁴

A comparison of Λ -doubling spectroscopic constants and corresponding splittings shows quantities that are much smaller for NO than for OH.^{25,28} For example, the constants p and q are smaller respectively by factors of 20 and 400 for NO($v=0$). Furthermore, the splittings within each spin component range from 0.012 to 0.282 cm^{-1} for $J=0.5-39.5$ in NO,²⁸ compared with 0.16 to 27.30 cm^{-1} for $J=0.5-30.5$ in OH.²⁵ Extrapolation of the spectroscopic constants of Amiot²⁸ to higher J indicates splittings of only 0.7 cm^{-1} (e) and 2.4 cm^{-1} (f) for $J=139.5$, $v=0$. The admixture of higher lying electronic states in the NO($X^2\Pi$) wavefunctions is thus probably much smaller than for OH($X^2\Pi$). Extrapolation of the results of Mies²⁴ for the vibration-rotation transitions of OH suggests that L-uncoupling introduces contributions to the P- and R-branch radiative rates of 20% or less for transitions originating from $J' \leq 39.5$.¹¹ The smaller constants and splittings for NO suggest correspondingly smaller intensity perturbations due to L-uncoupling, such that the effect is probably minor.

The influence of centrifugal distortion

The influence of centrifugal distortion on the $\text{NO}(X^2\text{II})$ radiative rates is most significant in the overtone transitions and at high J . Figure 2 shows the individual R- and P-branch Einstein coefficients for the $\Delta v = 1-4$ transitions arising from $v' = 10$. These coefficients were calculated with the dipole moment function of Langhoff et al.²¹ For comparison purposes, this figure also shows coefficients calculated without the rotational energy term in Eq. (1), thus omitting the effects of centrifugal distortion. Q-branch coefficients are not included since they rapidly become very small with increasing J and only those coefficients for the intramultiplet transitions from the F_1 spin component are shown since the influence of centrifugal distortion is similar for the transitions arising from either spin component. The two sets of $\Delta v = 1$ Einstein coefficients show only small differences except for the highest J values, where the P-branch transitions are slightly more intense, and the R-branch transitions somewhat less intense, than predicted in the absence of centrifugal distortion. Even for J values exceeding 100.5, the differences are small. Larger deviations occur in the overtone transitions, where the R-branch transitions become more prominent and the P-branch transitions less prominent with increasing J and Δv than predicted in the absence of centrifugal distortion. In the $\Delta v = 2$ band, centrifugal distortion increases the R-branch intensities by 25% at J' of ≈ 80.5 , and increases the R/P ratios by $\approx 55\%$.

The trends observed for $v' = 10$ hold for the other vibrational levels as well. Centrifugal distortion exerts a weak influence on all fundamental transitions regardless of dipole moment function, but has a substantially larger influence on the overtone transitions. This is shown in Fig. 3, where the squares of the ratio of the R- and P-branch transition moments are compared as a function of J' for a series of fundamental and overtone transitions. These calculations were performed with the dipole moment function of Langhoff et al.²¹ We note that if centrifugal distortion is neglected, the R/P transition moment ratio is unity since the wavefunctions for the upper and lower states in either transition are then independent of J and are thus identical. Consequently, this figure shows the deviation of the R/P intensity ratio from that predicted in the

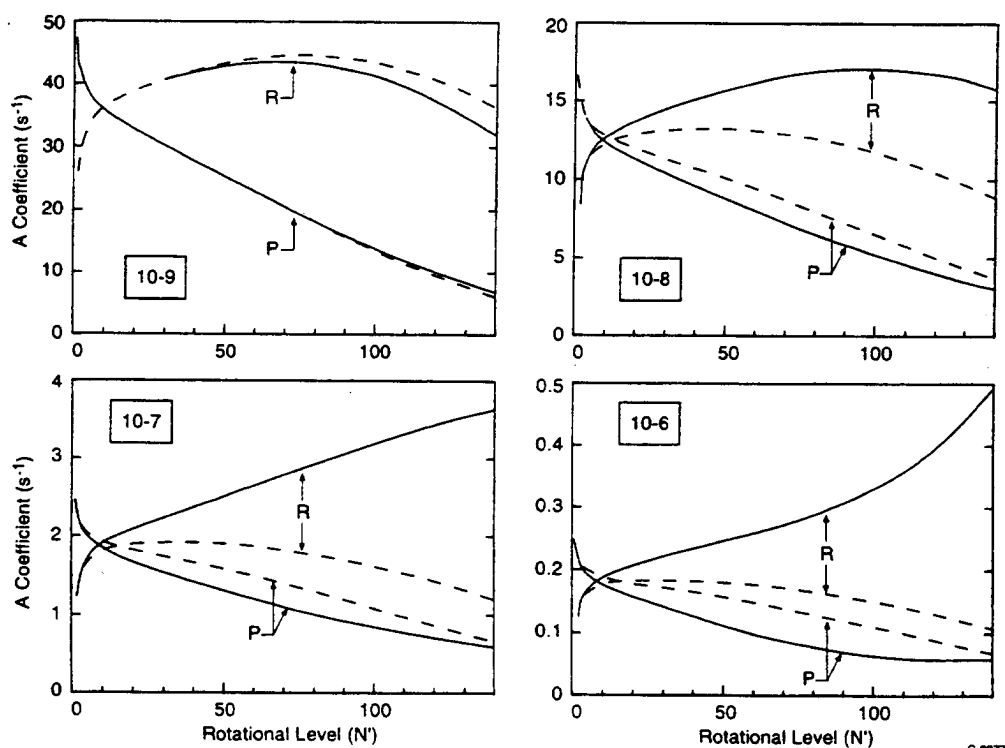


Fig. 2. Einstein coefficients for the R- and P-branch transitions from $v' = 10$ (F_1 sublevel), computed using the dipole moment function of Langhoff et al.²¹ The data in the solid curves were calculated including the effects of centrifugal distortion; the dashed curves were calculated neglecting centrifugal distortion.

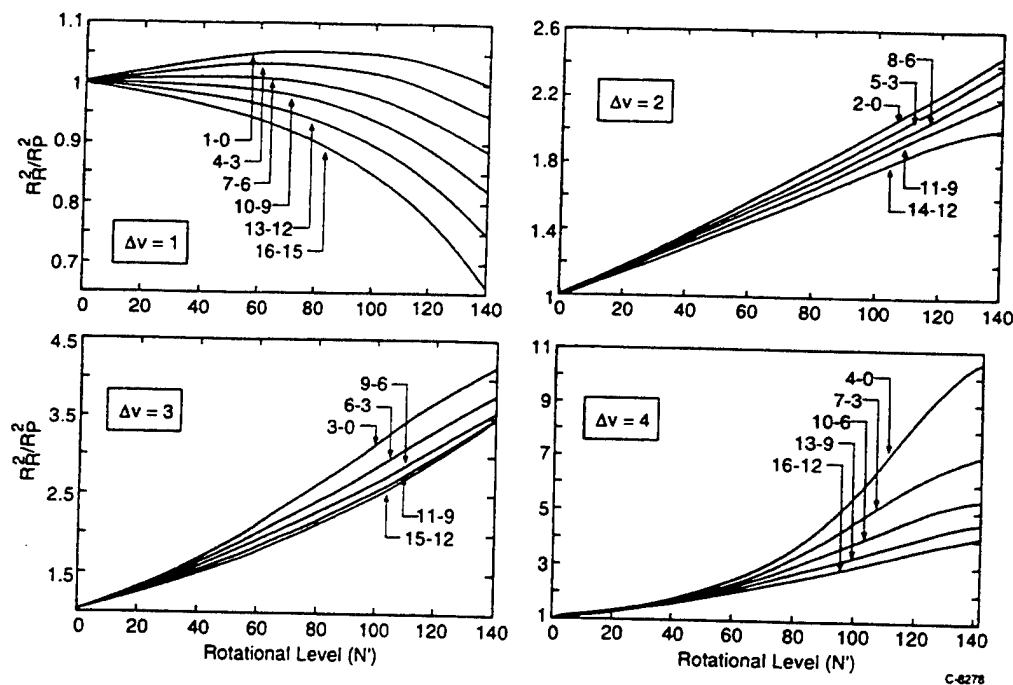


Fig. 3. The effect of centrifugal distortion on R-branch/P-branch intensity ratios of common J' . R_R and R_P are the R-branch and P-branch transition moment integrals computed with the dipole moment function of Langhoff et al.²¹

absence of centrifugal distortion, i.e., as predicted by the intermediate case line strength formulae of Hill and van Vleck.²⁰ Vertex transitions in the $\Delta v = 1$ R-branch (those forming the short wavelength edge of the band head) occur for J' near 80.5. The P- and R-branch $\Delta v = 1$ transitions from these states for $v' = 1-11$ exhibit relative intensities within $\pm 7\%$ of those given by the standard line strength formulae. In contrast, the $\Delta v = 2-4$ transitions exhibit substantial deviations (factors of 1.6–3.5 at $J' = 80.5$) from standard line strength scaling; these deviations become larger with increasing Δv .

These trends are not strongly dependent on the choice of dipole moment function for the $\Delta v = 1$ and $\Delta v = 2$ sequences. For example, the $\Delta v = 2$ R/P intensity ratios computed with the functions of Rawlins et al and de Vivie and Peyerimhoff differ by no more than 20% from those computed with the Langhoff dipole moment and the differences are smaller for the $\Delta v = 1$ sequence. Larger differences occur in the $\Delta v = 3$ and $\Delta v = 4$ sequences. The dipole moment function of de Vivie and Peyerimhoff predicts significantly higher R/P intensity ratios (approx. 25%) than do either of the other functions in the $\Delta v = 3$ sequence. The Rawlins function predicts lower R/P ratios than either of the *ab initio* functions for the $\Delta v = 4$ sequence although we note that the ratios are consistently high with the Peyerimhoff function (R/P 4.2- $v' = 4$ to 3.5- $v' = 16$, $J' = 80.5$) while the ratios span a wider range with the Langhoff dipole moment function (R/P 10.4- $v' = 4$ to 4.0- $v' = 16$, $J' = 80.5$). These results suggest that, although certainly a challenge experimentally, examination of the R/P-branch intensity ratios in high overtone spectra could be used to help establish a molecular dipole moment function in much the same manner that band-integrated intensity ratios of common v' have been used previously.⁷

The thermally averaged radiative rates for the $\text{NO}(X^2\Pi)$ transitions also reflect the influence of centrifugal distortion although the effects are more subtle. As noted above, these rates are only weakly dependent on temperature, although the character of the temperature dependence differs as a function of v' and Δv . Examples of these dependencies are shown in Table 4 where band-integrated Einstein coefficients are presented for several transitions over the temperature range from 300 to 10,000 K. In general, the integrated band intensities decrease with increasing temperature for the $\Delta v = 1$ and $\Delta v = 2$ transitions, with the decrease being more prominent in the fundamental bands and becoming progressively larger with increasing v' . For example, the 1-0

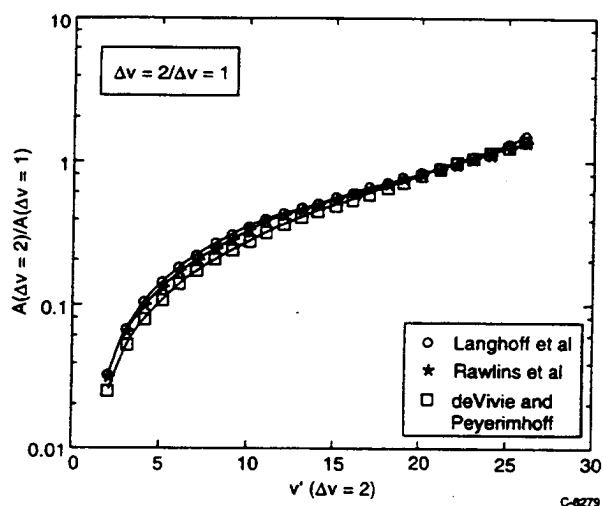


Fig. 4. $\Delta v = 2/\Delta v = 1$ branching ratios given by band-integrated A -coefficients calculated for a rotational temperature of 300 K.

Einstein coefficient decreases by 7.7% over the temperature range from 300 to 10,000 K, while the corresponding decrease for the 16–15 transition is 17.8%.

For the second and third overtones, the integrated intensities become somewhat larger with increasing temperature, however these changes with temperature become smaller and even change sign with increasing v' . The corresponding calculations neglecting centrifugal distortion show significant *decreases* in the integrated band intensity for all transitions. Consequently, the increases with temperature in the second and third overtones are a manifestation of centrifugal distortion. Decreases in the absence of centrifugal distortion range from 10 to 18% for all v' and Δv shown in Table 4 over the range from 300 to 10,000 K. These decreases arise due to the v^3 factor in Eq. (3) as the rotational intensity distribution broadens and additional emission occurs at lower frequencies. As might be expected from the trends shown in Figs. 3 to 5, the inclusion of centrifugal distortion markedly increases the intensity of the high- J R-branch transitions, thus offsetting the v^3 factor to a progressively greater extent for larger Δv .

Although significant, the influence of centrifugal distortion on the rotational intensities for NO is less prominent than for the diatomic hydrides such as OH^{10,11} or HF.²⁷ Indeed, in the rotational envelopes of several bands of these species, a range of R-branch or P-branch transitions is either extremely weak or completely absent while the corresponding opposing ΔJ transitions are

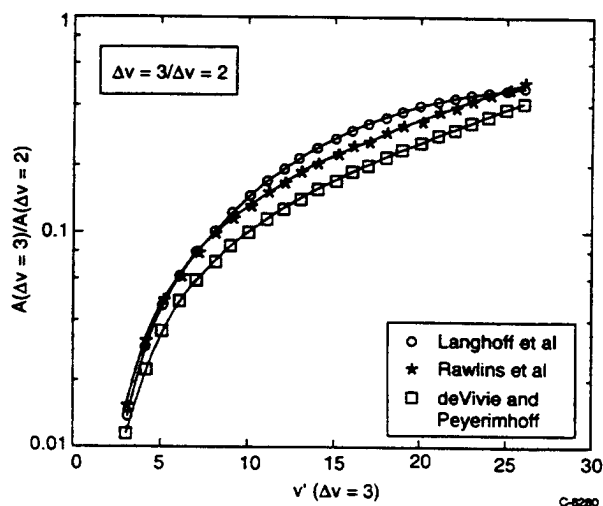


Fig. 5. $\Delta v = 3/\Delta v = 2$ branching ratios given by band-integrated A -coefficients calculated for a rotational temperature of 300 K.

unusually intense (e.g., see Fig. 2 of Ref. 11). This discrepancy is due, in part, to the smaller permanent dipole moment of NO. As noted by Herman and Wallis,²⁹ molecular rotation has the effect of mixing the vibrational wavefunctions that diagonalize the Hamiltonian in the absence of centrifugal distortion. This introduces additional contributions from the permanent dipole moment (and derivatives of the dipole moment) to the transition moment integral that would otherwise be absent. These additional contributions vary in sign and magnitude with J and ΔJ and so can produce constructive interference or cancellation within the integral. Since the permanent dipole moment is large for both OH (≈ 1.7 D) and HF (≈ 1.9 D), the interference involves substantial contributions from the permanent dipole moment introduced by molecular rotation. NO, in contrast, has a smaller permanent dipole moment (≈ -0.18 D near r_e), thus, the permanent dipole contributions to the transition moment integral are less pronounced and the resulting interference effects more subtle.

The larger moment of inertia of NO relative to OH or HF also plays a role in the diminished influence of centrifugal distortion for NO. As shown by Eqs. (1) and (2), the rotational kinetic energy, and thus the B_v rotational constant, plays a role in determining the rotating molecule potential. The wavefunctions and transition moments are thus directly influenced by the moment of inertia, and the extent to which the rotating molecule wavefunctions differ from those of the non-rotating molecule depends on B_v . In the low order perturbation theory treatment of Herman and Wallis,^{8,29} the magnitude of the component of the $v = 1$ wavefunction allowing the permanent dipole contribution in the $1-0$ transition is proportional to B_v . Since the B_v values for NO are much smaller than the corresponding B_v values for OH or HF, the vibrational wavefunction for a given J is less perturbed by molecular rotation and the corresponding intensity perturbations are less severe.

Comparison of the dipole moment functions

While the characteristic influence of centrifugal distortion does not strongly vary with dipole moment function, each function produces somewhat different Einstein coefficients. This can be seen in the thermally averaged Einstein coefficients calculated with each dipole moment function (Tables 1-3). The corresponding $\Delta v = 2/\Delta v = 1$, $\Delta v = 3/\Delta v = 2$, and $\Delta v = 4/\Delta v = 3$ branching ratios from each dipole moment function, shown in Figs. 4-6, further illustrate the differences between each of the dipole moment functions. Rawlins et al⁷ deduced their dipole moment function from the intensity ratios of individual overtone and fundamental transitions of common v' . The $\Delta v = 2/\Delta v = 1$ ratios produced by the experimentally derived function of Rawlins et al are very similar to those predicted by the dipole moment functions of Langhoff et al²¹ and differ somewhat from those of de Vivie and Peyerimhoff.²² The function of Langhoff et al predicts only slightly larger overtone/fundamental ratios, while that of de Vivie and Peyerimhoff predicts ratios which are

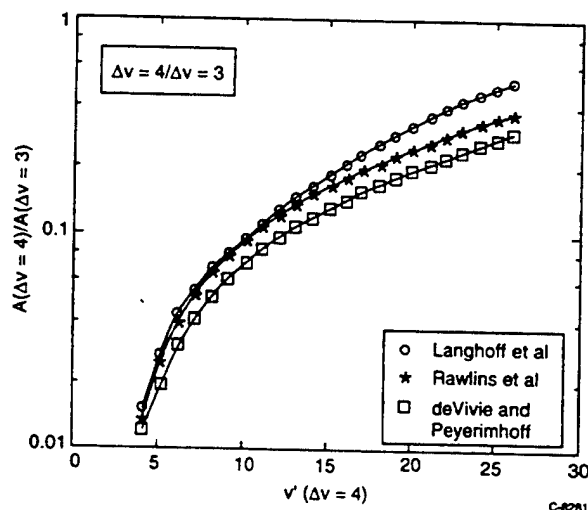


Fig. 6. $\Delta v = 4/\Delta v = 3$ branching ratios given by band-integrated A -coefficients calculated for a rotational temperature of 300 K.

smaller. We note, however, that both *ab initio* functions predict ratios within the errors of most of the data of Rawlins et al.¹³

Observation of the higher overtone transitions offers an additional opportunity for improved experimental determination of the $\text{NO}(X^2\Pi)$ dipole moment function. Figure 5 shows the $\Delta v = 3/\Delta v = 2$ ratios predicted from each of the dipole moment functions. Each function predicts ratios that differ somewhat over a significant v' range. Consequently, quantitative measurements of the second overtone branching fractions for higher v' would prove valuable in establishing the $\text{NO}(X^2\Pi)$ dipole moment function, particularly at larger internuclear separation. Measurement of the third overtone branching fractions, although very difficult due to their low intensity, would also prove useful as illustrated by the spread in the computed values in Fig. 6. We note that transitions in the $\Delta v = 3$ sequence for v' up to 22 have been observed in a d.c. discharge by Amiot¹⁷ who used the data to deduce the spectral constants employed in this work.

CONCLUSIONS

We have calculated an extensive set of rotationally resolved Einstein A -coefficients for the vibration-rotation transitions of $\text{NO}(X^2\Pi)$ for $v' = 1-26$ and $\Delta v = 1-4$. These coefficients include rotational transitions originating from J' up to 139.5. The effects of centrifugal distortion are specifically accounted for in our calculations. The influence of centrifugal distortion is far less prominent than that observed in diatomic hydrides such as OH or HF, but is nonetheless significant for higher J' overtone transitions. In the overtone transitions, centrifugal distortion manifests itself in larger R-branch intensities, and weaker P-branch intensities, than would be predicted from appropriate line strength formulae. This in turn alters the shape of the rotational envelope for high rotational excitation.

We have used the detailed J -dependent Einstein coefficients to compute thermally averaged Einstein coefficients for temperatures up to 10,000 K and find that the effect of rotational temperature on the integrated band intensities is most significant for the $\Delta v = 1$ transitions at temperatures above about 2000 K. The effects of increasing temperature are less prominent with increasing Δv although the errors incurred in neglecting centrifugal distortion are larger with increasing Δv . Einstein coefficients were calculated using three dipole moment functions. Both *ab initio* dipole moment functions are largely consistent with the experimentally derived function of Rawlins et al.¹⁷ although the function of Langhoff et al.²¹ is in better absolute agreement. However, since the experimentally derived function and that of de Vivie and Peyerimhoff require significant extrapolation to calculate the high- v high- J' radiative rates, we suggest that the function of Langhoff et al is the most reliable for this purpose currently available. Additional experimental data for higher overtones and higher v' would nonetheless serve to more accurately characterize the $\text{NO}(X^2\Pi)$ dipole moment function at larger internuclear distance.

The influence of centrifugal distortion on the radiative properties of $\text{NO}(X^2\Pi)$ has significant implications in the analysis of spectra. Detailed analysis frequently takes the form of a comparison between observed and calculated spectra reflecting a particular vibrational and rotational population distribution. The influence of centrifugal distortion on NO rotational intensity distributions is minor for the fundamental band, but can be substantial for the first and higher overtones. Consequently, the effects documented here should be included in the analysis of NO overtone spectra if a high degree of rotational excitation is present. Omission of this effect, e.g., by using only standard line strength formulae to describe the rotational intensity distributions, will result in mismatched R-branch/P-branch intensity ratios which can lead to erroneous determinations of the individual vibrational band intensities from overlapped spectra.

Acknowledgements—We are grateful for numerous technical discussions and data interchanges with J. C. Person and S. R. Langhoff. This work was supported by funding under Contracts F19628-88-C-0069 and F19628-93-C-0131 with the Geophysics Directorate of the Phillips Laboratory, in support of the Air Force Office of Scientific Research under Task 2303EP1/PL007 and the Defense Nuclear Agency under MIDR 94-511, Work Unit 00042.

REFERENCES

1. W. T. Rawlins, R. R. Foutter, and T. E. Parker, *JQSRT* **49**, 423 (1993).
2. W. T. Rawlins, T. E. Parker, R. R. Foutter, and M. G. Allen, *AIAA J.* **31**, 499 (1993).
3. W. T. Rawlins, M. E. Fraser, and S. M. Miller, *J. Phys. Chem.* **93**, 1097 (1989).
4. S. J. Lipson, P. S. Armstrong, J. A. Dodd, J. R. Lowell, W. A. M. Blumberg, and R. M. Nadile, *Geophys. Res. Lett.* **21**, 2421 (1994).
5. P. S. Armstrong, S. J. Lipson, J. A. Dodd, J. R. Lowell, W. A. M. Blumberg, and R. M. Nadile, *Geophys. Res. Lett.* **21**, 2425 (1994).
6. M. E. Fraser, W. T. Rawlins, B. D. Green, D. E. Paulsen, P. S. Armstrong, S. J. Lipson, W. A. M. Blumberg, and R. E. Murphy, Paper SA42C-7, *Proceedings of the American Geophysical Union (abstract)*, *Eos* **74**, 469 (1993).
7. W. T. Rawlins, J. C. Person, M. E. Fraser, S. M. Miller, and W. A. M. Blumberg, manuscript in preparation.
8. D. D. Nelson, Jr., A. Schiffman, D. J. Nesbitt, and D. J. Yaron, *J. Chem. Phys.* **90**, 5443 (1989).
9. D. D. Nelson, Jr., A. Schiffman, and D. J. Nesbitt, *J. Chem. Phys.* **90**, 5455 (1989).
10. D. D. Nelson, Jr., A. Schiffman, D. J. Nesbitt, J. J. Orlando, and J. B. Burkholder, *J. Chem. Phys.* **93**, 7003 (1990).
11. K. W. Holtzclaw, J. C. Person, and B. D. Green, *JQSRT* **49**, 223 (1993).
12. A. Goldman and S. C. Schmidt, *JQSRT* **15**, 127 (1975).
13. W. T. Rawlins, M. E. Fraser, S. M. Miller, and W. A. M. Blumberg, *J. Chem. Phys.* **96**, 7555 (1992).
14. J. K. Cashion, *J. Chem. Phys.* **39**, 1872 (1963); *ibid.* **41**, 3988 (1963).
15. J. W. Cooley, *Math. Comput.* **15**, 363 (1961).
16. G. Herzberg, *Spectra of Diatomic Molecules*, pp. 425-426, Van Nostrand-Reinhold, New York (1950).
17. C. Amiot, *J. Molec. Spectrosc.* **94**, 150 (1982).
18. C. Amiot and J. Verges, *J. Molec. Spectrosc.* **81**, 424 (1980).
19. R. Engleman, *Spectrosc. Lett.* **3**, 93 (1970).
20. E. Hill and J. H. van Vleck, *Phys. Rev.* **28**, 250 (1928).
21. S. R. Langhoff, C. W. Bauschlicher, Jr., and H. Partridge, *Chem. Phys. Lett.* **223**, 416 (1994).
22. R. de Vivie and S. D. Peyerimhoff, *J. Chem. Phys.* **89**, 3028 (1988).
23. H. Lefebvre-Brion and R. W. Field, *Perturbations in the Spectra of Diatomic Molecules*, p. 37, Academic Press, Orlando (1986).
24. F. H. Mies, *J. Molec. Spectrosc.* **53**, 150 (1974).
25. J. A. Coxon, *Can. J. Phys.* **58**, 933 (1980).
26. C. W. Bauschlicher, Jr. and S. R. Langhoff, *J. Chem. Phys.* **87**, 4665 (1987).
27. D. Oba, B. S. Agrawalla, and D. W. Setser, *JQSRT* **34**, 283 (1985).
28. C. Amiot, R. Bacis, and G. Guelachvili, *Can. J. Phys.* **56**, 251 (1978).
29. R. Herman and R. F. Wallis, *J. Chem. Phys.* **23**, 637 (1955).

APPENDIX 4

Rotational Relaxation of High-N States of OH ($X^2\Pi$, $v=1-3$) by O_2

Journal of Geophysical Research

(reproduced in its entirety)

Rotational relaxation of high-N states of OH ($X^2\Pi$, $v=1-3$) by O_2

K.W. Holtzclaw, B.L. Upschulte, G.E. Caledonia, J.F. Cronin, and B.D. Green

Physical Sciences Inc., Andover, Massachusetts

S.J. Lipson and W.A.M. Blumberg

Phillips Laboratory, Hanscom Air Force Base, Massachusetts

J.A. Dodd

Stewart Radiance Laboratory, Bedford, Massachusetts

Abstract. We have studied the relaxation of OH($X^2\Pi$, v , N) produced by the reaction $O(^1D) + H_2 \rightarrow OH^* + H$. Infrared emission measurements of the fundamental vibration-rotation band of OH were acquired at a temperature of 100 K in a large cryogenic chamber. Trace amounts of ozone were added to mixtures of H_2 , O_2 , and Ar at low (≤ 38 mT) pressures. The ozone was photolyzed to produce $O(^1D)$. Rapid reaction with H_2 produced OH^* . Spectrally and temporally resolved emissions from levels up to the exothermic limit were observed with sufficient spectral resolution to permit kinetic analysis of individual level populations. The production rate was observed to scale as the rotational quantum number except at the highest levels populated. At early times we observed inverted rotational state distributions that subsequently relaxed to form thermal distributions in each vibrational level. Under these conditions, rotational relaxation was rapid in comparison with vibrational relaxation. Rotational relaxation within a given vibrational state could be represented by single quantum collisional exchange at near-gas-kinetic rates. The rotational level dependence of the deduced relaxation was determined.

Introduction

Hydroxyl population distributions have been used to quantify mesospheric temperatures, reactive species concentrations [Llewellyn *et al.*, 1978], and the altitude dependence of OH concentrations [McDade, 1991]. The atmospheric kinetic temperatures are based on measurement of the OH rotational temperature inferred from OH rotational distributions. For lower rotational states, Boltzmann distributions at temperatures characteristic of the mesosphere [Turnbull and Lowe, 1983; Sivjee and Hamwey, 1987] have been observed. More recent observations, however, have demonstrated that higher rotational states are not in thermal equilibrium. Pendleton *et al.* [1989] observed rotational distributions in $v' = 7$ that were characterized by effective temperatures of 200 K for $N = 2$ to 5 but 1900 K for $N \geq 6$.

Orbital observations of long-wavelength infrared radiances from the upper atmosphere nighttime airglow [Smith *et al.*, 1992; Dodd *et al.*, 1994] display pure rotational emission from high-lying rotational-vibrational states of OH. In the airglow, rotational levels up to $N = 33$ for vibrational levels $v=0-3$ were observed, suggesting that these levels are not easily relaxed at pressures characteristic of the airglow altitude. Knowledge of the nature and magnitude of collisional relaxation processes occurring in the mesopause region (85 to 95 km) is essential to relate the observed distributions to the aeronomical production process(es).

We have investigated the nature of the relaxation mechanisms operating in highly rotationally excited OH under controlled laboratory conditions at 100 K. Several groups have studied

vibrational relaxation of OH (produced from the reaction of $H + O_3$) by atmospheric species [Knutsen *et al.*, 1996; Dodd *et al.*, 1991]. To understand OH produced with substantial rotational excitation, we chose to study rotational relaxation rates for high rotational states of OH produced in the reaction



This reaction has sufficient exothermicity to populate states up to (v,N) of (0,29), (1,26), (2,22), (3,17), and (4,10). Relaxation studies of similar molecules such as HF have provided evidence of slow relaxation rates for high rotational states of molecules with large rotational spacings. Taatjes and Leone [1988] measured rotational relaxation rate coefficients for HF($v = 0$, $J = 13$) in the 10^{-12} cm³ molecule⁻¹ s⁻¹ range for room temperature quenching by rare gas species. Because the rotational spacings are significant ($\Delta E = 550$ cm⁻¹), models for vibrational relaxation were successfully used to explain the results. We report here the observation of large rotational relaxation rates for the OH molecule with an O_2 collision partner.

Experimental Method

The experiments were performed in the LABCEDE chamber at the Phillips Laboratory Geophysics Directorate. The apparatus is shown in Figure 1. Controlled gas mixtures were introduced through a porous array to produce a plug flow inside a temperature-controlled shroud 90 cm in diameter and 270 cm long. For these experiments the shroud walls were maintained near 100 K to reduce infrared backgrounds and slow diffusion out of the reaction volume. Optical ports viewing across the plug flow permitted optical access. Ozone was photolyzed to produce $O(^1D)$ using a KrF excimer laser at 248 nm. The OH chemiluminescence was observed by an InSb

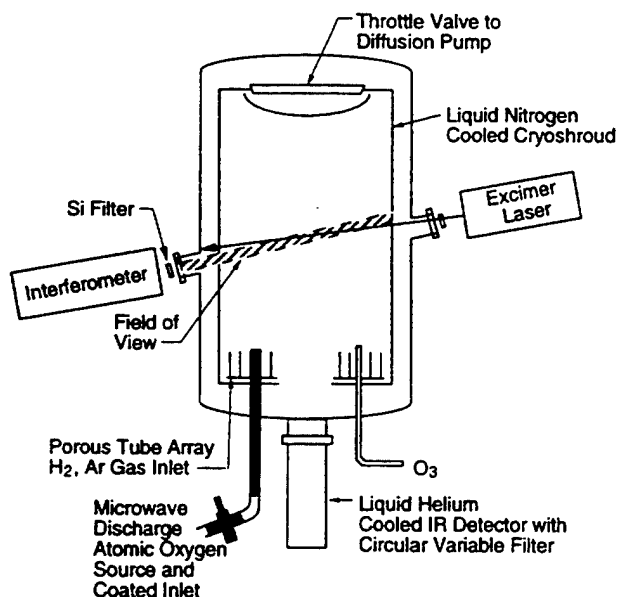


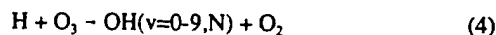
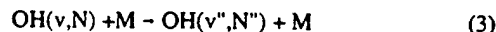
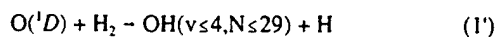
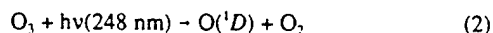
Figure 1. Cryogenic LABCEDE apparatus with excimer photolysis laser, gas inlets, ozone generator, and Michelson interferometer detection system.

detector viewing the photolysis region through a Michelson interferometer. The optical axis of the interferometer was aligned with the photolysis region to maximize signal collection. An antireflection coated Si blocking filter prevented the intense laser and plasma tube radiation from affecting the IR detector. Absorption of 248 nm radiation by O_3 was in the optically thin limit ($\sigma Nl < 0.1$); hence $O(^1D)$ was produced uniformly along the laser beam path.

Gas mixtures of Ar, H_2 , and O_2 with a trace of O_3 were used for these experiments. All stable gases were ultrahigh-purity grade. Argon was the dominant gas (27 mT), with hydrogen added at 9 mT. The Ar buffer gas inhibits diffusion, confining the $O(^1D)$ reactant and OH product to the detector field of view but not contributing significantly to the OH rotational relaxation. This procedure simplifies the kinetic interpretation of the data while improving the signal-to-noise ratio. The H_2 density was chosen to complete OH production on a timescale much faster than its relaxation. Higher concentrations of H_2 were not used so as to prevent its contributing significantly to the observed total OH relaxation. The O_2 pressure was varied between 1.3 and 2.6 mT to isolate its contribution to the relaxation rate. Except for O_3 , all gases were precooled to 100 K before entering the chamber through a porous tube array. Total pressures for these experiments were 38 mtorr with Ar the dominant gas.

Ozone was generated each day with a commercial ozonator and stored in a silica gel trap cooled to -78 °C. Ozone was introduced directly into the chamber through a room temperature Teflon inlet tube. Its concentration was monitored by UV absorption prior to entering the chamber and held constant by adjusting the O_3 trap temperature. Sufficient molecular collisions occurred between the gas inlet and the reaction zone to thermally equilibrate the O_3 at 100 K. The O_3 partial pressure at the photolysis region, < 0.3 mtorr, was far below the limiting vapor pressure of O_3 at these temperatures.

The principal reactions are



The timescales for the experiment were as follows: a laser photolysis pulse of 20 ns initiated the experiment, the $O(^1D)$ reacted to form OH in 30 μ s, and the OH relaxed rotationally over several hundred μ s. The next laser pulse occurred 59 ms later, after diffusion had replaced the gas in the photolysis volume. Reaction (4), involving the interaction of two trace species in a relatively inefficient chemical process, does not significantly impact the experimental results.

The time dependent fluorescence signal on the InSb detector from each laser pulse was recorded at 5 μ s intervals. The detection system response time was also about 5 μ s. The interferometer was scanned at 1 s per HeNe reference laser fringe. The fluorescence signals from multiple (≈ 17) laser pulses occurred between adjacent fringes of the reference laser and could be averaged. An interferogram was accumulated from the time dependent fluorescence due to sequential sets of laser pulses at 3000 different mirror positions (path differences). Each experiment lasted nearly 1 hour and contained 50,000 laser pulses. The fluorescent signal typically remained constant to better than 3% over this period. The resulting time histories as a function of mirror position were sorted to generate interferograms as a function of time and then were transformed to produce complete spectra (1850 to 7900 cm^{-1}), monitoring the reaction progress at 5 μ s intervals. This approach has been described previously for electron beam excitation [Dodd *et al.*, 1991; Green *et al.*, 1982]. For the current experiments the data acquisition is synchronized to the laser trigger pulse.

Although OH has widely separated rotational lines, many states are populated in the exothermic reaction, and the observed spectrum is quite complex. Thus the interferometer was carefully aligned prior to measurements to achieve close to its theoretical maximum spectral resolution of 6 cm^{-1} (based on scan distance and detector size). This resolution was adequate to permit most $OH(v, N)$ lines to be isolated and their time history to be measured. The data were transformed by using triangular apodization to minimize spectral ringing. At this resolution, individual P and R branch lines (as well as spin sublevels for $N \leq 6$) from each vibration and rotational level created could be resolved. Overlaps of the different transitions were significant, but the ability to use the pair of P,R branch intensity ratios dictated by Einstein coefficients [Holtzclaw *et al.*, 1993] permitted most level populations to be determined through spectral fitting.

Spectral data at several times after the laser photolysis that were acquired by this process are shown in Figures 2a-2c. In Figure 2a, taken at 30 μ s after laser pulse, the $OH(v, N)$ production by $O(^1D)$ is nearly complete. Little relaxation has occurred, and fluorescence from levels near the exothermic limit is observed. The prominent sharp features at 3760 and 3960 cm^{-1} are the $v = 2$ and $v = 1$ R branch rovibrational bandheads composed of emission from levels $N = 18$ through 22. As production stops, the highest rotational level populations begin to relax rapidly. In Figure 2b the $v = 2$ bandhead has disappeared, and rotational distribution is relaxed to lower N (shifting of the intensity of the P and R branch lines toward band center). In Figure 2c the late time spectrum at 1000 μ s is displayed. The spectrum is much simpler; only rotational levels up to $N = 4$ are observed.

To permit quantitative analysis, we employed a spectral fitting procedure. The relative population in each rovibrational level was determined by the linear solution vector that minimized the least squares difference between the computed and observed spectra. The rotational population in each vibrational level is determined by best matching its observed P and R branch intensities to the experimental

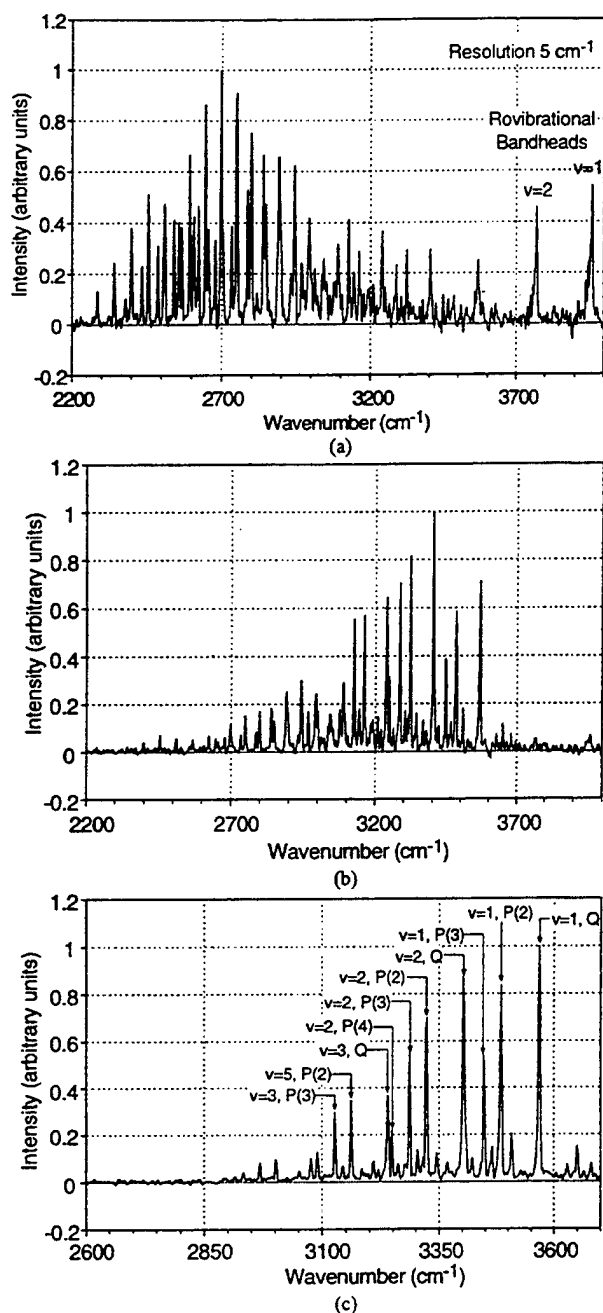


Figure 2. Spectrally resolved fluorescence from OH(v,N) transitions at various delays after the photolysis pulse (individual peaks are labeled by the upper state rotational and vibrational quantum number): (a) 30 μ s after the pulse near the end of the production period, (b) at 110 μ s while relaxation is cooling the distribution, and (c) at 1000 μ s.

data at each time interval after the photolysis pulse. The 2600 to 3200 cm^{-1} portion of an example fluorescence spectrum is shown in Figure 3 along with the synthetic spectral fit. The comparison is seen to be excellent, with the line positions accurately matching the observed features and the intensities agreeing to within a few percent. The high- N rotational P and R branch lines are widely separated; e.g., for $v=1$, $N=25$ the R branch transition occurs at 3937.9 cm^{-1} , while the corresponding P branch transition occurs at 2282.8 cm^{-1} , a 1655 cm^{-1} separation. For isolated lines, good agreement is observed, indicating accurate knowledge of the Einstein

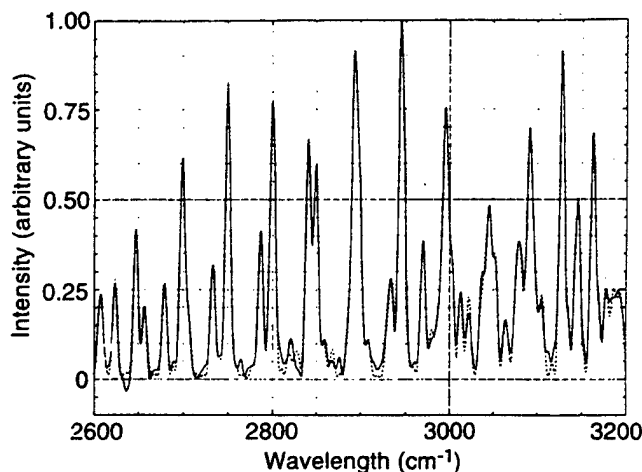


Figure 3. Comparison of observed fluorescence (solid line) with the synthetic spectral fit (dashed line).

coefficients [Holtzclaw *et al.*, 1993] and the detection system response function. The time dependence of these population histories deduced from these fits provides the basis for the kinetic analysis provided in the next section.

Data Analysis

For purposes of discussion we will consider a data set taken at conditions of 38 mtorr and a nominal temperature of 100 K. The relative species concentrations were Ar, $2.5 \times 10^{15} \text{ cm}^{-3}$; H_2 , $8 \times 10^{14} \text{ cm}^{-3}$; O_2 , $2.5 \times 10^{14} \text{ cm}^{-3}$; and O_3 , $< 3 \times 10^{13} \text{ cm}^{-3}$.

From the fitting procedure described in the previous section, rotational population relaxation histories for $v=1$ to 4 were determined (the data are relatively noisy for $v=4$). In other data sets the Ar concentration was reduced by a factor of 2 with no significant change in the relaxation behavior. Although the H_2 concentration was not changed, we found that the observed relaxation times increased by a factor of 2 when the O_2 concentration was reduced by a factor of 2. We concluded then that oxygen molecules provide the dominant source of collisional relaxation in this gas mix. On the basis of these observations we conclude that rotational relaxation by H_2 is at least an order of magnitude less efficient than that by O_2 .

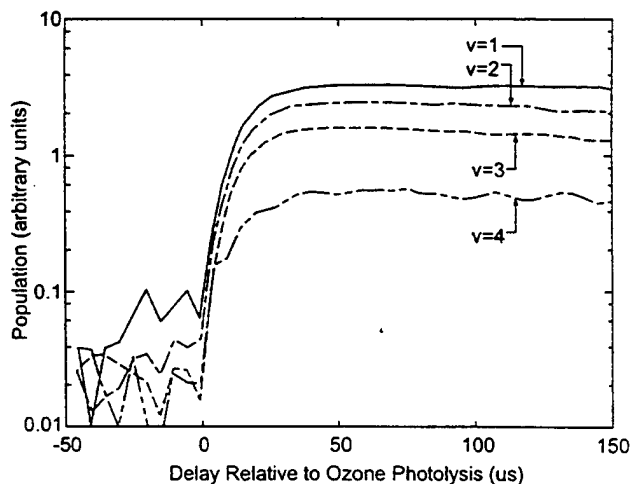


Figure 4. Deduced OH vibrational populations versus time $N_{O_2} = 2.5 \times 10^{14} \text{ cm}^{-3}$, $N_{H_2} = 8 \times 10^{14} \text{ cm}^{-3}$, and $N_{Ar} = 2.5 \times 10^{15} \text{ cm}^{-3}$.

Table 1. Relative Populations of OH(v)

Vibrational Level	Relative Population					
	Present Work	Butler et al. [1983]	Huang et al. [1986]	Aker and Sloan [1986]	Kuntz et al. [1991]	Berg et al. [1991]
1	1	1	1	1	1	1
2	0.75 ± 0.04	1.11 ± 0.19	0.92 ± 0.06	1.10 ± 0.20	0.63	0.67
3	0.48 ± 0.03	1.08 ± 0.19	0.87 ± 0.14	0.86 ± 0.20	0.35	0.42
4	0.16 ± 0.01	0.62 ± 0.19	< 0.77	0.45 ± 0.20	0.17	0.19

Argon-induced rotational relaxation is at least 2 orders of magnitude less efficient than relaxation by O_2 .

The observed vibrational population history, i.e., summed over all rotational levels, is shown in Figure 4. As can be seen, the populations rise after O_3 photolysis, reflecting OH(v) production via reaction (1). The vibrational populations flatten out as the $O(^1D)$ is depleted through reaction (1). The characteristic e -fold rise time observed is $\sim 12 \mu s$, corresponding to a rate constant for reaction (1) of $1.1 \times 10^{-10} \text{ cm}^3 \text{ s}^{-1}$. This value is in reasonable agreement with the recommended value $1.2 \times 10^{-10} \text{ cm}^3 \text{ s}^{-1}$ from earlier measurements made at temperatures of 200 K and above; see the review of Atkinson et al. [1992].

Note from Figure 4 that no significant vibrational relaxation is observed in the first 150 μs after O_3 photolysis. As will be shown, rotational relaxation is largely complete on that timescale. Thus vibrational and rotational relaxation can be treated separately. Indeed, vibrational relaxation under these conditions is found to be quite slow with a characteristic time of $\geq 600 \mu s$. This observation is not surprising given earlier measurements, e.g., those of Dodd et al. [1991] among others, of OH vibrational relaxation by O_2 , which show that the characteristic relaxation time for vibrational levels of OH ($v \leq 4$) would exceed 1000 μs under our experimental conditions. Since excited state diffusion out of the field of view is also important on this timescale (τ_D is estimated to be 900 μs), we were not able to evaluate the vibrational level dependent relaxation rate constants.

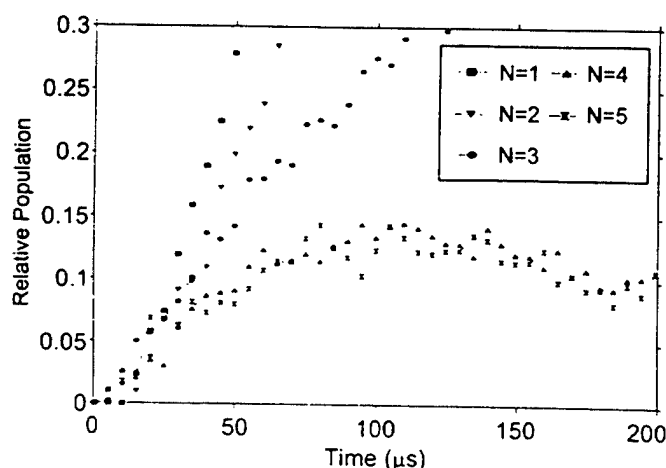
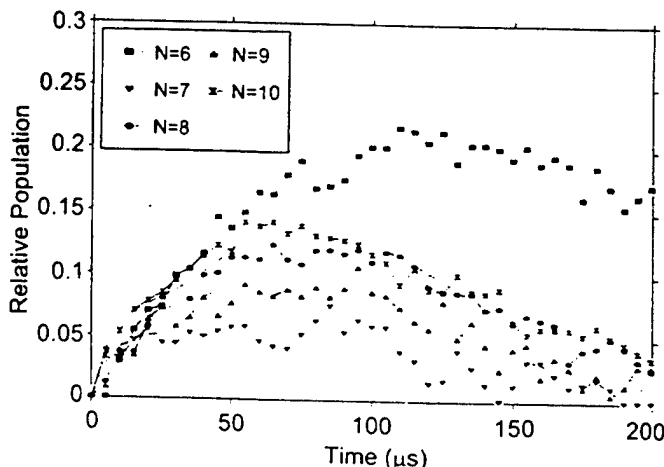
One additional interesting feature in Figure 4 is the relative vibrational populations. Since vibrational relaxation is unimportant on this timescale, these populations directly reflect the relative production efficiencies of reaction (1) for OH formation in specific vibrational levels. These relative production efficiencies are listed in Table 1. The listed values are the average of four sets of measurements, all at 100 K (two sets for $v=3,4$), but with varying

total pressures and mixture ratios. The standard deviations shown are statistical. We estimate that systematic errors should introduce an additional uncertainty of less than 15%.

The database on reaction efficiencies for reaction (1) was recently reviewed by Mikulecky and Gericke [1992]. Other infrared chemiluminescence measurements [Butler et al., 1983; Huang et al., 1986; Aker and Sloan, 1986] of the reaction efficiencies performed at room temperature are also shown in Table 1. Note that our measurements, which were performed at 100 K, exhibit noticeably less vibrational excitation than these earlier data. There is still some uncertainty in this database, since several laser-induced fluorescence studies on adjacent vibrational levels show population ratios different from those observed in these earlier infrared measurements reported above [see Mikulecky and Gericke, 1992]. Furthermore, recent theoretical evaluations for 300 K [Kuntz et al., 1991; Berg et al., 1991] shown in Table 1 are more in accord with our observations than with these earlier studies.

We now address the rotational relaxation of the OH($X^2\Pi$) state. An example set of rotational population histories for $v=1$, $N=1$ to 25, arbitrarily normalized, is shown in Figures 5 to 9. Data of similar quality pertain for $v=2,3$. Only a few rotational levels are available at $v=4$, and the signal to noise ratio of these data is too low to permit rotational relaxation analysis for this level.

It can be seen from the early time behavior of these data that the highest rotational levels are populated largely by reaction (1), reaching a peak density when the $O(^1D)$ state is consumed, and then relaxing thereafter. The lowest levels, on the other hand, reach peak concentrations at longer times and are populated dominantly by relaxation from the higher states. This observation is borne out in Figure 10, which contrasts the time history of the sum of the populations for $N=7$ to 27 with that for the lower levels $N=1$ to 6. An important point to note is that the total rotational population

Figure 5. Deduced rotational population histories $v=1$, $N=1-5$.Figure 6. Deduced rotational population histories $v=1$, $N=6-10$. Dashed lines are model comparisons for $N=8-10$.

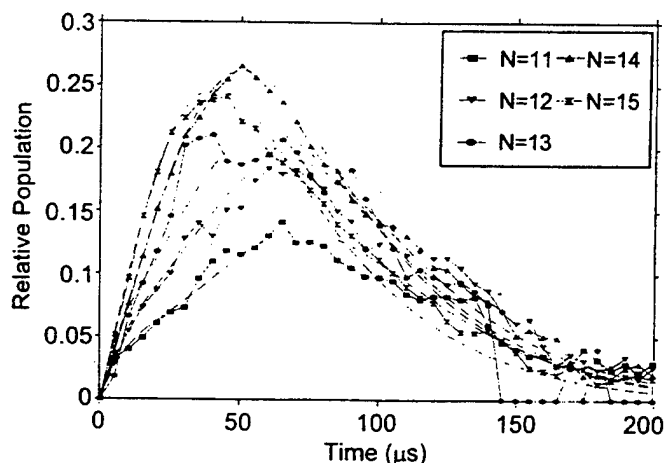


Figure 7. Deduced rotational population histories $v = 1$, $N=11-15$. Dashed lines are model comparisons.

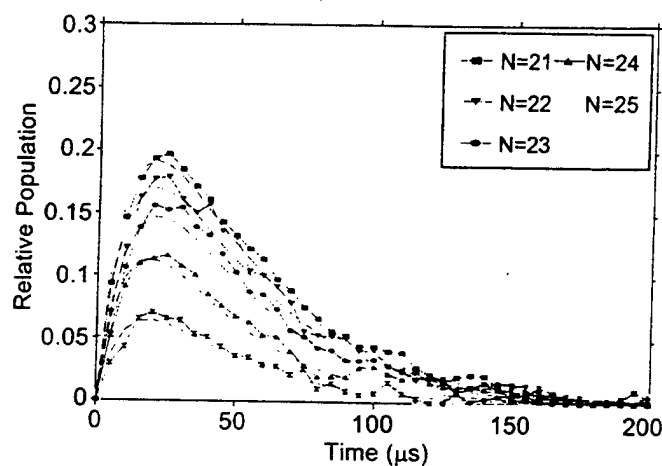


Figure 9. Deduced rotational population histories $v = 1$, $N=21-25$. Dashed lines are model comparisons.

decreases by less than 10% as the distribution relaxes from high to low rotational levels; for example, in Figure 10 it can be seen that the sum of the populations at, say, a time of 50 μs is nearly the same as that at 150 μs . The same is true for all three vibrational levels analyzed, a strong suggestion that the observed rotational relaxation occurs in the absence of vibrational exchange.

Last, at longer times, we found that the population of the lowest levels corresponds to that of a Boltzmann distribution with a rotational temperature of 100 K, consistent with the translational temperature of the experiment. Thus we conclude that the observed rotational relaxation is consistent with a rotational cascade from high levels to low levels. We have analyzed the data assuming single-quantum transitions. The corresponding master equations are, for each vibrational level,

$$\begin{aligned} d[\text{OH}(N)]dt = & k_p(N) [\text{O}(^1D)] [\text{H}_2] + k_r(N+1) \\ & \cdot [\text{OH}(N+1)] [\text{O}_2] - k_r(N) \cdot [\text{OH}(N)] [\text{O}_2] \\ & + k_r(N) [\text{OH}(N-1)] [\text{O}_2] e^{-\Delta E_{N,N-1}/kT} \\ & - k_r(N+1) [\text{OH}(N)] [\text{O}_2] e^{-\Delta E_{N+1,N}/kT} \end{aligned} \quad (5)$$

where $\text{OH}(N)$ is the population of rotational level N , $k_p(N)$ is

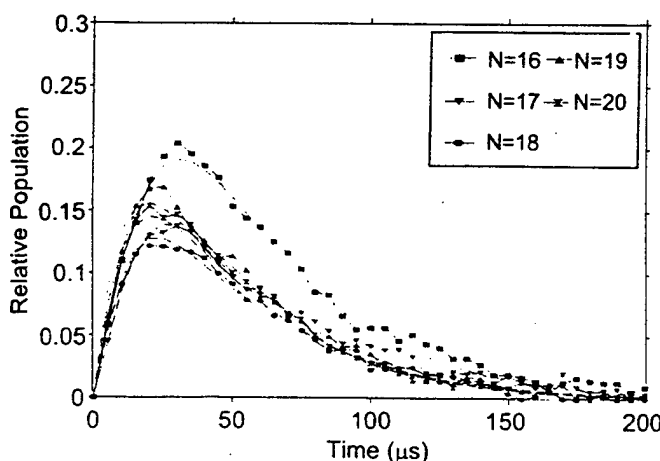


Figure 8. Deduced rotational population histories $v = 1$, $N=16-20$. Dashed lines are model comparisons.

the production rate constant for reaction (1) into level N , $k_r(N)$ is the rotational relaxation rate constant from level N to $N-1$, the bracketed quantities represent the densities of the respective chemical species, and $\Delta E_{N,N-1}$ represents the energy difference between states N and $N-1$. Note the rotational detailed balancing terms, e.g., $N-N+1$, have been included in (5), although these terms are only important at the lowest rotational levels considered.

$\text{O}(^1D)$ is being consumed in reaction (1) and is thus not constant in (5). The defining relationship for $\text{O}(^1D)$ is

$$d[\text{O}(^1D)]/dt = -k_1[\text{O}(^1D)] [\text{H}_2] \quad (6)$$

which has the solution

$$[\text{O}(^1D)] = [\text{O}(^1D)_0] e^{-k_1 \text{H}_2 t} \quad (7)$$

The quantity $k_1 \text{H}_2$ is the inverse of the characteristic reaction time observed in the data, Figure 4, of 12 μs , thus $k_1 \text{H}_2 = 8.3 \times 10^4 \text{ s}^{-1}$. The expression for $\text{O}(^1D)$, equation (7), can be substituted into (5), which can be integrated, resulting in the relationship

$$\begin{aligned} [\text{OH}(N, t_f)] - [\text{OH}(N, t_i)] = & -b_N [e^{-8.3 \times 10^4 t_f} - e^{-8.3 \times 10^4 t_i}] \\ & + k_r(N+1) \int_{t_i}^{t_f} [\text{OH}(N+1)] [\text{O}_2] dt \\ & - k_r(N) \int_{t_i}^{t_f} [\text{OH}(N)] [\text{O}_2] dt \\ & + k_r(N) \int_{t_i}^{t_f} \text{OH}(N-1) [\text{O}_2] e^{-\Delta E_{N,N-1}/kT} dt \\ & - k_r(N+1) \int_{t_i}^{t_f} [\text{OH}(N)] [\text{O}_2] e^{-\Delta E_{N+1,N}/kT} dt \end{aligned} \quad (8)$$

where

$$b_N = \frac{[\text{O}(^1D)] [\text{H}_2] k_p(N)}{8.3 \times 10^4} \quad (9)$$

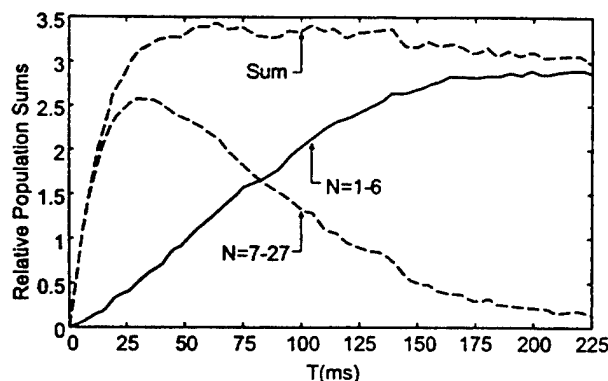


Figure 10. Relative partial rotational populations versus time for vibrational level 1. Conditions of Figure 4.

Now the individual relative rotational populations and their integrals are known from the data for all times t_i . The unknowns in (8) are the quantities $k_r(N)$, b_N . As will be shown below, these parameters can be evaluated directly from the data.

There are $2m$ unknowns with m defining equations, where m is the total number of rotational levels analyzed. Rather than employ a linear regression analysis, we have used a simple algorithm to interpret the data in terms of these unknown quantities. Specifically, the quantities $k_r(N)$, b_N have different regions of dominance in the time domain. With the exception of the lowest levels the quantity b_N dominates at early times, where chemical production is important. Therefore we evaluated (8) over the time domain $t = 0$ to $30 \mu s$, about twice the reaction time for reaction (1), to develop a relationship between b_N and $k_r(N)$. Equation (8) was then evaluated between approximately 30 and $150 \mu s$, where relaxation dominates, with the former relationship substituted in to eliminate b_N . The resulting values of $k_r(N)$ were then substituted into the early time relationship to deduce b_N .

This algorithm obviously breaks down at the lowest levels whose whole time history is dominated by rotational relaxation. Given the accuracy of the data, it would be difficult to deduce values for b_N at these levels in any case. Coincidentally, as we analyzed the data, we noted that the population of level $N = 6$ was anomalous. Although its temporal behavior is appropriate, its population is larger than that of both levels $N = 7$ and $N = 5$, a behavior difficult to rationalize in terms of our cascade relaxation assumption. The kinetic analysis breakdown at (v, N) levels (1,6) and (2,5) appears to be due to severe spectral overlaps. As a result we performed our analysis only for $N = 7$ and higher.

The same analytical procedure was applied to the data for levels $v = 2, 3$, again excluding the lowest levels from the analysis. The deduced rotational relaxation rate constants for these three vibra-

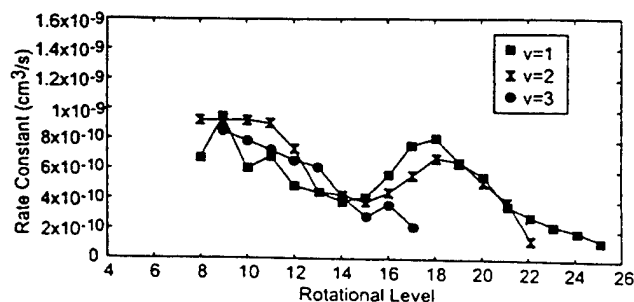


Figure 11. Deduced rate constants for rotational relaxation by oxygen molecules. Conditions of Figure 4.

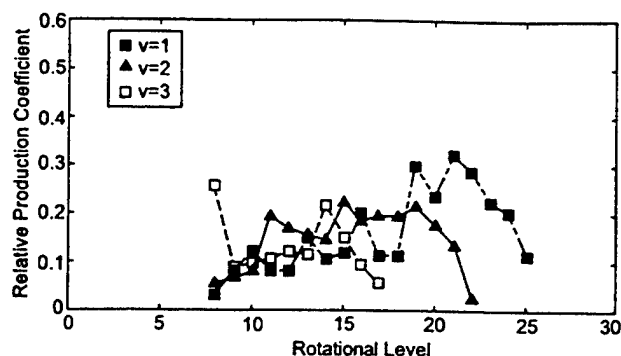


Figure 12. Relative excitation rates for reaction (1) conditions of Figure 4.

tional levels are shown in Figure 11. The relative production efficiencies for reaction (1), e.g., the b_N , are shown in Figure 12. Before discussing these results we must test the validity of the single quantum cascade relaxation model. This is done by solving (5) from time zero, using the deduced values of b_N , $k_r(N)$. These solutions are shown in Figures 6 to 8, in comparison with the data. As can be seen, although there are some variations between data and model, the comparison is generally quite good, demonstrating that a single quantum relaxation model is sufficient to explain the temporal behavior of the observations.

We have performed this analysis on four sets of data taken under similar conditions but on different days. The results of this analysis are also shown in Figure 13 for $v = 1$, and it can be seen that the data sets are in very good agreement. The average value and standard deviations of the deduced relaxation rate constants for $v = 1$ to 3 are summarized in Table 2.

The rate constants exhibit two interesting features. First, the relaxation rate constants are of gas kinetic order. Rotational relaxation from these vibrational levels is apparently very efficient. We know of no other measurements to directly compare these results to. An observation [Copeland and Crosley, 1984] at low N for other collision partners suggests that rotational relaxation is relatively efficient, however. Sears *et al.* [1989] did study OD ($N=40$) relaxation in a mix of H_2 and O_2 and deduced an efficient relaxation rate constant of $7 \times 10^{-11} \text{ cm}^3 \text{ s}^{-1}$.

More interesting is the rotational level dependence observed in the rate constants. These rate constants initially decrease with increasing N , not unexpectedly, given the increasing amount of rotational energy involved in the deactivation process. However, an unexpected change in the rate constant distribution appears around $N = 14$ (for $v = 1$), with a subsequent increase in rate constant peaking at about $N = 18$ before falling again. As can be seen in

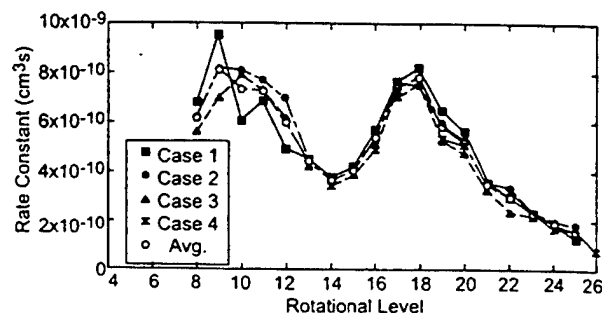


Figure 13. Deduced rate constants for rotational relaxation at oxygen molecules for OH vibrational level 1. Four data sets.

Table 2. Relaxation Rate Constants OH(v,N) + O₂ → OH(v,N-1) + O₂

N	k(N,v=1) × 10 ¹⁰ , cm ³ s ⁻¹	k(N,v=2) × 10 ¹⁰ , cm ³ s ⁻¹	k(N,v=3) × 10 ¹⁰ , cm ³ s ⁻¹
8	6.2 ± 0.6	7.2 ± 1.6	
9	8.2 ± 1.3	7.5 ± 1.4	7.6 ± 1.1
10	7.4 ± 1.1	7.9 ± 1.2	7.2 ± 0.8
11	7.3 ± 0.4	8.3 ± 1.0	6.8 ± 0.4
12	6.0 ± 1.0	6.5 ± 0.7	6.3 ± 0.4
13	4.4 ± 0.2	4.3 ± 0.5	5.1 ± 0.8
14	3.7 ± 0.2	4.0 ± 0.4	3.5 ± 0.6
15	4.1 ± 0.2	3.5 ± 0.3	2.7 ± 0.3
16	5.4 ± 0.4	4.1 ± 0.3	3.2 ± 0.5
17	7.5 ± 0.3	5.1 ± 0.5	2.0 ± 0.3
18	7.9 ± 0.4	6.1 ± 0.6	
19	5.8 ± 0.6	5.8 ± 0.6	
20	5.2 ± 0.4	4.8 ± 0.3	
21	3.5 ± 0.1	3.7 ± 0.8	
22	3.0 ± 0.4	1.9 ± 1.6	
23	2.3 ± 0.1		
24	1.9 ± 0.2		
25	1.6 ± 0.3		

Figure 11, vibrational levels v = 2 and possibly 3 exhibit a similar behavior.

The "bottleneck" in the relaxation of the rotational distribution is shown in Figure 14, which presents snapshots of the rotational population at five times. Note the buildup in the population around N = 14 with increasing time, even after OH(v,N) production by reaction (1) ceases. (The previously mentioned anomaly in the population of N=6 can also be seen in this figure.)

A single bottleneck in the relaxation of a rotational distribution has been observed previously, for example, in CN created highly excited through chemical reaction [Hay *et al.*, 1985]. Here an initially highly excited rotational distribution is observed to relax via a bimodal distribution of high and low rotational states. Presumably, this relaxation reflects the slow relaxation of the higher levels (large energy gap) in contrast with the more rapid relaxation of the lowest rotational levels.

Polanyi and Woodall [1972] provided a detailed discussion of the systematics of rotational relaxation in their analysis of observed bimodal rotational distributions in HCl created highly excited through chemical production. In that work they explored the possibility of multiple quantum relaxation and discussed the relaxation of double-peaked nascent rotation distributions. In the present work, as seen in Figure 14, we observe that a single-peaked nascent distribution collisionally relaxes at intermediate times to a distribution characterized by a double peak at high N and a thermalized distribution.

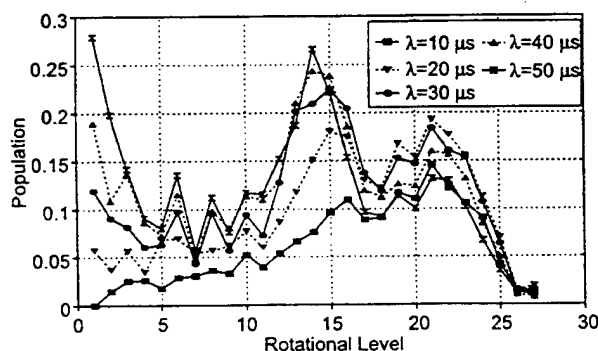


Figure 14. Deduced rotational population distribution for v=1 at five times.

While we find that the single quantum relaxation model agrees very well with the data, we cannot exclude a possible contribution from multiple quantum transitions. Our procedure was to deduce the rate constants individually from the experimental data without assuming any form of N dependence. The introduction of multiple quantum transitions introduces too many unknowns to make this approach tenable.

It can be seen that the relative production efficiencies shown in Figure 12 for v = 1 to 3 of the data set quantity have greater scatter than the relaxation rate constants. This discrepancy is the result of at least two effects: (1) The data were taken in 5 μs intervals, and thus the data must be extrapolated to time zero. Any uncertainty here, while unimportant in evaluating rotational relaxation, can be critical in evaluating the excitation rate. (2) The lower rotational levels are increasingly dominated by feed from above, rather than direct excitation, thus making deduction of the excitation rate more difficult.

The general trend in the excitation data is similar to that reported by others [e.g., Mikulecky and Gericke, 1992; Smith and Butler, 1980; Butler *et al.*, 1986; Cleveland *et al.*, 1987] for this range of rotational levels. The excitation rate is found to increase approximately linearly with increasing rotational level and then fall off at total internal energies near the reaction exoergicity.

Conclusions

Highly rotationally and vibrationally excited OH produced by the photolytically initiated O(¹D) + H₂ reaction has been observed under low-pressure conditions with sufficient spectral and temporal resolution to permit relaxation processes to be observed. The dominant mechanism is consistent with pure single quantum rotational relaxation within each vibrational manifold. The rate constants for OH (X²Π, v=1-3,N) rotational relaxation by O₂ are approximately gas kinetic. An unexpected bottleneck is observed in the rate constants around N=14. Similar relaxation by H₂ and Ar is at least an order of magnitude and 2 orders of magnitude less efficient, respectively.

These rate coefficients suggest that rotational relaxation of high rotational levels of OH produced in the airglow layer will compete with radiative decay of these levels. Assuming an oxygen density of 1.5 × 10¹³ cm⁻³ at 90 km, we find rotational collisional quenching rates of about 4500 s⁻¹, an order of magnitude larger than the pure rotational radiative decay rates. In light of the recent observations

of hot rotational distributions in the airglow layer, and the fast relaxation of these populations, the production rate for the rotationally excited component may be larger than was previously estimated. Future work will examine the relaxation of these populations by the other significant atmospheric quenchers N_2 and O.

Acknowledgments. The authors acknowledge useful discussions with William Marinelli and Karen Carleton of Physical Sciences Inc. This effort was supported by the Air Force Office of Scientific Research under task 2303EP1/PL007.

The Editor thanks J.P. Doering and E.J. Llewellyn for their assistance in evaluating this paper.

References

- Aker, P.M., and J.J. Sloan, The initial product vibrational energy distribution in the reaction between $O(^1D)$ and H_2 , *J. Chem. Phys.*, **85**, 1412, 1986.
- Atkinson, R., D.L. Baulch, R.F. Cox, J.R. Hampson, and J. Troe, Evaluated kinetic and photochemical data for atmospheric chemistry, *J. Phys. Chem. Ref. Data*, **21**, suppl. IV, 1125, 1992.
- Berg, P.A., J.J. Sloan, and P.J. Kuntz, The effect of reagent excitation on the dynamics of the reaction $O(^1D_2) + H_2 \rightarrow OH(x^2\Pi) + H$, *J. Chem. Phys.*, **95**, 8038, 1991.
- Butler, J.E., R.G. MacDonald, D.J. Donaldson, and J.J. Sloan, Vibrational excitation of OH ($x^2\Pi$) produced in the reaction of $O(^1D)$ with H_2 , *Chem. Phys. Lett.*, **95**, 193, 1983.
- Butler, J.E., G.M. Jursich, J.A. Watson, and J.R. Wiesenfeld, Reaction dynamics of $O(^1D_2) + H_2$, HD, D_2 : OH, OD($x^2\Pi$) product internal energy distributions, *J. Chem. Phys.*, **84**, 5365, 1986.
- Cleveland, C.B., C.M. Jursich, M. Troler, and J.R. Wiesenfeld, Dynamics of the reaction $O(^1D_2) + H_2 \rightarrow OH(x^2\Pi, v''=2,3) + H$: Full characteristics of the product energetics, *J. Chem. Phys.*, **86**, 3253, 1987.
- Copeland, R.A., and D.R. Crosley, Λ - doublet transfer and propensities in collisions of OH($x^2\Pi$, $v=2$) with H_2O , *J. Chem. Phys.*, **81**, 6400, 1984.
- Dodd, J.A., S.J. Lipson, and W.A.M. Blumberg, Formation and vibrational relaxation of OH($X^2\Pi$, v) by O_2 and CO_2 , *J. Chem. Phys.*, **95**, 5752, 1991.
- Dodd, J.A., S.J. Lipson, J.R. Lowell, P.S. Armstrong, W.A.M. Blumberg, R.M. Nadile, S.M. Adler-Golden, W.J. Marinelli, K.W. Holtzclaw, and B.D. Green, Analysis of hydroxyl earthlimb airglow emissions: Kinetic model for state-to-state dynamics of OH(v,N), *J. Geophys. Res.*, **99**, 3559, 1994.
- Green, B.D., G.E. Caledonia, R.E. Murphy, and F.X. Robert, The vibrational relaxation of NO($v=1-7$) by O_2 , *J. Chem. Phys.*, **76**, 2441, 1982.
- Hay, S., F. Shokoohi, S. Callister, and C. Wittig, Collisional metastability of high rotational states of CN($x^2\Sigma^+$, $v''=0$), *Chem. Phys. Lett.*, **118**, 6, 1985.
- Holtzclaw, K.W., J.C. Person, and B.D. Green, Einstein coefficients for emission from high rotational states of the OH($X^2\Pi$) radical, *J. Quant. Spectrosc. Radiat. Transfer*, **49**, 223, 1993.
- Huang, V., Y. Gu, C. Liu, X. Yang, and Y. Tao, The nascent product vibrational energy distribution of the reaction $O(^1D) + H_2$ by the grating selection technique, *Chem. Phys. Lett.*, **127**, 432, 1986.
- Knutsen, K., M.J. Dyer, and R.A. Copeland, Collisional removal of OH($x^2\Pi$, $v=7$) by N_2 , CO_2 and N_2O , *J. Chem. Phys.*, **104**, 5798, 1996.
- Kuntz, P.J., B.J. Niefer, and J.J. Sloan, A multisurface classical trajectory study of the dynamics of the reaction $O(^1D_2) + H_2 \rightarrow OH(v, J, T, \theta) + H$ using the diatomics-in-molecules method, *Chem. Phys.*, **151**, 77, 1991.
- Llewellyn, E.J., B.H. Long, and B.H. Solheim, The quenching of OH* in the atmosphere, *Planet. Space Sci.*, **26**, 525, 1978.
- McDade, I.C., The altitude dependence of the OH($X^2\Pi$) vibrational distribution in the nightglow: Some model expectations, *Planet. Space Sci.*, **39**, 1049, 1991.
- Mikulecky, K., and K.H. Gericke, The influence of vibrational and translational motion on the reaction dynamics of $O(^1D) + H_2(^1\Sigma_g^+, v)$, *J. Chem. Phys.*, **96**, 7490, 1992.
- Pendleton, W., P. Espy, D. Baker, A. Steed, M. Fetrow, and K. Henricksen, Observation of OH Meinel (7,4) P($N''=13$) transitions in the night airglow, *J. Geophys. Res.*, **94**, 505, 1989.
- Polanyi, J.C., and K.B. Woodall, Mechanism of rotational relaxation, *J. Chem. Phys.*, **56**, 1563, 1972.
- Sears, T.J., G.E. Hall, and J.J.F. McAndrew, Rotational populations in OD formed in the reaction $O(^1D) + D_2$ investigated by infrared rotational absorption spectroscopy, *J. Chem. Phys.*, **91**, 5201, 1989.
- Sivjee, G.G., and R.M. Hamway, Temperature and chemistry of the polar mesopause OH, *J. Geophys. Res.*, **92**, 4663, 1987.
- Smith, D.R., W.A.M. Blumberg, R.M. Nadile, S.J. Lipson, E.R. Huppi, N.B. Wheeler, and J.A. Dodd, Observation of high-N hydroxyl pure rotational lines in atmospheric emission spectra by the CIRRIS 1A space shuttle experiment, *Geophys. Res. Lett.*, **19**, 593, 1992.
- Smith, G.K., and J.E. Butler, OH($X^2\Pi$) product internal energy distribution formed in the reaction of $O(^1D_2)$ with H_2 , *J. Chem. Phys.*, **73**, 2243, 1980.
- Taatjes, C.A., and S.R. Leone, Laser double-resonance measurements of rotational relaxation rates of HF($J=13$) with rare gases, H_2 , and D_2 , *J. Chem. Phys.*, **89**, 302, 1988.
- Turnbull, D.N., and R.P. Lowe, Vibrational population distribution in the hydroxyl night airglow, *Can. J. Phys.*, **61**, 244, 1983.

W.A.M. Blumberg and S.J. Lipson, Phillips Laboratory, Hanscom Air Force Base, MA 01731. (e-mail: blumberg@plh.af.mil)

G.E. Caledonia (corresponding author), J.F. Cronin, B.D. Green, K.W. Holtzclaw, and B.L. Upschulte, Physical Sciences Inc., 20 New England Business Center, Andover, MA 01810. (e-mail: caledonia@psicorp.com)

J.A. Dodd, Stewart Radiance Laboratory, Bedford, MA 01730. (e-mail: dodd@plh.af.mil)

(Received July 1, 1996; revised November 18, 1996; accepted November 18, 1996.)

APPENDIX 5

Products of the Reaction of 8 km/s N(⁴S) and O₂

Journal of Geophysical Research

(reproduced in its entirety)

Products of the reaction of 8 km/s N(⁴S) and O₂

G. E. Caledonia, R. H. Krech, and D. B. Oakes

Physical Sciences Inc., Andover Massachusetts

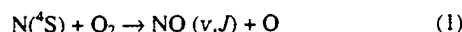
S. J. Lipson and W. A. M. Blumberg

Space Vehicles Directorate, Air Force Research Laboratory, Hanscom Air Force Base, Bedford, Massachusetts

Abstract. Reactions involving fast nitrogen atoms are of importance both in the upper atmosphere and in defining the near-field environment around orbiting spacecraft. We present the first quantitative study of the distribution of vibrationally excited ground state NO produced in the reaction of 8 km/s N atoms with O₂. A pulsed beam of energetic nitrogen atoms was interacted with thermal oxygen molecules under single-collision conditions in a crossed beam configuration. The fundamental and first overtone band emissions of the reaction product NO (X²Π) were measured using both band-pass-filtered radiometers and a circular variable filter. The spectrally resolved emissions were analyzed to determine the nascent NO vibrational distribution and the vibrational state-specific reaction cross sections. The present results are compared with earlier measurements performed at thermal energies and contrasted with theoretical predictions.

1. Introduction

We present the first experimental study of the reaction between ground state nitrogen atoms and oxygen molecules, that is,



with atomic species velocities of 8 km/s. Reactions such as this not only are of interest in their own right, but have applications in ionospheric physics and in low-Earth orbit (LEO) studies. Translationally "hot" atomic species are formed in the ionosphere and upper thermosphere by a variety of interactions including photodissociation, electron impact dissociation and dissociative ionization, and dissociative recombination. These species can then react prior to collisionally equilibrating (see, for example, *Gerard et al.* [1991] and *Lie-Svendsen et al.* [1991]). Indeed, evidence of products of reaction (1) which require fast atom interaction have been observed in the upper atmosphere [*Sharma et al.*, 1993]. Additionally, in the LEO environment, ambient or surface-scattered ambient species such as O and N can react with spacecraft outgas or exhaust species at and around orbital velocities of 8 km/s [*Green et al.*, 1985].

Reaction (1) is exothermic by ~1.4 eV at thermal energies, and even though the rate constant of this process exhibits an Arrhenius factor of ~0.27 eV, the reaction is known to produce vibrationally excited NO at room temperature, up to $\nu = 7$. There have been four measurements of the vibrational product distribution of reaction (1) under thermal conditions. Two studies [*Whitson et al.*, 1976; *Rahbee and Gibson*, 1981] utilized first-overtone chemiluminescent measurements, a

third [*Herm et al.*, 1983] utilized laser-excited fluorescence, and the most recent study utilized two-photon ionization [*Winkler et al.*, 1986]. The measured distributions are summarized by *Winkler et al.* [1986]. There is a notable variation in the measurements, particularly at the higher vibrational levels. Furthermore, two of the measurements [*Whitson et al.*, 1976; *Winkler et al.*, 1986], most clearly in the work of *Winkler et al.*, show a preferential production of even over odd vibrational levels, whereas the other two show smoothly decreasing production with increasing vibrational level. These experimental differences have not been resolved.

There are two recent theoretical studies of reaction (1). *Duff et al.* [1994] performed a classical dynamics study of the reaction using potential energy surfaces developed by *Walch and Jaffe* [1987], predicting the vibrational/rotation distribution of the NO product for several values of the nitrogen atom kinetic energy. That work predicts highly rotationally/vibrationally excited NO, with the vibrational distributions remaining relatively flat out to levels near the reaction energetic limit. *Gilibert et al.* [1995] published an analysis comparing quantum and classical predictions of the reaction products. The classical trajectory predictions in this work also show smoothly varying vibrational distributions, although these fall off more rapidly with increasing vibrational level than those of *Duff et al.* The quantum predictions show an oscillating vibrational distribution with the probabilities for production of even vibrational levels enhanced over those of odd levels, much as observed by *Winkler et al.* [1986]. This effect was predicted to decrease with increasing N atom velocity.

We have studied the fundamental and overtone band emissions of NO produced via reaction (1), primarily at an N atom velocity of 8 km/s, corresponding to a center-of-mass energy of ~3 eV, under single-collision conditions. Deduced population distributions and reaction cross sections are compared with theory.

Copyright 2000 by the American Geophysical Union.

Paper number 1999JA000432.
0148-0227/00/1999JA000432\$09.00

2. Experiment

The measurements were performed under single-collision conditions in a crossed beam experiment as shown in Figure 1. A pulsed beam of fast nitrogen atoms is made by a laser breakdown technique described in detail by Caledonia *et al.* [1987]. The fast beam is then crossed with a thermal pulsed beam of oxygen molecules. Infrared emissions of the product species are measured at right angles using both a circular variable filter (CVF) and band-pass-filtered radiometers for spectral resolution. The details of the measurement approach and data analysis technique have been described in detail previously [Upschulte and Caledonia, 1992; Upschulte *et al.*, 1992; Oakes *et al.*, 1994].

The $N+O_2$ cross-section measurements were conducted in our FASTTM-2 test facility which combines a 20 cm o.d. stainless steel six-way cross N atom beam source chamber coupled to a 40 cm o.d. stainless steel six-way cross-beam interaction chamber pumped with a 30 cm, 4000 L/s cryopump which maintains approximately a 1×10^{-6} torr base pressure before each gas pulse. A third 6.25 cm o.d. stainless steel six-way cross houses a quadrupole mass spectrometer employed for beam characterization and is pumped by a 300 L/s diffusion pump. A 1 mm skimmer separates the quadrupole chamber from the beam interaction chamber.

The atomic beam source utilizes a 12 J per pulse CO_2 laser to heat and partially dissociate pure molecular nitrogen. A General Valve pulsed molecular beam valve controls the gas flow into a 12.5 cm long, 20° full angle conical copper nozzle. The CO_2 laser is focused into the throat of the nozzle and fired after the nozzle is partially filled with molecular nitrogen. About one third of the CO_2 laser energy is delivered in an initial 200 ns gain-switched spike which induces a plasma breakdown in the high-pressure region near the throat via an inverse Bremsstrahlung absorption mechanism. The resulting plasma, which is heated in excess of 24,000 K by a laser-supported detonation wave, absorbs the remaining energy in the tail of the 2 μ s laser pulse. The rapidly expanding plasma continues to dissociate much of the remaining molecular nitrogen in the nozzle. During the expansion the directed kinetic energy increases as the gas temperature and density drop. The nozzle limits the expansion to favor electron-ion recombination while largely inhibiting the recombination of nitrogen atoms into molecules, and thus a cold, high-energy, large area beam of predominately atomic nitrogen flows out of the nozzle.

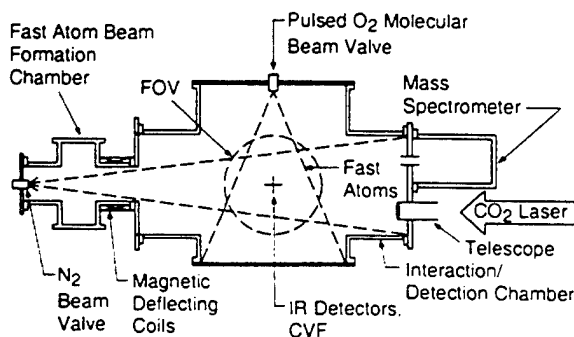


Figure 1. Schematic of experimental configuration. FOV denotes field of view.

The N atom beam velocity is measured by determining the time delay of the $N^+ + e^-$ recombination glow on two filtered photomultiplier tube radiometers separated by 7.6 cm downstream of the nozzle exit. A 0 to 50 cm^3/min STP Teledyne mass flowmeter was used to measure the nitrogen input, and a PCB Piezotronics piezoelectric transducer was used to measure the temporal profile of the cold gas pulse. These two measurements are combined to determine the fraction of the input flow that is processed by the laser pulse. A Balzers mass spectrometer with a cross-beam ionizer was used to measure the beam composition.

The oxygen flow is introduced from another General Valve pulsed molecular beam valve located on the top flange of the beam interaction chamber. The mass flow into the chamber is monitored by an Aalborg 0 to 50 cm^3/min STP mass flowmeter, and the stagnation pressure is measured with a Baratron (0 to 1000 torr) capacitance manometer. The temporal profile of the gas pulse was measured with a PCB piezoelectric transducer to determine the pulse width, typically 1 to 1.5 ms. The system was operated at a 1 Hz pulse rate, and the oxygen flow was triggered 1 ms prior to the nitrogen flow to maximize the overlap in the beam interaction region. The center of the beam interaction chamber is 85 cm from the N atom nozzle throat and 41 cm from the O_2 beam valve.

The temporally resolved measurements with 0.05 μm spectral resolution were made with a CVF radiometer consisting of a three-segment 90° filter wheel, a pair of $f/1.5$ off-axis parabolic reflectors, and an 0.8 mm Cincinnati Electronics InSb detector. A second radiometer (band-pass filtered) consisting of a set of interference filters and a 1 mm Cincinnati Electronics InSb detector was used to normalize the CVF spectra and to obtain lower-resolution band-pass-filtered spectra. The band-pass-filtered radiometer views the whole of the interaction region of the crossed beams. The amplified detector signals were sent through Ithaco and Stanford Instruments band-pass amplifiers. Signals from 256 to 512 pulses were averaged on a Lecroy 9310 digital oscilloscope.

The FAST beam contains a small concentration of ionic species, $\leq 1\%$, which can be reduced (by up to a factor of 5) with magnetic coils placed in a quasi-Helmholtz configuration. No change in infrared intensity levels was observed as the ion concentration was varied, ensuring that the observations were the result of interactions between O_2 and the neutral component of the FAST beam.

The mass spectrometer was operated with a 1 mA emission current and an 80 V ionizing potential. To determine the composition of the beam, the mass spectrometer signals at mass to charge values equal to 14 and 28 (N atoms and molecules, respectively) were measured and compared. To determine the beam composition from the measured signals, the signals were normalized by the relative cross section for ionization by 80 eV electrons in the ionizer and the transmission function of the mass spectrometer. The transmission function describes the sensitivity of the mass spectrometer as a function of mass-to-charge ratio. Previous measurements of the transmission function for this mass spectrometer found that its sensitivity decreased by a factor of 0.73 from $m/e = 14$ to $m/e = 28$. In addition, molecular nitrogen will contribute to the mass 14 signal due to dissociation in the ionizer. Therefore a quantitative measurement of the beam composition must also take into

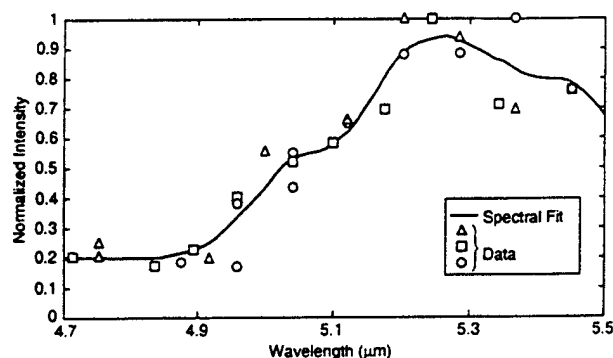


Figure 2. NO fundamental band emissions observed in the interaction of 8 km/s nitrogen atoms with O₂. A spectral fit of the data is also shown.

account the cracking pattern for N₂. It was found that the mass 14 signal resulting from dissociation of N₂ in the ionizer was 10.2% of the mass 28 signal. FAST beam nitrogen atom concentrations determined during the course of the measurements varied between 16% and 50%. Observed radiation intensities scaled linearly with the N atom concentration.

3. Data and Analysis

Several measurements were taken for the interaction of 8 km/s N atoms with O₂. Representative NO fundamental band emission data taken with the CVF are shown in Figure 2. The data presented are normalized, but are in units of W/μm. The signal-to-noise ratio is only ~5; however, the data are highly reproducible, showing excursions of less than 20% at any one wavelength. We anticipate that there is a strong emission beyond 5.5 μm since the reaction exothermicity allows production of NO $v \geq 23$. The responsivity of the InSb detectors falls sharply at wavelengths above 5.5 μm, precluding measurements at these longer wavelengths.

The emission spectra show clear evidence of highly vibrationally excited NO, with the most notable feature being a flattening in the signal at about 5.1 μm. We have performed a spectral fit of the data using a standard least squares routine with the spectral shapes of the emission spectrum of individual vibrational transitions as basis functions. The NO Einstein coefficients of Rawlins *et al.* [1998] were applied in this analysis. A rotational temperature of 7000 K was assumed, based on the analysis of Duff *et al.* [1994]. Spectral fits performed with rotational temperatures varied between 4000 and 10,000 K resulted in similar vibrational populations.

The spectral fit is shown in Figure 2 with vibrational populations tabulated in Table 1. Since these measurements are performed under single-collision conditions with short duration/residence times, the population distribution reflects the nascent product states of reaction (1).

The spectral fit shows the population of $v = 3$ to be significantly below that of $v = 2$ and $v = 4$. This observation is consistent with the observed flattening in the spectrum at wavelengths between 5 and 5.1 μm. The fit also shows a slight depression of the population of $v = 1$ relative to $v = 2$. Lastly, the fit population for $v = 7$ is more uncertain inasmuch as the spectral fit does not account for radiation contributions from higher vibrational levels whose fundamental band

transitions center at wavelengths beyond 5.4 μm but which partially radiate at wavelengths below 5.4 μm.

To first order we observe an NO product vibrational distribution which oscillates somewhat between odd and even levels, similar to the observation of Winkler *et al.* [1986] at thermal velocities. The effect is most noticeable at $v = 3$. A more smoothly varying population distribution would overpredict the radiation level near 5.1 μm.

As noted, there may be significant NO fundamental band radiation at wavelengths beyond the InSb detector wavelength cutoff, ≥ 5.5 μm. We had hoped to evaluate the contribution of NO excited states whose fundamental band transitions radiate in this spectral region by providing similar CVF measurements of the NO first-overtone band emissions. Unfortunately, we found that the S/N of these data was too low to be useful. We then performed a series of band-pass-filtered radiometer measurements in the NO overtone region, with each band-pass filter having a spectral width of 0.5 to 1.0 μm. Several similar measurements were also performed in the NO fundamental band spectral region to ensure continuity between the absolute calibrations of the radiometer and the CVF system band-pass-filtered radiometers.

The resulting radiometer data coupled with the CVF data are shown in Figure 3. Also shown is the spectral fit of the NO fundamental band and the predicted overtone band spectra based on the vibrational populations associated with that fit. As can be seen, the predicted NO overtone spectrum exhibits a peak spectral intensity similar to that measured, but falls off in intensity considerably more rapidly than the data with increasing wavelength.

Thus the overtone band data clearly imply that a number of higher vibrational states of NO beyond $v = 7$ are produced. We have provided a spectral fit of the overtone band data in order to assess the population of those states. Such a fit is quite speculative, given the broad spectral width of the

Table 1. NO Vibrational Populations Determined From Spectral Fits Arbitrarily Normalized to the $v = 2$ Population of the Fundamental Band Fit

v	Fundamental Fit	Overtone Fit
1	0.76	
2	1.00	0.64
3	0.30	0.80
4	1.06	0.88
5	0.57	0.45
6	0.30	0.19
7	0.39	0.29
8		0.19
9		0.14
10		0.13
11		0.15
12		0.12
13		0.089
14		0.084
15		0.12
16		0.059
17		0.033
18		0.026

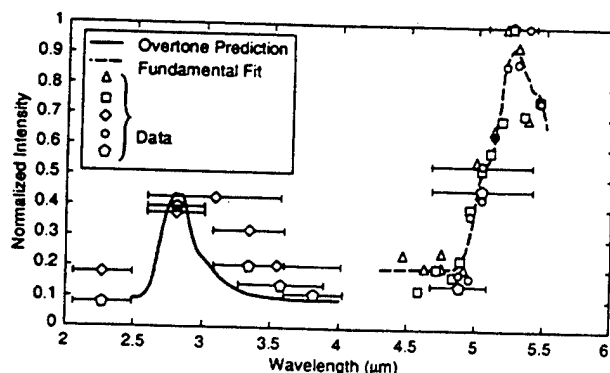


Figure 3. NO fundamental and overtone band data. Predicted overtone band spectrum based upon population distribution of fundamental band spectral fit.

individual data points, but can provide a crude estimation of the vibrational population distribution at higher levels. This fit is shown in Figure 4, compared with the data. The relative vibrational populations corresponding to this fit are provided in Table 1, compared with those from the fit of the NO fundamental band data. This overtone vibrational population distribution has also been used to predict the NO fundamental band spectrum (assuming the population of NO($v = 1$) from the fundamental band fit), and as can be seen in Figure 4, that prediction compares reasonably well with the fundamental band data, although falling somewhat on the low side. Note that the depression in the $v = 3$ population is not seen in this fit; the populations of the lower NO vibrational levels cannot be deduced with any certainty from the overtone measurements given the low spectral resolution of the radiometric data. Note the significant amount of fundamental band radiation which is predicted to fall at wavelengths beyond 5.4 μm .

The procedure for deducing cross sections from the data has been described in detail by *Upschulte and Caledonia* [1992]. We provide an absolute measurement of the fundamental band emission intensity of vibrational states created during the interaction of 8 km/s N atoms with the oxygen molecule target. Thus the observed emission from

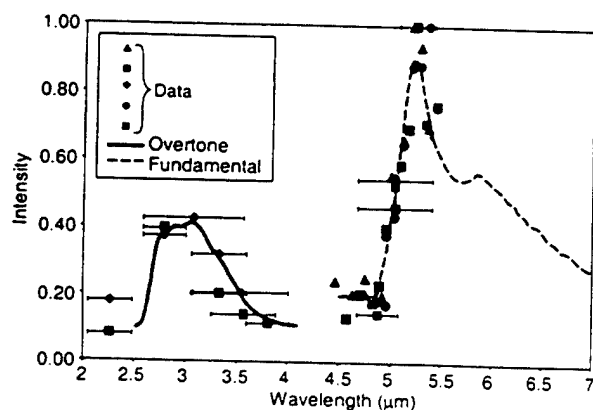


Figure 4. Data of Figure 3 with spectral fit of overtone band data. NO fundamental band spectral distribution is predicted using populations determined by fit of first-overtone data.

each level is directly proportional to the excited state concentration at level v in the field of view, that is,

$$J_v = N_v A_{v,v-1} h \nu_{v,v-1}, \quad (2)$$

where J_v is the total fundamental band emission from vibrational state NO(v) and N_v is the total population of NO(v) in the field of view. The remaining quantities in expression (2) are the Einstein coefficient and photon energy of the transition from vibrational level v to $v-1$.

The quantity N_v is specified by [Upschulte and Caledonia, 1992]

$$N_v = \sigma_v C_N O_2, \quad (3)$$

where σ_v is the desired cross section for production of NO(v) by reaction (1), C_N is the local line density of nitrogen atoms in the FAST beam, and O_2 is the total number of oxygen molecules intercepted by the FAST™ beam.

The latter two quantities are determined by measured mass flow rates, beam shapes, and mass spectrometric evaluation of the nitrogen atom content of the FAST™ beam. The intensities of individual transitions, J_v , are determined from the total spectrally resolved fundamental band emission through the curve fitting procedure described earlier.

The state-specific cross sections for production of NO by 8 km/s nitrogen atoms impacting thermal oxygen molecules are summarized in Table 2 as determined by our NO fundamental band emission data. We estimate these cross sections to have an uncertainty of a factor of 2. As described above, they rely on the absolute evaluation of several experimental quantities, each with a finite uncertainty. The uncertainty in the relative cross sections is considerably lower.

The experimentally derived cross sections are compared with recent classical trajectory predictions (J. Duff, private communication, 1997) performed for 8 km/s nitrogen atoms using the same techniques published earlier [Duff *et al.*, 1994]. As can be seen, the evaluated cross sections are similar in magnitude to the predicted ones, although they exhibit the oscillatory behavior noted earlier. The sum of the cross sections for $v = 1-7$ agrees with the prediction to within 20%.

We have now added a high-velocity validation to theoretical predictions which previously had only been tied to data taken at thermal energies. These predictions remain the only source available to modelers in the aeronomically interesting range of nitrogen atom velocities of 2 to 3 km/s.

Table 2. Cross Section for N (8 km/s) + O₂ → NO(v) + O

Vibrational Level	Present Results $\times 10^{17} \text{ cm}^2$	Theory* $\times 10^{17} \text{ cm}^2$
1	4.9	3.7
2	6.5	4.2
3	2.0	3.9
4	6.9	3.6
5	3.7	3.1
6	2.0	2.7
7	2.5	2.3

*From J. W. Duff (private communication, 1997).

Our results may be used directly to predict (partial) infrared radiation signatures produced in the near field around orbiting satellites.

Interestingly, Walch [1995] recently published an updated potential surface for N + O₂ which suggests the presence of a low-lying stable state not included in the previous calculations. It would be of interest to provide an updated theoretical prediction for this reaction using the revised surface potential.

In summary, we have studied the fundamental and first-overtone emissions produced in the reaction of 8 km/s nitrogen atoms and O₂. The product NO is highly vibrationally excited. Vibrational population distributions deduced from the emission signatures show the population of $v = 3$ to be depressed relative to $v = 2, 4$. Experimental reaction cross sections for production of NO($v = 1-7$) are found to be in reasonable agreement with those predicted by Duff et al. [1994], with the exception of the depressed population of $v = 3$.

Acknowledgments. The spectral fitting of the NO emission data was performed by John F. Cronin. J. Duff kindly provided us classical trajectory rate calculations for reaction (1) at the velocity of the measurements. B. D. Green provided useful comments on the data interpretation. This work was supported by the Air Force Office of Scientific Research under project 2303ES, task 92V504COR.

Janet G. Luhmann thanks Øystein Lie-Svendsen and Alexander Dalgarno for their assistance in evaluating this paper.

References

- Caledonia, G.E., R.H. Krech, and B.D. Green, A high flux source of energetic oxygen atoms for material degradation studies, *AIAA J.*, 25(1), 59-63, 1987.
- Duff, J.W., private communication, 1997.
- Duff, J.W., F. Bien, and D.E. Paulsen, Classical dynamics of the N(⁴S) + O₂ ($x^3\Sigma_g^-$) → NO ($X^2\Pi$) + O(³P) reaction, *Geophys. Res. Lett.*, 21, 2043-2046, 1994.
- Gerard, J.C., V.I. Shamatovic, and D.V. Bisikalo, Non-thermal nitrogen atoms in the Earth's thermosphere, 2, A source of nitric oxide, *Geophys. Res. Lett.*, 18, 1695-1698, 1991.
- Gilibert, M., X. Gimenez, M. Gonzalez, R. Sayos, and A. Aguilar, A comparison between experimental, quantum and quasiclassical properties for the N(⁴S) + O₂ ($x^3\Sigma_g^-$) → NO ($X^2\Pi$) + O(³P) reaction, *Chem. Phys.*, 191, 1-15, 1995.
- Green, B.D., G.E. Caledonia, and T.D. Wilkerson, The shuttle environment: gases, particulates and glow, *J. Spacecr.*, 22, 500-511, 1985.
- Herm, R.R., B.J. Sullivan, and M.E. Whitson, Jr., Nitric oxide vibrational excitations from the N(⁴S) + O₂ reaction, *J. Chem. Phys.*, 79, 2221-2230, 1983.
- Lie-Svendsen, O., M.H. Rees, K. Stamnes, and E.C. Whipple, Jr., The kinetics of "hot" nitrogen atoms in upper atmosphere neutral chemistry, *Planet. Space Sci.*, 39, 929-943, 1991.
- Oakes, D.B., D.M. Sonnenfroh, G.E. Caledonia, and W.A.M. Blumberg, Velocity dependent O atom IR excitation cross sections: Connections with flight data, *J. Geophys. Res.*, 99, 23,249-23,255, 1994.
- Rahbee, A., and J.J. Gibson, Rate constant for the formation of NO in vibrational levels $v = 2$ through 7 from the reaction N(⁴S) + O₂ → NO² + O, *J. Chem. Phys.*, 74, 5143-5148, 1981.
- Rawlins, W.T., J.C. Person, M.E. Fraser, S.M. Miller, and W.A.M. Blumberg, The dipole moments and infrared transition strengths of nitric oxide, *J. Chem. Phys.*, 109, 3409-3417, 1998.
- Sharma, R.D., Y. Sun, and A. Dalgarno, Highly rotationally excited nitric oxide in the terrestrial thermosphere, *Geophys. Res. Lett.*, 20, 2043-2045, 1993.
- Upschulte, B.L., and G. E. Caledonia, Laboratory measurements of infrared excitation cross sections of fast O-atom collisions with CO, CO₂, and CH₄, *J. Chem. Phys.*, 96, 2025-2033, 1992.
- Upschulte, B.L., D.B. Oakes, and G.E. Caledonia, Infrared emissions arising from the reactions of fast O/O* with N₂, *Geophys. Res. Lett.*, 19, 993-996, 1992.
- Walch, S.P., A new potential energy surface for N + O₂: Is there an NOO minimum?, *J. Chem. Phys.*, 102, 4189-4192, 1995.
- Walch, S.P., and R.L. Jaffe, Calculated potential surfaces for the reactions: O + N₂ → NO + N and N + O₂ → NO + O, *J. Chem. Phys.*, 86, 6946-6956, 1987.
- Whitson, M.E., Jr., L.A. Darnton, and R.J. McNeal, Vibrational energy distribution in the NO produced by the reaction N(⁴S) with O₂, *Chem. Phys. Lett.*, 41, 552-556, 1976.
- Winkler, I.C., R.A. Stachnik, J.I. Steinfeld, and S.M. Miller, Determination of NO ($v = 0-7$) product distribution from the N(⁴S) + O₂ reaction using two-photon ionization, *J. Chem. Phys.*, 85, 890-899, 1986.

W. A. M. Blumberg and S. J. Lipson, Air Force Research Laboratory, Space Vehicles Directorate, Hanscom Air Force Base, MA 01731.

G. E. Caledonia, R. H. Krech, and D. B. Oakes, Physical Sciences Inc., 20 New England Business Center, Andover, MA 01810-1077. (caledonia@psicorp.com)

(Received November 24, 1999; revised January 26, 2000; accepted January 30, 2000.)

APPENDIX 6

Infrared Emission Produced in the Reaction of Fast Oxygen Atoms and Amine Molecules

Journal of Spacecraft & Rockets

(reproduced in its entirety)

Infrared Emission Produced in the Reaction of Fast Oxygen Atoms and Amine Molecules

B.L. Upschulte, R.H. Krech, D.B. Oakes and G.E. Caledonia
Physical Sciences Inc.
Andover, MA 01810

W.A.M. Blumberg and S.J. Lipson
Air Force Research Laboratories, VSBM
Hanscom AFB, MA 01731

Abstract

We report a study of the interactions of 8 km/s oxygen atoms with a group of molecules including unsymmetrical di-methyl hydrazine, mono-methyl hydrazine, methylamine, and propane. Infrared band emissions were measured over the 2 to 5 μm region. In all cases, the dominant emissions observed resulted from direct excitation of CH and NH stretch transitions. Evidence of vibrationally excited OH formation was also observed. Spectral observations, excitation cross sections, and comparison with data obtained in a low earth orbit experiment are presented.

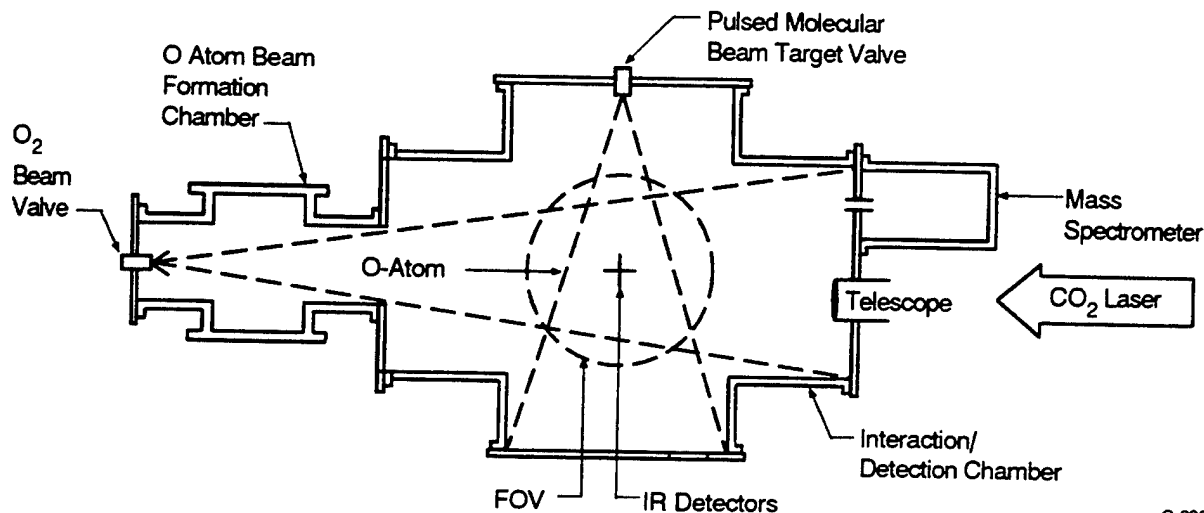
1. Introduction

In this work we have used the PSI FASTTM oxygen atom source^{1,2} to study the infrared emissions arising from the interaction of 8 km/s oxygen atoms and selected amine molecules under single collision conditions. We have measured spectral emissions in the 2 to 5 μm region arising from reactions between 8 km/s oxygen atoms and mono-methylamine (MMA), monomethyl hydrazine (MMH), and unsymmetrical dimethyl hydrazine (UDMH). Fast oxygen atom interactions with propane were studied for comparison. These measurements, although of interest in their own right, are useful in interpreting chemical interactions which can occur in the low earth orbit (LEO) environment.

We provide an overview of our experimental approach in the next section. This is followed by a presentation of our data base with both spectral interpretation and reaction cross section evaluations. We have identified one set of flight measurements for comparison with our data, that of an MMA release during a space shuttle experiment.³ We will show that the comparison between flight and lab data is quite good. Lastly, we provide a summary and conclusions from our work.

2. Experimental

The hyperthermal oxygen atom source^{1,2} and the experimental techniques used to measure infrared cross sections^{4,5} have been described in detail previously. A schematic of the experimental system is shown in Figure 1. It is comprised of two stainless steel six-way crosses, including an 8 in. cross source chamber housing the pulsed oxygen valve/nozzle assembly connected to a 16 in. cross expansion chamber. The system is pumped by a cryopump attached to the large cross which maintains a base pressure of 1×10^{-6} Torr.



C-2895a

Figure 1. Schematic of the Fast O-atom source.

The hyperthermal (2 to 12 eV, tunable) oxygen atoms are generated in a pulsed laser discharge of O_2 . A 12 J/pulse CO_2 laser is focused with a 100 cm focal length BaF_2 lens into the throat of a 20-deg full angle, 12.5 cm long conical expansion nozzle which has been partially filled with O_2 by a pulsed beam valve (General Valve). The plasma, ignited at the throat, expands out the nozzle, dissociating the molecular oxygen in front of it. The nozzle was designed to allow ion and electron recombination while the slower kinetics of atom/atom recombination maintains a highly dissociated beam. The result, at 8 km/s, is an approximately 50 μs pulse of highly dissociated oxygen (> 80% atoms) with less than 1% ion content. The beam expands from approximately 15 cm^2 at the exit aperture of the nozzle to greater than 1000 cm^2 in the expansion chamber. The ion content of the beam can be reduced by up to 80% using the magnetic coils arranged in a pseudo-Helmholtz configuration and positioned outside the vacuum system at the transition from the small to large cross. We were able to demonstrate by use of the coils that the observed emissions were due to neutral rather than ionic reactions.

The beam velocity (5 to 12 km/s) is selected by varying the time delay between the pulsing of the O_2 valve and the triggering of the CO_2 laser. The delay determines the mass of O_2 processed by the pulsed discharge which is inversely related to the beam velocity. The velocity is determined by measuring the time of flight between two radiometers attached to the source

chamber, mounted along the beam axis and separated by 7.6 cm, and filtered to monitor the $^5\text{S} - ^5\text{P}$ oxygen atom line (777 nm).

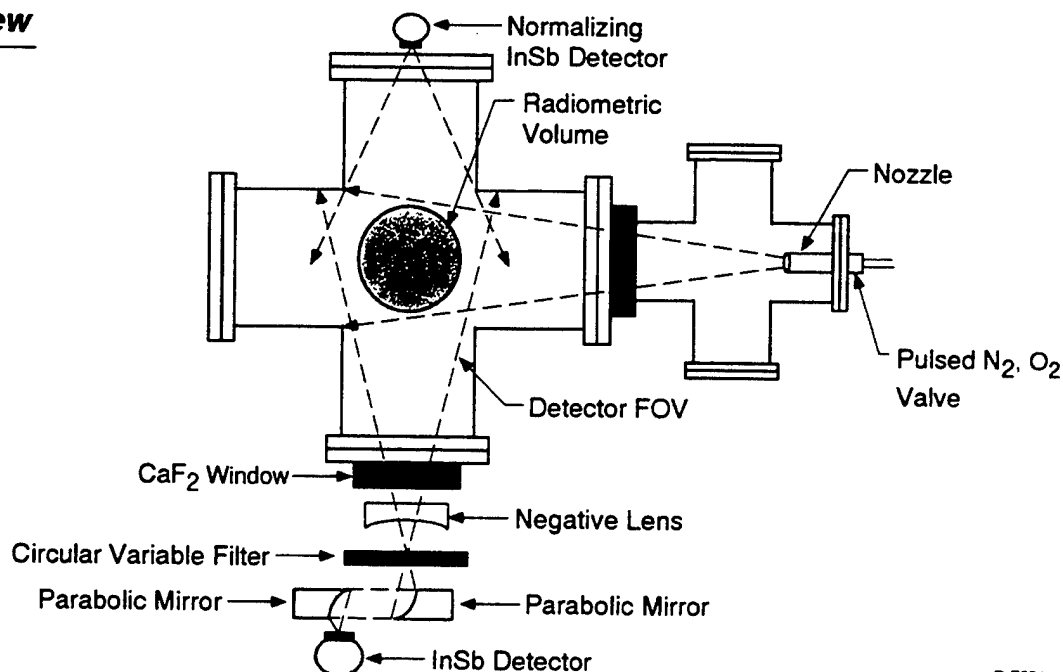
Infrared emitting species are generated in the large expansion chamber by crossing the fast oxygen beam with a supersonic molecular beam formed from the reactant. The reactants in the current study include: 1,1-dimethylhydrazine (UDMH), monomethylhydrazine (MMH), monomethylamine (MMA) and propane. The reactant beam is generated at a 90 degree angle with respect to the O-atom beam at a position 85 cm downstream from the oxygen valve. The reactant beam is produced from a second pulsed molecular beam valve. The reactant gas pulsed valve will be referred to as the target valve. The backing pressure in the target valve was typically set to a few hundred torr (40 torr in the case of MMH) which produced a gas density in the vacuum chamber such that only a single collision between the reactant gas and the fast oxygen atoms was expected. Operation in this single collision regime was verified experimentally by demonstrating a linear relationship between infrared emission and target valve backing pressure.

The experiment is run with a master clock operating at 2 Hz and two digital delay generators. The master clock triggers the target valve which opens for approximately 1000 μs . After a 1000 μs delay, the oxygen valve is pulsed and after an additional ~ 500 μs delay the CO_2 laser is triggered. The delay between the oxygen valve trigger and the CO_2 laser trigger is chosen to produce the desired oxygen atom beam velocity (8 km/s). The delay between the pulsing of oxygen and target valves is chosen so that the fast oxygen atom beam pulse reached the center of the interaction region concurrent with the arrival of the peak of the reactant gas pulse.

Infrared emissions are measured with two different approaches having different sensitivity and spectral resolution. The first approach uses an Indium Antimonide (InSb) detector (Cincinnati Electronics, 0.8 mm diam, 60 deg field-of-view (FOV), at 77°K) in conjunction with a Circular Variable Filter (CVF) to measure spectra from 1.7 μm to the cut-off of the InSb detector (ca. 5.5 μm). Two of the three segments of the filter wheel were used to collect the data presented in this paper with a resolution of better than 1.5% of the detection wavelength (i.e., 0.05 μm at 3.5 μm). This detection system and its position on the measurement apparatus are shown schematically in Figure 2.

The centerline of the detector FOV for this system is positioned 85 cm downstream from the throat of the oxygen valve and directly in front of a calcium fluoride window mounted onto the vacuum chamber. Light is collected from the interaction volume and through the CVF by one of two parabolic mirrors in the CVF system. The second parabolic mirror directs the collected (and filtered) light onto the InSb detector element. A negative CaF_2 lens was used to increase the FOV of the detection system up to 56° so that the entire interaction volume could be detected. The wavelength calibration of the CVF system was periodically verified by positioning a narrow band filter (2.685 μm , FWHM of 0.017 μm) between the two parabolic mirrors (where the FOV is collimated to avoid angle of incidence effects). With a 1000 C blackbody positioned in the FOV, the detection wavelength was scanned by rotating the CVF and the signal level was monitored.

Top View



D-72012

Figure 2. Schematic of the CVF detection system interfaced with the vacuum chamber.

Both the wavelength calibration and the resolution of the system could be checked in this manner. The relative response of this detection system as a function of wavelength was determined by measuring the signal detected from a 1000 C blackbody through the CVF as the CVF is rotated. All spectra were adjusted by this response curve to correct for the dependence of the transmission of the CVF and the spectral sensitivity of the InSb detector on wavelength.

The second infrared detection system used the InSb detector with a bandpass filter (3.05 to 3.57 μm). The filtered InSb was positioned in front of the CaF_2 window and its 60 deg FOV was sufficient to detect the entire interaction volume. With less elements in the optical path and lower resolution this system had greater sensitivity than the CVF system. Its relative simplicity was better for determining IR excitation cross sections for the reaction between molecules and fast oxygen atoms over this bandpass.

The InSb detector uses an integral transimpedance amplifier with a gain of 1.58×10^5 volts/amp. The detector output was further amplified by a factor of 200 to 5000 using a voltage amplifier with a 30 kHz bandwidth. The resulting signal was then detected with a digital oscilloscope. To obtain a signal-to-noise ratio of greater than 3, the signal from the CVF system was averaged for 500 or 1000 pulses (depending on the signal level). There are two possible sources of background radiation which can contribute to the measured signals. The first is due to emission from the oxygen beam itself. The second source of background radiation is from the reaction (or interaction) of the oxygen beam with species (including the target molecules) on the vacuum chamber walls. Both sources of background radiation were measured by triggering the oxygen valve 0.47 seconds after the target valve pulse. This delay enabled the reactant in the gas

phase to be completely removed by the pumping system so that when the fast oxygen beam was formed, emissions would only be detected from the oxygen beam itself and any interaction with the chamber walls. The background radiation was subtracted from the measured radiation to determine the signal from the gas phase interaction of the fuel and the fast oxygen beam.

Since the system was operated at 2 Hz and each point on a spectrum required two measurements of up to 1000 pulses each, data collection for many spectra took in excess of 20 hours. To correct for long term drift of the system (up to $\sim 20\%$), a second InSb detector (see Figure 2), bandpass-filtered to detect emission from 3.0 to 3.5 μm , was operated during each measurement with the CVF. This second detector was positioned directly opposite the primary detector and detected the entire interaction volume. The signal from the CVF at each wavelength position was normalized by the signal measured with this second detector to correct for system drift.

3. Data/Analysis

We have measured the 2 to 5 μm emission resulting from the interaction of 8 km/s oxygen atoms with MMA, MMH, UDMH, and propane under single collision conditions. Normalized spectra for these four gases are shown in Figures 3 through 6. Each data point corresponds to an average of 500 to 1000 measurements with background (i.e., no target gas) subtraction. At least two separate measurements are taken at different times for each gas. The reproducibility is quite good. Signal-to-noise of the data is typically greater than 5.

In Figure 7 we contrast the laboratory observation for MMA with that observed during a space shuttle experiments involving a liquid MMA release. Again the spectral comparison between the two data sets is quite good with all major spectral features seen in both data sets.

Analysis of the amine data, Figures 3 through 5, shows that all exhibit a broad emission peak spanning approximately 3.2 to 3.7 μm at half-height. This spectral region corresponds to the range of fundamental band emissions of both NH and CH moieties. We interpret the emission to arise from direct O-atom excitation of these stretch modes. In contrast, the peak observed in propane is narrower and shifted to the red of the peak observed for the amine molecules. This is presumably because only CH stretch emissions contribute to this signature.

There is a second spectral feature near 2.9 μm clearly evident in the MMA data, and to a lesser extent in the spectra of the other amine molecules, but which is not evident in the spectrum for propane. In previous analysis of the MMA flight data,³ this feature has been identified as fundamental band emission from OH, dominantly $\nu = 1$. A representative OH spectrum is also shown for comparison in Figure 7.

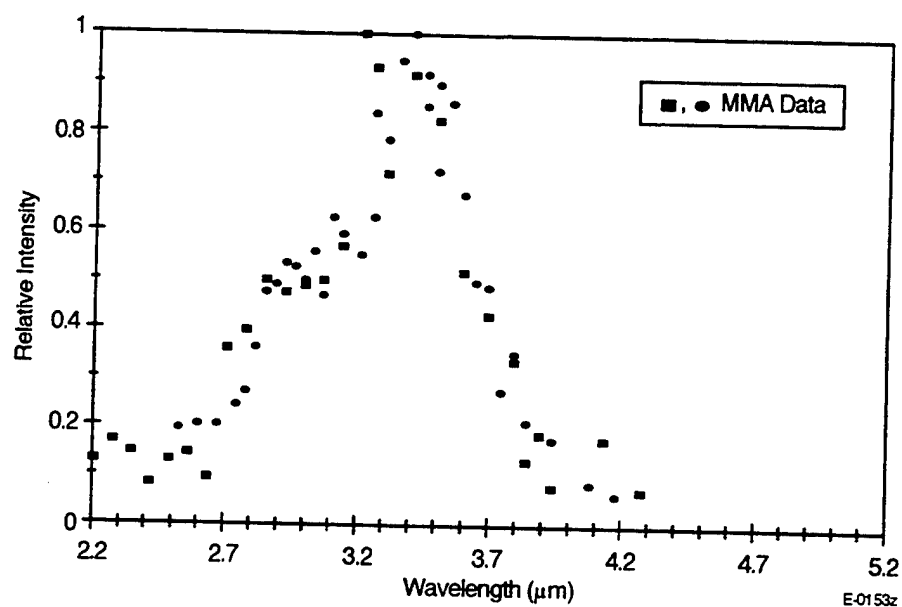


Figure 3. IR emission observed in the interaction of 8 km/s O-atoms with MMA.

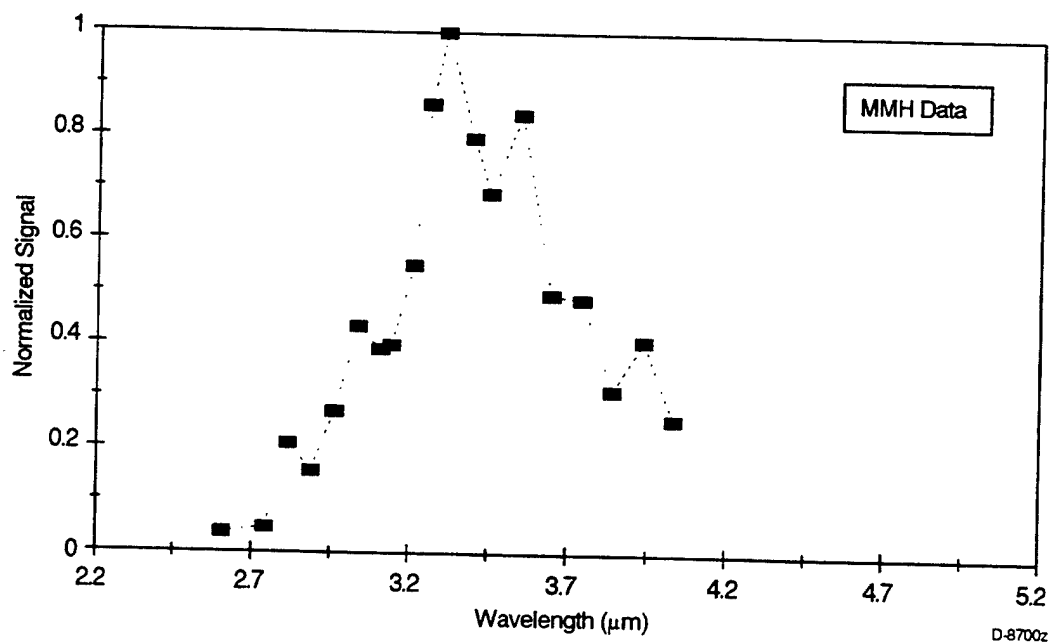


Figure 4. IR emission observed in the interaction of 8 km/s O-atoms with MMH.

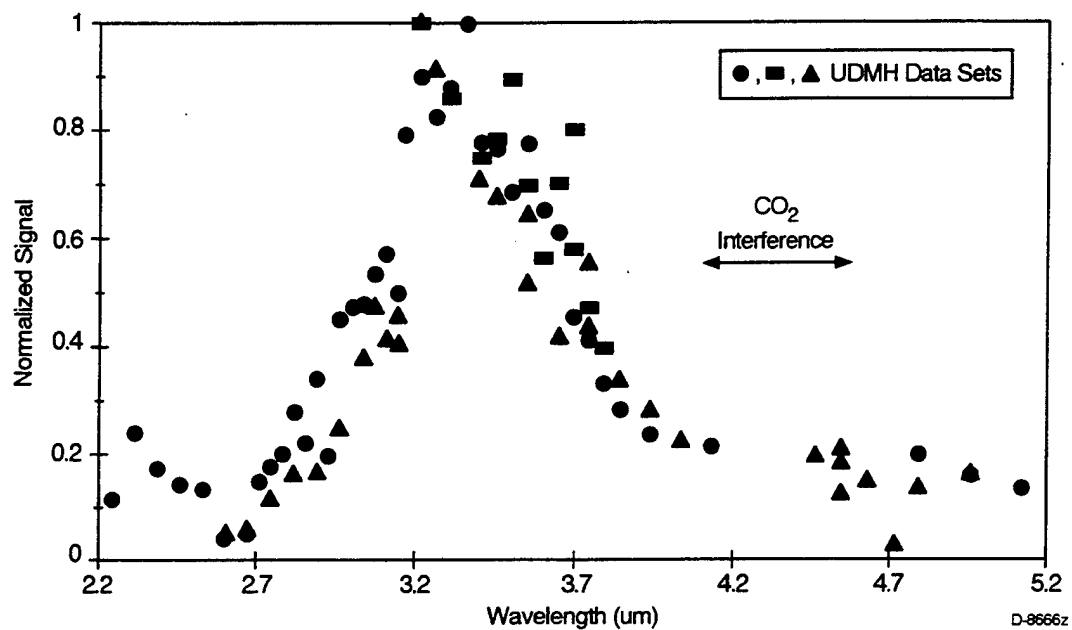


Figure 5. IR emission observed in the interaction of 8 km/s O-atoms with UDMH.

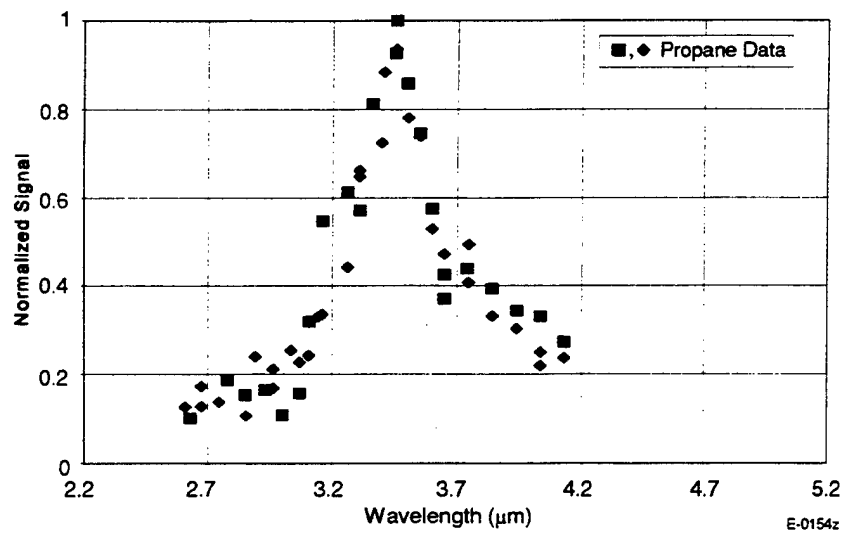


Figure 6. IR emission observed in the interaction of 8 km/s O-atoms with propane.

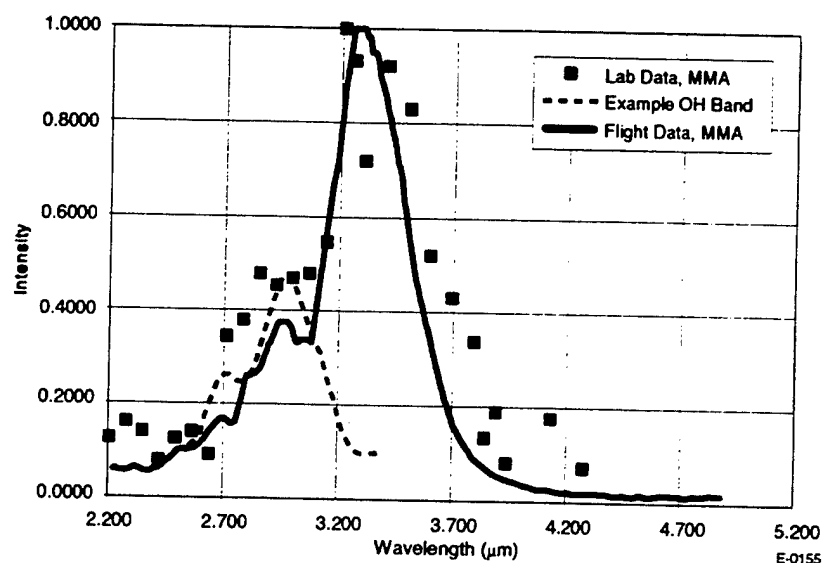


Figure 7. Laboratory MMA data contrasted with Delta 181 LEO flight data.³ A representative theoretical spectrum of OH($v=1$) fundamental band and emission is shown for comparison purposes.

IR excitation cross sections for the observations are summarized in Table 1. The first entry is for the average cross section for producing emission in the 2.7 to 4.2 μm spectral region. This cross section must be presented normalized by an average band lifetime inasmuch as the radiating states have not been uniquely identified.^{4,5} This quantity is effectively a measure of the direct excitation cross section although it can contain a small contribution ($< 15\%$) due to OH emission in the band. A characteristic radiative lifetime for these band systems would be O (0.1 s) suggesting cross sections of O (10^{-16} cm^2). The excitation cross section increases with increasing target molecule size.

Table 1. Evaluated Cross Sections: 8 km/s Oxygen Atoms Impacting Target Molecules

Gas	σ/τ (2.7 to 4.2 μm) cm^2/s	$\sigma_{\text{OH}} (v = 1)$ cm^2
MMA	3×10^{-15}	$\leq 5 \times 10^{-17}$
MMH	8×10^{-15}	$\leq 2 \times 10^{-16}$
UDMH	9×10^{-15}	$\leq 2 \times 10^{-16}$
Propane	3×10^{-15}	—

The cross sections are determined by combining both radiometer bandpass and CVF measurements. The absolute radiance is measured with the calibrated radiometer covering the spectral region of 3.05 to 3.57 μm . The spectral shapes presented in Figures 3 through 6 are used to determine the total radiance covering the range of strong emission, ~ 2.7 to 4.2 μm .

The measurement-to-measurement repeatability in these cross sections is typically better than $\pm 30\%$. Nonetheless, the cross section measurement requires absolute evaluation of the flux of the O-atom beam and the target-gas beam over the optical field of view as well as an absolute radiometric calibration of the optical train and detection system. We estimate that the combined uncertainties could result in a factor of ~ 2 uncertainty in the presented cross sections. However, the relative cross sections for different target gases are accurate to better than $\pm 50\%$.

The second entry in Table 1 is an evaluation of the cross section for producing vibrationally excited OH ($v = 1$). This is determined using the $v = 1$ radiative lifetime of 0.12 seconds and should be considered an upper bound inasmuch as the spectral resolution of the data precludes clear separation of OH and CH, NH stretch emissions. Again, these cross sections are significant, perhaps reflecting the large amount of reaction energy provided by the kinetic energy of the oxygen atoms.

4. Summary and Conclusions

We have provided the first laboratory measurement of the 2 to 5 μm infrared emissions produced in the single collision interactions between 8 km/s oxygen atoms and thermal MMA, MMH, UDMH and propane molecules. Strong emissions in a band centered near 3.3 μm are observed for all target gases, reflecting direct vibrational/rotational excitation of the CH, NH stretch modes. The observed emission feature for propane is narrower than that observed for the amine molecules, presumably reflecting the fact that only CH stretch modes are available for excitation in that system.

Strong evidence of OH ($v = 1$) formation is observed in the emission spectra obtained from the amine fuels. In the case of MMA this identification is borne out by earlier³ analysis of separate flight data. The formation of OH ($v = 1$) is not apparent in the propane spectra.

Both direct vibrational excitation and OH chem-excitation cross sections for the reactions have been deduced from the data.

Acknowledgment

This work was supported by the Air Force Office of Scientific Research.

References

1. G.E. Caledonia, R.H. Krech and B.D. Green, "A High Flux Source of Energetic Oxygen Atoms for Material Degradation Studies," AIAA J. 25, 59 (1987).
2. G.E. Caledonia, R.H. Krech, and D.B. Oakes, "Laboratory Simulation of Low Earth Orbit (LEO) Atomic Oxygen Effects," J. Inst. of Env. Sci., 391(2) (1996).
3. B.D. Green, K.W. Holtzclaw, P.B. Joshi, and M.K. Burke, "Analysis of Radiances From Orbital Gas Releases, " J. Geophys. Res, 97 (A8), 12161-12172, August 1, 1992.
4. B.L. Upschulte and G.E. Caledonia, "Laboratory Measurements of Infrared Excitation Cross Sections of Fast O-Atom Collisions with CO, CO₂, and CH₄," J. Chem. Phys. 96(3), 2025 (1992).
5. D.B. Oakes, D.M. Sonnenfroh, G.E., Caledonia, and W.A.M. Blumberg, "Velocity Dependent O-Atom IR Excitation Cross Sections: Connections with Flight Data," J. Geophys. Res. 99, 23, 249 (1994).

APPENDIX 7

AIRIS Hyperspectral Imaging of Aircraft and Backgrounds

IRIS Targets, Backgrounds, and Discrimination Specialty Group Meeting

(reproduced in its entirety)

AIRIS HYPERSPECTRAL IMAGERY OF AIRCRAFT AND BACKGROUNDS

February 1997

William J. Marinelli and Byron David Green
Physical Sciences Inc.
20 New England Business Center
Andover, MA 01810-1077

Anthony J. Ratkowski and E Ray Huppi
USAF Phillips Laboratory (PL/GPO)
Hanscom AFB, MA 01731-3010

ABSTRACT

The Adaptive InfraRed Imaging Spectroradiometer (AIRIS) is a hyperspectral imaging system comprising a low-order tunable Fabry-Pérot étalon coupled to an InSb focal plane. This system was developed by Physical Sciences Inc (PSI) under the sponsorship of the Armament Division, Air Force Wright Laboratories for high speed multispectral imagery of countermeasures and missile systems. The system has been transferred to PSI under a bailment agreement and is currently being used in a joint effort with the Geophysics Directorate of the Air Force Phillips Laboratory to examine the utility of multispectral imagery for strategic and tactical applications. In this paper we report on: 1) the use of *AIRIS* to image surrogate aircraft targets against cluttered background scenes, including airfields, 2) approaches used to select the critical wavelengths for sampling the scene, and 3) processing methods to isolate targets from the background clutter. Surrogate targets include a range of commercial and smaller private jet aircraft observed during takeoff and landing. A key feature of the approach is the ability to rapidly image the scene at only those wavelengths needed for identification and clutter suppression. This capability reduces the data rate, data volume, and processing requirements needed to effectively employ hyperspectral imagery for these applications.

INTRODUCTION

The Adaptive Infrared Imaging Spectroradiometer (*AIRIS*) is an innovative imaging, piezoelectrically actuated Fabry-Pérot interferometer developed under BMDO and Air Force sponsorship by Physical Sciences Inc. (PSI). The distinguishing feature of the approach is the operation of the interferometer in low orders such that continuous images over a wide field-of-view are produced with high sensitivity. A computer is used to control mirror spacing, alignment, and processing of the infrared images. A staring focal plane array is used to capture an image of the interferometer field-of-view with high sensitivity.

The beneficial features resulting from this approach include: 1) an extended free spectral range (up to λ to 2λ), 2) a narrow spectral bandwidth (approximately 2% of λ), 3) flexible and adaptive sampling and processing of the image to isolate specific spectral features or signatures, 4) high spatial resolution and

radiance sensitivity, 5) a common pixel registry for all detection wavelengths, and 6) an extended field-of-view (as great as 40 deg full angle) for the survey of wide areas.

These features allow full spectral coverage of the SWIR, MWIR, and LWIR atmospheric transmission windows at a spectral resolution consistent with the detection of structured molecular absorption or emission bands in a compact package. These capabilities allow for the isolation of vehicle plume emissions across several bands, the detection of camouflaged targets in a cluttered environments, as well as the observation and quantification of absorption or emission from specific airborne hazardous chemicals in the presence of spectrally structured and cluttered backgrounds. Typical scenarios include:

- Detection of aircraft, cruise missiles, and theatre ballistic missiles in both the 4.3 and 2.7 μm bands, from ground, UAV, aircraft and space platforms;
- Imaging and quantification of battlefield chemical agent plumes and damage assessment of chemical production facilities;
- Monitoring of facilities important in treaty compliance;

In this paper we report on the initial use of and *AIRIS* instrument operating in the MWIR region for the observation of commercial jet aircraft as surrogates for a number of military applications. The paper will initially describe the *AIRIS* concept, subsequently review operational characteristics of the instrument, and conclude with data from both laboratory and field observations conducted under a Phase I SBIR effort with PL/GPO at Hanscom AFB.

LOW ORDER IMAGING FABRY-PÉROT INTERFEROMETRY CONCEPT

The *AIRIS* instrument comprises an IR focal plane array (FPA) coupled to a Fabry-Pérot interferometer through imaging optics. In this configuration the interferometer operates as a tunable interference filter, selecting the wavelength viewed by the FPA. In this section we describe the theoretical basis for the development of the interferometer as well as the consequences and advantages of low-order operation.

In a Fabry- interferometer light is selectively transmitted by constructive interference through the faces of two partially-reflecting parallel mirrors. Light is transmitted for wavelengths which satisfy the expression:

$$\lambda_t = \frac{2\ell}{m} \cos\theta \quad (1)$$

where

ℓ	=	mirror spacing	m	=	order of interference
θ	=	incidence angle	λ_t	=	transmitted wavelength.

A range of mirror spacings, incidence angles, and orders will all lead to the transmission of a single wavelength. The **free spectral range**, $\Delta\lambda_{\text{FSR}}$, determines the range of wavelengths transmitted between successive orders of interference:

$$\Delta\lambda_{\text{FSR}} = \frac{\lambda_{\text{max}}}{m_{\text{max}} + 1} \quad (2)$$

where m_{max} is the order in which λ_{max} is transmitted for paraxial rays.

The **finesse**, F , determines the spectral resolution of the interferometer, $(\Delta\lambda_{1/2})$, which is always a fraction of the free spectral range:

$$\Delta\lambda_{1/2} = \frac{\Delta\lambda_{FSR}}{F} \quad (3)$$

The elements which define the finesse of the interferometer arise from the reflectivities of the mirrors as well as "defects" in their configuration, such as mirror flatness and parallelism. The total finesse of the interferometer is obtained from the inverse root mean square sum of each finesse component. For practical operation in the infrared, the defect finesse is the limiting factor in determining total finesse. The total finesse can seldom be greater than approximately 30 to 50 due to these limitations. We have developed a novel alignment technique employing a digital high speed variant of capacitance micrometry which can achieve mirror spacings with an accuracy of $6 \times 10^{-3} \mu\text{m}$. Hence, mirror parallelism is seldom a limitation in the overall finesse of the system.

The interferometer field of view (focal length and detector element size) determine the range of angles incident and detected by the system. Equation (1) shows that a range of incidence angles and interference orders will allow transmission of a common wavelength through the interferometer for a single mirror spacing. The **aperture finesse** defines the degradation in spectral resolution within a single order due to this effect:

$$F_A = \frac{2}{m(\Delta\theta)^2} \quad \Delta\theta = \text{half angle FOV in radians} \quad (4)$$

As a consequence of Eq. (4), the field of view over which an acceptable finesse can be obtained increases as the interferometer is operated in lower orders. When using IR focal plane arrays, system instantaneous fields-of-view ranging from 6 to 15 deg are generally consistent with an overall finesse of 35. If external FOV scanning elements such as galvanometers are employed, the Field of Regard can be expanded to as great as 40 deg with no impact on spectral resolution. The innovative combination of an expanded free spectral range coupled with a wide field of view for low order operation of the interferometer is the focus of U.S. Patent 5,461,477 granted to Physical Sciences Inc.

OPERATIONAL CONSIDERATIONS

In contrast to typical thermal imagers, which may have spectral bandwidths of 2 to 4 μm , the high spectral resolution of the Fabry-Pérot imaging spectroradiometer limits the amount of light from the farfield incident on the detector. A consequence of the reduction in spectral bandwidth is that light originating from the nearfield optics, such as the imaging lens, interferometer mirrors and their enclosures, plays a more important role in determining the total intensity incident on the detector. A significant improvement in system performance can be obtained if the optics and their cavity are cooled to reduce their thermal radiation incident on the detector. The temperature and extent to which the optics must be cooled is a function of the detector, optics, free spectral range, and viewing geometry.

The use of focal plane arrays (as opposed to scanning single element detectors) also offers a significant improvement in performance. The primary benefit arises from the reduction in signal bandwidth which ensues from the ability to stare at a single point in space for the entire framing time. In most viewing scenarios the photon flux from the scene over the small wavelength interval sampled, compared to the inherent read noise in the FPA, determines the signal quality. If self radiance in the imager is carefully

managed, such that the detector charge wells are not filled by the near field optics, the framing time is typically controlled by the radiant intensity and the characteristic time of motion in the scene.

MWIR IMAGING INTERFEROMETER CONFIGURATIONS

Two configurations of the imaging system operating in the MWIR have been developed, with two additional systems currently under design and construction. The existing systems are described below.

Single-Order Mid-Wavelength Infrared System

This system employs a tunable interferometer module with capacitance micrometry mirror position measurement and tube-type piezoelectric mirror actuators. A concept diagram of the optical system is shown in Figure 1. A commercially available Cincinnati Electronics IRC-160, 160 x 120 InSb focal plane array (FPA) is coupled to the Fabry-Pérot tunable filter module using a 50 mm focal length $f/2.3$ lens to provide image acquisition. The capacitance micrometry system is unique in that it is entirely digital and that it communicates directly to the control system as a plug-in card on a 486-processor based ISA bus. Similarly, the high speed (< 1 ms) high voltage control card for the piezoelectric actuators is on the same bus. The 486 processor provides active control of mirror spacing and alignment of the interferometer as well as the process of image acquisition with the FPA. The IRC-160 FPA is equipped with the ISA-compatible IRDCB-2 12-bit data acquisition and control card, which includes a 27 frame memory buffer. The entire acquisition and

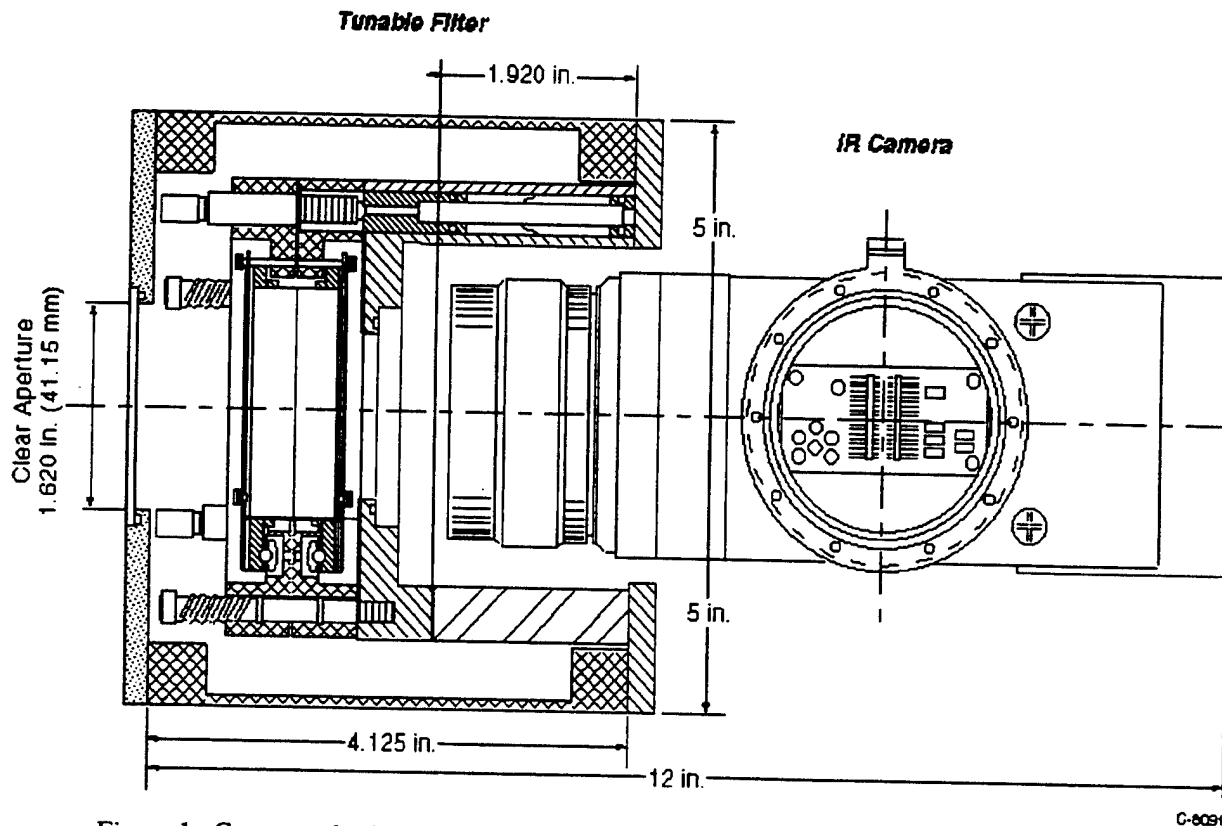


Figure 1. Conceptual schematic, with approximate dimensions, of piezoelectrically actuated imaging interferometer with interface to InSb FPA.

control system is thus contained in a single small AT-style desktop PC chassis. The system is completely compatible with ruggedized industrial PCs for field use. Custom routines allow the synchronization of image acquisition with interferometer mirror motion, all on the same processor platform. Our data processing uses the Interactive Data Language (IDL) from Research Systems Inc. Recently, we have developed routines under Microsoft C++ which allow the imager control system to function under Windows 3.1 as a DLL. This advance allows the control routine to be called directly from IDL, making possible adaptive analysis and acquisition of data. The system is capable of framing at about half the inherent rate of the camera (50 Hz), due to the synchronization of the rolling readout with the interferometer mirror motion. Limitation on data transfer from the FPA over the ISA bus further limits the framing rate to about 10 per second. These limitations are entirely a function of the FPA.

Dual-Order Mid-Wavelength Infrared System

A variant of the *AIRIS* system (*AIRIS-DF*), recently delivered to the Air Force Wright Laboratories Armament Division, uses an Amber 5128C InSb FPA capable of framing at 1000 Hz (Figure 2). Using a 286-processor based interferometer control system interfaced to a four-channel ProView system with 8 megapixels of memory, we have been able to obtain 128 x 128 hyperspectral images at a rate of approximately 165 frames per second. This system is unique in that it accepts simultaneously, two orders of interference transmitted by the interferometer (5 and 6) and directs them on to separate halves of the 128 x 128 FPA to broaden the wavelength coverage of the system while maintaining high spectral resolution.

All of the interferometer optics for the 3.5 to 5.0 μm region are at ambient temperature with the exception of the order-sorting filter. This filter is incorporated into the FPA and is held at the 77 K temperature of the focal plane. The dual-order system can be converted to single order operation by removal of the order-splitting optical train and a change of order-sorting filters. This configuration of the system was used in some of the measurements reported in this paper in order to enhance sensitivity while taking advantage of the high framing rate of the 5128C FPA.

Recently we have been very successful with both of these systems in reducing the self radiance of the optics by cooling the imaging lens assembly, which is typically focussed at infinity, while maintaining the interferometer at ambient temperature. Cooling of the lens assembly is accomplished thermoelectrically, by sealing it in a hermetic enclosure equipped with an air or water cooled heat exchanger. This configuration preserves the ability to adjust the focus while the lens is cooled. The interferometer mirrors reflect at all wavelengths, except on resonance. Thus, system self radiance is comprised of the radiance from the FPA

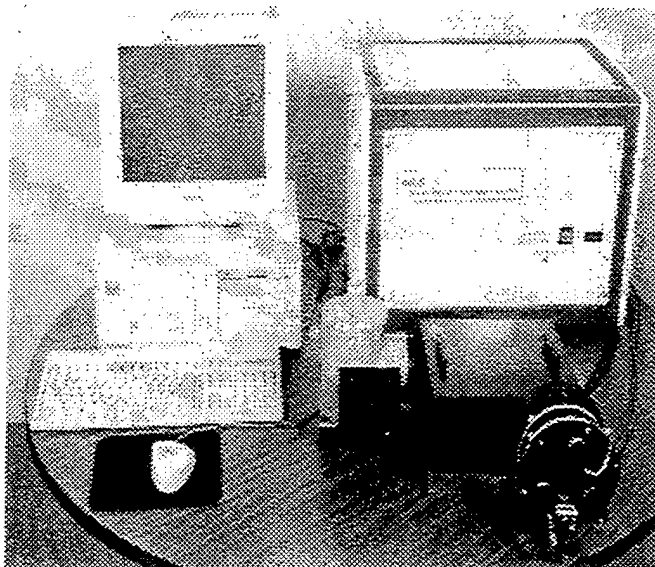


Figure 2. *AIRIS-DF* dual order imaging system showing control computer, electronics module, and Amber 5128C FPA interfaced to interferometer via dual band lens assembly.

(small) summed with self radiance and scattering from the imaging lens assembly, which is stronger for off-

axis rays. The impact of the cooled imaging lens is to reduce the self radiance of the lens assembly in direct proportion to its blackbody temperature. Supporting data for this approach is shown in Figure 3, where the centerline radiance for a system viewing an LN_2 -cooled plate is plotted as a function of lens temperature. The expected behavior for a unit emissivity blackbody is shown for comparison. The data clearly shows the comparable scaling as well as nearly a factor of 5 reduction in self radiance of the system. The use of lens cooling allows us to increase the FPA integration time while avoiding saturation. This approach is applicable to many commercially available InSb FPAs, allowing us to adapt these to multispectral imaging applications.

PERFORMANCE CHARACTERISTICS

Three key performance characteristics for the *AIRIS* system are spectral resolution, out of band rejection, and radiant sensitivity. The spectral resolution of the system was measured by placing the interferometer in the cavity of an FTIR spectrometer. A sample spectrum is shown in Figure 4, which includes a fit to an Airy function - the expected lineshape. The experimental spectrum is consistent with a finesse of 56 (spectral resolution of $0.015 \mu\text{m}$). The lineshape indicates a maximum filter transmission of 60% and a minimum in the filter transmission of 2×10^{-3} . The *AIRIS* system is calibrated radiometrically using a two-temperature blackbody approach for each pixel at each wavelength. The average radiant sensitivity of the dual-order system at each wavelength, at a temperature of 34.5°C , is shown in Figure 5. The data shows an average noise-equivalent spectral radiance (NESR) of $1.3 \mu\text{W}/(\text{cm}^2 \text{ sr } \mu\text{m})$ at a framing rate of 160 per second.

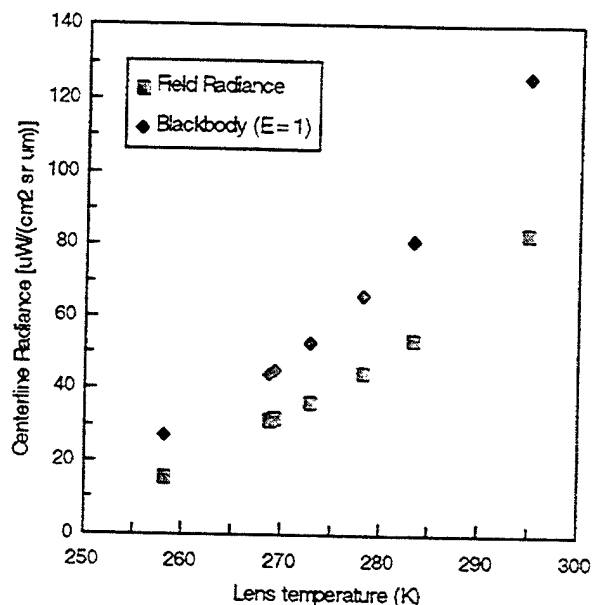


Figure 3. Apparent field radiance and calculated blackbody radiance as a function of lens assembly temperature.

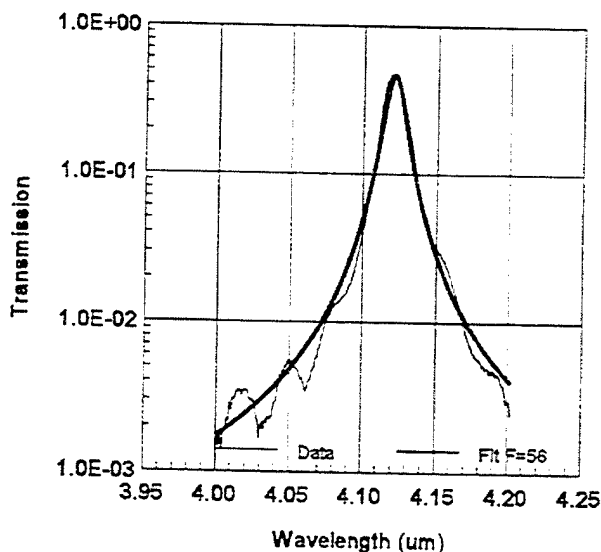


Figure 4. spectral resolution function for MWIR spectrometer measured using FTIR.

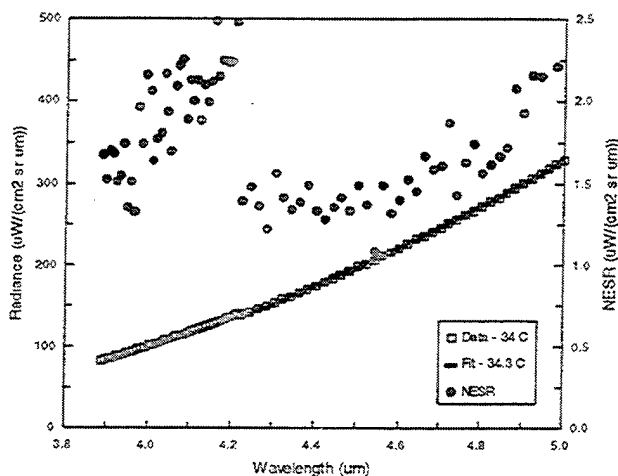


Figure 5. Radiance calibration and NESR for *AIRIS*-DF system at a temperature of 34.3°C.

gases and spectral lines were used to test resolution and provide laboratory simulations. Full spatial/ spectral data sets of several different types of clouds and aircraft have been acquired. Advanced image processing techniques are currently being developed to analyze these data sets. An example of a vehicle located in wooded terrain is presented in Figure 6 for a standoff distance of 100 meters. This scene, viewed through *AIRIS*, is a 7 x 9 deg image at 4.66 μm ($\pm 0.008 \mu\text{m}$). In the scene, an automobile is parked on the shoulder of a curved road. A grassy field is in the foreground, with trees behind. Individual tree trunks can be observed in the original data. A clear undistorted image is obtained across the entire field of view of the monochromatic scene. The tires (and even the tailpipe) are discernable. Heat reflected from the gravel under the operating engine is clearly observed. As the transmission wavelength is swept over the 4.1 to 4.8 range, the contrast and relative brightness of different objects in this scene vary. These spectral differences permit roads, trees, grass, and vehicles to be spectrally identified and processed automatically to catalog scene content and highlight regions of interest. Figure 7 shows the spectrum of the reflected engine radiance region of the base of the car. This spectrum was compiled from 28 discrete images of the scene at 0.02 μm separation.

EXAMPLES OF IMAGING INTERFEROMETER APPLICATIONS

Ambient temperature Scenes

In the MWIR, the system employing the CE IRC-160-based FPA operates at mirror separations from 12.3 to 14.4 μm ($m = 6$) with a cold bandpass filter positioned over the FPA to restrict the response to the free spectral range of 4.1 to 4.8 μm . In this spectral region thermal signatures, solar and thermal reflections, and spectral signatures from hot gases can all be observed.

AIRIS has been used to observe a variety of scenes both in the laboratory and in the field. Hot

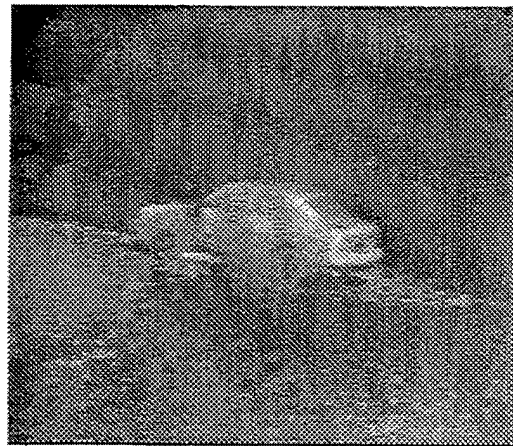


Figure 6. Image of automobile in treed scene at 4.66 μm .

Combustion/Exhaust Gasses

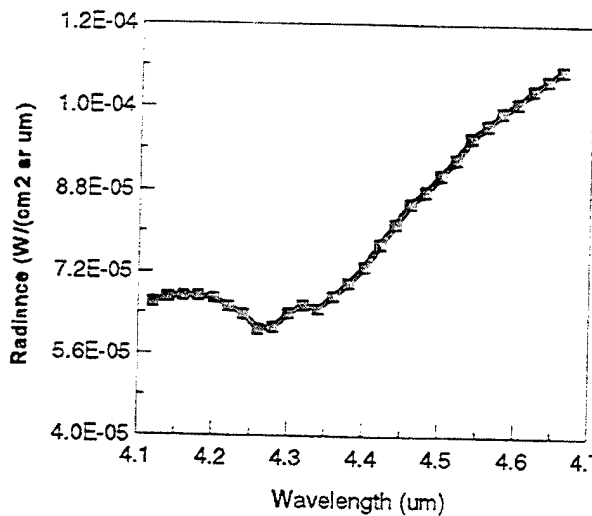


Figure 7. *AIRIS* spectrum from base region of automobile.

The *AIRIS*-DF system was optimized for the observation of countermeasures (flares) and missile exhaust plumes. In the laboratory these sources are simulated using road flares or propane torches. An example imagery from such data is shown in Figure 8 for the observation of a propane torch at a range of 2 meters. The FPA integration time is reduced to eliminate saturation in the flame region. As a result of the reduced sensitivity, emission from the scene background falls below the detection limit. The scene is viewed at 80 discrete wavelengths over the range from 3.80 to 4.95 μm . The spectrum of the region at the base of the torch is shown in Figure 9. The calibrated spectrum clearly shows the CO_2 emission from the flame region, as modified by the 4.3 μm atmospheric absorption band.

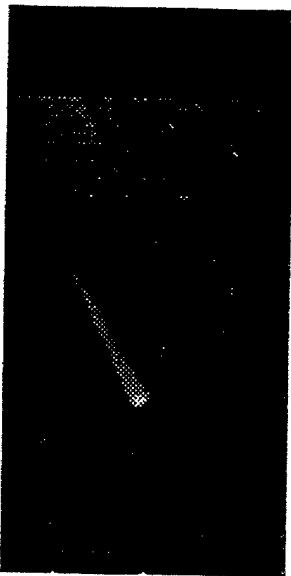


Figure 8. Propane torch image at 4.48 μm .

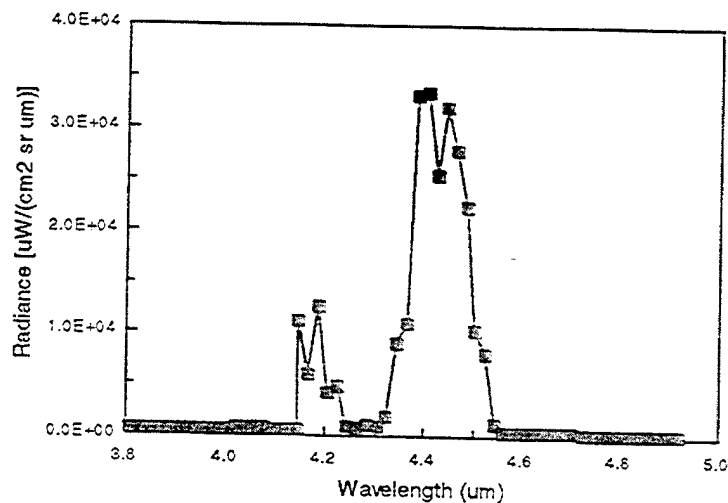


Figure 9. Spectrum of base region of propane torch.

Field Observations of Propane Torch

The *AIRIS* system has been used to detect similar emission spectra in cluttered scenes. In this paper we report on preliminary data employing a simple correlation analysis to use spectral signatures to identify the torch at a sub-pixel level size scale. A visible image of the test scene is shown in Figure 10, with a comparable IR image of the scene, recorded at 4.56 μm , shown in Figure 11. The location of the torch in the

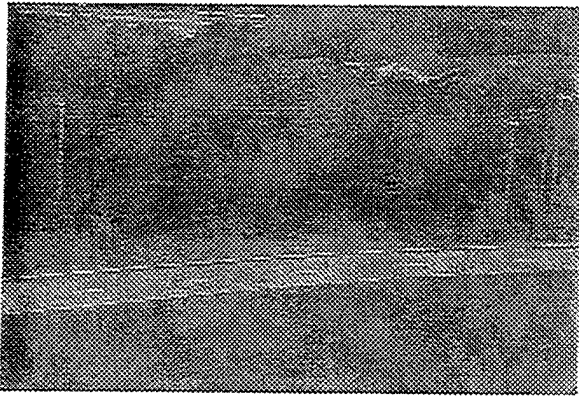


Figure 10. Visible image of scene containing propane torch used in correlation analysis.

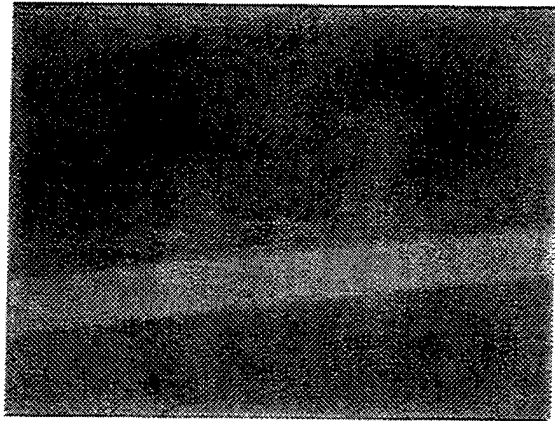


Figure 11. IR image of scene containing propane torch at 4.56 μm .

scene is somewhat evident in the IR image. From the spectral/spatial data cube of this scene we extracted feature spectra of various elements in the scene. Examples are shown in Figure 12 for the torch, road, and treed background. These spectra show a clear difference in the spectra of these various regions, although some residual calibration issues remain in the data as a result of thermal drift in the optics temperature. This data was used to conduct a two band correlation analysis using 4.36 and 4.56 μm images. The goal of the analysis was to isolate the spatial region containing the torch in the scene. The correlation analysis is shown in Figure 13. The data was fit using a linear least squares analysis to define the characteristics of the background. This fit, as well as the 5σ error limits, are also shown in the figure. Points lying outside the 5σ error limits are then plotted as white points on a black field in Figure 14 to reveal the location of the torch in the scene, isolated from other scene clutter. We are currently working on additional data acquisitions and analysis approaches to improve the ability to detect much weaker sources against comparably cluttered scenes.

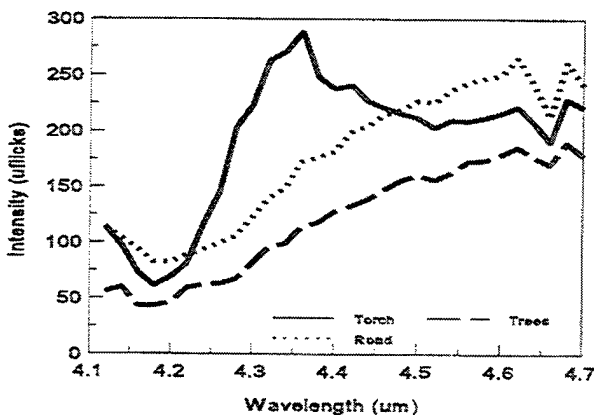


Figure 12. Feature spectra of various scene elements recorded using *AIRIS* imager.

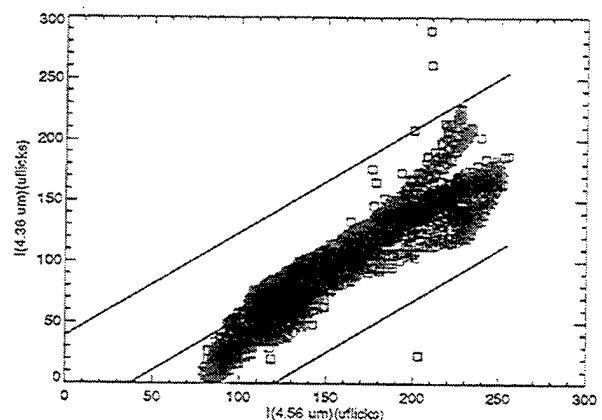


Figure 13. Correlation plot for IR imagery showing data (□), fit to data, and $\pm 5\sigma$ bounds on fit.

IMAGING OF AIRCRAFT

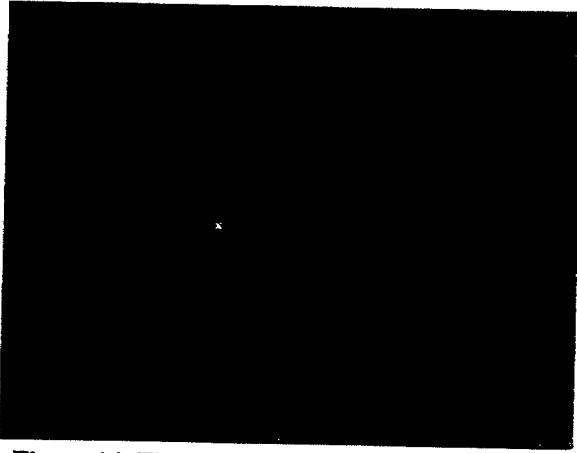


Figure 14. High contrast image from correlation analysis of IR imagery identifying the location of a sub-pixel flame in the scene.

Initial field evaluations of AIRIS with aircraft have been conducted at Hanscom AFB using commercial jet aircraft as surrogate targets. The AIRIS-DF system was reconfigured for single order operation at high framing rates in order to freeze motion within a single data cube. In these initial evaluations a data cube was comprised of 4 wavelengths, 4.18, 4.40, 4.50, and 4.60 μm . Due to delays in equipment availability, these measurements were not conducted until January 1997. The rather cold ambient backgrounds limited system S/N, even with the use of the cooled lens assembly. This factor severely limited scene backgrounds. To further enhance signal quality 8 exposures of the FPA were averaged at each wavelength. A typical scene imaged in the preliminary measurements is shown in Figure 15 (visible) and

Figure 16 (infrared). In this acquisition the primary emission overserved in the scene is simple blackbody emission from the engine, which was in low idle. This data is shown in Figure 17 where differential radiance is shown for the exit duct, expected plume region, and the background. These measurements will be continued and expanded to include full spectral/spatial data sets.

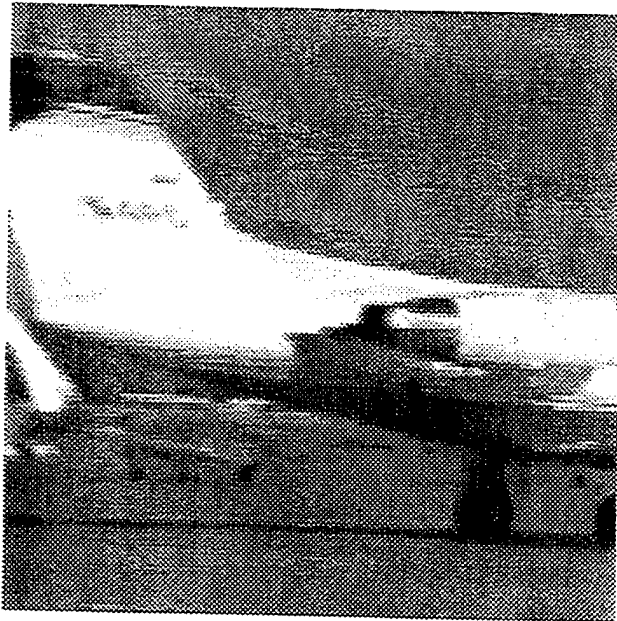


Figure 15. Visible image of commercial jet aircraft at low idle on taxiway at Hanscom AFB.

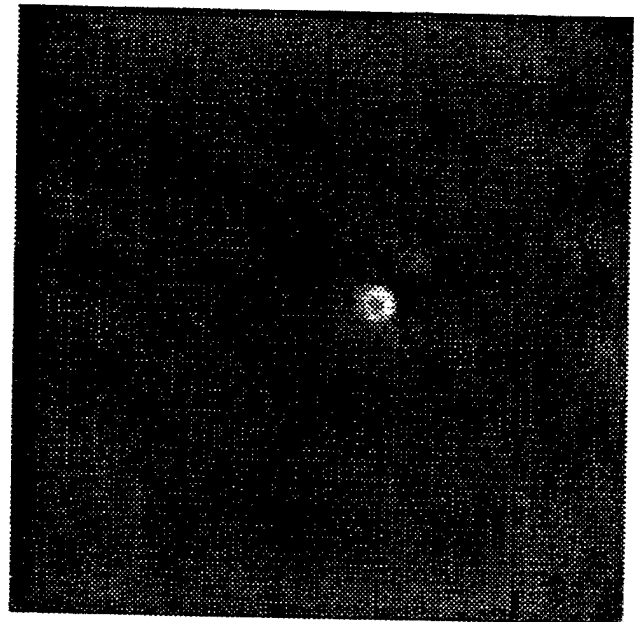


Figure 16. IR image of scene in Figure 15 at 4.18 μm recorded with AIRIS.

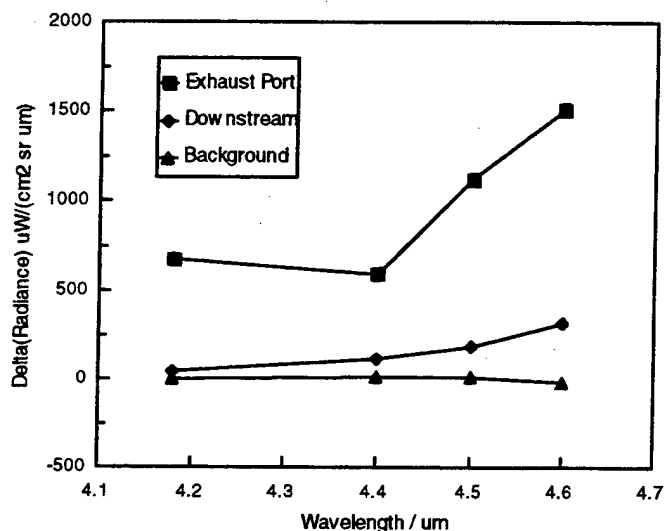


Figure 17. Differential radiance as a function of band in the scene of Figure 16.

SUMMARY AND STATUS

The ability of the Adaptive IR Imaging Spectroradiometer to produce monochromatic scene radiances over an extended field of view has been demonstrated in the laboratory and in limited field testing. These measurements will continue under the current and related programs. In Phase II the *AIRIS* system capability will be extended into the $2.7 \mu\text{m}$ SWIR region using a second FPA. An airborne system will be developed and tested having co-registered hyperspectral imagery in the visible, SWIR and MWIR regions. In the visible region a CCD camera, coupled to a liquid crystal tunable filter will be used to provide the multispectral capability.

ACKNOWLEDGMENTS

This effort was funded under a Phase I SBIR contract with the USAF Phillips Laboratory under contract F19628-96-C-0092. The authors would like to thank Steve Lipson and Pete Armstrong at PL/GPO and Chris Gittins at PSI for their assistance in data acquisition and analysis. We would also like to thank Howard Kuenzles at PL/GPIA for accommodating the staging of *AIRIS* from their location on the penthouse of Building 1105B at Hanscom AFB. Finally, PSI would like to acknowledge the assistance of the Wright Laboratory's Armament Directorate (Eglin AFB) and Ron Rapp for the use of *AIRIS*-DF under a bailment agreement.